Preparation and Characterization of Ligand Functionalized Solid Support for the Selective Extraction of f- Elements

By

SUMIT PAHAN

CHEM01201504001

BHABHA ATOMIC RESEARCH CENTRE

A thesis submitted to the

Board of Studies in Chemical Sciences

In partial fulfillment of requirements
for the Degree of

DOCTOR OF PHILOSOPHY
of
HOMI BHABHA NATIONAL INSTITUTE

December 2020

Homi Bhabha National Institute

Recommendations of the Viva Voce Committee

As members of the Viva Voce Committee, we certify that we have read the dissertation prepared by Shri. Sumit Pahan entitled "Preparation and Characterization of Ligand Functionalized Solid Support for the Selective Extraction of f- Elements" and recommend that it may be accepted as fulfilling the thesis requirement for the award of Degree of Doctor of Philosophy.

Chairman-Dr. P. K. Mohapatra	18-4.21
Guide / Convener –Dr. C. P. Kaushik	3/5/21
Co - guide – Dr. D. Banerjee	18.4.21
External examiner –Prof. J. K. Singh	**18.04.21**
Member 1-Dr. Manmohan Kumar	Manmohan Kumar 3/5/21
Member 2-Dr. Sk. M. Ali	18-4-2021
Member 3-Dr. P.S. Dhami	

Final approval and acceptance of this thesis is contingent upon the candidate's submission of the final copies of the thesis to HBNI.

I/We hereby certify that I/we have read this thesis prepared under my/our direction and recommend that it may be accepted as fulfilling the thesis requirement.

Date: 03/05/2021

Place: Trombay

Signature

Guide

3/5/21

STATEMENT BY AUTHOR

This dissertation has been submitted in partial fulfillment of requirements for an advanced degree at Homi Bhabha National Institute (HBNI) and is deposited in the Library to be made available to borrowers under rules of the HBNI.

Brief quotations from this dissertation are allowable without special permission, provided that accurate acknowledgement of source is made. Requests for permission for extended quotation from or reproduction of this manuscript in whole or in part may be granted by the Competent Authority of HBNI when in his or her judgment the proposed use of the material is in the interests of scholarship. In all other instances, however, permission must be obtained from the author.

Sumit Pahan

Sumit Pahan

DECLARATION

I, hereby declare that the investigation presented in the thesis has been carried out by me. The work is original and has not been submitted earlier as a whole or in part for a degree / diploma at this or any other Institution / University.

Sumit Pahan

Sumit Pahan

1. **Name of the Student: Sumit Pahan**
2. **Enrolment Number: CHEM01201504001**
3. **Title of the Thesis : Preparation and Characterization of Ligand Functionalized Solid Support for the Selective Extraction of f- Elements**

Publications from Present Investigation

Journal

1. Pahan, S.; Boda, A.; Ali, Sk. M. Density functional theoretical analysis of structure, bonding, interaction and thermodynamic selectivity of hexavalent uranium (UO_2^{2+}) and tetravalent plutonium (Pu^{4+}) ion complexes of tetramethyldiglycolamide (TMDGA). *Theor.Chem. Acc.* **2015**, *134*, 41.
2. Ali, Sk. M.; Pahan, S.; Bhattacharyya, A.; Mohapatra, P. K. Complexation thermodynamics of diglycolamide with f-elements: solvent extraction and density functional theory analysis. *Phys.Chem.Chem.Phys.* **2016**, *18*, 9816.
3. Singh Deb, A. K.; Pahan, S.; Dasgupta, K.; Panja, S.; Debnath, A. K.; Dhami, P. S.; Ali, Sk. M.; Kaushik, C. P.; Yadav, J. S. Carbon nano tubes functionalized with novel functional group amidoamine for sorption of actinides. *J. Hazard. Mater*. **2018**, *345*, 63.
4. Pahan, S.; Panja, S.; Banerjee, D.; Dhami, P. S.; Yadav, J. S.; Kaushik, C. P. Preparation of chitosan functionalized polyamidoamine for the separation of trivalent lanthanides from acidic waste solution. *Radiochim. Acta.* **2019**; *107(5)*, 415.
5. Pahan, S.; Sengupta, A.; Yadav, A. K.; Jha, S. N.; Bhattacharyya, D.; Ali, Sk. M.; Khan, P. N.; Debnath, A. K.; Banerjee, D.; Vincent, T.; Manohar, S.; Kaushik, C. P. Exploring functionalized titania for task specific application of efficient separation of trivalent f-block elements. *New J. Chem*. **2020**, *44*, 6151.

a. Accepted: NO

b. Communicated:

1. Pahan, S.; Dutta, B.; Panja, S.; Barick, K. C.; Dhami, P. S.; Banerjee, D.; Manohar, S.; Sugilal, G.; Kaushik, C. P. Novel polyphosphate – grafted Fe_3O_4 nanomagnets for removal of trivalent radionuclides from acidic nuclear waste solution.
2. Pahan, S.; Panja, S.; Yadav, A. K.; Jha, S. N.; Bhattacharyya, D.; Ali, Sk. M.; Debnath, A. K.; Banerjee, D.; Vincent, T.; Manohar, S.; Sugilal, G.; Kaushik, C. P. Preparation of DGA functionalized titania for the separation of trivalent actinides and lanthanides from acidic waste solution.
3. Pahan, S.; Sengupta, A.; Ali, Sk. M.; Banerjee, D.; Vincent, T.; Sugilal, G.; Kaushik, C. P. Dipicolinamide functionalized titania for highly efficient separation of tetra and hexavalent actinide.

Other Publications:

---

a. Book/Book Chapter: NO

b. Conference/Symposium

1. Pahan, S.; Singhadeb, A. K.; Dasgupta, K.; Ali, Sk. M.; Shenoy, K. T.; Shah, J. G.; Banerjee, K. Separation of Actinides by Amidoamine Functionalized Carbon Nanotube. *DAE-BRNS SESTEC-2016;* IIT Guwahati, *Assam, INDIA, May* 17-20, *2016*

2. Pahan, S.; Panja, S.; Banerjee, D.; Kaushik, C. P.; Shah, J. G.; Agarwal, K. Preparation of Chitosan Functionalized Polyamidoamine for the Separation of Trivalent Lanthanides from Acidic Waste Solution. *SESTEC-2018; BITS Pilani, Goa, INDIA, May 23-26, 2018.*

3. Pahan, S.; Sengupta, A.; Ali, Sk. M.; Khan, P. N.; Banerjee, D.; Vincent, T.; Manohar, S.; Kaushik, C. P. Complexation of Trivalent f-Block Elements with DPA Functionalized TiO_2. *DAE-CCS -2019*; *BARC, Mumbai, INDIA, November* 7-9, 2019.

Sumit Pahan

Dedicated to
- *My family*

Bhattacharya, Dr. K. C. Barick, Dr. A. Ghosh, Dr. A. Boda, Mr. P. Sinharoy, Mr. P. N. Khan, and all the others in **PSDD** and **FRD** laboratory for their help, cooperation and suggestions during the course of the work.

The technical support of **A. Joseph, A. M. Majrekar, V. Jaiswal, S. A. Khot, P. J. Yevale** and other colleagues is gratefully acknowledged.

I would like to acknowledge all the ***teachers***; I learnt from since my childhood. I acknowledge all the reviewers to make my work fruitful.

No words of acknowledgment will be sufficient for my family. I am indebted to my parents, uncle, aunties, sister, brothers and my wife **Sarmistha** for their care, dedication and love. Words fail me to express my appreciation for my little daughter **kaushiki** who in her own way geared me up to reach the goal.

Apart from all the people mentioned in this acknowledgement there are many others who helped me in various ways during this thesis work. My sincere thanks and apologies to those I may have forgotten to mention.

Last but not least I am thankful to Almighty without Him / Her I could do nothing.

Sumit Pahan

Sumit Pahan

Contents

6 Chapter 6: Studies of Metal Ligand Complexation Using Density Functional Theory 172

List of Tables

List of Figures

Chapter 7: Conclusion and Future Directions

Chapter 7

Conclusion and Future Directions

This thesis is devoted to the study and understanding of solid phase extractants (SPE). This work is motivated by the limitations of extant solvent based extraction processes including the copious use of volatile organic compounds (VOC) and the attendant economic/emvironmental footprint. The advantages of SPE include simplicity, rapidity, convenience, easy operation, cost effectiveness and low secondary waste generation. However, balancing the benefits of SPE is often challenging synthesis processes with poor yields.

The work on SPEs is broadly directed along two avenues:

i) supported liquid – liquid extraction

ii) solid – liquid extraction

Supported liquid – liquid extractions are mainly operated by coating/impregnating the chelating agents on solid substrate. The main disadvantage of impregnated solid support is leaching of chelating agent from solid support which results in gradual loss of capacity and useful lifetime.

In this thesis, SPE for solid – liquid extraction have been developed using chemically anchored ligands on solid supports. Compared to supported liquid - liquid extractants, the chemical anchoring is expected to improve the life of these extractants significantly. Furthermore, owing to their selective and effective extractive nature enable the extraction of f – elements with a limited number of separation steps, which should translate positively in terms of waste volume reduction.

In order to study the sequestration of f elements from nuclear waste using solid phase extraction technique, efforts have been made during the present dissertation to synthesize five different ligand fictionalization over suitable solid supports. The ligands such as amido-amine, PAMAM, polyphosphate, dipicolinamide and diglycolamide are chemically functionalized over the different solid supports such as MWCNT, Chitosan, TiO_2 and Fe_3O_4.

The synthesized extractants were characterized using BET for surface area analysis, XPS, Zeta Potential measurements and Raman spectroscopy to study the functionalization.

Surface morphology and presence of various functional groups on the developed materials were characterized by using scanning electron microscope hyphenated with energy dispersive spectrometer (SED-EDS) and attenuated total reflectance Fourier transform infra red spectrometry (ATR-FTIR) respectively. The developed materials were used for removal of f – elements from nuclear waste solution. Various parameters (e.g. pH, contact time) for uptake were optimized. Isotherm and kinetics were tested for all the developed materials.

The main objectives of the present work can be summarized as:

1. Preferential extraction of the target metal ions from the nuclear waste solution by chemically functionalized solid supports. As a part of this objective, the effect of competing metal ions, radiolytic stability and possible avenues for recycling of the solid supports was also investigated
2. To overcome the problem of large quantities of chemicals used in the liquid phase extraction processes by using chemically functionalized organic extractant on a solid support, where only sub-milli molar concentration of organic ligands are required
3. Understand the complexation and thermodynamic behavior associated with the extraction procedure using density functional theory (DFT) based calculations

The following functionalized materials were synthesized and the results of the contaminants removal are summarized below.

i) **Amido-amine functionalized MWCNTs**

Briefly, the above functionalized material is prepared by oxidation of MWCNT followed by coupling of EDA with it in presence of DCC. The material obtained was characterized using the above mentioned techniques. The salient findings are:

- The sorption process was found to be highly dependent on the pH of the feed solution with maximum sorption for both ^{233}U, $^{152+154}$ Eu and ^{241}Am at pH 6.0
- Kinetics of sorption was found to be fast with equilibrium reached in~15 minutes for all the radionuclides
- The sorption for both ^{233}U and $^{152+154}$Eu followed Langmuir sorption model with maximum sorption capacity of 20.66 mg/g and 16.1 mg/g respectively
- Complexation of the metal ions with carbonyl and amine part of the functional group was validated by DFT calculations
- Sorbed metal ions from AA-MWCNTs was efficiently recovered using 1M HNO_3.

ii) PAMAM functionalized Chitosan

The PAMAM polymers were introduced into Chitosan by two step processes i.e. Michael addition reaction between methyl acrylate and Chitosan followed by the coupling reaction using EDA. Salient findings for this material are:

- The results of the extraction study clearly showed the potential of this material to extract Am and Eu from nuclear waste

- The sorption process for both trivalent f – elements show increasing trend with the increase of feed solution pH
- The adsorption kinetics is pseudo-second order for both metal ions, and equilibrium is attained in ~ 10 minutes
- Langmuir isotherm model was found to fit the sorption process for Eu(III) and maximum sorption capacity was calculated.
- The effect of the generation of PAMAM dendron on the extraction efficiency and kinetics of extraction show that with increasing functionalization, the improved extraction efficiency is balanced by steric hindrance, resulting in similar extraction performance across generations
- The material shows excellent recycling potential

iii) DPA functionalized TiO_2

Dipicolinic acid (DPA) functionalized anatase through an amino ethoxysilane bridge was synthesized, characterized and evaluated for extraction of Ln and Ac. The key findings are:

- DPA functionalized anatase showed highly efficient sorption of f – elements from aqueous acidic medium through chemical interaction.
- The DPA functionalized TiO_2 contain a hard base donor atoms so preferential interaction with trivalent lanthanide compared to trivalent actinide and Th over uranium was observed due to higher effective charge.
- The adsorption process predominately follow Langmuir isotherm model where as kinetics of extraction found to be operative pseudo 2nd order model.

- Maximum sorption capacity for U(VI), Th (IV), Am (III) and Eu(III) were experimentally calculated. Complexation of radioresistant sorbent with Am^{3+}/Eu^{3+} was experimentally investigated using EXAFS, XANES and XPS.
- Complexation structure of f – elements with functionalized titaniawere optimized using DFT. The Gibbs energy of extraction for aqueous phase complexation of the metal ions were also calculated.

iv) DGA functionalized TiO_2

Diglycolamide (DGA) was functionalized on the surface of titania by two step chemical reaction. Salient findings for this material are:

- The synthesized material applied for the sequestration of Am(III) and Eu(III) from nuclear waste solution.
- Sorption of Am(III) and Eu(III) metal ions by DGA functionalized TiO_2 is highly dependent on the pH of the aqueous feed solution.
- The kinetics of sorption for both the radionuclides by the DGA –TiO_2 is found to follow pseudo second order kinetic model with equilibrium attained in ~ 30 min.
- The maximum sorption capacity for Eu(III) was found to be approx. 34 mg g^{-1} .
- The DFT calculated solvent phase free energy of adsorption for Am (III) was found to be lower than Eu(III) as observed in the experiments.
- The material shows good recylalable property.

v) Poly phosphate functionalized Fe_3O_4

Polyphosphate grafted Fe_3O_4 nanomagnets were synthesized by precipitation of Fe^{2+} and Fe^{3+} ions in alkaline medium followed by surface functionalization using sodium tripolyphosphate. Salient findings are as follows:

- Characterization techniques (discussed previously) show the formation of a single phase Fe_3O_4 nanostructure with average diameter of 40 nm with a coating of sodium tripolyphosphate on the surface of the Fe_3O_4 nanoparticles
- Extraction study shows that the sorption efficiency of PPNMs for both Am and Eu increases with solution pH, whereas increasing ionic strength of the medium led to a decreasing trend
- The kinetics of sorption for both the radionuclides by the PPNMs is found to follow pseudo second order kinetics with equilibrium attained in ~ 5 min
- The isotherm study indicates that the Langmuir model is relevant for this material. A maximum sorption capacity 10.60 mg/g for Eu(III) was demonstrated
- The reusability study shows that even after 10 successive cycles of operation the PPNMs maintain their sorption efficiency.

Therefore, this thesis has successfully demonstrated the preparation, characterization and operation of several novel ligand functionalized materials with sorption capacities. The work can then be extended in the following directions.

i) The extraction studies in this thesis have been demonstrated in batch mode. Extension to column mode will greatly improve the applicability of this technology

ii) While the efficiency of the functionalized sorbents is encouraging compared to conventional solvent extraction, methods to avoid pH adjustment have to be evaluated

iii) Further development into novel synthesis protocols to increase yield through more facile synthesis has to be evaluated. The effect on selectivity, kinetics and potential to scale-up must also be carefully evaluated

As such, the ligand functionalized solid sorbents can fulfill an important role in nuclear waste management to allow fast and efficient waste treatment. The efforts in this field are in a nascent stage and concerted collaborations between research, development and industry are pushing new boundaries. Since nuclear waste management is an integral part of harnessing the power of the atom, the work into ligand functionalized solid sorbents is vibrant and full of potential.

1. **Name of the Student: Sumit Pahan**
2. **Enrolment Number: CHEM01201504001**
3. **Title of the Thesis: Preparation and Characterization of Ligand Functionalized Solid Support for the Selective Extraction of f- Elements**

Abstract of thesis

Present thesis discusses synthesis of ligand functionalized solid supports, characterization, their application for separation of f – block radionuclides like Uranium, Americium and Europium from radioactive waste solution and the metal ligand complexation pattern. The thesis has been divided into seven chapters. The first chapter describes overview of present waste management scenario highlighting the basic aspects like generation of waste, waste classification, waste management practices in India. Major focus has been given on the advantages of solid phase extraction strategy over the conventional solvent extraction technique for the separation of radionuclides from nuclear waste. In this study five different solid phase sorbents (Amidoamine functionalized carbon nanotube, Poly amidoamine functionalized chitosan, Dipicolinamide functionalized titania, Diglycolamide functionalized titania and Poly phosphate functionalized magnetite) were synthesized. The functionalization were confirmed by different characterization techniques (XPS, Raman, FTIR, XRD, EDEX etc). All these synthesized materials were evaluated for the extraction of f-elements from nuclear waste solution. The effect of pH, equilibration time, ionic strength and other ions during extraction and their ability to use in multiple cycle of operation has been investigated. The radiolytic stability of the materials also appraised for their use in nuclear waste management. Based on isotherm sorption data it was concluded that the sorption follows chemisorption mechanism.

The study elaborated the mechanism of complexation between the modelled metal ions and the synthesized sorbents using Density functional Theory (DFT). By the evaluation of structural parameters and their electronic interaction values the mechanism of complexation were predicted. Again the thermo dynamical parameters study gave his experimental results an additional support.

In summary, the dessertation presented an exciting overview of selective complexatio of f-elements with the synthesized solis phase sorbents his, has important relevance to nuclear waste management practises in present scenario.

Chapter 1 Introduction

Introduction

Energy requirements are increasing worldwide, and more particularly in developing countries including India. At present, most of the energy requirement of developing countries is met with fossil fuel resources such as natural gas; and pre-dominantly coal and oil. In addition to their non-ubiquity in most parts of the world, fossil fuels cause considerable pollution, which is increasingly unsustainable. Indeed, it is expected that the increasing consumption of fossil fuels will directly affect the quality of lives of billions of people due to diseases, pollution and climate change.

Nuclear power promises to replace fossil fueled thermal energy generation by combining high cost efficiency, low environmental impact and high energy density. At present, nuclear power is the fourth largest source of electricity in India after thermal, hydro and renewable sources of electricity. Around 37813 million Units electricity was produced by nuclear power in India in 2018-2019.

Even globally, nuclear power plays an important role as evidenced by the 450 operational nuclear power plants worldwide having capacity of 396.4 GW(e) with 55 further reactors under construction [1] . Out of these, India presently has 22 nuclear reactors in operation at seven sites, producing 6255 MW and 7 more reactors are presently under construction to generate an additional 4824 MW. Keeping with anticipated demands for energy from an ever growing India, the nation's nuclear power program is undergoing a rapid expansion with plans to increase the power output to 64,000 MW by 2032 with 25 % nuclear contribution to the power grid envisaged by 2050 [2, 3]. Therefore, nuclear power is an important contributor to the future energy security of the nation.

Consequently, optimum management solutions for highly active, long-lived wastes are important to ensure safe and socially acceptable adoption of nuclear power. Among the various waste generated, actinides combining α-activity with a very long half life are of particular concern. Additionally, some actinides such as ^{241}Am are valuable as sources in smoke detectors and energy sources for space craft. Therefore, separation and recovery of actinides is an interesting and technologically relevant problem. In this introductory chapter, a brief historical perspective of the discovery of actinides is presented followed by a discussion on their occurrence in the nuclear fuel cycle.

1.1 Historical Perspective of Actinides

The first discovery of radioactivity is widely credited to Henry Becquerel in 1896. He used Uranium metal for his discovery and observed the effects of its radiations on photographic plates. While Becquerel was the first to discover radioactivity in Uranium, the metal itself had been isolated from pitchblende in 1841 by Eugène-Melchior Péligot by reducing UCl_4 with metallic K. Indeed, Péligot also proved that U in pitchblende occurs as an oxide UO_2. Of course, history records that U was discovered in pitchblende by Martin Heinrich Klaproth in 1798, and named after the then newly discovered outer planet, Uranus.

For the first part of the 20th century the strange rays emitted by pitchblende and indeed Uranium were a matter of academic interest only. However, the emergence of quantum mechanics in the early decades of the 20th century brought about a deeper understanding of the atom, and motivated further studies into the constituents of the atom itself. The electron was already known in 1897 thanks to J. J. Thomson and the layout of the atom with a nucleus and electron orbiting the same was favored due to the gold foil experiments of Ernst Rutherford. However, the nucleus itself remained mysterious till the discovery of the proton in 1919 by Rutherford and the discovery of the neutron in 1932 by

James Chadwick. Indeed, the entirety of nuclear energy rests on the foundations of Chadwick's discovery.

In the 1930s, Enrico Fermi suggested the use of neutron bombardment for the synthesis of new radioactive elements and carried out a series of neutron induced reactions on a range of target elements. He also proposed that uranium after capturing a neutron can be converted into heavier beta-radioactive uranium isotope, which on decay would give birth to a new transuranic with atomic number 93.

$$238_{U} \quad (n, \gamma) \rightarrow 239_{U} \overset{\beta}{\rightarrow} 239_{Np} \qquad (1.1)$$

The experiments that would lead to the synthesis of this new element were carried out in 1940 at the Berkley radiation laboratory by Edwin McMillan and Philip Abelson. As the next element after Uranium, it was named Neptunium. Neptunium would be the first in a long list of synthesized elements.

At the same time, with the clouds of World War-II looming over Europe, renowned radiochemists led by Irene Curie and Frederick Joliot in Paris; and Otto Hahn and Lise Meitner, in Berlin were working on a deeper understanding of nuclear fission. The latter group of Hahn and Strassmann discovered nuclear fission in 1939 and opened new avenues in the field of nuclear research related to uranium.

$$n \quad + \quad 235_{U \rightarrow} \ 236_{U^*} \rightarrow 92_{Kr} \quad + \quad 14\ 2_{Ba} \quad + \quad 3n \quad (1.2)$$

This work and the reaction given above would form the basis for the harnessing of nuclear power. However, the ploughshare of nuclear energy would first be hammered into the sword of nuclear weapons in the crucible of World War – II, aided by the discovery of Pu.

By 1941, Glenn T. Seaborg, Edwin McMillan, Joseph Kennedy and Arthur Wahl (Berkeley, California) discovered element 94 (^{238}Pu) after deuteron bombardment of ^{238} U in a cyclotron.

$$238_{U} \quad (d,2n) \rightarrow 238_{Np} \overset{\beta}{\rightarrow} 238_{Pu} \qquad (1.3)$$

^{239}Pu was produced by the bombardment of uranium with slow neutrons. It was also discovered that ^{239}Pu could sustain chain reactions similar to ^{235}U.

$$238_{U} \quad (n,\gamma) \rightarrow 239_{U} \overset{\beta}{\rightarrow} 239_{Np} \overset{\beta}{\rightarrow} 239_{Pu} \qquad (1.4)$$

Seaborg and his coworkers made significant contributions towards the discovery of transuranic elements by identifying thirteen new elements (element 94-106) in a span of 30 years (1944-1974). Based on their chemical properties, Seaborg proposed the actinide concept in 1944 [4], and placed the 15 elements, Actinium (89) to Lawrencium (103) below the lanthanides in the periodic table [5].

Thus, the discovery of actinides opened the gateway to the nuclear age for human civilization. The capability of fissile isotopes of U and Pu to sustain chain reaction has been employed in the production of nuclear energy. The fission reactions and attendant neutron capture processes results in the formation of a large quantity of transuranics such as Np, Pu, Am, Cm, etc., with many of their isotopes having long half-life and decaying by alpha decay. However, this reactor operation results in the formation of transuranic elements by neutron capture and beta decay as shown in **Fig. 1.1**. The long lived radionuclides are depicted by the grey background.

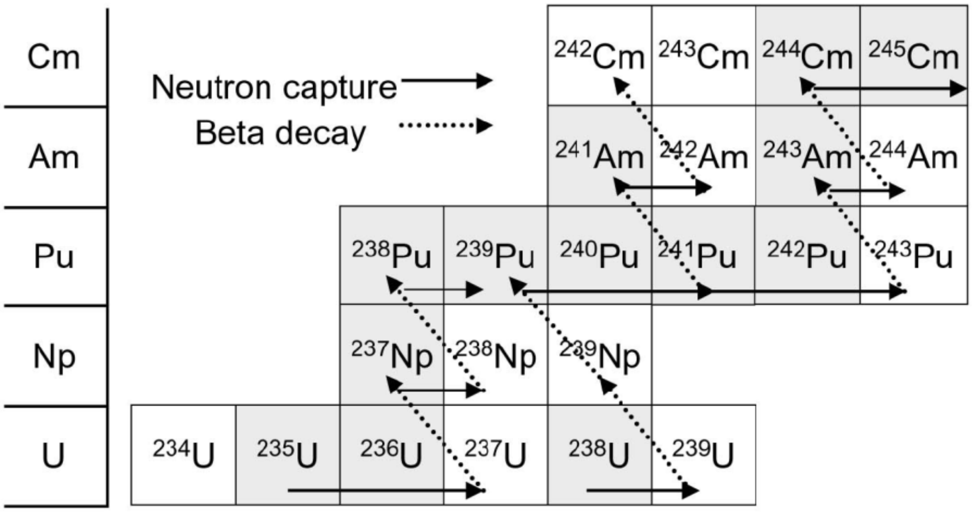

Figure 1.1: Production of transuranium radionuclides in the reactor [6]

Out of these transuranium elements Np, Am and Cm are known as minor actinides (MA) in the spent fuel.

1.2 Principle of Nuclear Fission and Nuclear Reactor

The discovery of nuclear fission is an important landmark in the history of nuclear science. When any fissile materials like ^{235}U, ^{239}Pu, ^{233}U etc are bombarded by thermal neutrons ($E_n < 0.025$ eV), two or more fission fragments are produced. Additionally, approximately three neutrons are also released, which may (depending upon the density and arrangement of fissile material) cause further fissions, furthering a chain reaction. The mass difference between the products and the parent atoms in fission is released as energy in accordance with Einstein's famous mass energy equivalence relationship.

^{235}U is the only naturally occurring fissile material that undergoes fission process as shown in Equation (1.2) where fission products and neutrons released per fission per atom of ^{235}U are shown. [7]

The mass-yield curve of thermal neutron induced fission of ^{235}U is shown in **Fig. 1.2.** At low energies, typical of thermal neutrons, asymmetric fission is more probable. This results in two maxima in the mass yield curve centered around 95 and 140 amu. As mentioned previously and shown in **Fig. 1.3**, the fission process also releases neutrons which can initiate further fissions. Given adequate density of fissile material, the chain reaction can exponentially grow leading to a nuclear explosion.

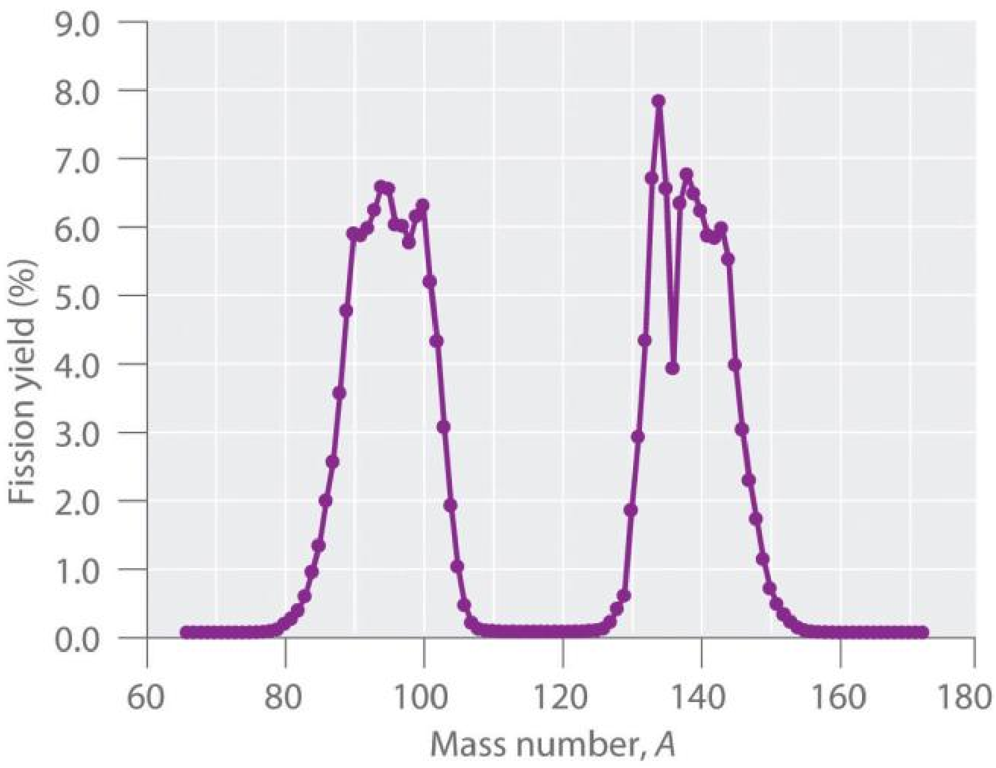

Figure 1.2: Thermal neutron fission yield curve for ^{235}U [8]

In contrast, a nuclear reactor uses suitable neutron absorbers to control the number of neutrons, thereby preventing runaway chain reactions, allowing long term energy generation.

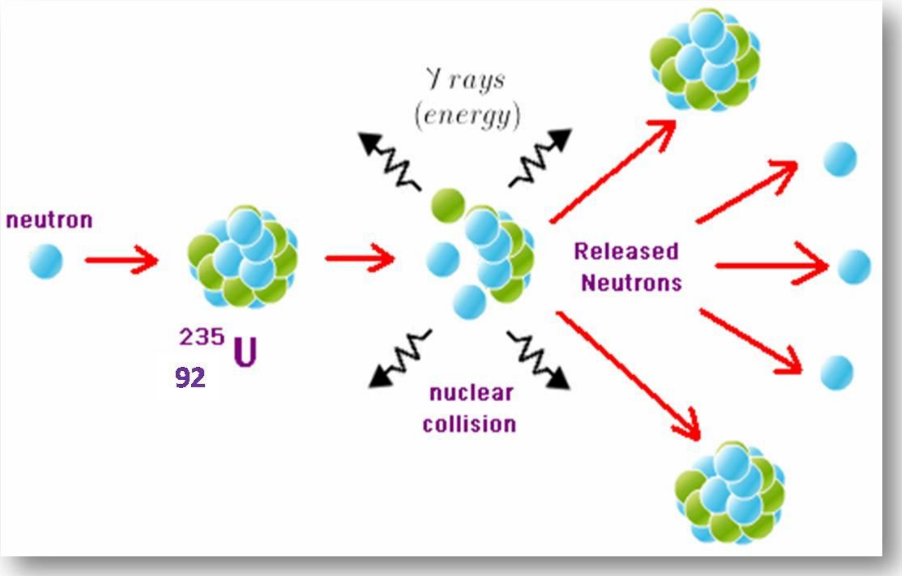

Figure 1.3: Nuclear fission of ^{235}U

Since the 1950s when Enrico Fermi perfected the first atomic pile, various designs and types of nuclear reactors have been designed and implemented. These nuclear reactors can be classified on the basis of their applications, coolant /moderator system and energy of neutrons. Typically, global reactor design has gone down two paths: The first requires enriched uranium, but uses light water as a moderator. The second path eschews the challenges of uranium enrichment by utilizing natural uranium; but requires the use of heavy water as a moderator. India, with extensive experience in the preparation of heavy water, has chosen to proceed down the second path. Consequently, most operational Indian power reactors are pressurized heavy water reactors (PHWR) [9].

1.3 Nuclear Fuel Cycle

Various stages of nuclear fuel cycle

Nuclear fuel cycle processes can be classified broadly into the front end and backend operations. Usually, all processes including (i) mining and milling; (ii) purification; (iii) enrichment; (iv) fuel fabrication and (v) reactor operation constitute the front end of the fuel cycle. All the steps post removal of the spent fuel from the reactor constitutes the back end of the fuel cycle. This usually includes (i) Reprocessing and (ii) Waste Management.

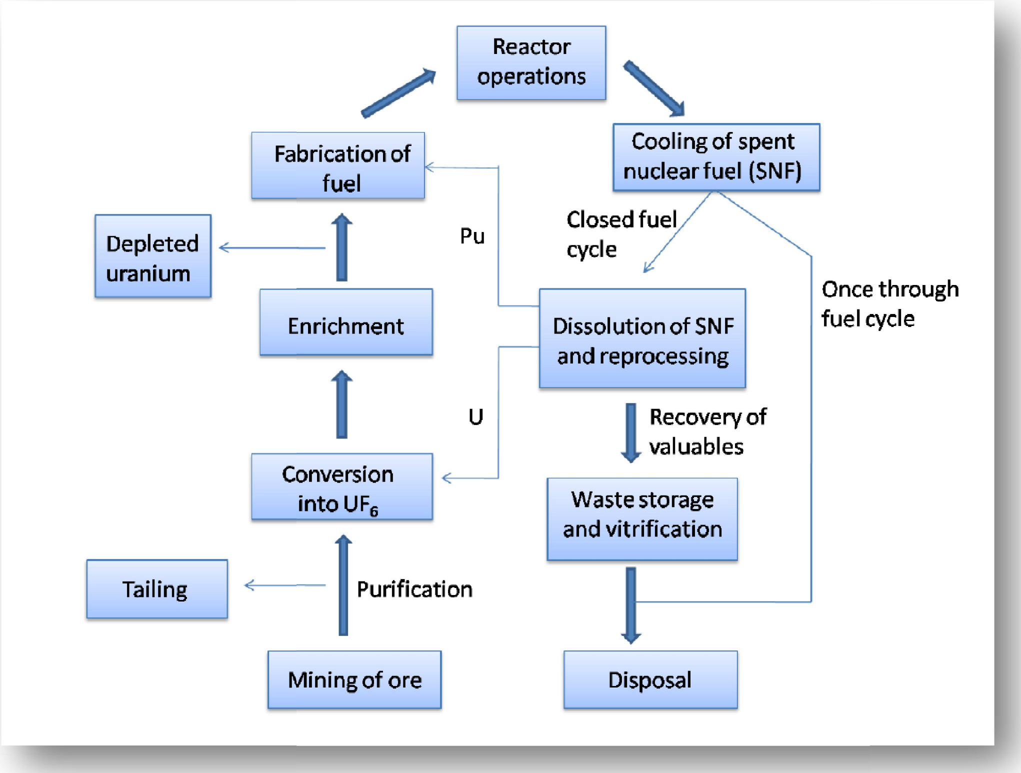

Figure 1.4: Schematic of nuclear fuel cycle

At present, there are two dominant strategies used by various countries at the back end. The first involves a single use of the fuel in the reactor, followed by suitable disposal. This scheme is known as the once through process or the open fuel cycle.

The other, more technically challenging, avenue is known as the closed cycle. As the name suggests, reprocessing is the centre piece of this strategy where elements such as U and Pu are recovered from spent fuel and recycled for fuel fabrication. This strategy also relies upon the development of partitioning strategies which may minimize the radiotoxic footprint of the HLLW [10]. Indeed, the closed fuel cycle places great premium on waste management to isolate long lived, toxic HLLW from the biosphere.

1.4 Reprocessing of Spent Fuel

The spent nuclear fuel containing uranium, plutonium, minor actinides, fission products and activation products **(Fig. 1.5)** is cooled to allow the decay of short lived radionuclides followed by reprocessing using the PUREX process. PUREX (Plutonium Uranium Reduction Extraction) is an aqueous reprocessing scheme which is used for the recovery of uranium and plutonium from spent nuclear fuels. The PUREX process was developed by Anderson and Asprey at the Metallurgical Laboratory at the University of Chicago, as part of the Manhattan Project [11], and has been adopted by virtually all the nuclear reprocessing plants worldwide. In PUREX process, the irradiated fuel is dissolved in nitric acid solution (dissolver solution), which is then treated with an organic solvent, usually TBP dissolved in an inert diluent (n-dodecane). The PUREX process can be divided into seven major steps [12]:

1. De-jacketing of fuel sub-assembly, dissolution of spent fuel in Nitric acid and feed preparation.
2. Recovery of uranium and plutonium from fission products.
3. Partitioning of uranium and plutonium.
4. Plutonium purification cycle.
5. Uranium purification cycle.
6. Solvent recovery.
7. Waste disposal and nitric acid recovery.

During extraction, mass transfer takes place and U(VI) and Pu(IV) are transferred to the organic phase leaving behind the minor actinides (trivalent and pentavalent), fission products and structural elements due to their poorer extraction [13]. The mutual separation of uranium and plutonium is achieved by partitioning the plutonium from the organic to the aqueous phase after adjusting its valence to trivalent state employing U(IV) salt as the reducing agent. Plutonium is reduced to Pu(III), since its lower ionic potential precludes its extraction in TBP. If the TBP solution of extracted actinides is subsequently contacted with dilute (~0.1 M) nitric acid, the U(VI) is easily stripped into the aqueous phase. The chemical reaction for U(VI) extraction from nitric acid medium is:

$$UO_2^{2+} + 2NO_3^- + 2TBP \rightleftarrows UO_2(NO_3)_2.2TBP \qquad (1.5)$$

The Equation for the Pu in the +4 oxidation state is

$$Pu^{4+} + 4NO_3^- + 2TBP \rightleftarrows Pu(NO_3)_4.2TBP \qquad (1.6)$$

^{237}Np in particular requires special attention owing to its long half life (~ 2.14 X 10^7yrs). U, Pu and Np are separated by making use of the variable oxidation states of Pu and Np. Np exists mainly as Np(V), which is not extracted by TBP under the PUREX feed condition. At low HNO_2concentration (10^{-4} – 10^{-3} M) in the dissolver solution, Np(V) is oxidized to Np(VI) and co extracted with U and Pu. When HNO_2 concentration is $>10^{-2}$ M, Np follows the raffinate along with the fission products. The raffinate of the PUREX process, containing long lived structural elements and process chemicals (at g/L scale), minor actinides (at mg/L scale) along with large quantities of fission products, which are either inactive or short lived, is referred to as high active waste (HAW). The HAW is concentrated by evaporation to obtain High Level Liquid Waste (HLLW). Increase in acidity on evaporation is addressed by adding acid scavengers [14].

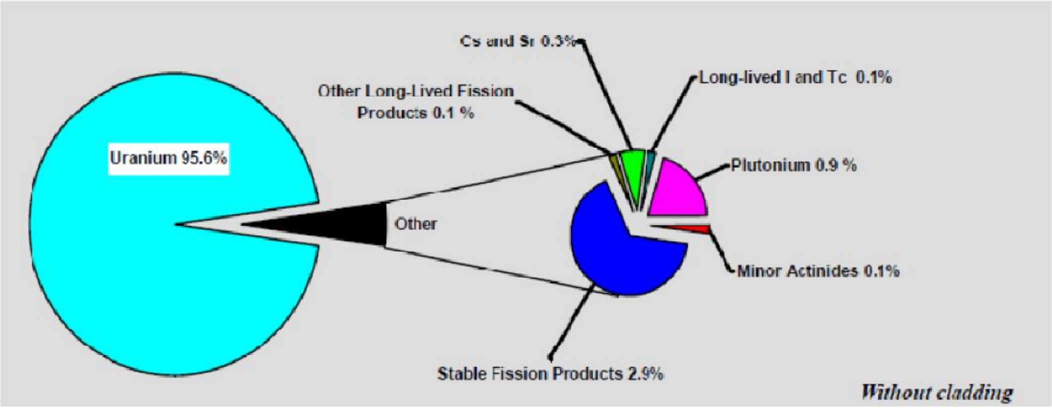

Figure 1.5: Composition of spent nuclear fuel

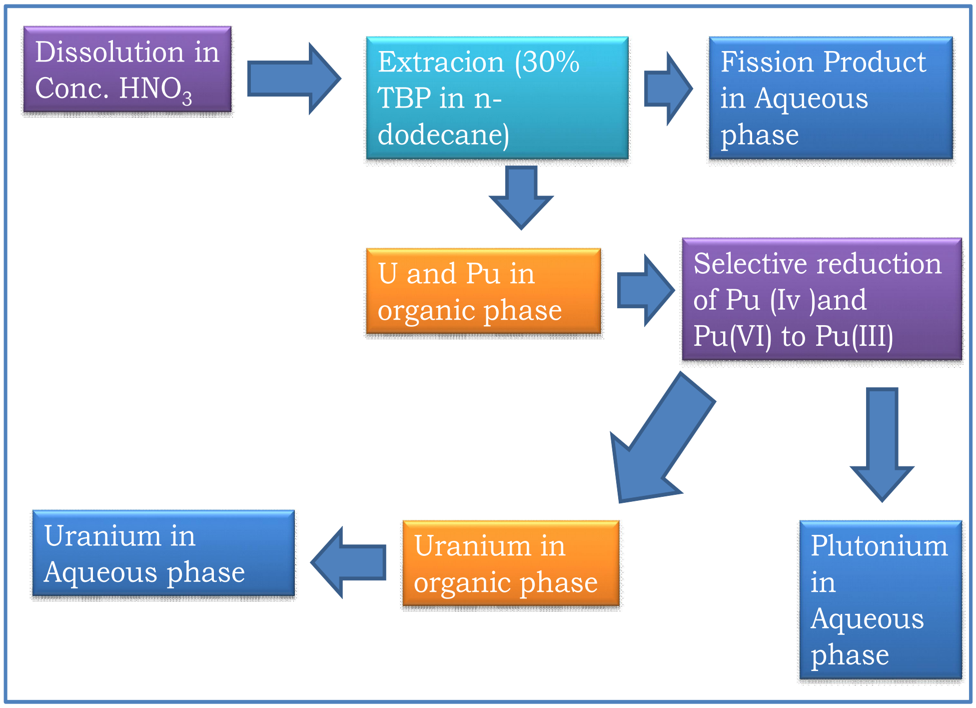

Figure 1.6: Schematic of fuel reprocessing

1.5 Radioactive Waste

While nuclear energy is clean and plentiful, judicious management of waste generated at each step is critical for safe and socially acceptable operations. Nuclear wastes are generated right from mining of fuel ores to reprocessing / final disposal of spent fuel. It is the onus of the waste management technologist to ensure that these wastes are suitably contained and isolated from the biosphere.

Typically, U mining generates radioactive dust comprising decay products of ^{238}U / ^{233}U. Additionally, milling operations generate radioactive radium, which is then sequestered in the mine and encased in rock and clay. The uranium oxide generated from mining and milling operations is accompanied by only a fraction of the total concentration of decay products and most of these are directed back to the tailings.

In terms of activity, the majority of the waste originates from nuclear fuel reprocessing, with the fuel rods accounting for over 99.9% of the activity and less than 0.01% distributed in other systems of the reactor, including ion-exchangers used for the water purification in PHT / coolant channels, chemical sludge, reactor components, etc. The spent fuel from nuclear reactors is processed for separation of useful fissile elements like Pu, U etc. leaving behind the alpha emitting long lived actinides and beta/gamma emitting fission products, which are responsible for most of the dose [15] associated with the spent fuel solution. The spent fuel is often allowed to cool for a few years to allow the short lived radio nuclides to decay. After cooling the spent fuel for about one year, only ^{106}Ru, ^{106}Rh, ^{90}Sr, ^{90}Y, ^{144}Ce, ^{144}Pr, ^{134}Cs, ^{137}Cs and ^{147}Pm contribute significantly to the activity.

1.6 Classification of Waste

The classification of radioactive wastes takes into account the physical, chemical, radiological and biological properties of the waste. Waste classification is a useful tool in segregation, waste treatment selection, storage and disposal. Radioactive waste is generated in various forms in the entire fuel cycle viz., solid, liquid or gaseous. Since the present thesis work deals with separation of radionuclides from liquid waste, an elaborate discussion on liquid waste is presented subsequently.

Liquid radioactive waste

Depending on the basis of associated radioactivity, liquid waste is characterized as low level, intermediate level and high level waste [16].

1.6.1.1 Low level liquid waste

The total radioactivity of low level liquid wastes (LLLW) is typically less than 1 $mCi.l^{-1}$. It is generated as the effluent from the treatment of ILLW, evaporator condensate of secondary liquid waste during nuclear fuel reprocessing, from the decontamination of equipments; and from radioactive laboratories and hospitals using radiopharmaceuticals. The level of radioactivity and half-lives of radioactive isotopes present in LLLW are relatively small. The LLLW comprises about 90% of the total volume of the radioactive waste, while it contains < 1% radioactivity of all the radioactive waste. The treatment of LLLW involves the precipitation of the majority of radionuclides using suitable reagents [17]. The solid residue is stored in a near surface repository and the supernatant is monitored and then discharged after dilution.

1.6.1.2 Intermediate level liquid waste

The activity of intermediate level liquid waste (ILLW) ranges from $1mCi.l^{-1}$ - $1Ci.l^{-1}$. Since ILLW is more radioactive, it may require special shielding. Main sources of ILLW are the condensate during the evaporation and concentration of HLLW, components of nuclear reactor materials originating from the treatment of high active waste, resins used for concentration of activity, chemical sludge, reprocessing equipments etc. The ILLW is treated with resorcinol formaldehyde polycondensate resin and iminodiacetic acid resin to remove ^{137}Cs and ^{90}Sr respectively [18].

1.6.1.3 High level liquid waste

If the radioactivity level of waste is higher than $1 Ci.l^{-1}$, then the waste is termed as High Level Liquid Waste (HLLW). HLLW contains unextracted uranium and plutonium, fission products (Sr, Zr, Mo, Tc, Ru, Pd, Cs, Ba and lanthanides), structural materials, activation products and minor actinides (MA) [19]. Typical composition of HLLW [20] is given in **Table 1.1.** The long lived radionuclides of interest from long term surveillance, point of view includes ^{99}Tc, ^{129}I, ^{135}Cs, ^{237}Np, ^{241}Am, ^{243}Am, ^{245}Cm etc., apart from residual plutonium. MAs viz., Np, Am and Cm are considered most toxic due to their alpha emitting properties and long half life. HLLW comprises major radioactivity of nuclear waste and occupies 3% of total volume, yet >95% of total radioactivity generated in nuclear fuel cycle. For safe management, HLLW is first immobilized in glass matrices followed by containment in stainless steel canisters with planned long term disposal in deep geological repositories [21].

1.7 General Strategy of Nuclear Waste Management

Management of the HLLW generated during spent fuel reprocessing is a significant challenge due to its chemical heterogeneity and the radiotoxicity associated with the minor actinides, which have half lives ranging from few hundred to millions of years. Effective isolation of the waste from the biosphere is of paramount importance till its radio-toxicity reduces to innocuous levels. Following a global precedent, India has adopted a three step process for the management of HLLW [22]. These steps are:(a) Vitrification of waste in stable and inert solid matrix, viz., glass (b) Interim storage of solidified waste with continuous cooling (c) Disposal in deep geological repositories, which is still under planning.

Table 1.1: Typical calculated composition of high level waste for thermal and fast reactor spent fuel

Reactor	Thermal	Fast
Burn up (MWD/t)	6700	150000
Cooling Time (y)	5	1
Volume (L/t)	800	13000
U	6182	500
Np	30	3.4
Pu	23.6	30
Am	52	13.6
Cm	0.09	0.05
Se	14.33	2.81
Sr	210.2	28.6
Y	115	16.5
Zr	906.8	176.3
Nb	--	0.13
Mo	857.6	218.3
Tc	213	57.6
Ru	543.1	212.6
Rh	149.9	68.5
Pd	328.2	167.9
Ag	22.4	19
Cd	19.28	9
In	1.02	0.8
Sn	18	8.96
Sb	4.86	3.35
Te	122.3	31.2
Cs	623.2	275
Ba	379	95
La	309.6	81.8
Ce	613.3	150.6
Pr	285.7	80.25
Nd	1024.8	232.2
Pm	19.2	11.1
Sm	215.6	66.6
Eu	26.45	10.1
Gd	22.9	6.23
Tb	0.62	0.58

Vitrification of HLLW in glass matrix

Borosilicate glass matrix has been adopted for vitrification of HLLW in India [23]. This family of glass compositions combines high radiation and thermal stability, chemical durability and is suitable for large scale production in remotely handled facilities. In the vitrification process, pre-concentrated waste is feed into a furnace with suitable glass additives. Within the furnace, water and nitric acid are evaporated; nitrates are decomposed into oxides followed by fusion when the wastes and the glass forming additives and the waste melt to form molten glass. This glass is then poured into stainless steel canisters. Three canisters are packed into a stainless steel overpack and placed in interim storage. Post interim storage to allow decay of heat producing radionuclides, the overpacks are proposed to be stored in a deep geological repository.

Partitioning and transmutation (P&T)

A deep geological repository adds significantly to the cost of a nuclear programme. Therefore, partitioning and transmutation (P&T) has the potential to reduce the long term impact of radioactive waste by separation of long lived α-emitters, thereby reducing repository footprint. **Fig. 1.7** shows the variation in radiotoxicity of HLLW with and without actinide partitioning [24]. Indeed, **Fig. 1.7** shows that MA separation from HLLW allows a rapid roll down of α-activity, which can possibly obviate long term surveillance of radioactive wastes, reducing cost and environmental impact of the program.

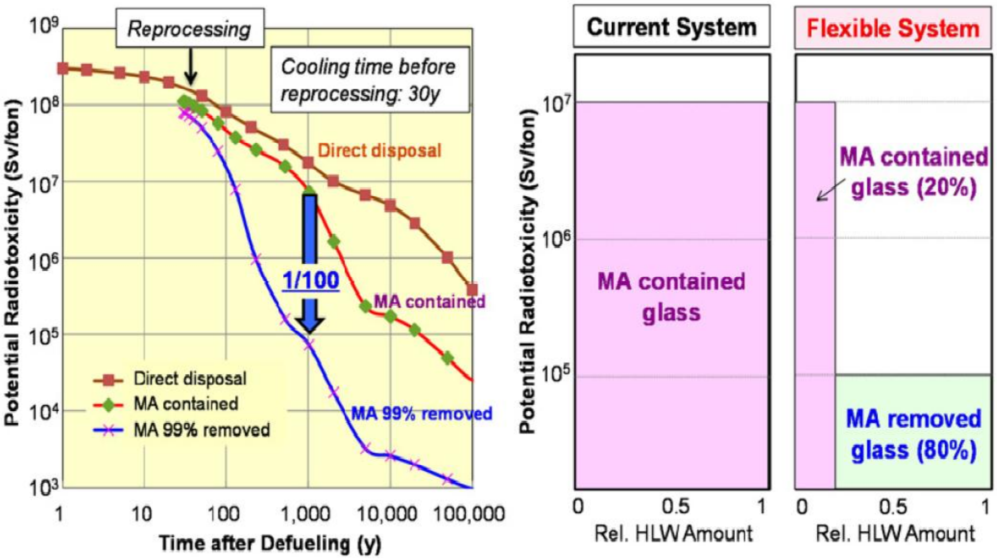

Figure 1.7: Relative profile of activity of HLLW with and without actinide partitioning

Minor actinide partitioning is, therefore, one of the important steps in the management of HLLW. After separation of actinides from HLLW, they can be transmuted to short lived radionuclides by neutron bombardment, in an accelerator driven sub-critical (ADS) or in a fast reactor system.

Actinide partitioning

Partitioning strategies used for reprocessing and to make the waste amenable for safe disposal rely on the following four separation steps: (1) Partitioning of U and/or Pu from spent-fuel; (2) Co-extraction of the trivalent actinides and lanthanides; (3) Separation of beta/gamma emitting, heat generating fission products and (4) Separation of the trivalent actinides from trivalent lanthanides **Fig. 1.8.**

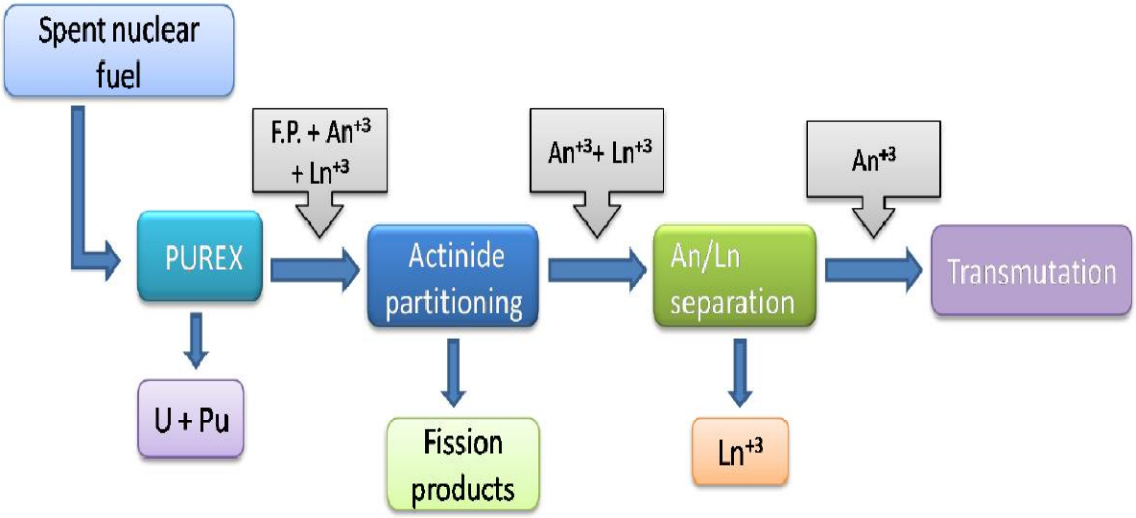

Figure 1.8: Spent fuel partitioning strategies

Co-extraction of the trivalent actinides and lanthanides

The chemical similarity of trivalent actinides and lanthanides caused a significant presence of lanthanides accompanying the extracted actinides. This is particularly challenging since the lanthanides comprise 1/3rd of the mass of fission products generated, and as such exceed the concentration of actinides by several times. The challenges in selective trivalent actinide extraction have motivated co-extraction of An(III) and Ln(III) while avoiding all other fission products. Significant progress has been made in this area in the last two decades and the process maturity is attested to by the various pilot scale plants operational around the world [25]. A brief review of some of these processes is presented subsequently.

1.7.1.1 Processes with organo phosphorous extractants

The TRUEX process

The Trans Uranium Extraction (TRUEX) process is a solvent extraction process designed to separate transuranic elements from various types of high level waste solutions. The key ingredient in this process is a phosphine oxide based extractant, viz.octyl(phenyl)-N,N-diisobutyl carbamoyl methyl phosphine oxide (CMPO). The TRUEX extractant is usually 0.2 M CMPO + 1.2 M TBP (used as a phase modifier) in paraffinic hydrocarbon like *n*-dodecane [26]. In TRUEX solvent, TBP suppresses third phase formation, contributes to better acid dependencies for D_{Am}, improves phase compatibility, and reduces hydrolytic and radiolytic degradation of CMPO [27]. High distribution ratio of tri-, tetra- and hexavalent actinides from solutions of moderate acid concentration and good selectivity over fission products is the key feature of this extractant.

Lanthanides such as Eu, Ce and Pr behave similar to the trivalent actinides, viz. Am(III). Other fission products, except Zr, show relatively small distribution values. From the process perspective, the insensitivity of distribution values of actinides between 1 M and 6 M HNO_3 is important as it allows efficient extraction of these ions from waste with little or no adjustment of feed acidity. Generally, 1-hydroxyethylene-1,1-diphosphonic acid (HEDPA) is used for stripping of Am, Pu and U from loaded organic phase [28]. The oxidation state specific stripping of actinide ions from loaded TRUEX solvent can be achieved in three steps: 0.04 M HNO_3 to remove trivalent actinides, dilute oxalic acid for selective stripping of tetravalent actinides, and finally 0.25 M Na_2CO_3 for uranium recovery. A formic acid, citric acid and hydrazine hydrate mixture has reportedly shown promise for efficient stripping of Am and Pu from TRUEX solvent loaded with HLLW in both batch as well as counter current modes. Though CMPO shows high extraction efficiency and is a promising reagent for the separation of actinides, the TRUEX process exhibits certain limitations. Stripping of trivalent actinides is cumbersome and requires several stages of contact. Degradation products of CMPO can also inhibit the stripping of Pu and U. The presence of acidic degradation products can cause an increase in the D_{Am} values under stripping conditions. More stringent stripping condition of metal ions from the loaded organic phase is the major drawback of the TRUEX process.

TRPO Process

Trialkyl Phosphine Oxide (TRPO) process uses four alkyl phosphine oxides as extractants. This process has demonstrated excellent selective extraction of actinides while avoiding fission products extraction from 0.2–1 M HNO_3through a single extraction with 30% (v/v) TRPO in kerosene [29, 30, 31].

While the low cost and extraction efficiency are advantages, the low acidity range for the TRPO process (0.1 - 1 M HNO_3) necessitates dilution of HLLW (~3 M HNO_3). Additionally, poor stripping of actinide ions also presents a problem in this process.

The DIDPA Process

The extraction behavior of actinides and other fission products with di-isodecyl phosphoric acid (DIDPA) has been studied by Morita et al., at the Japan Atomic Energy Research Institute (JAERI). They have demonstrated simultaneous extraction of Am(III), Cm(III), U(VI), Pu(IV) and even Np(V) from a solution of low ~ 0.5 M HNO_3 [32], [33]. A limitation of the process is the formation of Mo and Zr precipitates that carry over 90% of the Pu with them.

1.7.1.2 Processes with amide extractants

The DIAMEX Process

The diamide extraction (DIAMEX) process was developed in France for the extraction of transuranic elements from the HLLW solutions. Among the numerous diamides synthesized and tested for the extraction of actinides, N,N-dimethyl-N,N-dibutyl tetradecyl malonamide (DMDBTDMA) has shown the greatest promise [34, 35, 36, 37.] Advantageously, DMDBTDMA dissolved in *n*-dodecane does not give any third phase when contacted with 3-4 M HNO_3 mitigating the use of additional phase modifiers. Generally, 1 M DMDBTDMA has been proposed for actinide partitioning which gives D_{Am} value of ~10 at 3 M HNO_3 [38], [39]. Zirconium(IV) is strongly extracted by DMDBTDMA, which is a limitation. However, complexation with oxalic acid greatly reduces the problem. Extraction of molybdenum can also be suppressed by complexation with hydrogen peroxide. Iron, which is almost always present in HLLW from corrosion of the process equipments, also has high affinity for DMDBTDMA. However, the extraction kinetics for Fe(III) is slow and it may be separated from actinides and lanthanides by the judicial choice of contact time. Recently, a new diamide, viz. N,N-dimethyl-N,N-dioctyl-2-(2-hexylethoxy) malonamide (DMDOHEMA) has been reported as a substitute of DMDBTDMA for DIAMEX solvent [40]. Amongst several extractants described for actinide partitioning, diamides have been found to be particularly promising in view of their improved back extraction properties for Am(III) / Cm(III), their complete incinerability, and the innocuous nature of their radiolytic and hydrolytic products (mainly carboxylic acids and amines) that can be easily washed out. However, the major drawback of DMDBTDMA is that it shows only moderate extraction of trivalent actinides (Am and Cm) from HLW at acidity ≤ 3 M HNO_3. Therefore, it necessitates the structural modification of diamides so as to enhance the extraction efficiency of trivalent actinides in particular.

1.7.1.3 Digylycolamides: a class of Promising extractants for actinide partitioning

In view of the limitation of the extraction processes discussed previously, a series of diamide compounds have been synthesized by introducing different substituents on amide nitrogen or introducing ether oxygen into the bridging chain of malonamide [41]. Experiments reveal a significant enhancement in the extraction of trivalent actinides and lanthanides. Indeed, the work on diglycolamides was initiated after the seminal work of Stephan et. al., who reported the extraction of various metal ions with multi-dentate amido-podants [42], [43].

Sasaki and Choppin were probably the first to report the extraction of lanthanides and actinides with diglycolamides [44], [45], [46], [47], [48]. They used dimethyl dihexyl diglycolamide and its analogous compounds for the solvent extraction studies on lanthanides and actinides. These preliminary studies, however, were focused on the extraction of metal ions from aqueous solutions of pH ranging from 1 to 4. Narita et al., studied the extraction of lanthanides from acidic solutions employing N,N‘-dimethyl N,N‘-

diphenyldiglycolamide [49]. They proved by XRD and EXAFS studies that the diglycolamide forms tridentate complex with lanthanides in solid complexes as well as in solution [50]. Sasaki et al [51] synthesized a series of diglycolamides having the same central frame with different alkyl chains (ranging from *n*-propyl to *n*-dodecyl) attached to amidic nitrogen atoms. The diglycolamide derivatives with lower alkyl chain (*n*-propyl and *n*-butyl) were insoluble in paraffinic solvents like *n*-dodecane due to the presence of three polar oxygen atoms. Though the higher homologues of diglycolamide were freely soluble in *n*-dodecane, the distribution values for Am(III) were found to decrease due to the steric hindrance during complexation of the bulky molecules. Amongst the different derivatives synthesized, N,N,N‘,N‘-tetraoctyl diglycolamide (TODGA) was demonstrated to be the best candidate with reference to its free solubility in *n*-dodecane and significantly high distribution values for trivalent actinides.

Separation of the trivalent actinides from trivalent lanthanides

The chemical similarity in terms of charge/radius ratio and coordination behavior makes separation of actinides from lanthanides non trivial. It may be mentioned that both An(III) and Ln(III) are hard acids. However, An(III) exhibit enhanced covalency toward ligand compared to Ln(III)complexes possibly due to the larger spatial extent of the 5f shell in An as compared to the 4f shell in Ln. This results in an advantageous discrimination in bonding between An(III) and Ln(III) ions, using soft donor atoms like sulfur, nitrogen etc. The concept of using soft donor ligands for actinide selectivity was first proposed by Glenn Seaborg in 1954 [52].This strategy may allow separation of An from Ln.

An(III) separation from Ln(III) was first achieved by cation exchange from concentrated chloride media. Common processes employed for Ln(III)/An(III) separation are:

(i) Trans Americium Extraction (TRAMEX) process [53] where the trivalent actinides are separated selectively from the bulk of lanthanides in presence of a large concentration of chloride ion (11M LiCl) at pH 1-2 using a tertiary amine.

(ii) Trivalent Actinide Lanthanide Separation by Phosphorus Extractants Aqueous Complexes (TALSPEAK) process [54]where trivalent lanthanides are selectively extracted here from the actinides using di-2-ethylhexyl phosphoric acid (D2EHPA) in presence of aqueous complexing agent.

(iii) Selective ActiNide EXtraction (SANEX) processes, where a series of processes have been developed for the Ln(III) / An(III) separation employing 'N' donor hetero polycyclic ligands. These SANEX processes have three different categories, SANEX I, SANEX II and SANEX III [55], [56], [57], [58], [59] Various other nitrogen donor extractants such as Terpyridyl, Amido-bis pyridyl triazene (ADPTZ), Bis-triazenylpyridine (BTP) and bis-triazenyl bipyridine (BTBP) are also used in different processes. Besides the N donor extractants, a number of S donor extractants have also been used in the separation of trivalent actinides from lanthanides, usually at low pH. Thiopyrazolone, aromatic dithiophosphinic acids (SANEX-IV process) [60], [61], [62]and Cyanex ligands are commonly used S donor extractants. All these ligands except Cyanex show a maximum separation factor of ~100, however, in 1996 Zhu et. al. have reported a separation factor of ~5900 with S donor Cyanex301 [63]. Commonly used ligands for An/Ln separation and their separation factors are shown in **Fig. 1.9**.

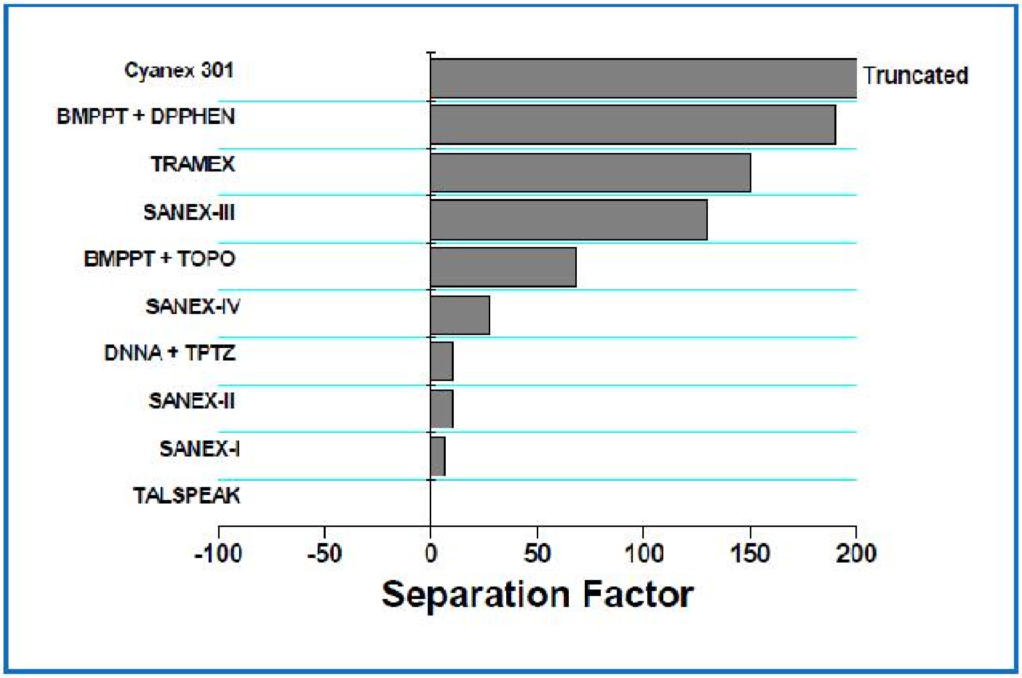

Figure 1.9: Different ligands for actinide-lanthanide separation and their separation factors

1.8 Chemistry of Actinides

A brief survey of the rich chemistry of actinide elements is considered relevant to understand its extraction and complexation behavior.

Electronic configuration

The actinide hypothesis was advanced by Seaborg, according to which successive electrons are added to the inner 5f shell beginning formally with Th (Z=90). These elements following Ac are placed in the 7th row of the periodic table separately, analogous to lanthanides. In the lanthanide series, fourteen 4f electrons are added beginning formally with cerium (Z=58) and ending with lutetium (Z=71). Intensive chemical studies have revealed many similarities between the lanthanides and actinides. Though there is over all similarity between the two groups of elements, some important differences also exist mainly because the 5f and 6d shells are of similar energy in actinides and 5f electrons are not as well shielded as 4f electrons in lanthanides [64].

The first member of the lanthanides series (La) does not have any 4f electron, and has electronic configuration, $6s^2$ $5d^1$. In the case of lanthanides, the 4f orbital becomes appreciably lower in energy compared to 5d orbital immediately after La. Consequently the electrons preferentially fill the 4f orbitals among the lanthanides (except in the case of half filled 4f shell). However, in the case of actinides the difference between energies of 5f and 6d orbitals is very small for the first four elements, Th, Pa, U and Np. Consequently, electron may occupy either 5f or 6d or both. Only in the latter actinides, the 5f orbital gets appreciably lower in energy than 6d and hence from Pu onwards 5f shell is preferentially filled [65] as shown in Table 1.2**.**

Table 1.2: Electronic configuration of lanthanide and actinide elements

Element	Atomic Number	Electronic configuration (Xe core)	Element	Atomic Number	Electronic configuration
La	57	$5d\ 6s^2$	Ac	89	$6d\ 7s^2$
Ce	58	$4f\ 5d\ 6s^2$	Th	90	$6d^2\ 7s^2$
Pr	59	$4f^3\ 6s^2$	Pa	91	$5f^2\ 6d\ 7s^2$
Nd	60	$4f^4\ 6s^2$	U	92	$5f^3\ 6d\ 7s^2$
Sm	61	$4f^5\ 6s^2$	Np	93	$5f^4\ 6d\ 7s^2$
Pm	62	$4f^6\ 6s^2$	Pu	94	$5f^6\ 7s^2$
Eu	63	$4f^7\ 6s^2$	Am	95	$5f^7\ 7s^2$
Gd	64	$4f^7\ 5d\ 6s^2$	Cm	96	$5f^7\ 6d\ 7s^2$
Tb	65	$4f^9\ 6s^2$	Bk	97	$5f^9\ 7s^2$
Ho	66	$4f^{10}\ 6s^2$	Cf	98	$5f^{10}\ 7s^2$
Dy	67	$4f^{11}\ 6s^2$	Es	99	$5f^{11}\ 7s^2$
Er	68	$4f^{12}\ 6s^2$	Fm	100	$5f^{12}\ 7s^2$
Tm	69	$4f^{13}\ 6s^2$	Md	101	$5f^{13}\ 7s^2$
Yb	70	$4f^{14}\ 6s^2$	No	102	$5f^{14}\ 7s^2$
Lu	71	$4f^{14}\ 5d\ 6s^2$	Lr	103	$5f^{14}\ 6d\ 7s^2$ or $5f^{14}\ 7s^2\ 7p$

The relative energies of electronic configurations of actinides that can interchange 5f and 6d electrons are shown in **Fig. 1.10**. The inversion from one electronic configuration to other, for the elements in which 5f-orbitals extend closer to 6d and 7s orbital, is inevitable. Therefore, early actinides up to americium (Z = 95) show variable valency. On the contrary, in lanthanides the large energy differences between 4f and 5d orbitals do not favor the interchange of electrons among them and consequently all the lanthanides exhibit predominantly single valence.

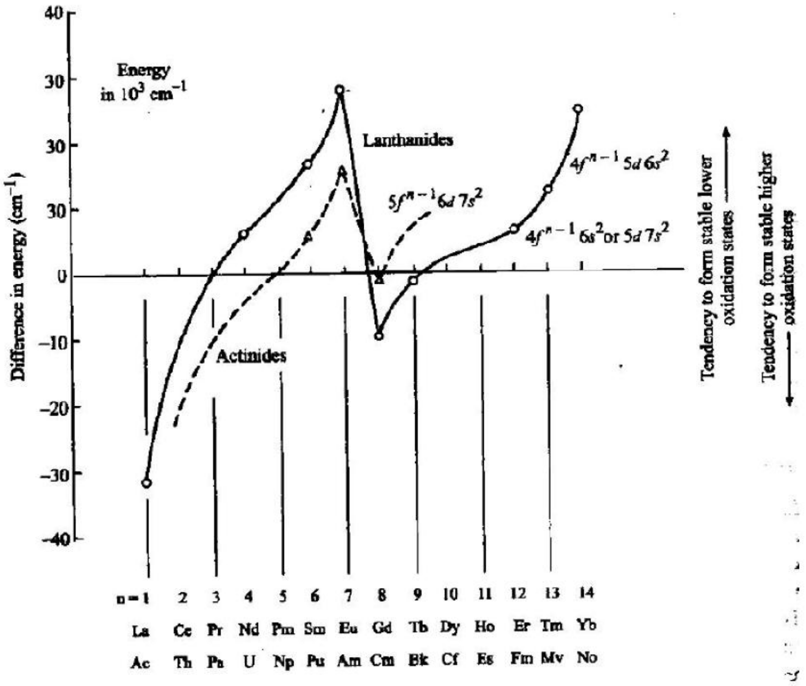

Figure 1.10: Approximate relative energies of the f^{n-1}d^{1}s^2 and f^{n}s^2 electron configurations [66]

Solution chemistry of actinides

As the processes of separation and purification of actinides on large scale are essentially based on hydrometallurgical techniques, the study of solution chemistry of actinides has received considerable attention. Lanthanides and actinides are hard acids (like alkali and alkaline earth metals ions) and have strong preference for 'O' donor ligands. The early actinide elements (upto Pu) exist in multiple oxidation states but the Chemistry of actinides is similar to that of lanthanides, especially in case of trans-plutonium elements which exist predominantly in 3+ oxidation state in solution. Lanthanides and actinides do not show strong ligand field effects due to shielding of f orbital by outer orbital (d, s, p) electrons which is more pronounced in lanthanides. However this becomes advantageous as other phenomena can be easily studied in the absence of ligand field effects. In absence of ligand, the difference in the complexation behavior of lanthanides and actinides can clearly be attributed to the properties of 4f and 5f orbitals. The lanthanide and actinide ions interact and form solvent structure around them and hence the solvent effects can be best studied [67]. Most of their separation processes are based on the effective exploitation of these properties. It is, therefore, desirable to understand the various oxidation states of actinides in solution.

Oxidation states

It is well established that the trivalent oxidation state is most stable for Ln, while An, especially the early members of the series exhibit multiple oxidation states. This is attributed to the close proximity of 5f, 6d and 7s orbitals. Ionization and hydration energies are then responsible for facilitating the conversion of one oxidation state to another in aqueous solutions. An interplay of these two energies will decide the most stable oxidation state for a given metal ion. The 5f electrons of actinides are subjected to a lesser attraction from the nuclear charge than the corresponding 4f electrons of lanthanides. The greater stability of tetra positive ions of early actinides is attributed to the lower fourth ionization potential for 5f electrons compared to 4f electrons of lanthanides. As the f orbitals are less stabilized in early actinides, f-electrons having low ionization energy result in f^0 as the most stable configuration for actinides up to uranium.

With increase in atomic number, f orbital becomes more stabilized compared to 6d and 7s orbital and therefore actinides beyond americium exhibit +3 as the most stable oxidation state except nobelium for which +2 state is most stable owing to stability of full filled 5f shell. **Table 1.3** lists the oxidation states of the actinides and lanthanides [68].

Table 1.3: Oxidation states of actinide elements

89	**90**	**91**	**92**	**93**	**94**	**95**	**96**	**97**	**98**	**99**	**100**	**101**	**102**	**103**
Ac	**Th**	**Pa**	**U**	**Np**	**Pu**	**Am**	**Cm**	**Bk**	**Cf**	**Es**	**Fm**	**Md**	**No**	**Lr**
						(2)		(2)				2	**2**	
3	(3)	(3)	3	3	3	**3**	**3**	**3**	**3**	**3**	**3**	**3**	3	**3**
	4	4	4	4	**4**	4	4	4						
		5	5	**5**	5	5								
			6	6	6	6								
				7	7									
57	**58**	**59**	**60**	**61**	**62**	**63**	**64**	**65**	**66**	**67**	**68**	**69**	**70**	**71**
La	**Ce**	**Pr**	**Nd**	**Pm**	**Sm**	**Eu**	**Gd**	**Tb**	**Dy**	**Ho**	**Er**	**Tm**	**Yb**	**Lu**
			(2)		2	2						(2)	**2**	
3	**3**	**3**	**3**	**3**	**3**	**3**	**3**	**3**	**3**	**3**	**3**	**3**	**3**	**3**
	4	(4)						4						

Bold: most stable oxidation state, in parenthesis: oxidation state not known in solution

All the oxidation states are well known in acidic conditions except 7+ states for Np and Pu which exist in alkaline medium [69]**.** Penta and hexavalent actinide ions exist in acid solution as oxygenated cations, viz. MO_2^{+} and MO_2^{2+}. in contrast, +3 oxidation state is predominant in lanthanides series owing to the large difference in binding energy of 4f and 5d, 6s electrons. However, +2 (Eu and Yb) and +4 (Ce and Tb) oxidation states also exist which corresponds to vacant or enhanced stability of half-filled or full filled 4f configuration. Thus, later members of actinides series behave like lanthanides and exhibit +3 as the most stable oxidation state**.**

Ion types

All actinides, essentially, exhibit the same structure for a given oxidation state. In trivalent and tetravalent oxidation states, actinide ions exist as hydrated ions in acidic solutions. In higher oxidation states, owing to very high ionic potential, actinide ions immediately accept electron from donor atoms in solvent medium and form oxygenated species of the type MO_2^+ and MO_2^{2+} which are termed as actinyl ions. The actinyl ions are highly stable and act as a single entity during chemical transformation but their formation decreases the effective charge on the central actinide atom. The effective charge on the metal ion is 3.3 ± 0.1 and 2.3 ± 0.2 in $MO_2^{2+}$and MO_2^+ respectively which is greater than the ionic charge on molecular entity and therefore coordinating field in the case of molecular ion is proportionately stronger [70].

The order of effective charge, which affects the different chemical properties, for different oxidation states is $M^{4+} > MO_2^{2+} > M^{3+} > MO_2^+$ [71].

Actinyls

Among the actinide compounds the dioxo ions $[AnO_2]^{m+}$ common for oxidation states V and VI (An = Pa–Am) are remarkably stable due to strong An-O bonds. They exhibit bond orders larger than 2 e.g. for uranyl. Thus, unlike some other oxo ions the actinyls can persist through a variety of chemical changes. Actinyls exhibit characteristic bond distances of about 1.7 to 1.8 Å in solution – distinctly shorter than corresponding distances to equatorial ligands such as water (2.4 to 2.5 Å) [72] Most actinyl ions are linear with the exception of the distinctly bent ThO_2 [73], [74].

The overall pattern comprises a (linear) axial O-An-O actinyl moiety that is surrounded by 4, 5, or 6 ligands in or close to its equatorial plane. This yields tetragonal, pentagonal, or hexagonal bipyramidal coordination, respectively [75].

Lanthanide and actinide contraction: effect on ionic radius

In lanthanides and actinides, as the atomic number increases, electrons sequentially enter f orbitals which provide incomplete shielding of the outer shell electrons from the steadily increasing nuclear charge due to their diffused character. Therefore, a steady decrease in the radius is observed in both the series. The phenomena are termed as the lanthanide and actinide contraction for lanthanide and actinide series respectively. Similar trend is observed in ionic radii of the elements of both the series. **Fig. 1.11** shows the variation of ionic radius for +3 and +4 oxidation states of lanthanides and actinides. The sufficiently small change in charge density, as a result of slight decrease in ionic radius, accounts for almost identical chemical properties of all elements across the series.

Disproportionation

Disproportionation refers to simultaneous self oxidation-reduction reactions. For disproportionation to occur an element must have at least three oxidation states. Since M^{4+} and MO_2^{2+} have the most pronounced effect, these ions must co-exist in the solution, which in turn depends on the closeness of the electrode potentials of the redox couple.

In Pu these values are so close that the four oxidation states, viz. III, IV, V and VI are in equilibrium with each other. The disproportionation reactions of U, Pu, Np and Am have been well studied [68] and their equilibrium constant (log K) values are given in **Table 1.4.**

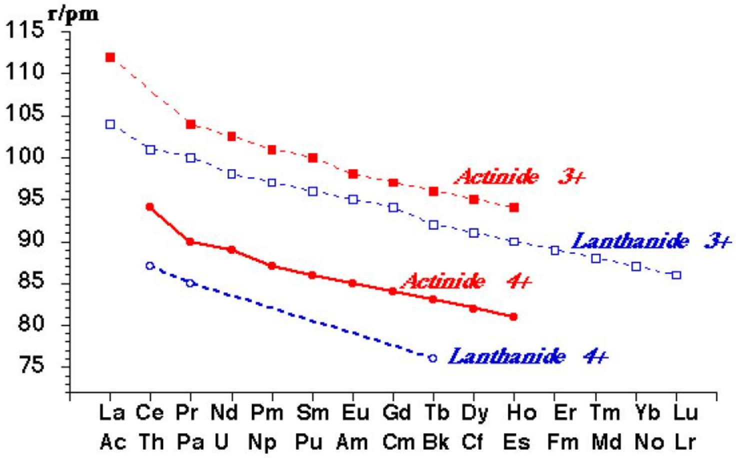

Figure 1.11: Ionic radious of lanthanides and actinides for +3 and +4 oxidation states

Table 1.4: Disproportionation reactions of actinides in aqueous solutions

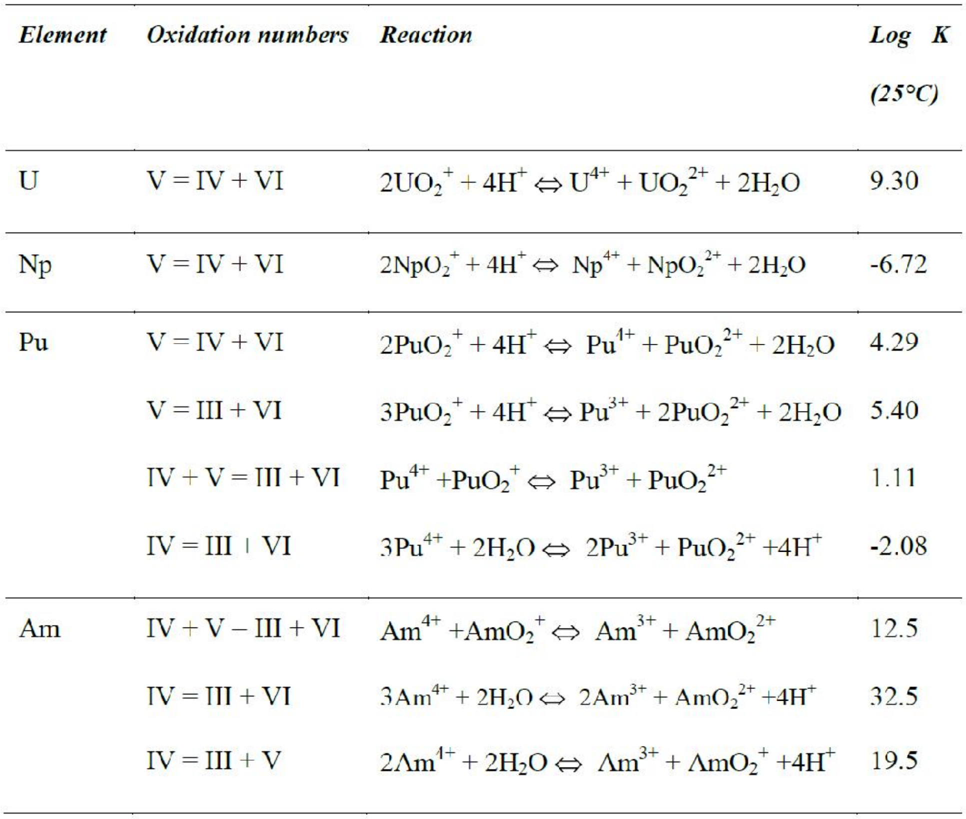

Element	*Oxidation numbers*	*Reaction*	*Log K (25°C)*
U	V = IV + VI	$2UO_2^{+} + 4H^{+} \Leftrightarrow U^{4+} + UO_2^{2+} + 2H_2O$	9.30
Np	V = IV + VI	$2NpO_2^{+} + 4H^{+} \Leftrightarrow Np^{4+} + NpO_2^{2+} + 2H_2O$	-6.72
Pu	V = IV + VI	$2PuO_2^{+} + 4H^{+} \Leftrightarrow Pu^{4+} + PuO_2^{2+} + 2H_2O$	4.29
	V = III + VI	$3PuO_2^{+} + 4H^{+} \Leftrightarrow Pu^{3+} + 2PuO_2^{2+} + 2H_2O$	5.40
	IV + V = III + VI	$Pu^{4+} + PuO_2^{+} \Leftrightarrow Pu^{3+} + PuO_2^{2+}$	1.11
	IV = III + VI	$3Pu^{4+} + 2H_2O \Leftrightarrow 2Pu^{3+} + PuO_2^{2+} + 4H^{+}$	-2.08
Am	IV + V = III + VI	$Am^{4+} + AmO_2^{+} \Leftrightarrow Am^{3+} + AmO_2^{2+}$	12.5
	IV = III + VI	$3Am^{4+} + 2H_2O \Leftrightarrow 2Am^{3+} + AmO_2^{2+} + 4H^{+}$	32.5
	IV = III + V	$2Am^{4+} + 2H_2O \Leftrightarrow Am^{3+} + AmO_2^{+} + 4H^{+}$	19.5

In general, disproportionation reactions of MO_2^{+} (M=U, Pu or Np) ions can be represented as follows

$$2MO_2^{+} + 4H^{+} \rightleftarrows M^{4+} + MO_2^{2+} + H_2O \qquad (1.7)$$

It is clearly demonstrated from the equilibrium reaction that the presence of hydrogen ion and complexing ions like F^{-} and SO_4^{2-}, which complex strongly with M^{4+} and MO_2^{2+} ions, have pronounced effect on the disproportionation reactions.

Hydrolysis and polymerization

The penta and hexavalent states are prone to very significant hydrolysis as compared to the lower oxidation states. The metal ions in these oxidation states exist as partially hydrolyzed actinyl ions, viz. MO_2^{+} and MO_2^{2+} and can get further hydrolyzed under high pH conditions. The degree of hydrolysis for actinide ions decreases in the order: $An^{4+} > AnO_2^{2+} > An^{3+} > AnO_2^{+}$ which is similar to their complex formation abilities. In general, the hydrolysis of the actinide ion (M^{n+}) can be represented as follows,

$$M(H_2O)_x^{n+} \leftrightarrow M(OH)_x^{(n-x)+} + xH^+ \qquad (1.8)$$

For U^{4+} and Pu^{4+}, the metal ion hydrolyzes first in a simple monomeric reaction followed by a slow irreversible polymerization of the hydrolyzed products. For Th^{4+}, however, various polymeric species exist even in very dilute solutions. Whereas the polymer formation of Pu^{4+} is irreversible, that of Th^{4+}can reversed. The hydrolysis of some of the trivalent actinides such asAm^{3+}, Cm^{3+} and Cf^{3+} is well studied which revealed the higher hydrolysis constant values for trivalent actinides as compared to their lanthanides homologs.

Pu^{4+} polymers with varying molecular weights ranging from a few thousands to as high as 1010 have also been observed [76]. In dilute HNO_3 or HCl solutions, Pu^{4+} polymer exhibits a bright green colour and a characteristic spectrum different from that of monomeric Pu(IV) in these solutions. The rate of polymerization depends on acidity, temperature, Pu(IV) concentration as well as the nature of ions present in the solution [77], [78].

Complexation of actinides

The rich and diverse complexation chemistry of actinides is applied extensively in separation and purification methods. The complexing strength of actinide ions in different oxidation states follows the order: $M^{4+} > MO_2^{2+} > M^{3+} > MO_2^{+}$ which can be explained on the basis of their decreasing trend in the ionic potential value. This order shows that the effective charge (Z_{eff}) felt by the ligand while binding to the actinyl cation is more than the formal charge of the cation, indicating that the oxygen atoms of the actinyl cation retain partial negative charge. The effective charge has been estimated to be +2.2 and +3.2 for NpO_2^{+} and UO_2^{2+} respectively [79].

Actinide ions in common oxidation states (+2 to +6) behave as hard Lewis acids. Consequently, they form predominantly ionic compounds having kinetically labile, non directional bonds. On the basis of Pearson's [80] hard – soft acid base principle, actinide ions being "hard acids" are expected to interact strongly with hard bases such as 'O' or 'F' rather than soft donor atoms like 'N', 'S' or 'P'. The thermodynamics of actinide complexation is mainly governed by electrostatic attraction between the actinide ion and the ligand, as well as the steric constraints.

The steric constraint arises due to the property of the actinide cation viz., ionic size and presence or absence of actinyl oxygen atoms, and that of the ligand, viz., number of ligands as well as the number and spatial relationship of donor atoms, size of chelate ring and rigidity. The steric constraints become dominant in the case of actinyl ions, wherein the ligand can approach the metal ion only in the equatorial plane. The ionic character of the actinide–ligand bonds is evident from the linear variation of stability constant (log K) of actinide amino poly carboxylate complexes as a function of inverse of cation radii [81], [82].

Complexes of actinides show greater degree of covalency compared to that of lanthanides, particularly in the case of ligands with soft donor atoms, viz., S, Cl, etc. This is evident from the large differences in the enthalpy of complexation of trivalent actinides and lanthanides both in aqueous and non-aqueous solutions [83].

Actinide cations can form inner sphere and outer sphere complexes. When the primary hydration shell is broken during complex formation, the resultant complex is referred to as 'inner sphere complex'. In contrast, 'outer sphere complexes' do not require breaking of the primary hydration shell. In aqueous solution, actinide cations are hydrated strongly forming $M(H_2O)_q^{z+}$ type of species. Interaction of the ligand (L^{x-}) with the hydrated metal ion may result in the formation of an outer sphere complex ($M(H_2O)_q^{z+}L^{x-}$) or inner sphere complex $(M(H_2O)_{q-1}L)^{z-x}$. The formation of outer sphere complex is rapid, while that of inner sphere complex is slow and is often the rate determining step [84]. The actinide ions interact with soft bases in organic solvents of low solvating power, but not in aqueous solutions where the soft bases would have to replace the inner sphere water molecules which are a hard base. Thus, depending on the nature of ligand and medium actinide cations form inner or outer sphere complexes. Thermodynamic quantities provide information about the inner sphere and outer sphere complex formation. In the case of outer sphere complex formation, the inner coordination of the metal ion is not affected and cation-ligand interaction resulting in exothermic enthalpy with negative entropy. On the other hand, in the case of inner sphere complexation the primary coordination sphere is disturbed significantly resulting in large positive entropy changes which far exceed the endothermic enthalpy changes. For monovalent ligands the complexing tendency decreases in the order: F^- > $CH3COO^-$ > SCN^-> NO_3^-> Cl^- > Br^-> I^-> ClO_4^-. The divalent anions usually from stronger complexes than the monovalent anions and their complexing ability decrease in the order: CO_3^{2-}> SO_3^{2-}> $C_2O_4^{2-}$> $SO_4^{2-.}$ The complexing ability of some of the organic ligands with Th(IV) varies as: ethelenediamine tetra acetic acid (EDTA) > citrate > oxalate > HIBA > lactate > acetate.

Spectroscopy of actinides

Similar to the transition metal ions, the actinide ions display a rich variety of colors in their aqueous solutions. The absorption spectra of actinides arise due to the electronic transitions and absorption bands appear mainly from three types of transitions, viz. i) f-f-transition, ii) f-d transition, and iii) charge transfer bands.

In the f-f transitions, the electronic transition occurs between the two 5f-5f orbitals of different angular momentum. As the transitions occur between the orbitals of the same sub-shell they are generally Laporte forbidden. The probabilities of transitions are, therefore, low and the absorption bands are consequently low in intensity. However, the bands are sharp because the transitions take place in the inner shell and are, therefore, not affected significantly by the surrounding environment.

The energy differences between the various energy levels due to the 5f-5f transitions appear in the UV, visible and the near IR regions. The molar absorption coefficients are in the range of ~10–50 $M^{-1}cm^{-1}$. On the other hand, in case of the f-d transitions the absorption bands are broad as these transitions are influenced by the surrounding environment. As transitions take place between the orbitals of different azimuthal quantum numbers they are Laporte allowed and therefore, these bands are relatively more intense. The molar absorption coefficients are of the order of ~10,000 $M^{-1}cm^{-1}$. These bands appear invariably in the UV region due to large energy differences between the d and f orbitals. In case of charge transfer transitions, the absorption bands occur due to the transition between 5f orbitals of actinide ions and ligand orbitals. Therefore, the nature of ligand plays an important role.

These transitions are significantly affected by the surrounding environment. As a consequence, the charge transfer bands are broad. The absorption bands appear in the UV region and are generally less intense than those resulting from the f-d transitions. The absorption spectra of actinide ions have been widely used in the analytical chemistry. The absorption spectra of actinide ions in different oxidation states differ widely,

1.9 Separation of Metal Ions

Several methods are adopted for the separation of the metal ions of interest from the nuclear waste. Solvent extraction, solid phase extraction, liquid membrane, precipitation are some of the commonly used techniques for metal ion separation. All these methods utilize some common principles like equilibrium kinetics, chemical reactions, fluid mechanics, and mass transfer from one phase to another. Though solvent extraction or liquid-liquid extraction is well established techniques solid phase extraction promises to alleviate some of the drawbacks of solvent extraction techniques.

Solvent extraction

Separation by liquid–liquid extraction (also known as solvent extraction) is based on the preferential partitioning of a given solute between two immiscible liquids that are in contact with each other [85]. In this process, a substance is transferred from one liquid phase to another liquid phase. Usually, an aqueous solution containing the metal ion to be isolated is contacted with a specific organic extractant in an organic solvent. The extractant and the hydrated metal ion produce a neutral organic-soluble metal complex which is transferred to the organic phase.

After the metal ion carrying organic phase is suitably isolated, the metal ion is then stripped back into a new aqueous phase in a process known as back-extraction. This mechanism first demonstrated in 1805 by Bucholz for uranium extraction from a nitric acid solution into ether, followed by stripping from ether into distilled water. It remains an excellent method even now combining speed, simplicity and versatility.

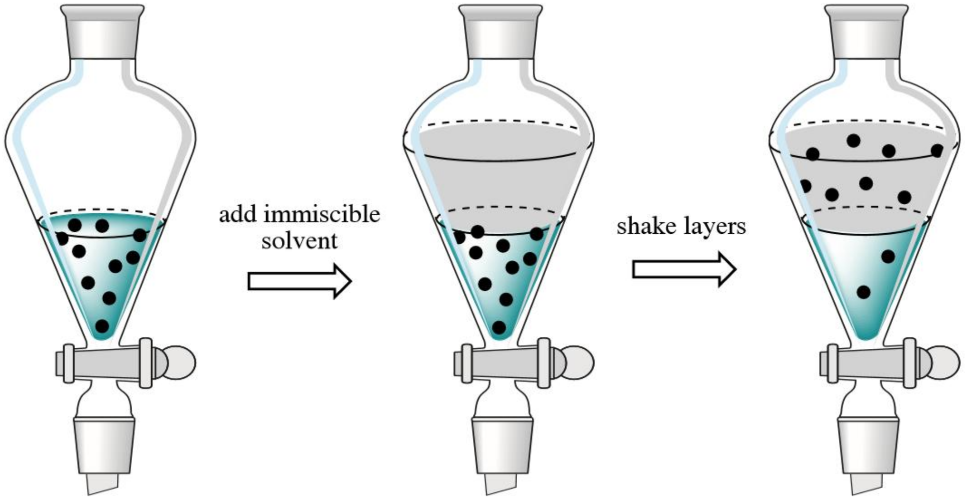

Figure 1.12: Diagrammatic presentation of solvent extraction

The thermodynamics of distribution of metal ion can be explained by the phase rule (Equation 1.9) which can be written as:

$$C - P + 2 = F \tag{1.9}$$

Where C, P and F denotes the number of components, number of phases and degrees of freedom respectively. For a binary system such as liquid-liquid extraction, number of phase is two i.e. P = 2 and number of components can be three or more including two solvents and one or more solutes. Therefore, the ratio of concentration of solute in the two phases is constant as long as the temperature and pressure of system remain the same. According to Nernst distribution law, the concentration of a particular species (M) in the organic phase and in the aqueous phase at equilibrium can be expressed as

$$[\mathrm{Metal}]_{aq} \rightleftarrows [\mathrm{Metal}]_{org} \tag{1.10}$$

In Equation 1.10, the term in subscripts org and aq denote the organic and aqueous phases, respectively. If the solute species (M) remains same in both the phases, the ratio of solute concentration in the organic and aqueous phase is termed as the ‘distribution coefficient’ (K_d) or ‘partition coefficient’.

$$K_d = \frac{M]_{Org}}{[M]_{Aq}} \tag{1.11}$$

Distribution ratio

The distribution ratio‘D’ is defined as the ratio of the total metal ions concentration in organic and aqueous phase. Here total concentration of metal represents all forms of metal ion in that particular phase. For a given metal species M it can be written as Equation 1.12

$$D_M = \frac{[M]_{t,org}}{[M]_{t,aq}} \qquad (1.12)$$

Percentage extraction

The percent extraction E, is more commonly used term for expressing the extraction efficiency in separation science and can be related to D as shown in Equation 1.13.

$$\%\ E = 100 \times \frac{V_{org}[M]_{org}}{\{V_{org}[M]_{org} + V_{aq}[M]\}_{aq}}$$

$$= 100 \times \frac{D}{\left(D + \frac{V_{aq}}{V_{org}}\right)} \qquad (1.13)$$

Where, V represents solvent volume of two phases. When the volume ratio of two phases are one then the % E can be expressed as Equation 1.14.

$$\%\ E = \frac{D}{(D+1)} \qquad (1.14)$$

Separation factor

It is a measure of the ability of the system to separate two metal ions. If there are more than one metal ion (metal ions A and B) and the desired metal ion is A then, the selectivity of the solvent for metal ion A as against B is defined as the ratio of the distribution ratio of A to the distribution ratio of B. The separation factor (S.F.) is related to the individual distribution ratios as shown in Equation 1.15.

$$S.F. = \frac{D_A}{D_B} \qquad (1.15)$$

Decontamination factor

The ability of a process to remove a contaminant from a product is expressed by the decontamination factor. For example, if a process has a 1:9 mixture of M_A to M_B, and the product is a 1:99 mixture of M_A and M_B, then the decontamination factor (for the removal of MA) of the process is 0.10 / 0.01 = 10, assuming species A to represent the contaminant.

Membrane separation

Another frequently used technique for metal ion separation is use of membranes. Membrane separation technology has replaced solvent extraction technique due to a number of advantages like that of operational simplicity, high selectivity, simple technology and low energy requirements [86].

Solid liquid extraction

Solid-phase extraction refers to a liquid, semi-liquid or potentially solid complexing agent dispersed more or less homogeneously within an inert, solid medium. A solid-phase extraction material comprises three major components: a solid support or substrate, a stationary extractant phase, and a mobile fluid phase.

Various materials have been used for the solid support, e.g. inorganic materials such as silica gel, titania, carbon nano tube, magnetite etc. organic polymers such as polystyrene-divinyl benzene copolymers and poly methacrylate resins, or resins made of both organic and inorganic materials. The stationary phase is typically an organic extractant, many of which have been well characterized for their use in liquid-liquid extraction. Similar to liquid-liquid extraction, the target metals are converted from the hydrated ionic form to a neutral organophilic metal complex within the stationary phase.

The advantages of solid-liquid separation (SPE) over the conventional liquid – liquid extraction technique are minimization of secondary waste volumes, lowering the use of volatile organic substance, prevention of third phase formation, no requirement of organic diluent etc are summarized in **Fig. 1.13**. The most common method of making SPEs for lanthanide and actinide separations is impregnation of a ligand on a solid support. Since the ligand is impregnated, rather than being bonded to the support, ligand detachments are well known issues.

During solid – liquid extraction the targeted metal ions can get attached to the ligand by different mechanism of extraction. A comparative evaluation of energy of complexation is shown in Table 1.5.

Table 1.5: Energy of the interactions used by solid phase extraction

Interaction	Energy (kJ/mol)
Dipole - induced dipole	8-25
Dipole – dipole	25-40
Hydrogen bonding	25-40
Ionic	250-1050
Covalent	670-3360

Extraction chromatography

Extraction chromatography combines the selectivity of solvent extraction with the ease of chromatography. In industry, the most common supports used for the separation/purification steps are ion-exchange (IEC) and extraction (EXC) chromatographic-based resins [87].

Most of the sorbents used for the extraction/separation steps are based on the "physical" addition (impregnation) of the ligands to the solid support. The literature [88] lists the following methods for the preparation of extractant impregnated resins:

1. Dry impregnation. 2. Wet impregnation and 3. Modifier addition method.

Process	**Liquid Liquid Extraction (LLE)**	**Supported Liquid Liquid Extraction (SLE)**	**Solid Phase Extraction (SPE)**
Picture	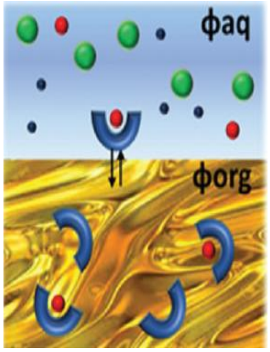	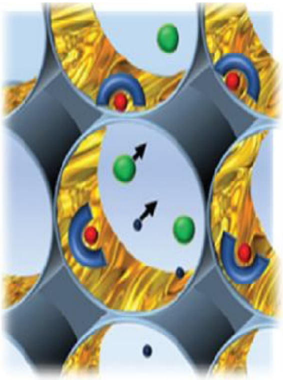	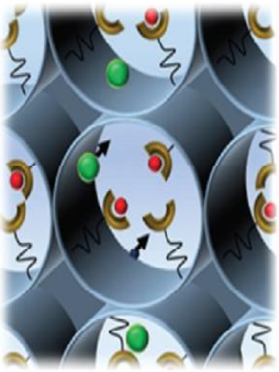
Advantages	• Automated • Continious • Ligand Varity	• Sub-milli molar solvent concentration • Independent of diluent used • Ease of operation	• No leaching of the functional group • Shape control • Ligand varity • No diluents requirement and no third phase formation
Limitations	• Third Phase formation • Volatile organic handling • Large secondary waste generation	• Solvent leach out during use • Loading of solvent is limited • Limitation in repeated use	• Stability • Synthesis

Figure 1.13: Pictorial comparison of liquid–liquid and liquid–solid extraction methods [89]

Most studies indicate that the impregnation of the macroporous, inert resin is a combination of adsorption via van der Waals forces and potentially physical trapping of the ligands within the pores of the solid support [90].

The extractants are generally classified on the basis of structure, extraction and stripping chemistry, and the type of metal complex formed [91]. The four primary groups are: solvating or neutral extractants, chelating extractants, organic acid extractants and ion pairing extractants.

Established solid-phase extraction resins for actinides and lanthanides

In Europe and the USA, investigations into a variant of the PUROCHROMEX [92, 93] (Plutonium Uranium Recovery On CHROMatographic EXtraction columns) have been carried out. This process is designed primarily for the recovery of Uranium and Plutonium. It has been shown that TRU chromatographic resin consisting of 13% CMPO and 27% TBP adsorbed onto AmberchromTM CG-71 can be used for the separation of transuranic elements [94]. TODGA impregnated SiO_2-solid-phase extraction resin was evaluated for performing group separation of MA and Ln elements from HLLW [95].

A solid-phase extraction resin consisting of 30% (w/w) TODGA and10%(w/w) TBP adsorbed onto Amber chrom CG-71 was evaluated for the separation of An and Ln elements from a simulated PUREX raffinate solution [96]. Various flow sheets using CMPO and TODGA sorbed onto SiO_2 have also been proposed and tested for partitioning An(III) and Ln(III) elements as part of the proposed Minor Actinides RECovery (MAREC)process based on solid phase extraction [97], [98], [99], [100]

Separation of An(III) from Ln(III) elements

A solid-phase extraction material developed by impregnating *n*-Bu-BTP into a silica-co-polymer support [101],[102],[103] for separating An(III) from Ln(III)and the material were tested in batch as well as small column mode. Excellent decontamination of Am, Cm, and heavy Ln(III) elements from fission products and light Ln(III) elements was achieved using a simulated HLLW solution containing 1 M $NaNO_3$in 0.01 M HNO_3.

A biopolymer microcapsule containing Cyanex 301 (bis(2,4,4-trimethylpentyl) dithiophosphinic acid) extractant[104] has been tested in a small chromatographic column mode and the researchers were able to achieve a separation factor of 20 between Am and Eu in a pH range of 1–2.

As a result of stripping of the extractant, diminishing extraction performances are often observed. In contrast, IEC resins offer good separation capacity and reusability, but lack the elemental selectivity required for the ultra-trace separation. To overcome these limitations, the development of new extraction strategies, such as SPE, has emerged over the past few years [92].

Solid phase extraction

The basic principle of SPE is transfer of metal ions from aqueous phase to the active sites of adjacent solid phase. The mechanism involved in SPE depends on the nature of the sorbent and metal ions. SPE is carried out by means of adsorption, ion exchange, chelation, ion-pair formation, etc. The metal ions sorbed on the solid phase shall be desorbed by changing the condition or using a suitable eluate and thus recovered.

The SPE approach usually provides shorter extraction times, greater separation factors and better reusability than its LLE counterpart. This will in turn help reduce environmental impact and cost.

In addition due to the chemical anchoring of the ligand on the solid support through covalent bonds, the thus-synthesized sorbents should exhibit greater regenerative capacities, ultimately increasing their marketable potential. Furthermore, these functionalized solid sorbents owing to their selective and effective extractive nature should enable the extraction of Rare Earths and actinides with a limited number of separation steps, which should translate positively in terms of generation of waste volume reduction.

The solid phase extractants have two components: 1) Solid support and 2) Extractant ligand.

1.9.1.1 Solid supports

The purpose of the solid support in a SPE is to create a stable, uniform platform for the extractant ligand. Depending on the pore size they are classified into three categories i) macro pores (> 50 nm), ii) mesopores (2-50 nm) and iii) microporores (<2nm). Porosity can offer the advantage of higher ligand loading on the support as a result of a higher surface area. For radionuclides, different solid phase sorbents have been investigated and have shown promising results. Various natural sorbents [105] like peat , silica , alumina , carbon , biomass , and clay minerals along with different synthetic sorbents like resins , zeolites , nanoparticles, and composites have been explored.

Zeolite

Zeolites are microporous crystalline aluminosilicates (tectosilicates) and over 60 types have been identified so far[106], [107], [108], including clinoptilolite, mordenite, phillipsite, chabazite, stilbite, analcime, laumontite and erionite. The zeolite structure, as shown in **Fig. 1.14** is made up of three components: the aluminosilicate framework [$Al_xSi_{1-x}O_2$], exchangeable cations ($M_{x/n}{}^{n+}$) and water (yH_2O). The simplified formula of aluminosilicate zeolites is $M_{x/n}{}^{n+}[Al_xSi_{1-x}O_2]\cdot yH_2O$, where x can vary from 0 to 0.5, y represents water molecules and M^{n+} can be either an inorganic or organic cation. Inorganic cations are usually alkaline or alkaline earth metals.

The cations in the zeolite structure are exchangeable, leading to a rich and diverse ion-exchange chemistry in these materials. Zeolite structures are described in terms of the pore size, geometry and connectivity/dimensionality of the pore space[109]. Zeolites with channels or pore openings around 2 Å and those with pore sizes around 4 Å are known as small pore, but those with pore size 5.5 Å and 7.5 Å are known as medium and large pore respectively. Zeolites are specially used as selective adsorbents and ion-exchangers for water and waste treatment.

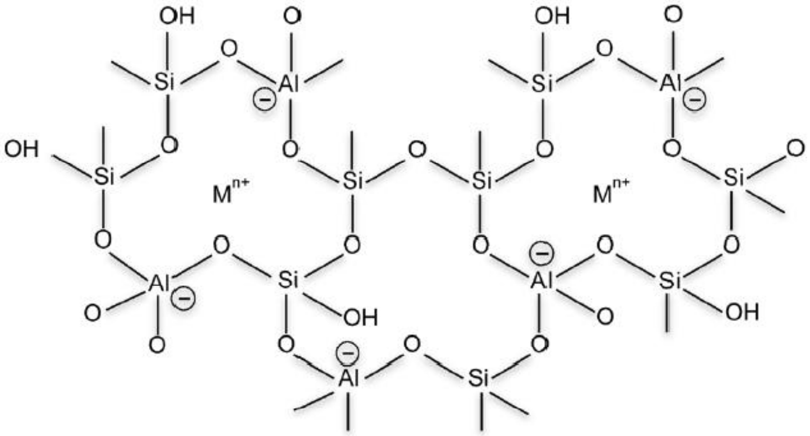

Figure 1.14: Two-dimensional representation of the framework structure of zeolites

Clay minerals

Clay minerals are layerd silicates, known as phyllosilicates. These include the kaolinite group, the smectite group (montmorillonite group), the illite group, and the chlorite group[110]. Although they possess a relatively large cation exchange capacity (CEC) for metals (~1 meq. g−1) but the lack of selectivity limits their practical application.

Bentonite

Bentonite is classed as natural clay of layered phyllosilicates, composed of alternating octahedral and tetrahedral sheets in the ratio of 2:1. The tetrahedral and octahedral sheets have a loose negative charge Si^{4+} and Al^{3+} in the crystal which is balanced out by reacting it with a lower valency cation such as sodium, calcium etc. The structure, chemical composition, exchangeable ion type and small crystal size contribute to the unique property of bentonite including a large chemically active surface area, high cation exchange capacity and high porosity. Montmorillonite can adsorb heavy metals via two different mechanisms: (1) cation exchange in the inter layers resulting from the interactions between ions and negative permanent charge and (2) formation of inner-sphere complexes through $Si–O^-$ and $Al–O^-$groups at the clay particle edges. The adsorption capacity depends on presence of micro and mesopores[111].

MWCNT

MWCNTs combine large surface area, strong affinity for ionic and organic species and hydro phobicity highlighting their potential for heavy ion removal [112],[113],[114],[115],[116],[117]. At present, MWCNTs are expensive, but surface functionalization allows conversion to highly selective and less hydrophobic materials. Further, surface of MWCNTs can be functionalized readily by reaction with a strong oxidizing agent like concentrated HNO_3 [118], which opens avenues to further functionalization using different ligands.

Chitosan

The adsorption capacity of several low-cost adsorbents, such as biopolymers which can be obtained from renewable sources, has been investigated. Among these biopolymers, chitosan (CTS) has proved to be an extremely promising material [119] Chitosan, a polymer made up of glucosamine units, an alkaline deacetylated product of chitin, a polymer made up of acetyl glucosamine units. This material combines high hydrophilicity, nontoxicity and high abundance in nature along with biocompatibility, and biodegradability. A large number of hydroxyl and amino groups presented on chitosan can act as adsorption sites conferring high surface activity.

Chitosan acts as an solid support for the removal of toxic metal ions from the environment as well as for the recovery of valuable metals in hydrometallurgy [120]. Recently, great attention has been paid to the chemical modification of the surface of chitosan with certain functional groups, to overcome the problems such as agglomeration, low porosity etc. as it can evidently improve the physical and chemical properties of chitosan for the removal of metal ions from waste solutions[121],[122].

Titanium oxide

Metal oxide nanoparticles such as TiO_2 are emerging materials due to their potential applications as solid support for separation purposes. Group IV metal oxides such as titania demonstrate superior hydrolytic, thermal and radiolytic stability, to silica and polymer based materials which provides them with an advantage as framework materials for separations in the nuclear context and selectivity toward heavy metal ions can be induced by surface functionalization[123]. Titania based sorbents are used for waste immobilization owing to its more leach resistant characteristics than vitrified silica[124]. Other advantages of titania include ready availability, cost effectiveness, and non-toxicity. Organo-functionalized titanium metal oxide sorbent materials are substantially less common than their silica or polymer resin counterparts, but the desired functional group can be anchored to the surface by ionic bonding. However, under acidic conditions some ionic bonded ligands are cleaved from the surface of titania materials. Therefore, studies have explored the possibility of covalent attachment of an organic extractant to provide superior stability to hydrolytic cleavage via Ti−O−C bonds for the extraction of actinides from nuclear waste[125].

Silica

The ability to achieve covalent bonding of ligands to the silica support is very important for the preparation of stable, reusable SPE. Several studies were carried out in this domain, particularly by Stucky and co-workers[126]. However, silica based materials are not ideal for separations in a nuclear context as they demonstrate relatively poor hydrolytic and radiolytic stability.

1.9.1.2 Different types of ligands

Organophosphorus ligands

Tri-*n*-butyl phosphate (TBP) is commonly used in the PUREX process with an aliphatic hydrocarbon solvent, typically kerosene or dodecane as the diluent. TBP enables almost complete separation of U and Pu from the spent fuel. Similarly, Trialkyl Phosphine oxides have been used to separate trans uranic elements (TRU) from highly active wastes. The TRPO process, based upon this idea was developed in China.

Octyl(phenyl)-*N,N*-diisobutyl carbamoylmethyl phosphine oxide (CMPO) have formed the focus of various studies for the extraction of actinides and lanthanides. The TRUEX process which uses a mixture of CMPO and TBP, developed in the 1980s allows all minor actinides and lanthanides to be extracted from a nitric acid medium.Structure of above metion ligands are shown in **Fig. 1.15**.

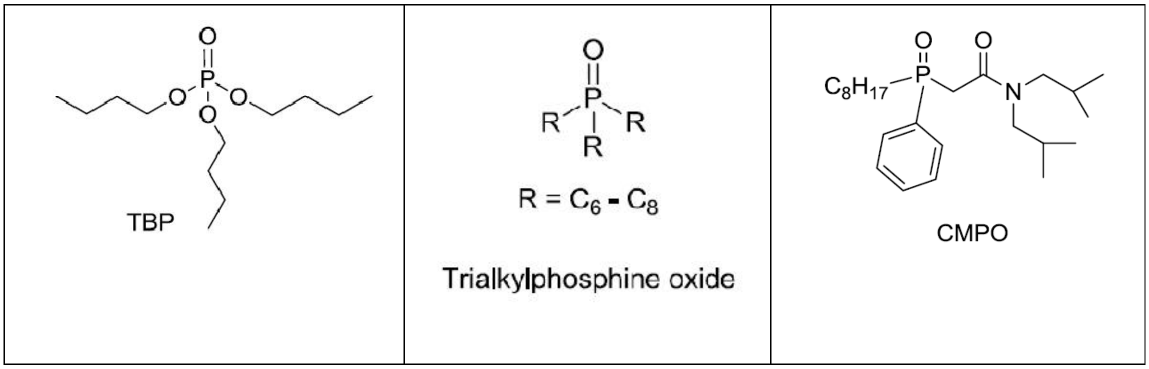

Figure 1.15: Phosphorus based ligands

Malonamides

The malonamides (general formula R1R2NCOCHR3CONR2R1), a bidentate oxygen donor are studied for the extraction of trivalent f-elements from the PUREX raffinates. These extractants are completely incinerable reducing secondary waste volume. Among its different derivatives, *N*,*N*-dimethyl-*N*,*N*-dibutyl tetradecyl malonamide (DMDBTDMA) and *N*,*N*-dimethyl-*N*,*N*-dioctyl-2-(2-hexyloxyethyl) malonamide (DMDOHEMA) have been used. The later one is found to have more extraction efficiency than DMDBTDMA. Extractability of actinides by malonamides is found to folow the order Pu(IV) > U(VI)O_2 > Am(III).Structure of malonamide based ligands are shown in **Fig. 1.16**.

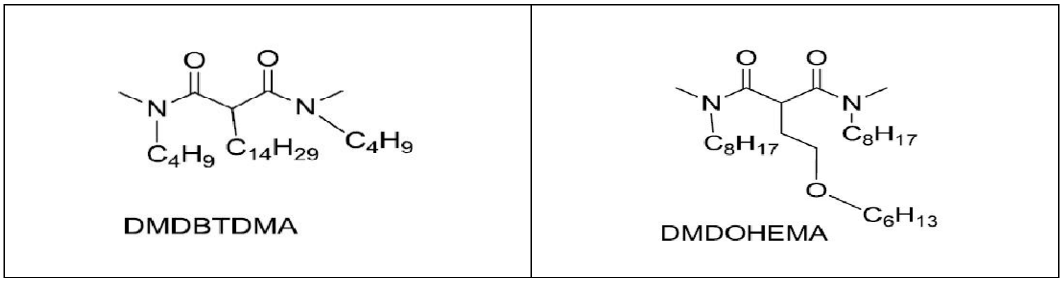

Figure 1.16: Malonamide based ligands

Diglycolamides

In recent past, a new class of ligand called diglycolamides (DGA) has been established for actinide partitioning [127]. This series of ligands are the new sequence of diamide compounds obtained by introducing ether oxygen positioned between two acetamide functionalities. This extra oxygen makes the DGA ligands tridentate, which enhances the effective complexation than diamides. Sasaki et al. synthesized a series of diglycolamides (DGA) ligands having different alkyl chains attached to amide nitrogen atom[51]. Amongst the different derivatives *N*,*N*,*N*‘,*N*‘- tetra octyl diglycolamide (TODGA) and *N*,*N*,*N*‘,*N*‘-tetra-2 ethyl hexyl diglycol amide (T2EHDGA) as given in **Fig. 1.17,** have been found to be most promising because of their significantly higher extraction for trivalent actinides.

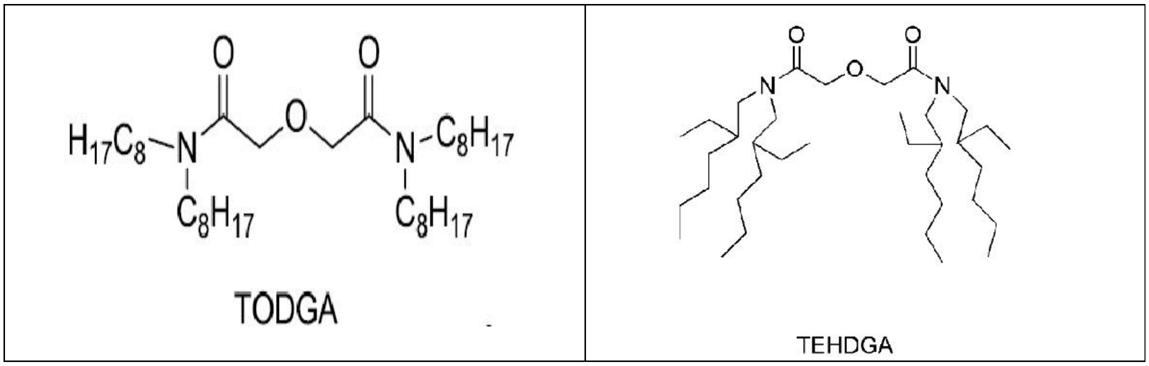

Figure 1.17: Diglycolamide based ligands

N-Donor heterocyclic ligands

N-donor heterocyclic ligands based on pyridine, pyrimidine, pyrazine, 1,2,4-triazine,1,3,5-triazine, 1,2,4-triazole, benzimidazole, benzothiazole, and benzoxazole ringsystems have been studied for selective extraction of actinides over lanthanides [128]. N-Donor ligands were used because they could impart better selectivity than O-donor ligands and extract in moderate acidities (0.1 M – 1 M) than S-donor ligands (at pH range). BTP, BTBP, Tphen and BTphen ligands as shown in **Fig. 1.18**, are extensively explored for the separation of An (III) from Ln (III).

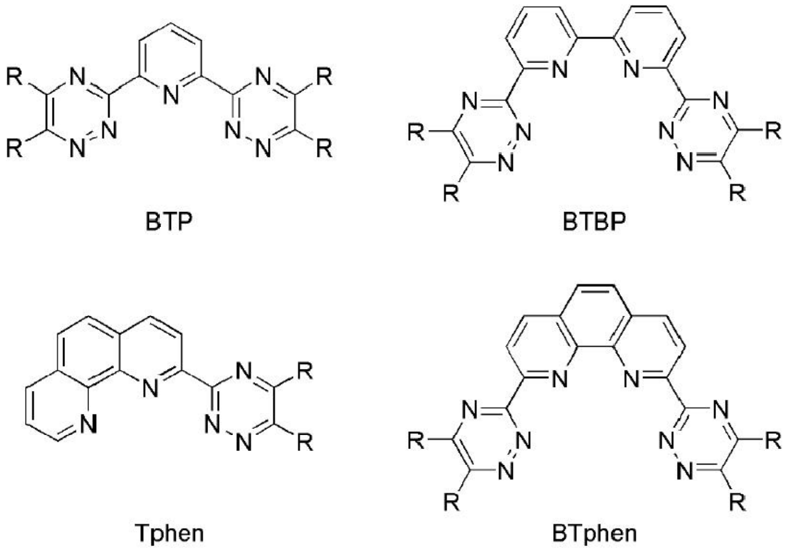
BTP
BTBP
Tphen
BTphen

Figure 1.18: N- donor heterocyclic based ligands

1.10 Criteria for the Selection of a Suitable Extractant

A number of factors are taken into account while choosing a suitable extractant for metal ion separation [129]. These are as follows:

Extractability

An ideal extractant will have high extractability, allowing maximum metal recovery with minimal steps. This is allowed by the ligand exhibiting better complexation ability for the metal ion of interest. Therefore, the distribution coefficient of the desired metal for the extractant in the solid phase must be as large as possible.

Selectivity

Extractability is by itself of little utility if other metal ions are co-extracted. Indeed, this will cause further steps in purification with increase in attendant waste generation. Therefore, in addition to extractability, selectivity plays an important role also. For most extractants, a judicious balance between extractability and selectivity is most important.

Easy and cost effective synthesis

To perform the extraction process at a reasonable cost the synthesis of ligand functionalized solid support should be easy and cost effective. The synthetic procedure should have as few steps as possible. Synthesis should be done using easily available and inexpensive starting materials.

Recoverability

Easy regeneration of the functionalized material for recycling is also important to make the process cost effective. For this purpose easy stripping of the metal ions from the loaded material is necessary.

Stability of extractant

Functionalized materials should be stable in particular extraction conditions. For separation of metal ions from spent nuclear fuel the ligand functionalized material should have high resistance to radiolytic and hydrolytic degradation during operation.

Other Criteria

For health and safety purpose the material should not have toxicity and flammability.

1.11 Scope of Thesis Work

Based on the above discussion, it is clear that the successful development of efficient solid phase adsorbent systems and its implementation towards separation of radio nuclides, particularly actinide ions, from various nuclear waste streams is advantages over the conventional liquid-liquid extraction method. The conventional solvent extraction technique has several limitations like large volume of secondary waste generated from the used volatile organic solvent, poor phase separation, third phase formation, and use of highly volatile, often flammable organics etc. Solid-liquid extraction is a better substitute for solvent extraction, to overcome some of these difficulties. Thus, organic ligand functionalized solid phase extractants can provide an alternative route for extraction of metal ions. In the thesis, a dedicated efforts have been made to synthesize five different organo functionalize solid phase extractants and evaluated for the separation of actinides. It is worthy to mention here that functionalize solid phase extractants are required only in sub milimolar quantities of organic extractant and there is no need of diluents.

The detailed work carried out during the course of the thesis work are outlined as follows:

1. Functionalization of the conventional ligand (DGA, DPA, Amidoamine, Polyamidoamine, Tripoly phosphate) on a solid support and their evaluation for the extraction of actinides from nuclear waste stream. Therefore, the extraction/separation behavior of actinides and lanthanides using the newly synthesized sorbents has been evaluated. The mechanism of metal ion extraction was studied. The elution of the metal ion from the solid phase, often a challenging area, was also explored.

2. A successful separation process involves the understanding of complexation, kinetic and thermodynamics associated with the extraction procedure. Therefore, it is very important and interesting to study complex formation, evaluate the degree of covalency of the metal-ligand bond, Gibb’s free energy of extraction etc. This is made possible by evaluation of the associated thermodynamic parameters using density functional theory calculations.

3. Finally, the central idea of developing a solid phase extractant system for removing actinides is its successful application in extraction of target metal ions from nuclear waste solution. It is also required to know the extraction behavior of the concomitant metal ions present in waste solution. For the long term application of the solvent system for actinide extraction, one needs to understand the radiolytic degradation behavior which can answer queries on the sustainability and recycling possibilities

Chapter 2: Experimental and Characterization Techniques

Chapter 2

Experimental and Characterization Techniques

2.1 Introduction:

Ligand functionalized solid phase extractants have been synthesized for the potential technological applications for the sequestration of radionuclides from waste solutions. This chapter discussed the methods used for sample synthesis and subsequent characterization of these samples. The characterizations include structural and sorption studies, which have been briefly discussed. The chapter begins with synthesis, while characterization is discussed subsequently.

2.2 Synthesis

Amido amine functionalized multiwall carbon nanotube

This section first covers the synthesis of amido-amine functionalized carbon nanotubes. In all the synthesis reported, the carbon nanotubes were procured as synthesized and then functionalized in our laboratory. Toward this synthesis, Multi wall carbon nanotubes (MWCNTs), Ethylenediamine (EDA), N,N'-dicyclohexylcarbodiimide (DCC), ethanol, methanol, nitric acid and sulfuric acid were utilized.

1 g MWCNTs were added to a 200 mL 3:1 mixture of concentrated sulfuric and nitric acid. This mixture was treated in an ultrasonic bath for 5 h at 60^0 C. Upon completion, the mixture was filtered and washed with distilled water until the pH of the filtrate was 7. The filter product was dried in a vacuum oven at 100 ^{0}C overnight. Thus synthesized carboxylic acid functionalized MWCNTs were further treated to functionalize with amido-amine. For this, MWCNT-COOH (500 mg) was suspended in 30 mL of EDA by using an

ultra-sonicator for 30 minutes at room temperature and then magnetically stirred at 300 rpm for 30 minutes. 70 mg of DCC was added slowly to the suspension and then it was refluxed at 90^0C for 48 hours. The black reaction mixture was then transferred to an Oak ridge centrifuge tube with ethanol and centrifuged at 5000 rpm for 15 minutes. After decanting the supernatant solution, the black residue was washed thrice with ethanol. The transparent supernatant solution was decanted and the product was transferred to a glass Petri dish with methanol and dried overnight at 80^0C in a vacuum oven

Polyamidoamine functionalized Chitosan

The second material synthesized was polyamidoamine functionalized Chitosan. Again, the thrust area of this work was directed towards functionalization up to the third generation. Chitosan (Alfa Aesar) was used as delivered without further analysis or purification. In addition, Methyl Acrylate (MA), methanol, and Ethylene diamine (EDA) were also used.

A series of samples were prepared with nomenclatures CTS – 0, 0.5, 1.0, 1.5, 2.0, 2.5 and 3.0.

Preparation of CTS – 1.5 to 3.0 is identical to CTS – 1.0. It may be noted that CTS – 1.0 is the first generation functionalized material, while CTS – 3.0 can be thought as a third generation functionalized material. The ‘generations’ here refer to the increasing number of functional groups rather than denoting any historical context.

2.2.1.1 Synthesis of CTS-0.5

CTS-0.5 was synthesized by the Michael addition reaction of Methyl Acrylate (MA) to amino groups on the surface of CTS-0. Using 80 mL Methanol in a 500 mL round bottom flask, 10 g of CTS-0 powder was swollen for 4 h. Under a nitrogen atmosphere, 50 mL of redistilled MA were added to a 500 mL round bottom flask that contained 10 g swollen

CTS-0 powder. The flask was sealed, and the mixture was stirred magnetically at 50^0C for 4 days. After this, the solid product was collected by filtration and thoroughly washed in MeOH, followed by vacuum drying at 50^0C for 48 h.

2.2.1.2 Synthesis of CTS-1.0:

CTS-1.0 was prepared by amidation of CTS-0.5 with Ethylene diamine (EDA). Using ~70 mL Methanol in a 500mL round bottom flask 9 g of CTS-0.5 powder was swollen for 4 h. The mixture was stirred magnetically at room temperature for 5 days and at 50 ^{0}C for 3 days. The resulting solid product was collected by filtration and thoroughly washed in MeOH, followed by vacuum drying at 50^0C for 48 h.

2.2.1.3 Synthesis of CTS-1.5

The reaction was carried out with 4 g of CTS-1.0 and ~40 mL of MA in 30 mL MeOH under an inert nitrogen atmosphere. The reactant mixture was stirred for 4 days at 50 ^{0}C, and then the product was collected by filtration, washed, and dired as above for CTS – 0.5.

2.2.1.4 Preparation of CTS-2.0

The reaction was carried out with 34 g of CTS-1.5 and 14 mL of EDA in 45 mL of MeOH under an inert nitrogen atmosphere, followed by magnetic stirring for 5 days and 50 ^{0}C for 3 days. The purification procedure was similar to that for CTS-1.0.

2.2.1.5 Preparation of CTS-2.5

The reaction was carried out with 3.0 g of CTS-2.0 and 60 mL of MA in 50 mL MeOH under an inert nitrogen atmospher, followed by stirring for 4 days at 50 ^{0}C, and filtration to obtain a solid product.

2.2.1.6 Preparation of CTS-3.0

The reaction was carried out with 3 g of CTS-2.5 and 25 mL of EDA in 80 mL of MeOH under an inert atmosphere of nitrogen gas, followed by magnetic stirring at room temperature for 5 days and 50 ^{0}C for 5 days. The final product was obtained by filtration as discussed for the previous samples.

Synthesis of diglycolamic acid functionalized TiO_2

Diglycolic anhydride, (3-aminopropyl) triethoxysilane, dichloromethane, $CaCl_2$, toluene, TiO_2 powder, isopropanol, acetone and Demineralized Water were the precursors. All the reagents used are of analytical grade, procured commercially and used as it is without further purification.

2.2.1.7 Synthesis of silane-diglycolamic acid (Silane-DGAH)

Silane–DGAH was obtained by the condensation reaction between diglycolic anhydride (0.03 mol) present in dichloromethane (30 mL) and 3-aminopropyltriethoxysilane (APTES, 0.03 mol). The diglycolic anhydride was taken in a round bottom flask equipped with a $CaCl_2$ guard tube and APTES was added drop-wise to the solution. Post strring at room temperature for ~ 6 h, a rotary evaporator was used to drive out the solvent at 353K. Vaccum drying then resulted in the final product.

2.2.1.8 Preparation of TiO_2-DGAH

Preparation of TiO_2-DGAH, was carried out by the reaction of $TiO_2$and Silane-DGAH in toluene medium under refluxing conditions for 6 h. This results in formation of diglycolamic acid functionalized TiO_2 through linkage between surface -OH groups of TiO_2 and Silane-DGAH. The product was then washed with toluene, isopropanol, acetone and water-acetone mixture.

Synthesis of dipicolinamide functionalized TiO_2

2,6 – pyridinedicarboxylic acid, xylene, PCl_5, (3-Aminopropyl)triethoxysilane (APTES), tri ethylamine (TEA), TiO_2 were the precursors. All of the reagents used in the present investigation are of analytical grade and used as received without further purification.

2.2.1.9 2,6-pyridinedicarboxylic acid chloride

2, 6 – pyridine dicarboxylic acid chloride was synthesized by dropwise addition of PCl_5 (6.0 mmol) to 2,6-pyridine dicarboxylic acid (3.0 mmol) in xylene. The resulting mixture was refluxed for 16 h. The excess solvent was removed using rota evaporator and high vacuum distillation at 0.1 mbar pressure and 90˚ - 110˚C.

2.2.1.10 Silane-dipicolinamide (Silane-DPA)

APTES (3.0 mmol) and TEA (3.0 mmol) dissolved in chloroform was charged into the reaction vessel kept in ice bath and cooled to 0-5^{0}C. Dipicoloylchloride dissolved chloroform was added drop wise for a period of 2 h with continuous stirring and after completion of addition, the ice bath was removed and the resulting mixture was stirred at room temperature for 16 h during which a white precipitate was formed.The reaction mixture was then filtered to remove the TEA. HCl precipitate, followed by consecutive washing of the filtrate with 0.1 N HCl and distilled water till neutral aqueous phase results. The washed chloroform phase was dried over anhydrous $MgSO_4$ and distilled in a rota vapourizer to obtain a pale yellow liquid.

2.2.1.11 TiO_2-DPA

The final product, TiO_2-DPA, was prepared by refluxing the $TiO_2$and Silane-DPA obtained in previous steps in toluene medium for 6 h. During this reaction the surface -OH groups present on TiO_2 react with Silane-DPA to form DPA functionalized TiO_2. The functionalized adsorbent was collected and washed several times with toluene, isopropanol, acetone and water-acetone mixture.

2.3 Preparation and Purification of Radiotracers

The separation studies on metal ions reported was demonstrated on the lab scale using various tracers. Procurement, preparation as well as purification of these are briefly discussed below:

Uranium-233

^{233}U tracer ($t_{1/2}$ = 1.59 x10^5 years) was produced by the irradiation of ^{232}Th followed by its purification [130]. Purification of ^{233}U from its daughter products and Thorium was carried out from 6 M HCl using anion exchange procedure [131].

The radiotracer, ^{241}Am was used from laboratory stock solutions after purification prior to their use by ion-exchange methods as reported earlier [132].

Other radiotracers

The radiochemical tracers such as $^{152-154}$Eu were procured from BRIT, Mumbai and their radiochemical purity was ascertained by gamma spectrometry employing high resolution HPGe detector.

2.4 Analytical Methods

Several techniques have been used for the physical and chemical characterization of the synthesized sorbents and extraction studies.

Gamma ray detection system

Gamma rays are detected by the charging produced by the γ-photons during interaction with the detector volume. Therefore, the γ-detector uses the photoelectric effect for detection. When a γ-photon enters the detector, it interacts with the atoms of the detector material and energetic electrons are ejected from one of the bound shells of the atom.Schematic of radiation counting system shown in **Fig. 2.1**.The two most common detector systems include: (i) NaI(Tl) scintillation detector and (ii) High purity HPGe detector for measurement of the concentration of ^{241}Am and $^{152+154}$Eu. A brief description of these two detector systems is given below.

2.4.1.1 Scintillation detector

0.1 – 0.2% thallium activated sodium iodide, NaI(Tl), is the most ubiquitous scintillator for gamma assaying of radionuclides. It combines low cost, ease of operation and ruggedness [133] [134]. The band gap of NaI is ~ 5 – 6 eV and when a charged particle or γ – ray falls on the detector, it is used to either excite electrons into the conduction band, or ionize the atoms of the crystal. The excited electrons de-excite by emission of UV light and return to the valence band. Since the light has to be amplified in a PMT, the UV light must be downshifted in frequency into the visible region. This is achieved by doping the crystal with activator impurities such as Tl.

The resolution of NaI(Tl) detector is about 7% at 662 keV. In the present work, a 3" x 3" well type NaI(Tl) detector coupled with a multichannel analyzer has been used for gamma counting. Nearly 100 % detection efficiency for moderate energy photons in a well type NaI(Tl) detector offers great advantages for counting of low activity samples. A suitable aliquot (0.1 - 0.5 mL) of the desired analyte solution was taken in glass counting tubes which was then placed in the cavity of detector coupled with PMT and associated electronics. Each sample was counted for sufficient time to get more than 10,000 counts to restrict statistical counting error within 1%.

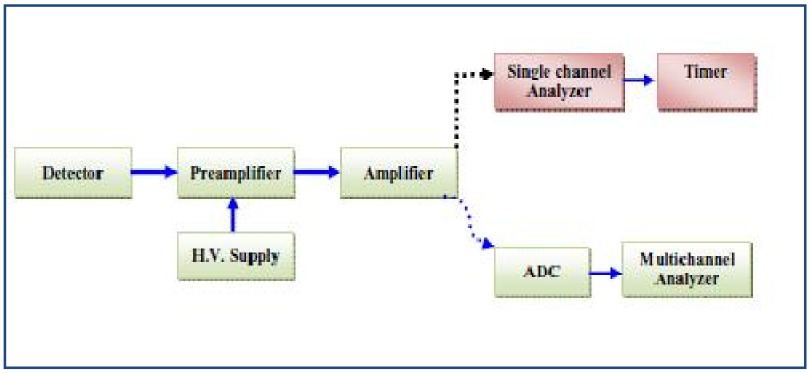

Figure 2.1: Block diagram of radiation counting system

2.4.1.2 High purity HPGe detector

HPGe detector employ high purity (~10^9 atoms/cm^3) Ge crystals. The band gap of Ge is ~ 0.7 eV and electron hole pair can be thermally generated at room temperature. These carriers constitute a background, which is minimized by cooling the detector in liquid nitrogen (LN_2).

The detector operates in reverse bias to ensure as wide a depletion layer as possible in the p-n junction. A typical planar HPGe detector is shown in **Fig 2.4.** The interaction of the detector with the γ – radiation results in typical radiation effects such as photoelectric effect, Compton scattering and pair production. The charges produced by these processes is collected across the reverse biased p-n junction and processed. Of course, the lighter Ge atom has a smaller photoelectric cross-section compared to NaI by a factor of ~ 20. Consequently, intrinsic efficiency is lower. However, the resolution (around 2 kev at 1332 Kev) compensates for the lower efficiency.

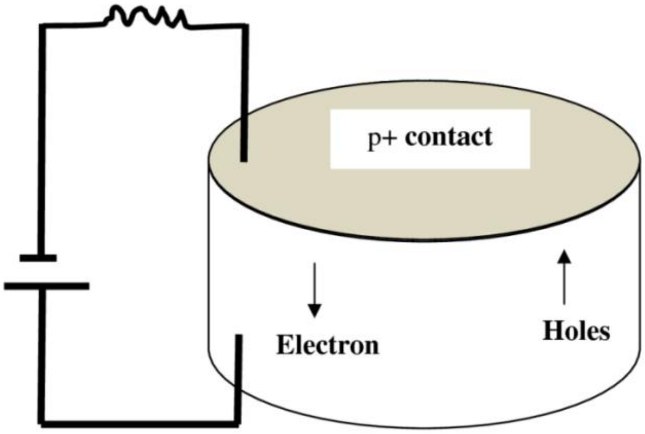

Figure 2.2: Typical planner configuration of HPGe detector applied in reverse bias

X-ray diffraction

X-rays are one of the most commonly used material characterization probes. At present, they are available on various scales from lab sized machines for rapid sample characterization to large central facilities with synchrotron XRD for detailed crystallographic investigations. X-rays were first discovered in 1895 by Wilhelm Röntgen, and he was the recipient of the first Nobel Prize in 1901 for the same. The utility of X-rays as a probe for materials was first postulated in 1912 by Max Von Laue. He showed that diffraction was observed when X-rays were passed through a grating. Since the grating element was of the order of angstroms, he postulated that crystalline materials, exhibiting similar interatomic distances, could be used as a 3-D grating. The father son duo of William Henry Bragg and William Lawrence Bragg made pioneering contributions to X-ray crystallography and along the way cemented the counter intuitive idea of wave-particle duality.

While X-ray based characterization and crystallography is an involved area, only an overview of the technique is presented here for brevity. The foundation of XRD is the Bragg's law which is presented in Equation 2.1

$$n\,\lambda = 2d_{hkl} \sin\theta \qquad (2.1)$$

In equation 2.1, λ represents the wavelength of the X-rays used, d_{hkl} represents the interplanar spacings between atomic planes with Miller indices h, k, l and θ, known as the Bragg angle. XRD relies upon irradiating the sample of interest by a monochromatic X-ray beam. This beam can be obtained by bombardment of accelerated electron on a suitable target such as Cu, Fe, Mo or Cr. Typically, Cu and Mo sources are ubiquitous. Irrespective, the accelerated electrons from the filament knock out inner shell electrons of the target material, and these vacancies are filled by outer electrons dropping into them. This results in the emission of characteristic X-rays. Usually there are several characteristic peaks in addition to a continuous background known as the Bremstrahlung. Filters and collimators remove all X-rays not necessary for the experiment including the Bremstrahlung, while collimators and slits are used to optimize beam divergence and spot size on the sample. The X-ray beam thus monochromated, and collimated is directed to the sample. **Fig. 2.3** show the schematic diagram of X-ray diffractometer.

The sample is scanned in either a θ – θ or θ – 2θ geometry to create a plot of intensity versus angle. Depending upon the values of 2θ for which equation (2.1) is satisfied, peaks are observed in the diffractogram. Based upon equation (2.1), suitable d-spacings can also be extracted for the material, allowing identification of the crystalline phase. In the present study, Philips 1710 diffractometer based on the Bragg-Brentano reflection geometry, was used for the characterization of all the glass samples. The Cu-K_α from sealed tube was used as the incident beam. A Ni foil was used as a filter and the diffracted beam was monochromatised with a curved graphite single crystal. The Philips

(PW-1710) diffractometer is attached with a proportional counter (Argon filled) for the detection of X-rays. The X-ray tube rating was maintained at 30 kV and 20mA. The goniometer was calibrated for correct zero position using silicon standard. Samples were mounted on glass slides after fine pulverization. The X-ray beam falling on the sample at a particular angle leads to the simultaneous exposure of several stacks of plane. The sample is scanned for varying incident angle and intensity of the diffracted beam is measured and plotted against 2 theta angle.

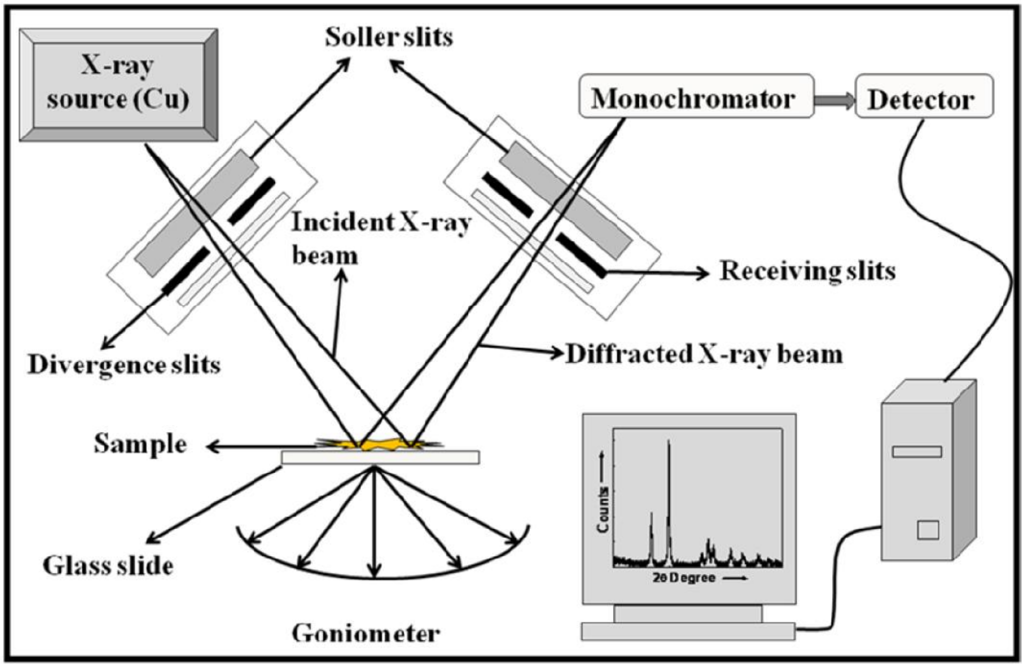

Figure 2.3: A schematic diagram of X-ray diffractometer

Scanning electron microscopy

The Scanning Electron Microscope (SEM) is a characterization technique that became viable in the1950s and achieved large scale application in the 1970s and 80s with the advent of solid state electronics and computerization. A SEM exploits the smaller De-Broglie wavelength of energetic electrons, compared to visible light, to achieve high resolution imaging of the surface topography of various samples. While there are several manufacturers of these systems and they differ in particular detail, all SEMs consist of an electron source, usually a filament or a high brightness field emission source; a column with beam steering/scanning coils, a suitable detector and a vacuum system in which they all are mounted. Indeed, the requirement of ultra-high vacuum necessitates the presence of a vacuum system comprising a rotary backed turbomolecular pump. Schematic diagram is shown in **Fig. 2.4**.

In some SEM systems, it is possible to maintain the sample chamber at near atmospheric pressure, while holding ultra-low vacuum in the gun assembly by differential pumping through pressure limiting apertures (PLA). This in turn allows direct imaging of non-conducting samples, and the build-up of surface charge is neutralized by water vapour. Such a mode is known as environmental SEM or ESEM. Several non-conducting samples in this work have been imaged using ESEM mode.

The electron beam generated from either the filament of field emission source is suitably accelerated through an anode set-up to appropriate acceleration voltage. It is then passed through a set of condenser lenses and scanning coils. The scanning coils allow beam rastering across the sample surface. The interaction of the electron beam with the sample leads to the secondary electrons, backscattered electrons, Auger electrons and characteristic X-rays. Indeed, Auger electron Spectroscopy (AES) is a separate technique. In the present work, sample imaging has largely been achieved using secondary electrons, although back scattered electron imaging is also possible in cases where Z-contrast is desired. Further, it may be mentioned that in ESEM mode, secondary electrons are detected in the gas phase using a gaseous secondary electron detector (GSED). The required image is generated on the screen using the output generated by the relevant detector [135], [136]. The possible interactions of the energetic electrons in the beam with the sample are shown in **Fig.2.5**.

The X-rays produced due to emission of secondary electron are collected by a semiconductor detector (Si/Li) to obtain the elemental composition of the sample. The SEM micrographs in this thesis have been recorded on a Philips XL-30 ESEM. For the largely non-conducting samples in this study, environmental mode with differential pumping (as discussed previously) has been utilized. Elemental analysis was carried out using an Oxford Instruments XMAX 80 EDS set-up integrated with the SEM.

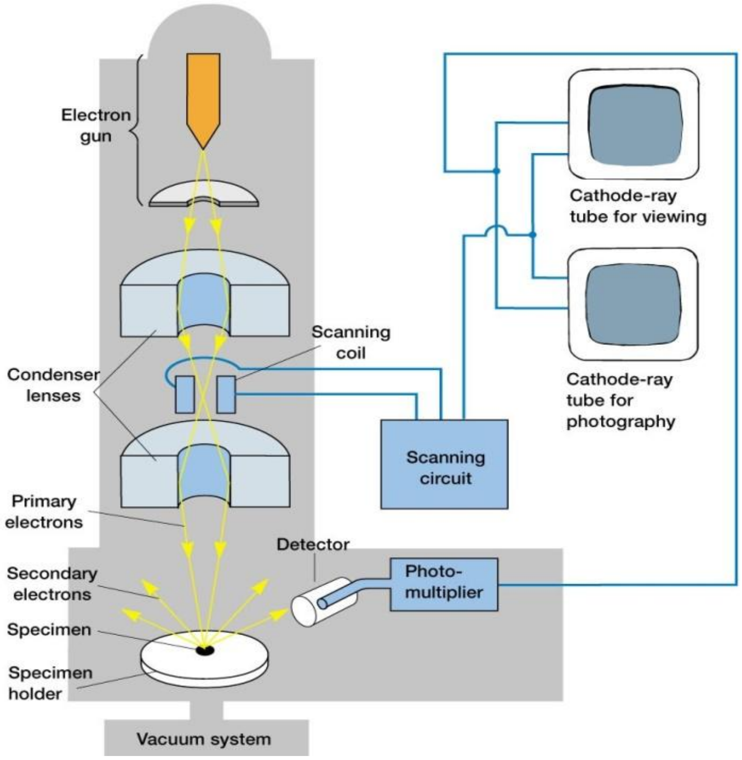

Figure 2.4: Schematic representation of SEM microscope

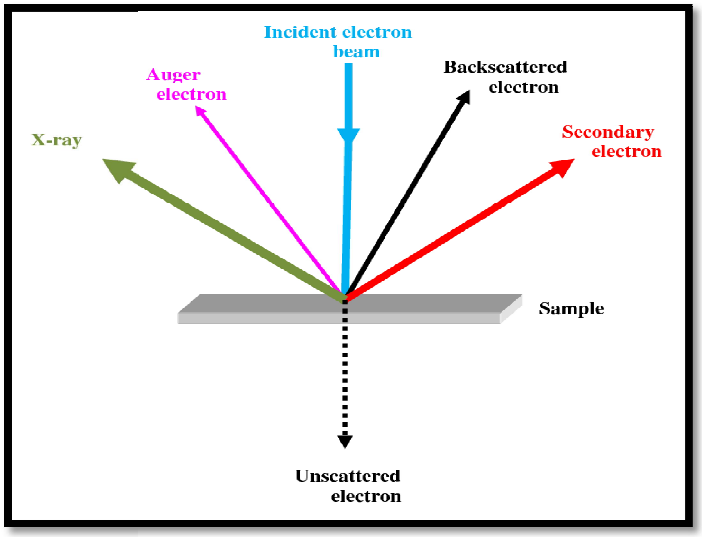

Figure 2.5: Interaction of electron beam with sample

X-Ray Photoelectron Spectroscopy

X-ray photoelectron spectroscopy (XPS) can be thought of as a converse technique to EDS. In EDS, an electron beam is used to generate characteristic X-rays, which are then analyzed for deduction of elemental composition. The penetration depth of the energetic electrons means that the probed depth in 1 – 3 µm. In other words, EDS is not very suitable for thin films or true surface analysis. In case of XPS, a beam of X-rays, usually Al K-α is directed at the sample, which causes emission of electrons due to the photoelectric effect. An electron energy analyzer is used to measure the energy of the emitted photoelectrons. From the binding energy and intensity of a photoelectron peak, the elemental identity, chemical state, and quantity of a detected element can be determined. Since X-ray penetration into samples is limited to ~ 500 nm, XPS is a truly versatile and rapid surface characterization technique.

Thermal analysis

Thermal analysis is an analytical method for investigating changes in a sample (either thermal events or mass change events) with temperature. The most common thermal analysis techniques include Thermo-Gravimetric Analysis (TGA), Differential Thermal Analysis (DTA) or Differential Scanning Calorimetry (DSC). Usually, TG is combined with either DTA or DSC in a single machine to give a TG-DTA or TG-DSC. A brief discussion of TG and DTA/DSC is provided below.

2.4.1.3 Thermogravimetric analysis (TGA)

TGA involves precise measurements of the sample mass as a function of time or temperature, while the sample is subjected to a controlled temperature programme. The technique is best suited to the detection of events such as evaporation, sublimation or oxidation, which cause a mass change in the sample. Processes such as melting, or phase changes where mass is conserved are TGA insensitive.

In its simplest form a TGA instrument consists of a precision balance and a high precision furnace for heating the samples. The instrument also has the provision for various inert gases such as N_2 or Ar, reactive gases like O_2 or air. Usually, thermal sensing is also provided in hybrid TG-DTA or TG-DSC instruments, but the mass sensitivity for hybrid machines is typically worse than dedicated TG set-ups. In most modern machines, a computer controlled heating protocol can be provided and thermal changes can be recorded and plotted suitably.

2.4.1.4 Differential thermal analysis (DTA) / Differential Scanning Calorimetry (DSC)

DTA and DSC are allied techniques and rely upon measurement of temperature difference between the sample and an inert reference material (usually alpha alumina). The Sample and reference are heated at a constant rate or can be measured isothermally as discussed in case of TGA. In case of DTA, the temperature difference between the sample and reference is monitored continuously as a function of time or temperature. If the sample undergoes an endothermic event such as melting, its temperature will lag the reference material and the corresponding event is displayed as an endothermic peak. In contrast, if the sample undergoes an exothermic event such as crystallization or combustion, the sample temperature will exceed that of the reference material and the corresponding event will be displayed as an exothermic peak. It is important to note that DTA measures only the temperature difference between the sample and reference as a function of temperature. Since heat flow is not recorded directly, enthalpy changes accompanying thermal transitions cannot be obtained by direct integration of the peak area and requires calibration to known standards.

In contrast, a DSC calculates heat flow by measuring the temperature difference and using the known thermal resistance of the base material on which the crucibles are mounted, using the thermal version of Ohm's law. Therefore, direct integration of the heat flow curve can be used to deduce the enthalpy change accompanying a thermal event without external calibration as in case of DTA. Needless to say, the assumption of the thermal Ohm's law remains valid only if radiant thermal losses are small, which can become a major concern at high temperature. Therefore, beyond 1000 – 1100^{o}C, DSC is more like a DTA. In the present studies, TG/DSC has been performed using a Mettler Toledo TG-DSC Star-e Model 3 system. All measurements were carried out under inert gas (N_2) at a heating rate of 10 K.min^{-1}.

Vibrational spectroscopy

Vibrational spectroscopy is a cornerstone in the identification of different functional groups and is a vast and vibrant technique in itself. In the following, a brief discussion is provided as relevant to the work reported.

The change in the dipole moment caused by the vibration of bonds and groups result in the absorption of infrared radiation and this is the basis of IR spectroscopy. Indeed, modern IR instruments use the Fourier Transformation principle to greatly reduce time of acquisition and increase signal to noise ratio. This is achieved by exposing the sample to a wide band of IR frequencies to simultaneously excite all the modes.

In the present study, infrared experiments were carried out using a FTIR spectrometer (model: Jasco-660) having a range of 200-4000 cm^{-1} and with resolution of 4 cm^{-1}. IR radiation was generated from globar source (silicon carbide rod). The instrument used CsI single crystal, as the beam splitter and deuterated triglycine sulphate (DTGS) as a detector. Prior to IR measurements, the samples were ground thoroughly by mixing with dry KBr powder, made in the form of a thin pellet and introduced into the sample chamber of the instrument. The background of the sample was corrected from the spectra of KBr.

Surface area measurements

Brunauer-Emmett-Teller (BET) surface area of the functionalized solid phase adsorbents were determined by N_2 adsorption-desorption measurement, using Quantachrome Autosorb Automated Gas Sorption System. The samples were out-gassed at 150 ºC in vacuum, before the measurement. The surface area of rest of the sorbents was determined by using SORPTOMATIC 1990 analyzer, from CE Instruments, Italy. Samples were outgassed at 100 ºC in vacuum, before the measurement. The conditioning of these samples was done at relatively lower temperature of ~100 ºC, to avoid thermal decomposition of the polymer matrix.

Dynamic Light Scattering for Zeta potential analyzer

A significant limitation in the adoption of nano materials is their agglomeration tendency driven by high surface to volume ratio and consequent surface charge. A measurement of the Zeta potential is an important parameter to understand the stability of nano particles in solution and bring detailed insights into the causes of dispersion, aggregation or flocculation.

Zeta potential of the samples was determined using a Malvern Zetasizer nano ZS instrument. 1 ml of the sample of interest in aqueous solution was taken in the transparent cell for carrying out the zeta potential measurements. Particle size analysis of the polyphosphate functionalized magnetite metal particles was carried out by Dynamic light scattering (DLS) method, using VASCO-γ particle size analyzer at 25ºC(laser wavelength 658 nm).

Sorption Studies

Sorption studies were carried out, by adding a fixed amount of the sorbent (m) into equilibration tubes, each containing a fixed volume (V) of the sorbate solution of different concentrations. After agitation for known time, a small portion of the aqueous phase was separated, and counted for radio-activity. Equilibrium sorption capacity, q_e, was determined, using Equation (2.2)

$$q_e = (C_0 - C_e)\frac{V}{m} \qquad (2.2)$$

Where, C_o and C_e are the initial and the equilibrium concentrations, respectively, of the sorbate in the solution. There are several models for predicting the equilibrium distribution. In the present work, sorption isotherm study was carried out using four different isotherm models, namely the Langmuir, Freundlich, Dubinin-Redushkevich (D-R) and Temkin isotherms. The applicability of the isotherm equation to describe the adsorption process was judged by the correlation coefficients, R^2 values

2.4.1.5 Langmuir isotherm

Langmuir was the first to propose a coherent theory of sorption onto a flat surface based on a kinetic viewpoint [137].The Langmuir sorption model is one of the best known and most frequently applied isotherms. The Langmuir equation initially was formulated on the basis of a dynamic equilibrium between the sorbent and the sorbate, that is, the rate of sorption (which is the impingement rate at the surface multiplied by a sticking coefficient, sometimes called the accommodation coefficient) is equal to the rate of desorption from the surface.

The assumptions of the Langmuir model are:

1. Surface is homogeneous, that is, sorption energy is constant over all the sites
2. Sorption on the surface is localized, that is, atoms or molecules are sorbed at definite, localized sites
3. Each site can accommodate only one molecule, or atom

Langmuir proposed that the rate at which the sorbate molecules (B) strike a surface of a sorbent (A) is proportional to the product of the concentration of the sorbent and the fraction of the surface remaining uncovered by sorbate.

To derive Langmuir Equation, a parameter ‘θ’ is introduced. Let θ be the fraction of the number of the sites on the surface which are covered with sorbate molecules.

Therefore, the fraction of surface which is unoccupied will be (1 – θ).

Now, the rate of the forward direction depends upon two factors: The fraction of sites available on the surface of sorbent, (1 - θ), and the concentration, C. Therefore, the rate of the forward reaction is directly proportional to both the mentioned factors.

$$\text{Rate of sorption } \alpha \; C \quad (1 - \theta) \qquad (2.3)$$

$$\text{Rate of sorption} = K_a C \quad (1 - \theta) \qquad (2.4)$$

Similarly, the rate of the backward reaction or rate of desorption depends upon number of the sites occupied by the sorbate molecules on the sorbent,

$$\text{Rate of desorption } \alpha\ \theta \qquad (2.5)$$

$$\text{Rate of desorption} = K_d\, \theta \qquad (2.6)$$

At equilibrium, the rate of sorption is equal to the rate of desorption.

$$K_a C \quad (1 - \theta) = K_d\, \theta \qquad (2.7)$$

On solving the above equation for θ, we get

$$\theta = \frac{K_a \quad C_e}{K_d + K_a \quad C_e} \qquad (2.8)$$

On rearranging the above equation, and substituting K_a/K_d with K_L (Langmuir constant)

$$\theta = \frac{K_L \quad C_e}{1 + \quad K_L \quad C_e} \qquad (2.9)$$

This is known as Langmuir sorption equation. θ can be expressed in terms of equilibrium sorption capacity, q_e, and maximum monolayer capacity, q_m, as given in Equation (2.10)

$$\theta = \frac{q_e}{q_m} \qquad (2.10)$$

Therefore, on substituting θ from Equation (2.10), and rearranging, becomes

$$q_e = q_m \frac{K_L \quad C_e}{1 + \quad K_L \quad C_e} \qquad (2.11)$$

The linearized form of the Langmuir sorption isotherm can be presented as

$$\frac{1}{q_e} = \frac{1}{q_m} + \frac{1}{K_L \ q_m \ C_e} \qquad (2.12)$$

From the linear plot of 1/qe vs 1/Ce, the values of q_m and K_L can be calculated from the intercept and the slope, respectively [138].

The basic characteristics of Langmuir equation have been often represented in terms of a dimensionless separation factor, (R_L), defined as [139]

$$R_L = \frac{1}{1 \ + \ K_L \ C_0} \qquad (2.13)$$

The value of parameter R_L indicates the nature of the isotherm as given below.

$R_L > 1$ unfavorable sorption

$0 < R_L < 1$ favorable sorption

$R_L = 0$ irreversible sorption

$R_L = 1$ linear sorption.

2.4.1.6 Freundlich isotherm

The Freundlich isotherm is an empirical equation and assumes sorption on to heterogeneous sites. It is also assumed that the stronger binding sites are occupied first, and that the binding strength decreases with increase in the degree of site occupation.

At low concentration, the amount of the sorbate sorbed is directly proportional to concentration of the sorbate (raised to power one).

$$q_e \ \alpha \ C_e \qquad (2.14)$$

At high concentration, the amount of the sorbate sorbed is independent of concentration, i.e., C_e raised to power zero

$$q_e \ \alpha \ C_e^0 \qquad (2.15)$$

Therefore, at an intermediate value of concentration, sorption is directly proportional to the concentration raised to power 1/n. Here, n is a variable, the value of which is greater than one.

$$q_e = K_F \quad C_e^{\frac{1}{n}} \qquad (2.16)$$

The above equation is known as Freundlich sorption equation [140]. The linearized form of the above equation can be represented as

$$\log q_e = \log K_F + \frac{1}{n} \log C_e \qquad (2.17)$$

The linear plot of log q_e versus log C_e has a slope of $1/n$ and an intercept of log K_F. However, in other case, when $1/n \neq 1$, the K_F value depends on the units in which q_e and C_e are expressed. On average, a favorable sorption tends to have Freundlich constant n between 1 and 10. Larger value of n (smaller value of $1/n$) implies stronger interaction between the sorbate and the sorbent, while $1/n$ equal to 1 indicates linear sorption, leading to identical sorption energies for all the sites.

2.4.1.7 Temkin isotherm

Temkin sorption isotherm considers a heterogeneous surface, where no molecular interaction exists. It is based on Langmuir sorption isotherm. However, like Langmuir model, it does not take into account the lateral interaction between the sorbates. Temkin isotherm assumes that the decrease in the heat of sorption as a function of temperature is linear rather than logarithmic [141]. The heat of sorption of all the molecules in the layer would decrease linearly with coverage due to sorbate-sorbent interactions.The linear form of the Temkin model is given as,

$$q_e = \frac{RT}{b} \ln K_T + \frac{RT}{b} \ln C_e \qquad (2.18)$$

where K_T is Temkin isotherm constant, b is a constant related to heat of sorption, R is the gas constant, and T is the absolute temperature. A linear plot of q_e versus $\ln C_e$ enables the determination of the isotherm constants K_T and b, from the intercept and slope, respectively.

2.4.1.8 Dubinin-Redushkevich isotherm

Dubinin and his co-workers conceived this equation for subcritical vapor in microporous solids, where the sorption process follows a pore filling mechanism onto energetically non-uniform surface. According to this model, the characteristic sorption curve is related to the porous structure of the sorbent [142]. The Dubinin–Radushkevich (DR) equation is excellent for sorption equilibrium of interpenetrating organic compounds (in gas phase condition) in porous solids. It has several advantages:

- it predicts quite fairly the experimental data over a wide concentration range
- it includes the effect of temperature
- it is based on physical parameters
- easy application.

This isotherm is generally expressed as follows:

$$\ln q_e = \ln q_m - K_{DR} \quad \varepsilon^2 \qquad (2.19)$$

where q_m is the theoretical maximum capacity, K_{DR} is the D-R model constant (mol^2/kJ^2), related to the mean free energy of the sorption, and ε is the Polanyi potential, and is equal to

$$\varepsilon = RT \ln\frac{C_0}{C_e} \qquad (2.20)$$

The plot of $\ln q_e$ vs $\boldsymbol{\varepsilon^2}$ gives a straight line, from the intercept and the slope of which, q_m and K_{DR}, respectively, can be obtained. The mean free energy of sorption per mole of the sorbate, as it is transferred to the surface of the sorbent from infinite distance in the solution, E, is calculated by the following equation

$$\mathrm{E} = \frac{1}{\sqrt{2K_{DR}}} \qquad (2.21)$$

The apparent free energy of sorption, for the physisorption process is upto 8 kJ/mol, and a negative value indicates the exothermic nature of the sorption process.

Sorption Kinetics

Sorption kinetics describes the time-dependent evolution of the sorption process until equilibrium is reached. Such studies yield information about the possible mechanism of the sorption and the different transition states involved on the way to the formation of the final sorbate-sorbent complex. The results of such study help to develop appropriate mathematical models, to describe the interactions. Among the most popular kinetic models/equations are the so-called "pseudo first-order" and "pseudo second order" rate expressions.

2.4.1.9 Pseudo first-order kinetic model

Lagergren's equation is probably the earliest known mathematical description of the rate of sorption in liquid-phase systems. This equation is called the pseudo first-order equation, or the Lagergren's rate equation, and can be written as [143], [144], [145]

$$\frac{dq_t}{dt} = K_1(q_e - q_t) \qquad (2.22)$$

where q_t is the amount of sorbate sorbed at time t, and k_1 is the rate constant of the first order sorption. After integration and applying the boundary conditions, $q_t = 0$ at $t = 0$, the Equation (2.22) can be written as

$$\log(q_e - q_t) = \log q_e - \frac{K_1 \; t}{2.303} \qquad (2.23)$$

The values of k_1 and q_e can be determined from the slope and intercept, respectively, of the straight line plot of log (q_e - q_t) versus t. Determining q_e accurately is a difficult task, because, in many sorbate-sorbent interactions, the chemisorption slows significantly, after the initial fast response, and it is difficult to ascertain whether equilibrium is reached or not.

Therefore, it has been reported that, many sorption processes follow Lagergren pseudo first-order model only for the initial 20 to 30 min of interaction. The k_1, the time-scaling parameter, decides the rate of equilibration in the system. Various experimental studies have confirmed that the value of k_1 parameter can be both dependent and independent of the applied operating conditions.

Its value depends on the initial concentration of the sorbate. It usually decreases with the increasing initial sorbate concentration in the bulk phase[146]. Since the model does not describe the interactions for the whole range of contact time, in many cases, higher order kinetic models are employed to analyze the experimental results[147], [148], [149].

2.4.1.10 Pseudo second-order kinetic model

The pseudo second-order kinetics is usually associated with the situation, when the rate of direct sorption/desorption process (seen as a kind of chemical reaction) controls the overall sorption kinetics. The pseudo second-order kinetic model is expressed as [150]

$$\frac{dq_t}{dt} = K_2(q_e - q_t)^2 \qquad (2.24)$$

Where k_2 is the rate constant of the pseudo second-order sorption. After integration and applying the similar boundary conditions, Equation (2.24) can be written as

$$\frac{t}{q_t} = \frac{1}{K_2 \; q_e^2} + \frac{t}{q_e} \qquad (2.25)$$

The above equation can be further simplified by substituting h for $k_2q_e^2$, where h can be considered as the initial sorption rate, when , $\frac{t}{q_t} \to 0$ and, hence the final form of the equation can be written as

$$\frac{t}{q_t} = \frac{1}{h} + \frac{t}{q_e} \qquad (2.26)$$

The plot of t/q_t vs t gives a straight line, from the slope and intercept of which, the values of q_e and h, respectively, can be determined[151]. Knowing h, it is then straightforward to determine k_2. Indeed, the literature suggests a strong dependence of k_2 on operating conditions such as initial solute concentration, pH and temperature [152], [153].

The value of k_2 is usually strongly dependent on the applied initial solute concentration, and it decreases with the increase in C_o, i.e., the higher is the Co value, the longer time is required to reach an equilibrium. The sorption kinetics is very complex in nature, and the importance of the various factors varies from one system to another. Any change in the pH and temperature brings about the changes in the equilibrium state. Due to these reasons, the influence of pH and temperature on the k_2 value has not yet been explored theoretically.

Chapter 3 : Extraction of Radionuclides Using Amido – Amine Functionalized Sorbents

Chapter 3

Extraction of Radionuclides Using Amido – Amine Functionalized Sorbent

3.1 Introduction

Various sorbents including nanoparticles of different materials, carbon nanotubes, activated carbon and chitosan to name a few have been extensively studied. The limited sorption ability of these materials limits the practical applicability of these sorbents. Surface functionalization of solid phase adsorbents is a promising method to overcome such a limitation.

This chapter presents studies on surface functionalized multiwalled carbon nano tubes (MWCNT) and chitosan functionalized by amido- amine group and poly amido – amine (PAMAM) repectively. Though f – block elements are harder but actinides are softer compared to lanthanides, so a ligand comprising of both hard and soft donor coordinating atoms is expected to extract both lanthanides and actinides. Amido-amine contains both amide and amine ligand allowing the above capability. Additionally, this ligand also contains C, H, O, N species, allowing it to be completely incinerable, which eases secondary waste management. These two functionalized solid phase adsorbents are used for the sorption of U(VI) , Am(III) and Eu(III). Parameters affecting the adsorption process such as pH, equilibrating time, metal ion concentration etc. were investigated in detail. The synthesized material and their metal extraction mechanism were characterized by different techniques such as FTIR, XPS, Raman spectroscopy, XRD etc.

3.2 Preparation of Adsorbents

Amido-amine functionalized multiwalled carbon nano tubes (AA-MWCNT)

The novel functional group amido –amine was introduced on the surface of multiwalled carbon nano tubes (MWCNT) by a two step chemical process.

I) Oxidation of the carbon nano tube by mixed acid.

II) Coupling reaction using EDA in presence of DCC.

MWCNT used in the synthesis process were prepared by CCVD method in a fluidized bed at 800◦C as deiscussed earlier [154]. Acetylene was used as the precursor for carbon and ferrocene was used as the catalyst. As produced MWCNTs were treated with hydrochloric acid to remove catalyst and further heated to 400◦C in air to remove amorphous carbon. MWCNTs with purity more than 98.5%, outside diameter (OD) 15–25 nm, inside diameter (ID) 5–8 nm, length ~200 µm, specific surface area (SSA) more than 150 m2/g, were obtained by this method.

The schematic of the preparation of amido – amine functionalized MWCNT is presented in **Fig. 3.1**. In brief, synthesis process is as follows:

MWCNTs were oxidized using 3:1 mixture of concentrated sulfuric and nitric acid in an ultrasonic bath. The product was filtered and dried. For further functionalization this product was suspended in EDA by using an ultra-sonicator at room temperature and then magnetically stirred. Then the suspension was refluxed in presence of DCC for 48 hr. Then the required product was recovered by filtration, washing and drying. Detail synthesis of the material was elaborately described in Chapter 2.

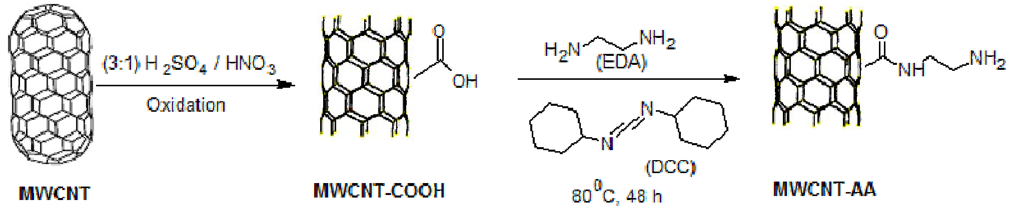

Figure 3.1: Schematic of the preparation of amido - amine functionalized MWCNT

Polyamidoamine (PAMAM) polymers functionalized chitosan

The PAMAM polymers (upto third generation) were introduced into the Chitosan surface by a two step process.

I) Michael addition reaction of methyl acrylate (MA) to amino groups present on the surface of Chitosan (CTS) .

II) Amidation reaction using ethylene diamine (EDA) in presence of ethanol.

Scheme of the synthesis from CTS-0 to CTS 1.0 was shown in the **Fig. 3.2**. Similar way the synthesis was carry furrowed to CTS 2.0 and CTS 3.0. Detail synthesis of the material was elaboratelydescribe in Chapter 2.

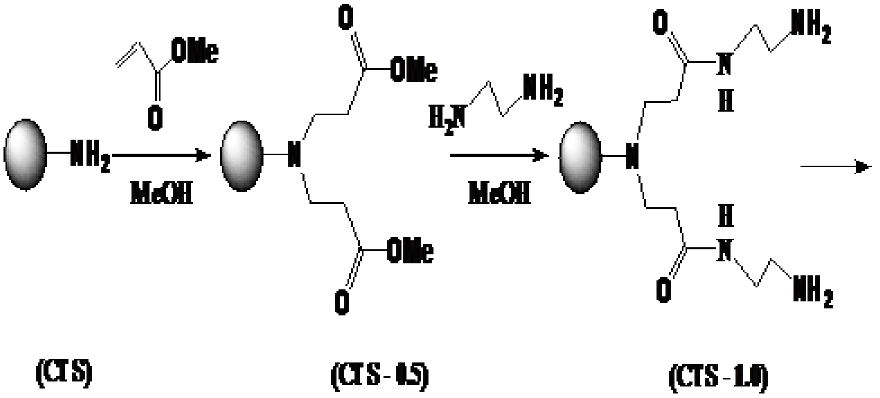

Figure 3.2 : Schematic of the preparation of PAMAM functionalized chitosan

3.3 Characterization

Amido-amine functionalized multiwalled carbon nano tubes

3.3.1.1 BET surface area

The specific surface area and the pore volume of the functionalized and unfunctionalized MWCNTs were determined by BET N_2 sorption method and the results are presented in **Fig. 3.3**. The specific surface area of the pristine MWCNT was found to be 150 m^2/g, which increased to190 m^2/g after functionalization (AA-MWCNTs). The functionalization also improved micro-pore volume by 30% as obtained by analyzing the data.

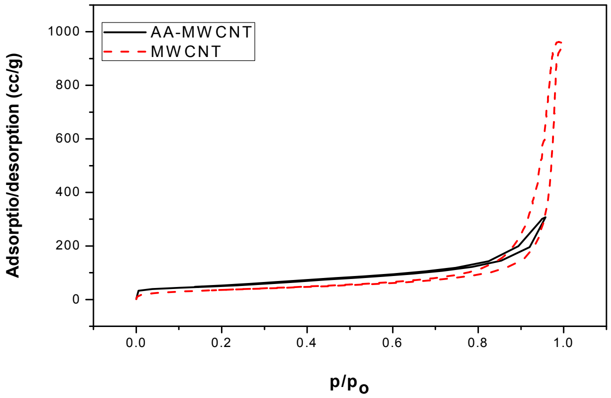

Figure 3.3: Comparative adsorption and desorption behavior of the pristine MWCNTs and AA-MWCNTs

3.3.1.2 XPS analysis

The nature of bond in the synthesized MWCNTs and functionalized MWCNTs were characterized by X-ray photoelectron spectroscopy (XPS). In order to confirm the functionalization on the surface of MWCNTs, XPS measurements were carried out for all three types of MWCNTs (MWCNT, MWCNT – COOH, AA-MWCNT).

The spectrum was recorded as the intensity (number of counts per second) versus binding energy (BE). The core level C–1 s XPS spectra of the MWCNT-COOH and AA-MWCNT are given in **Fig. 3.4 A** and **Fig. 3.5A** respectively, where curve fitting and deconvolution of the spectrum yields two and three separated spectra with different binding energy values given in Table 3.1.

The intense component peak of the deconvoluted C–1 s spectrum appeared at the lowest BE of 284.8 eV (FWHM: 1.44 eV) is ascribed to the non-oxygenated ring carbon of C-C or C-H. The broader and less intense peak appearing at BE of 286.1 eV (FWHM: 2.31 eV) refers to the carbon of O=C-OH functional groups for the MWCNT-COOH. The deconvoluted C–1 s spectra of AA-MWCNT (**Fig. 3.5**) shows the presence of another carbon with different chemical environment and is ascribed to the C-N of the amido-amine functional group thus indicating clearly the presence of amino group in AA-MWCNT.

The deconvoluted O–1 s XPS spectra of the more surface specific element O (the O–1s photoelectron kinetic energies are lower than those of the C–1s and so the sampling depth of O–1s is smaller) reveal that the oxygen in MWCNT-COOH and AA-MWCNT exists in a single electronic state. The existence of N–1 s XPS spectra (**Fig. 3.5C**) in AA-MWCNT and the absence of the same in MWCNT-COOH prove the existence of 'N' bearing functional groups in the AA-MWCNT. Evaluation of area under the constituent peaks for C–1s in AA-MWCNT reveals that a large proportion of amido-amine functional groups exist on the surface of AA-MWCNT.

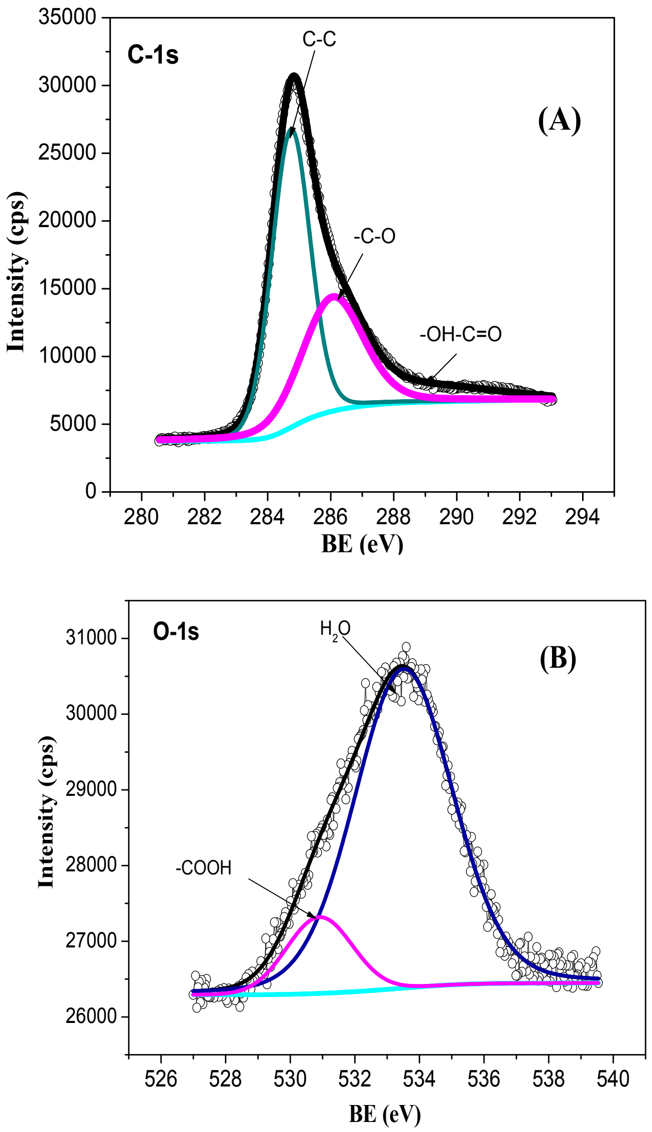

Figure 3.4: High resolution core level XPS spectra, (A) C-1s and (B) O-1s of the MWCNT-COOH (line with bullets: experimental data; solid line: curve fit for the experimental data)

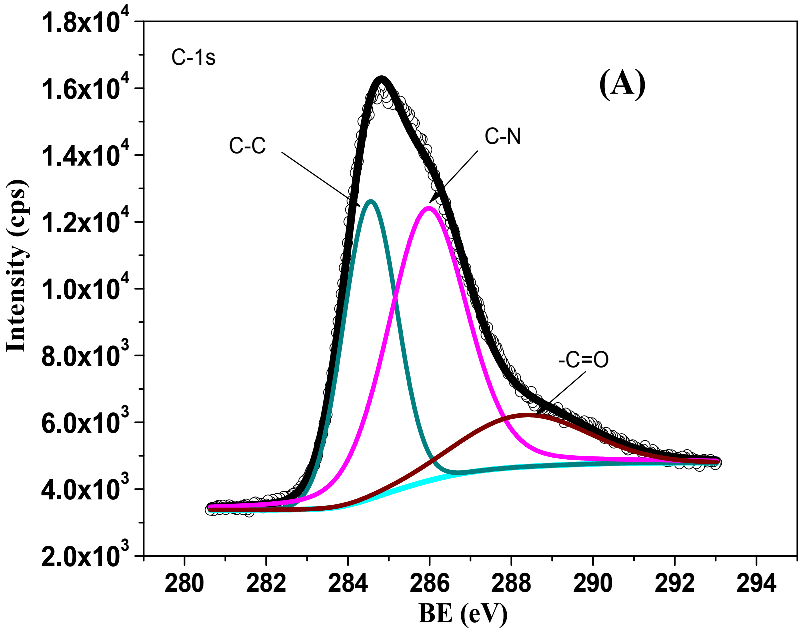

C-1s
(A)
C-C
C-N
-C=O
Intensity (cps)
BE (eV)
1.8x10^4
1.6x10^4
1.4x10^4
1.2x10^4
1.0x10^4
8.0x10^3
6.0x10^3
4.0x10^3
2.0x10^3
280
282
284
286
288
290
292
294

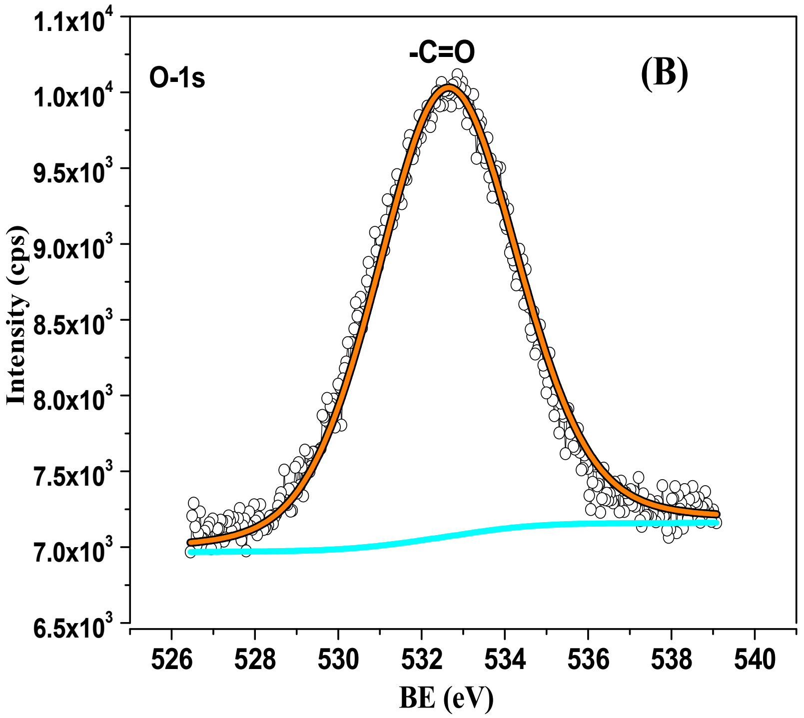

O-1s
-C=O
(B)
Intensity (cps)
BE (eV)
1.1x10^4
1.0x10^4
9.5x10^3
9.0x10^3
8.5x10^3
8.0x10^3
7.5x10^3
7.0x10^3
6.5x10^3
526
528
530
532
534
536
538
540

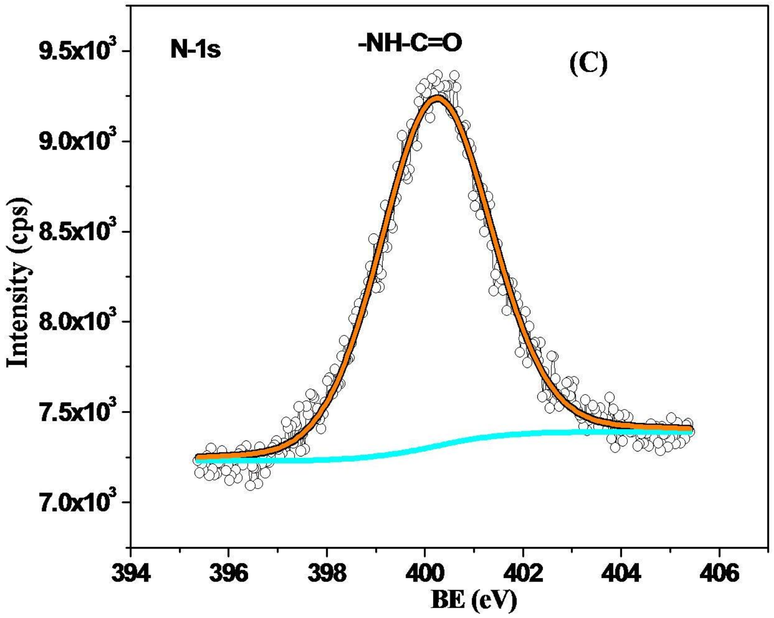

Figure 3.5: High resolution core level XPS spectra, (A) C-1s and (B) O-1s (C) N-1s of the AA-MWCNT material (line with bullets: experimental data; solid line: curve fit of the experimental data)

Table 3.1: Binding energy positions of different elements for MWCNT- COOH and AA-MWCNT

Material	**C-1s**			**O-1s**			**N-1s**		
	BE (eV)	FWHM (eV)	Peak Area (%)	BE (eV)	FWHM (eV)	Peak Area (%)	BE (eV)	FWHM (eV)	Peak Area (%)
MWCNT-COOH	284.8	1.44	64.06	530.8	2.41	12.90	-	-	-
	286.1	2.31	35.97	533.5	3.61	87.09	-	-	-
MWCNT-AA	284.6	1.56	34.14	532.6	3.99	100	400.2	2.67	100
	286	2.28	51.71						
	288.3	3.71	14.13						

3.3.1.3 Raman Spectroscopy

The disorderedness due to defects arising by the functionalization of MWCNT were characterized by Raman spectroscopy. The spectrum was recorded as the intensity versus wave number. There are two types of peaks observed in Raman spectra of MWCNTs, G lines (tan-gential mode peaks) and D lines (attributed to defects and disorder induced peaks). The G lines generally appear at 1560–1580 $cm^{-1}$and D lines are observed at 1338–1340 $cm^{-1}$for MWCNT, MWCNT-COOH and AA-MWCNT. The (I_D/I_G) ratio changes from MWCNT to MWCNT-COOH and AA-MWCNT indicating a partial destruction in the conjugation structure of the MWCNTs due to functionalization as shown in **Fig. 3.6**.

Significant differences in the tangential vibration mode (TM) can also be observed in the MWCNT functionalized with COOH and $CONHCH_2CH_2NH_2$ group. The tan-gential mode(TM) peak was found to shift downwards from MWCNT to AA-MWCNT sample (from 1579 $cm^{-1}$to 1569 cm^{-1}). The softening in the TM can be interpreted in terms of valence electron transfer from the electron donor i.e, the NH_2group into the π * band of carbon.

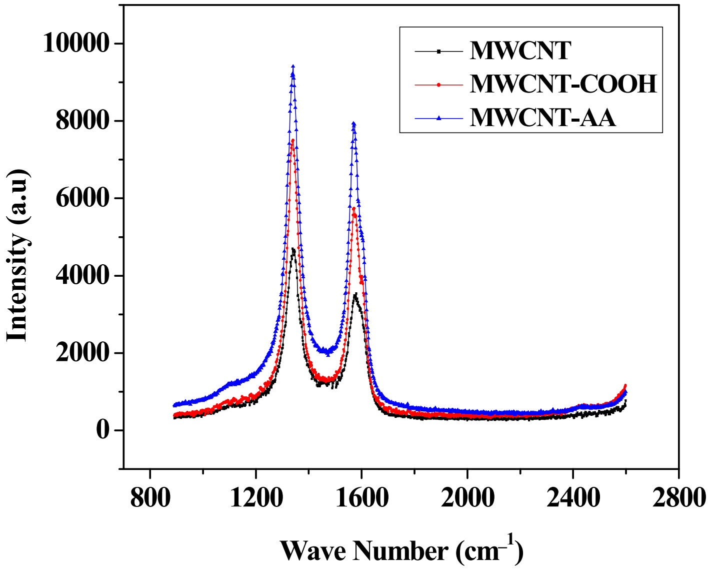

Figure 3.6: Raman spectra of the functionalized and un-functionalized MWCNT

3.3.1.4 Zeta potential measurements

Surface charge on the functionalized MWCNT is measured by zeta (ζ) potential analysis. The surface charge of the sorbent is sensitive to pH of the suspending medium. The isoelectric point, also referred to as PZC (point of zero charge), is the pH at which the sorbent particles in suspension have a net charge of zero. From the plot of zeta potential with pH (**Fig. 3.7**) isoelectric point (or PZC) of functionalized MWCNT was obtained around pH 4.8 which suggests positive surface charge on the sorbent particles below pH 4.8 and negative charge above pH 4.8. The surface charge of AA-MWCNT originates mainly from ionization of surface functional groups.

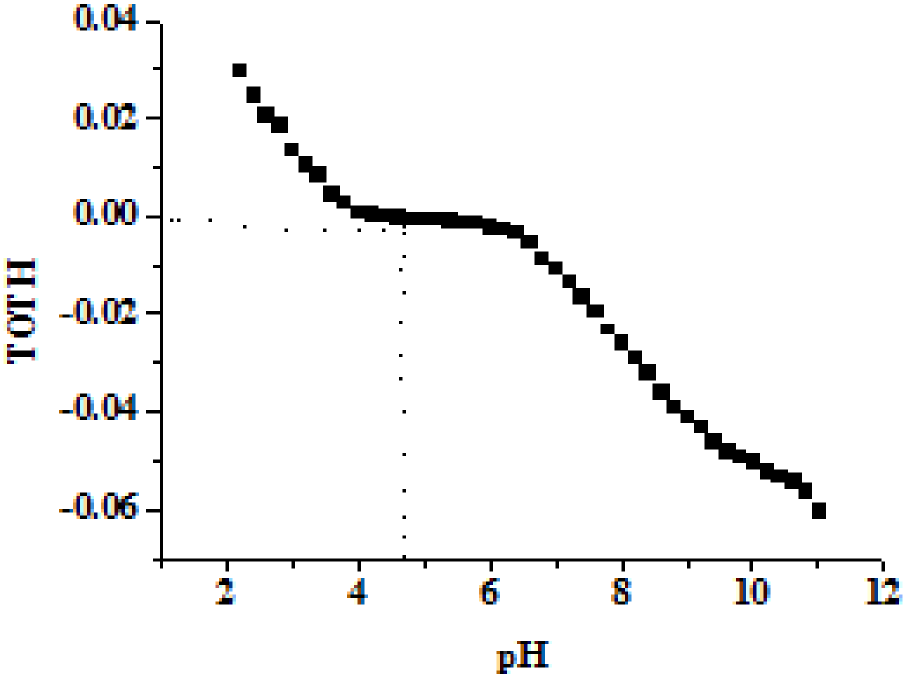

Figure 3.7: Potentiometric acid-base titration of AA-MWCNT sample

3.3.1.5 FTIR spectroscopy

In order to confirm the desired functionalization and sorption of the metal ion by the PAMAM functionalized chitosan, FTIR spectra were investigated. As all CTS1.0, CTS2.0 and CTS3.0 have similar functional group so CTS1.0 was taken as representative in **Fig. 3.8**. In the spectrum, stretching band of the amide C=O around 1651 cm^{-1} and the band at 1050–1100 cm^{-1} appear due to stretching vibrations of C–O–C bonds of the glycosidic ring of the chitosan molecule. The peaks at 1650 cm^{-1} are attributed to the characteristic peak of –NHCO and –NH_2 which were present in CTS-1.0 but absent in CTS-0 and confirm the functionalization. The broadening of the peak at 1650 cm^{-1} and a very strong new peak at 1383 cm^{-1} in the FTIR spectrum of CTS-1.0 after adsorption of Eu(III) confirm the extraction of metal ions. The peak at 1383 cm^{-1} is a characteristic peak for the stretching vibration of NO_2 in the NO_3^- ions [155].

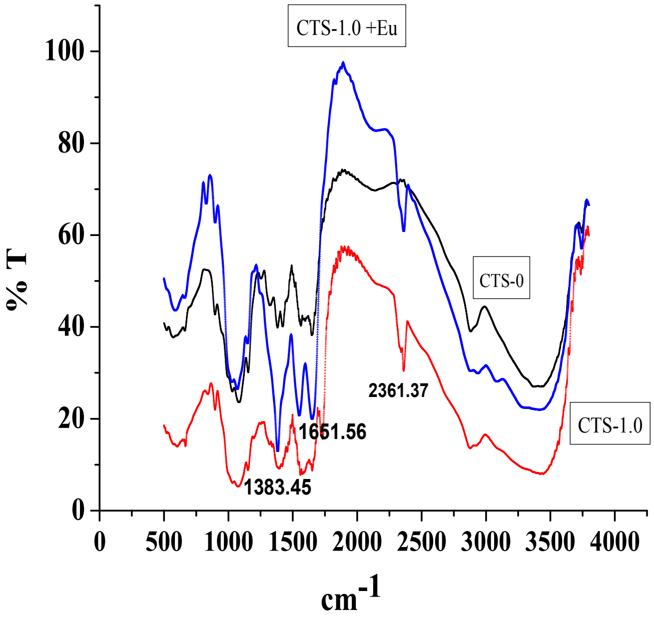

Figure 3.8: FTIR spectrum of CTS-0, CTS-1.0 and CTS-1.0 loaded with Eu

3.3.1.6 XRD analysis

Fig. 3.9 represents the comparative XRD pattern for chitosan before and after functionalization. The diffractogram shows two well defined peaks at 2θ ~ 17° and 2θ ~ 20° for chitosan. Overall the functionalized sample appears similar to the unfunctionalized form and there is no increase in the tendon form, which exhibits a peak at 2θ ~ 22°. The suppression of the tendon form is important to ensure sorbent performance.

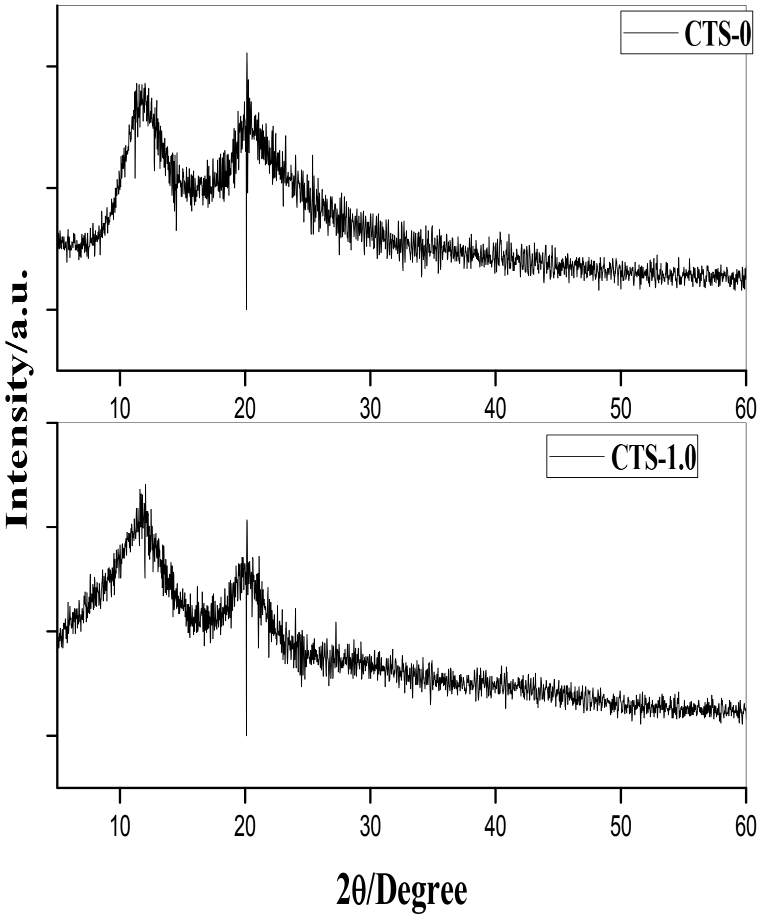

Figure 3.9: XRD pattern of CTS-0 and CTS-1.0

3.3.1.7 Thermogravimetric analysis

Thermogravimetric plot shown in **Fig. 3.10** for functionalized and unfunctionalized chitosan. Weight loss took place in two stages. The first one starts at 60 ^{0}C with a weight loss of 10%. The second stage starts at 240 ^{0}C and reaches a maximum at 380 ^{0}C with a weight loss of 41.4%.The first stage is assigned to the loss of water. The second stage corresponds to the decomposition (thermal and oxidative) of chitosan, vaporization and elimination of volatile products.

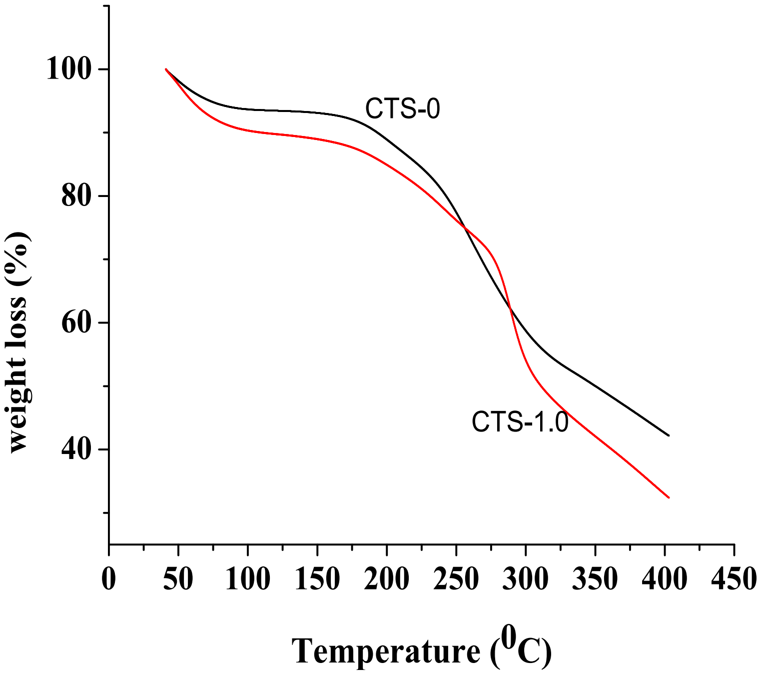

Figure 3.10: Thermo gravimetric plot for CTS-0 and CTS-1.0

3.4 Sorption Study

Uranium extraction by AA-MWCNT

3.4.1.1 Effect of feed pH on extraction

Extraction of Uranium by MWCNT-AA is strongly influenced by the pH of the feed solution as shown in **Fig. 3.11**. For U(VI) the percentage sorption increased with increasing pH of the feed solution in the range of 1.0–7.0. But at pH >7.0, the percentage sorption of U(VI) decreased with increasing pH value.

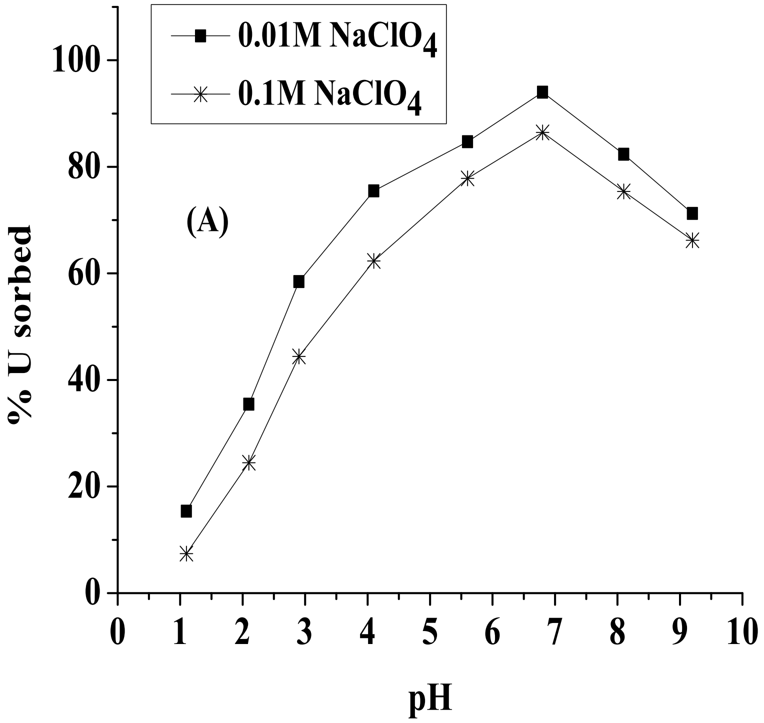

Figure 3.11: Effect of pH value of aqueous solution on the sorption of U by AA-MWCNT; volume of aqueous solution: 2 mL, weight of the AA-MWCNT-20 mg, time of equilibration- 1 h

This can be explained on the basis of electrostatic attraction between U(VI) and the surface charges of functionalized MWCNT which are affected by pH of the solution. Further, the protonation - deprotonation of the functional groups could enhance or suppress U(VI) sorption. The PZC of the surface of functionalized MWCNT was found to be at pH= 4.8. Different chemical species of uranium dominates in the aqueous solution at different pH: UO_2^{2+} (at pH < 4); UO_2^{+}, $UO_2(OH)^{+}$, and$(UO_2)^3(OH)_5^{+}$ (at pH 5); $(UO_2)_3(OH)_5^{+}$ (at pH 6–7); $UO_2(CO_3)_2^{2-}$, and $UO_2(CO_3)_3^{4-}$ (at pH 8) [[156]]. At pH < pH pzc, the surface of AA-MWCNTs is positively charged due to protonation reaction and negatively charged due to deprotonation at pH > pHpzc. The electrostatic repulsion between the positively charged surface of the sorbent and positively charged species of uranium resulted in a very low sorption capacity at lower pH. In the pH range of 5–7, the species of uranium are positively charged and the transition in the surface polarity of MWCNTs favored the sorption process and maximize the uptake capacity. But at higher pH values (pH > 7), the electrostatic repulsion between the negatively charged surface and the negatively charged uranium species $UO_2(CO_3)_2^{2-}$ and $UO_2(CO_3)_3^{4-}$ resulted in a rapid decrease of extraction [157, 158]. With increasing ionic strength i.e. with the increase of $NaClO_4$ concentration % sorption was found to decrease for Uranium. As the mechanism of sorption for the radionuclide involves interaction between two charged species as discussed above, increase in ionic strength of the medium will lead to more stabilization of the charged species. This creates a barrier for the ionic interactions between two charged species and hence the % sorption decreases at higher ionic strength.

3.4.1.2 Optimization of contact time

Literature reports are widely varied as far as time of equilibration for different types of MWCNT is concerned. Such as sorption of U(VI) by MWCNT/iron oxide composite was reported to be requiring ~8 h for attainment of equilibrium [159].

In order to optimize the required time for equilibration, experiments were conducted for uranium uptake at pH 6 using ^{233}U with a sorbent dose of 10 mg mL^{-1}. **Fig. 3.12** shows that the sorption of uranium increases with contact time upto 15 mins and thereafter it becomes almost constant. To ensure maximum uranium uptake, contact time for all the batch experiments were fixed at 1 hour.

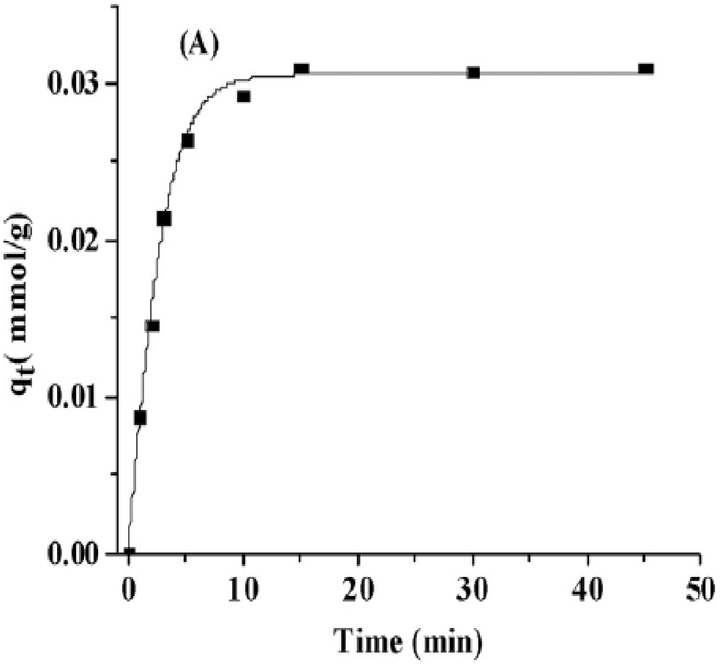

Figure 3.12**:** Effect of sorption time on the equilibrium sorption capacity of AA-MWCNT for U, pH of the solution- 6, weight of AA-MWCNT ~ 20 mg, volume of aqueous solution- 2 mL

3.4.1.3 Sorption kinetics

Sorption kinetics is controlled by various mechanisms of mass transfer and chemical reactions. Mass transfer of the metal ion from the bulk solution to the external surface of AA-MWCNT is the primary step which is followed by sorption of metal ions onto the surface by chemical reaction or the sorption into the central channels by internal diffusion. Kinetics of the sorption process using AA-MWCNT was studied for ^{233}U. Most frequently, two different kinetic models (Figure 3.13):

Lagergren's first order model, and Pseudo second order model have been considered for elucidating the sorption mechanism.

Lagergren's first order kinetic model [142]

$$\log\left(q_e - q\right) = \log q_e - \frac{k_{ads}\, t}{2.303} \tag{3.1}$$

where, q (mg g−1) is the metal ion concentration on the sorbent at time ‘t’,

q_e is the metal ion concentration on the sorbent at equilibrium, and k_{ads} (min^{-1}) is the first order rate constant.

Pseudo second order kinetic model [160]

$$\frac{t}{q} = \frac{1}{k_2 \; q_e^2} + \frac{t}{q_e} \tag{3.2}$$

Where, k_2 (g mg^{-1} min^{-1}) represents pseudo second order rate constant.

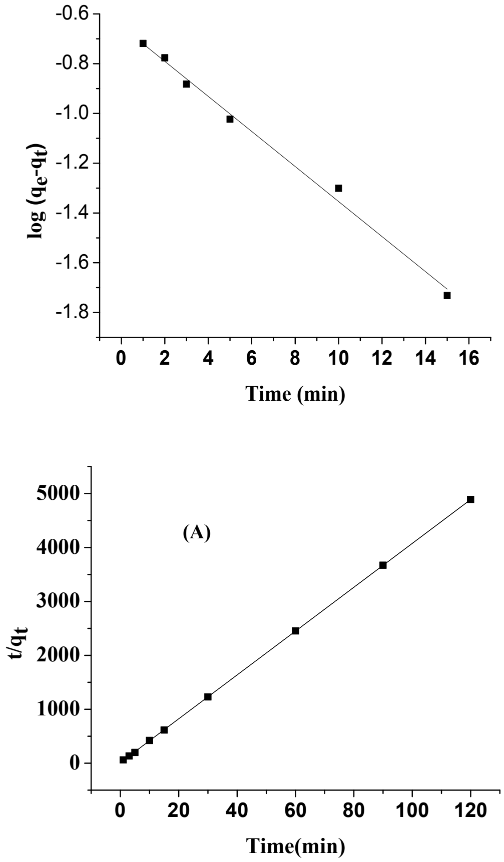

Figure 3.13: Lagergren’s first order kinetic model and Pseudo 2nd order kinetics model for the sorption of U, volume of aqueous solution: 2 mL, weight of the AA-MWCNT ~20 mg.

The linear curves of log (q_e–q) vs. t and t/q_t vs. t plotted for U adsorption by AA-MWCNT. The corresponding values are given in Table 3.2.

Table 3.2**:** Parameters for pseudo-second-order and pseudo-first-order kinetics modeling for the sorption of U(VI) by AA-MWCNT

Radionuclide	Pseudo second order kinetics			Pseudo first order kinetics
	q_e (mg/g)	K_2 (g/(mg min)	R^2	R^2
U	19.84	0.012	0.999	0.966

3.4.1.4 Sorption isotherm

The uranium sorption (Figure 3.14) on AA-MWCNT is plotted and fitted in both the Freundlich and Langmuir adsorption isotherms. As seen from the isotherm plots that experimental data fits Langmuir model (**Fig. 3.15**) well with a R^2 value of 0.996 while in case of Freundlich model (**Fig. 3.15**) R^2 was 0.979, the choice was made on the basis of linear regression value (R^2). Observation indicates that the sorption of uranium on AA-MWCNT is a monolayer adsorption. It can be due to the presence of one kind of chemical group on the surface of functionalized MWCNTs. Langmuir constant q_{max} which is the measure of the monolayer adsorption capacity was obtained as 20.66 mg g^{-1}. It is in close agreement with the experimentally determined sorption capacity19.84 mg g^{-1}. Detail results are given in Table 3.3.

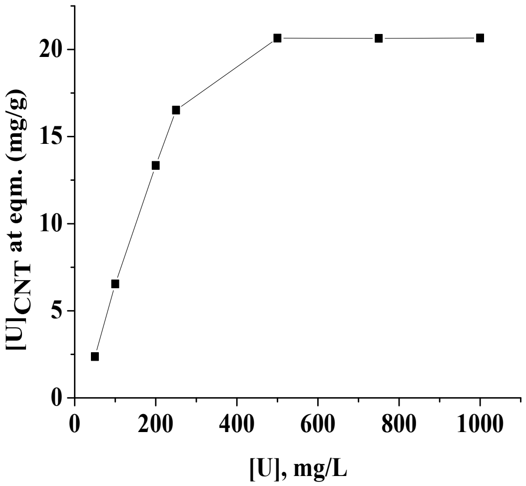

Figure 3.14: Effect of initial concentration of U for sorption by AA-MWCNT

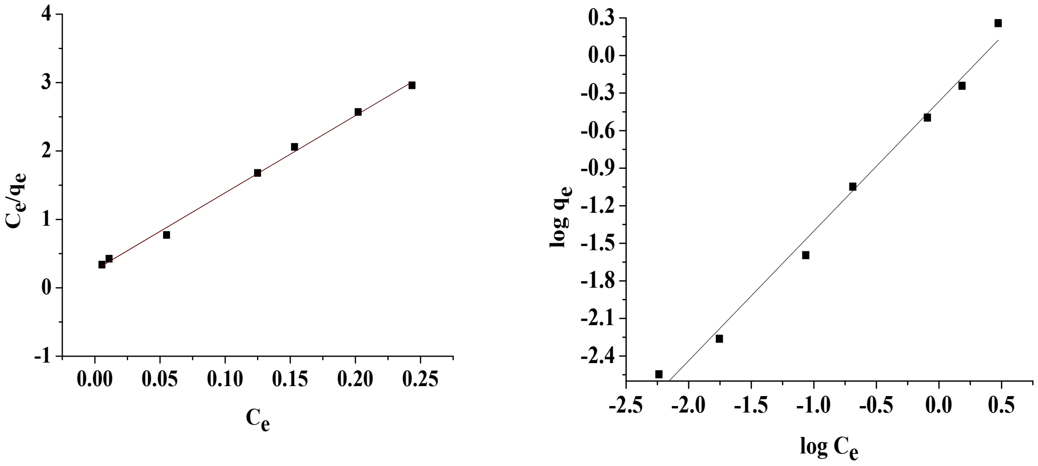

Figure 3.15: Langmuir and Freundlich adsorption isotherm for U using AA-MWCNT

Table 3.3: Different isotherm constants and corresponding R^2 values for the sorption of U by AA-MWCNT

Element	Langmuir isotherm			Freundlich isotherm		
	q_{max} (mg g-1)	B ($Lmmol^{-1}$)	R^2	k_f ($mmol^{1-n}L^n g^{-1}$)	n^{-1}	R^2
U	20.66	8.86	0.996	0.49	0.752	0.979

Am and Eu extraction by AA-MWCNT

3.4.1.5 Effect of pH

The sorption of metal ions by AA-MWCNT is strongly dependent on the pH of the aqueous feed solution. pH was found to have a profound effect on the sorption efficiency for both Am and Eu. The species formed by Am(III) at different pH medium includes Am^{3+}aq (major species up to pH 6), $Am(OH)^{2+}$ (mostly formed from pH 6–8) , $Am(OH)_2^+$ (predominant species above pH 8 up to pH 12), with little contribution from $Am(OH)_3$(aq) above pH 11 [161]. So for pH range studied, Am(III) is present as positively charged species and the interaction with negative surface charge of functionalized MWCNT leads to an increase in sorption efficiency.

Because of the nearly same ionic radius, Eu^{3+}can be considered as a homolog of trivalent actinides, which results in very similar physical and chemical properties[162] . $^{152+154}$Eu is an important radionuclide in nuclear waste and is a threat to the environment. At pH < 5, Eu exists in an aqueous medium as Eu^{3+} , $Eu(OH)^{2+}$ (mostly formed from pH 6–8), $Eu(OH)_2^+$(predominant species above pH 8 up to pH 12) , $Eu(OH)_3$ above pH 11[105]. Hence the trend of Eu(III) sorption with increasing pH was identical with that of Am(III). A striking feature of the graphs as shown in **Fig. 3.16**, is the change in% sorption of Am(III) &Eu(III) with change in ionic strength of the medium. With increasing ionic strength, % sorption was found to decrease for both the radionuclides. As the mechanism of sorption involves interaction between two charged species, so increase in ionic strength of the medium will lead to more stabilization of the charged species. This creates a barrier for the ionic interactions between two charged species and hence the % sorption decreases at higher ionic strength.

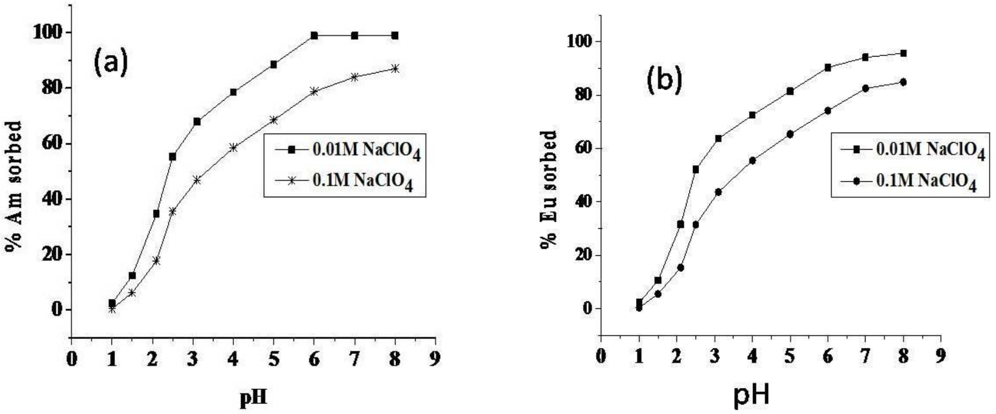

Figure 3.16: Effect of pH value of aqueous solution on the sorption of (a) Am (b) Eu by AA-MWCNT; volume of aqueous solution: 2 mL, weight of the AA-MWCNT ~20 mg, time of equilibration- 1 h

3.4.1.6 Optimization of contact time

For the optimization of required time to reach the equilibrium, experiments were conducted for Americium uptake at pH 6 using ^{241}Am tracer with a sorbent dose of 10 mg mL^{-1}. **Fig. 3.17** shows that the sorption of Am increases with contact time upto 15 mins and thereafter it becomes almost constant. To ensure maximum Am uptake, contact time for all the batch experiments were fixed at 1 hour. For the similar chemical properties the contact time was also maintain for Eu also.

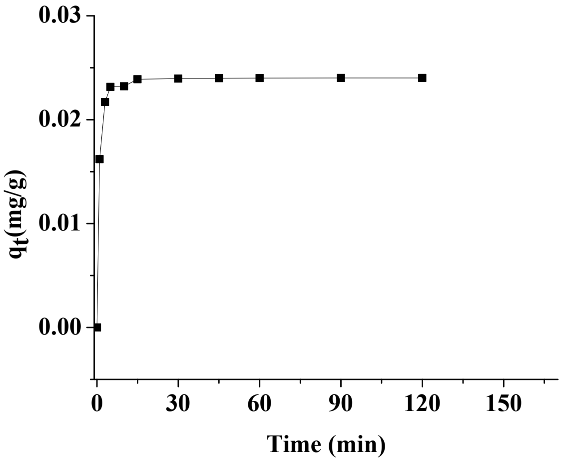

Figure 3.17: Effect of sorption time on the equilibrium sorption capacity of AA-MWCNT for Am pH of the solution- 6, weight of AA-MWCNT ~ 20 mg, volume of aqueous solution- 2 mL

3.4.1.7 Sorption kinetics

Kinetics of the sorption process using AA-MWCNT was studied for both^{241}Am and $^{152+154}$Eu as shown in **Fig. 3.18**. For both the radionuclides, the equilibrium was achieved within 15 min of contact time and hence in further experiments the contact time was kept for 1 h to achieve complete equilibrium. Generally, it is described that at the initial stages there are vacant surface sites available for sorption hence the sorption increases quickly. However, at the later stages the remaining vacant surface sites are difficult to occupy due to the repulsion from the sorbate molecules. Attempts were made to model the kinetic data with two different models i.e. Lagergren's first order model, and Pseudo second order model for both ^{241}Am and $^{152+154}$Eu. The corresponding linear regression coefficient (R^2) values for the linear curves of log (q_e–q) vs. t and t/q_t vs. t for both the metal ions showed that that sorption process follows the pseudo 2nd order kinetics model.Detail results are given in Table 3.4.

Table 3.4: Parameters for pseudo second order and pseudo first order kinetics modeling and corresponding R^2 values for the sorption of Am (III) and Eu (III) by AA-MWCNT

Radionuclide	Pseudo second order kinetics			Pseudo first order kinetics
	q_e (mg/g)	K_2(g/(mg min))	R^2	R^2
^{241}Am	16.92	0.055	0.997	0.958
$^{152+154}$Eu	15.86	0.062	0.998	0.946

3.4.1.8 Sorption isotherm

Isotherm studies were carried out for AA-MWCNT using Eu at pH 6. Initially, the amount of metal sorption increased quickly with increasing metal concentration in the solution and then plateaus as shown in **Fig. 3.19**. The experimental data were plotted using two most commonly used isotherms, i.e. Langmuir and Freundlich isotherms. The linear plots for Langmuir and Freundlich isotherms shows that Langmuir isotherm model fits the experimental data better than the Freundlich model as given in Table 3.5. Maximum sorption capacities of functionalized MWCNT for Eu(III) was observed to be 16.1 mg/g which is in excellent agreement with that of experimentally determined maximum sorption capacity (15.8 mg/g). Thus the sorption of Eu(III) on the functionalized MWCNT limited by the availability of the ligand complexing sites due to saturation effect according to Langmuir model and it is also proved that there is no multilayer sorption of Eu(III).

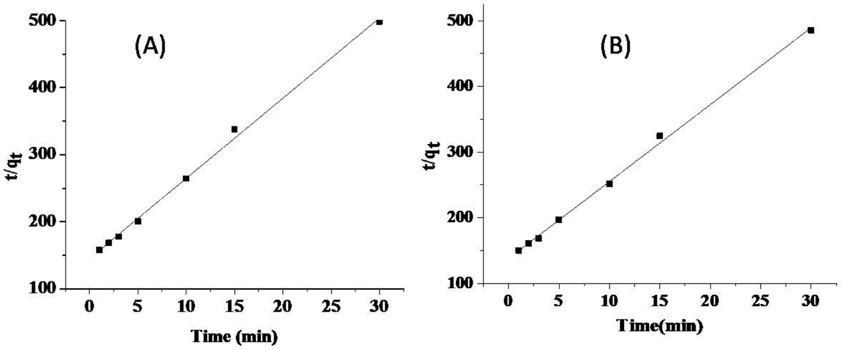

Figure 3.18: Pseudo 2ndorder kinetics model for the sorption of (A) Am (B) Eu by AA-MWCNT; volume of aqueous solution: 2 mL, weight of the AA-MWCNT ~20 mg, time of equilibration- 1 h

Table 3.5: Different isotherm constants and corresponding R^2 values for the sorption of Eu(III) by AA-MWCNT

Radionuclide	Langmuir isotherm			Freundlich isotherm		
	q_{max}(mg g-1)	B (Lmmol^{-1})	R^2	k_f (mmol^{1-n}L^n g $^{-1}$)	n^{-1}	R^2
Eu(III)	16.1	42.89	0.995	0.37	0.97	0.981

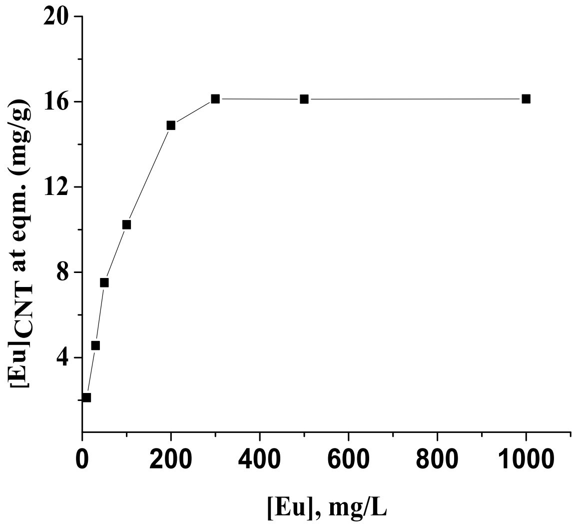

Figure 3.19: Effect of initial concentration of Eu for sorption by AA-MWCNT

3.4.1.9 Effect of nitrate ion

Metal ions are present in nitric acid medium where nitrate ion due to its complexing nature will play a role on the extent of sorption. In order to investigate the role of nitrate ions, sorption studies were carried out for Am(III) in two different pH solutions without any ClO_4^- in presence of varying concentrations of nitrate ion. The sorption plots are given in **Fig. 3.20**. From the figure it is evident that with increasing NO_3^- concentration in the feed, there was a decrease in sorption of Am(III) but the decrease was dependent on the pH of the medium. Sorption studies were carried out at two different pH values (pH 4 & 6) and trend was observed to be different. At pH 4, there was continuous decrease in Am(III) sorption efficiency with increasing nitrate concentration from 0.01 M to 1 M. However, at pH 6, sorption efficiency remained nearly constant up to a nitrate ion concentration of 0.15 M and beyond that there was significant decrease in the sorption efficiency. Increasing nitrate ion concentration plays a negative role on the sorption efficiency of Am(III) by AA-MWCNT due to its complexing nature with Am(III) which plays a competitive role with the sorption of Am(III). At higher pH, a larger number of functional groups of AA-MWCNT are deprotonated leading to more negative charge on the surface of AA-MWCNT which helps in competition with nitrate for sorption of Am(III).

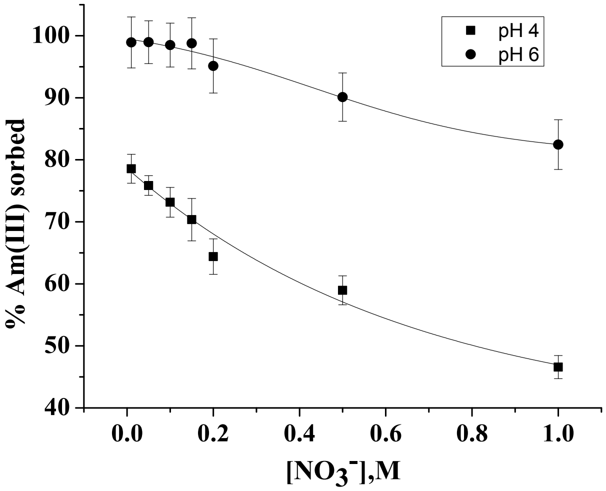

Figure 3.20: Effect of nitrate concentration on the sorption efficiency of Am by AA-MWCNT; volume of aqueous solution: 2 mL, weight of the AA-MWCNT ~20 mg, time of equilibration- 1 h

3.4.1.10 Effect of other ions

To understand the role of other competing ions present in real waste solution on the sorption efficiency of the targeted radionuclides, a typical simulated waste solution was prepared at pH 6. Table 3.6 gives the typical concentration of various elements present in the SHLW along with the K_d values for AA-MWCNT. It is clearly indicated that presence of macro concentrations of competitive ions did not affect the K_d values of AA-MWCNT for Am(III), Eu(III) and U(VI).

Table 3.6: Typical composition of a synthetic high level waste and K_d values for AA-MWCNT

Element	Concentration (ppm)	Kd (mL/g)
Fe	1000	0.2
Sr	0	0.25
Cs	20	0.15
Ce	100	154
La	100	176
Na	250	0.32
U	50	2986
Am	5	2452
Eu	20	2102
Ru	30	1.2
Mo	50	0.32
Ca	250	0.28

3.4.1.11 Reusability study

Am(III) and U(VI) was desorbed from loaded amido amine functionalized MWCNT (AA-MWCNT) using 1 M HNO_3solution and it was observed that quantitative desorption of the radionuclides is possible in two contacts. There were no change in the sorption efficiency for the radionuclides by the functionalized MWCNT for successive six cycles of operation. Periodic stability of the AA-MWCNT material for 45 days in $NaClO_4$as well as nitrate medium was also evaluated. The material was kept in contact with pH 6 (0.1 M $NaClO_4$or 0.5 M NO_3^-) solution and sorption studies of Am (III) were carried out after a cycle of five days. We observed no significant change in the sorption efficiency for Am (III) in both the medium up to 30 days. There was significant change in the sorption efficiency in

NO_3^-medium after 30 days (a decrease of more than 50%) but no change was observed in ClO_4^-medium up to 45 days studied.

Extraction of Am (III) and Eu(III) using polyamido amine functionalized chitosan

Chitosan functionalized with different generation of polyamido amine were used for the extraction of trivalent actinide and lanthanide such as Am and Eu.

3.4.1.12 Effect of pH

Sorption of the metal ion by the PAMAM functionalized chitosan varies due to the variation of the metal speciation and change of the surface properties by protonation and deprotonation with the change of pH in the feed solution. With increasing pH of the feed solution percentage sorption for both functionalized and unfunctionalized chitosan increases as shown in **Fig. 3.21**. At lower pH solution due to the protonation of the –NH2 group the surface become positively charge so there is eletrostatic repulsion between the metal ion and the surface this leads to lower sorption percentage. With increasing pH, due to the deprotonation the functional groups generating negative charge on the surface of the sorbent which lead to enhanced interaction with the positively charged species of Am(III) and Eu(III) present in the solution[163].There is distinct increase in percentage sorption for both Am(III) and Eu(III) for PAMAM functionalized chitosan over unfunctionalized chitosan .

This shows that functionalization of chitosan with PAMAM Dendron resulted in better chelating performance for the metal ions. However, there is identical sorption percentage for all the three (1st , 2nd and 3rd) generation of PAMAM functionalized CTS. This effect is due to the nullification of the increasing number of functional groups by steric hindrance, which makes diffusion of metal ion into the interior of the higher generation polymer more challenging.

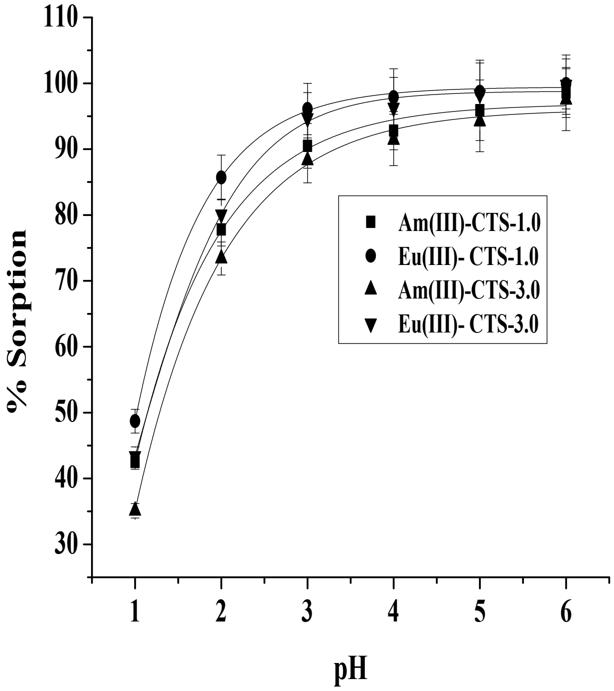

Figure 3.21: Effect of pH of the feed on the sorption of Am(III) and Eu(III) by different generation of PAMAM functionalized Chitosan: amount of different chitosan sorbent, 100mg, vol. of feed – 2 mL, time of equilibration 1 h.

3.4.1.13 Optimization of contact time

Sorption kinetics for both the metal ions, Am(III) and Eu(III) at pH 5 solution were studied using both CTS-1.0 and CTS-3.0 to optimize the required time for equilibration. **Fig. 3.22** shows that equilibrium was reached in 10 min and in further experiments the time of equilibration was kept at 1 h to ascertain attainment of complete equilibrium. Different Dendron generations showed near identical kinetics of sorption for both the metal ions.

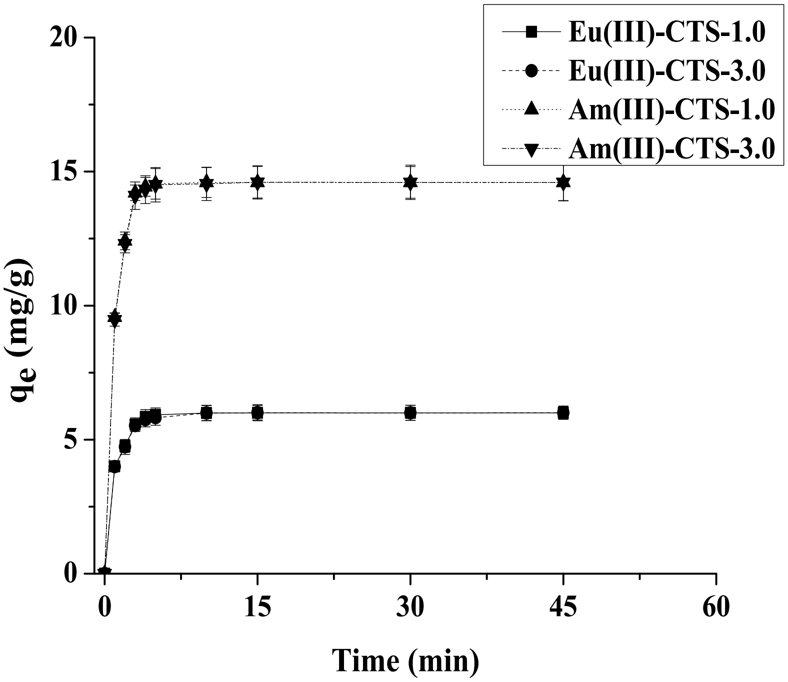

Figure 3.22: Effect of contact time on the sorption capacity of Am and Eu by 1st and 3rd generation PAMAM functionalized Chitosan :amount of different chitosan sorbent, 100mg, vol. of feed – 2 mL, pH of the feed solution - 5.

3.4.1.14 Kinetic study

Kinetics of the sorption process using chitosan-PAMAM$_1$ and chitosan-PAMAM$_3$ were studied for both^{241}Am and $^{152+154}$Eu and the results are given in Table 3.7. Kinetic data were tried to be modeled with two different kinetics models i.e. Lagergren's pseudo-first order model (Figure 3.23), and Pseudo second order model (Figure 3.24) for both ^{241} Am and $^{152+154}$Eu.The corresponding linear regression coefficient (R^2) values for the linear curves of log (q_e–q) vs. t and t/q_t vs. t for both the metal ions corroborating the fact that pseudo 2nd order kinetics model is being followed in the sorption process. The coefficients of pseudo-first-order kinetic equation for Am found to be 0.9296, 0.9248, respectively for

CTS-1.0 and CTS-3.0 but for Eu it were 0.9777 and 0.976 with respect to CTS-1.0 and CTS-3.0.

Table 3.7: Parameters for pseudo-second-order kinetics modeling for the sorption of Am(III) and Eu(III) by 1st and 3rd generation PAMAM functionalized chitosan

Radionuclide	CTS 1.0			CTS3.0		
	R^2	q_e (mg/g)	K_2 (g/mg.min)	R^2	q_e (mg/g)	K_2 (g/mg.min)
$^{152+154}$Eu	0.999	6.087	0.902	0.998	6.072	0.828
^{241}Am	0.998	15.038	0.215	0.999	15.015	0.216

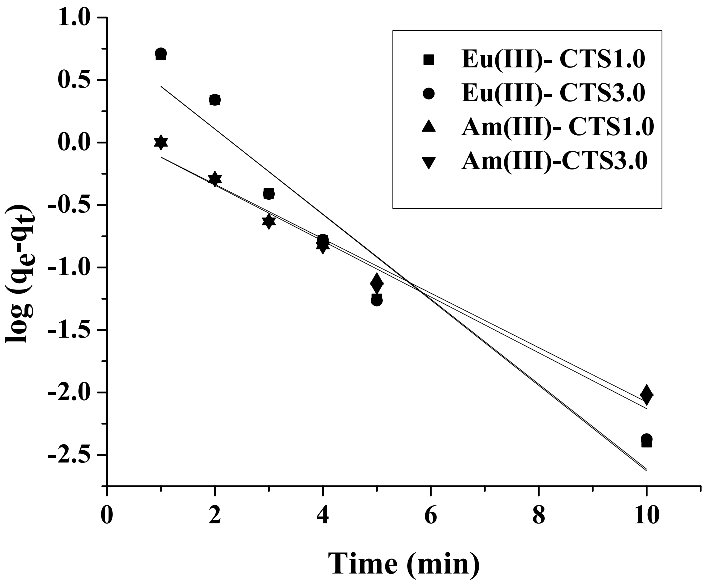

Figure 3.23: Pseudo-first-order plot for the sorption of Am and Eu by 1st and 3rd generation PAMAM functionalized Chitosan: amount of different chitosan sorbent, 100mg, vol. of feed – 2 mL, pH of the feed solution - 5

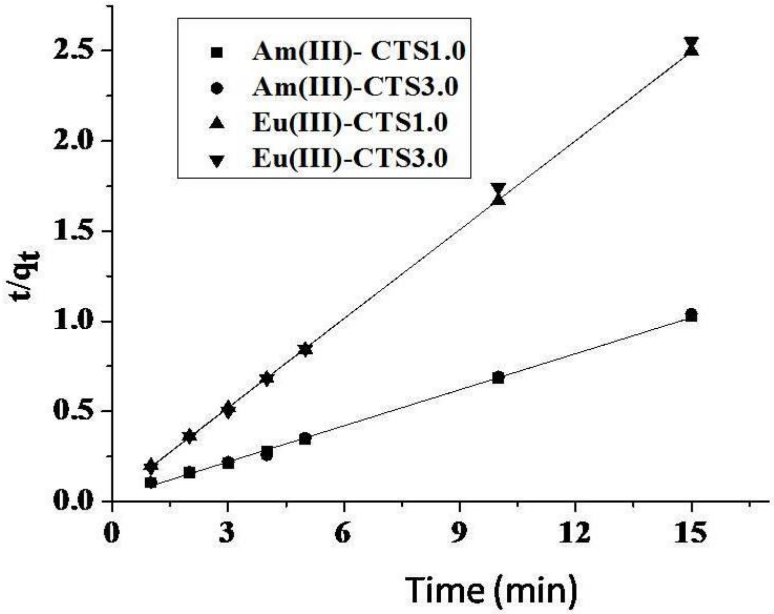

Figure 3.24: Pseudo-second-order plot for the sorption of Am and Eu by 1st and 3rd generation PAMAM functionalized Chitosan: amount of different chitosan sorbent, 100mg, vol. of feed – 2 mL, pH of the feed solution - 5

3.4.1.15 Sorption isotherm

In order to understand the effect of metal ion concentration in the feed solution we carried out sorption studies of Eu (III) from pH 5 solution with respect to varying concentrations of Eu employing CTS-1.0 and CTS-3.0.The behavior of first generation and third generation PAMAM functionalized chitosan were found to be identical. For CTS-1.0 and CTS-3.0 the maximum sorption capacity of Eu(III) was found to be 6.0 and 5.9 mg/g, respectively. In order to understand the sorption mechanism, we plotted the data using Langmuir and Fruendlich isotherm models. The regression coefficient analysis of the linear plots for Freundlich and Langmuir isotherms (Figures 3.26 and 3.27 respectively) show that Langmuir isotherm model fits the experimental data more than Freundlich model.Detail experimental results are shown in Table 3.8.

Table 3.8: Different isotherm constants and corresponding R^2 values for the sorption of Eu(III) by 1st and 3rd generation PAMAM functionalized chitosan

Sorbent	Langmuir			Fruendlich		
	q_{max} (mg/g)	B (L/mmol)	R^2	K_f ($mmol^{1-n} L^n g^{-1}$)	n^{-1}	R^2
CTS1	6.11	0.844	0.998	-1.058	0.35	0.969
CTS3	6.23	0.828	0.997	-1.151	0.32	0.977

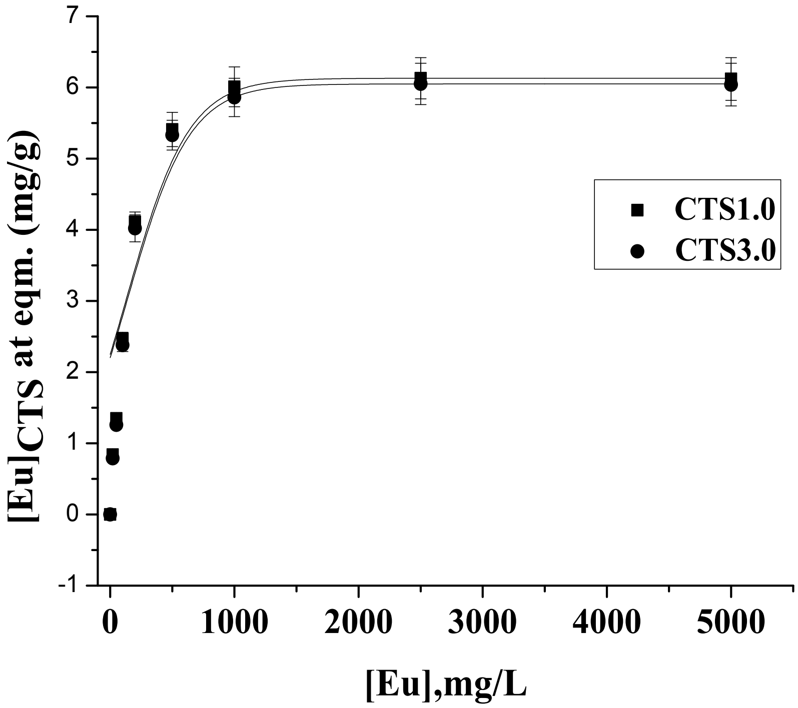

Figure 3.25: Effect of initial Eu concentration for sorption by 1st and 3rd generation PAMAM functionalized Chitosan

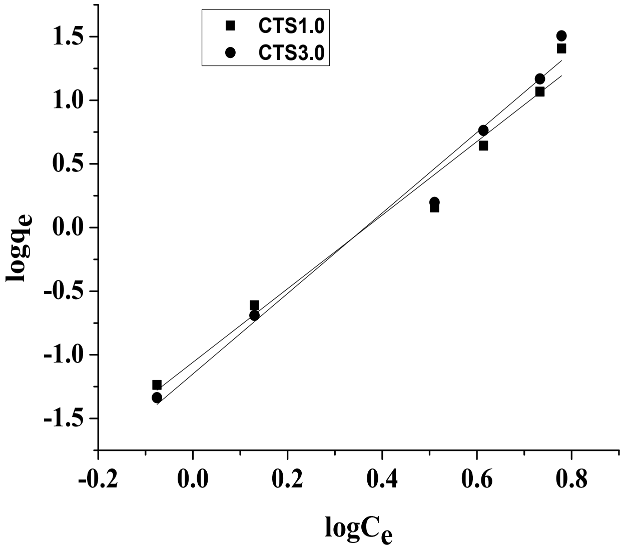

Figure 3.26: Freundlich isotherm plot for sorption of Eu by 1st and 3rd generation PAMAM functionalized Chitosan

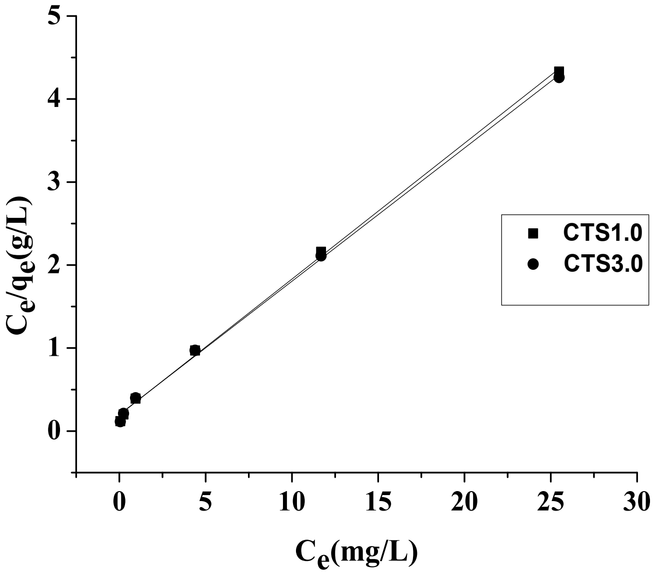

Figure 3.27: Langmuir isotherm plot for the sorption of Eu by 1st and 3rd generation PAMAM functionalized Chitosan

3.4.1.16 Desorption and reusability

For the reusability study the PAMAM functionalized chitosan material,the back extraction studies of Am(III) were carried out using different desorbing reagents. 2 mL of desorping stripping reagent was contacted with 100 mg of metal loaded CTS and the mixture was equilibrated for 60 min. Results given in Table 3.9, shows that the sorbed Am(III) can be easily desorbed using 1 M HNO_3.Then fresh feed solution of pH 5 was then contacted with the adsorbent and the results of sorption behavior after different number of cycles is shown in Table 3.10. There is lowering of sorption efficiency after 6th cycle of operation but the sorption efficiency was acceptable upto 10th cycle. But after that there was drastic decrease in sorption efficiency.

Table 3.9: Percentage desorption of Am(III) from PAMAM- chitosan

Desorbing agent	Desorption (%)
1 M HNO_3	98.89
1 M HCl	90.23
1M Oxalic acid (in 1 M HNO_3)	95.34

Table 3.10: Reusability studies for $PAMAM_1$-chotosan

No of cycle	% Am(III) sorption
1	98.89
2	99.01
3	98.54
4	98.56
5	99.03
6	98.02
7	97.34
8	95.12
9	93.11
10	90.22
11	82.12
12	68.32

3.5 Summary of the Investigations

Based on the study reported in this chapter following conlusion have been drawn.Tthe amido amine functionalized MWCNTs is prepared by oxidation of MWCNTs followed by coupling with EDA it in presence of DCC. The functionalization was confirmed by various characterization techniques. The sorption of the metal ions were dependent on the pH of the feed solution with maximum sorption for both U, Am and Eu at pH 7.0. Kinetics of sorption was found to be fast. Equilibrium attained in~15 minutes for all the radionuclides.The sorption for both U and Eu followed Langmuir adsorption model with maximum sorption capacity of approx. 20 mg/g and 16 mg/g respectively. DFT studies proved the experimental observation of higher sorption capacity of U compared to Am due to stronger complexation strength of U-AA-MWCNT over Am-AA-MWCNT and higher negative solvation energy of U(VI) compared to Am(III). Sorbed metal ions from AA-MWCNT was efficiently recovered using 1N HNO_3.

The PAMAM polymers were introduced into Chitosan by two step processes i.e. Michael addition followed by the coupling reaction using methyl acrylate and EDA respectively. The sorption process for both Am and Eu showed increasing trend with the increase of feed solution pH. The adsorption kinetics is pseudo-second order for both metal ions, and equilibrium is attained in ~ 10 minutes. Langmuir isotherm model was found to fit the sorption process for Eu(III) with maximum sorption capacity approx. 6 mg/g. The effect of the generation of PAMAM dendron on the extraction efficiency kinetics showed that with increasing functionalization, the improved extraction efficiency is balanced by steric hindrance, resulting in similar extraction performance across generations. The results of the extraction study clearly showed the potential of this material to extract Am and Eu from nuclear waste.

Chapter 4: Extraction of Trivalent f - Elements Using Polyphosphate-Grafted Fe_3O_4

Chapter 4
Extraction of Trivalent f - Elements Using Polyphosphate-Grafted Fe_3O_4

4.1 Introduction

Magnetic nanoparticles (MNPs) have been the focus of considerable scientific attention in the last decades with application in diverse fields such as medicine, sensing, electronics and environmental remediation [164], [165]. Due to the high surface area and surface reactivity, nanomaterials have sometimes far different properties from their bulk counterparts.

Indeed, the high surface area and surface activity imply that they could be used as highly efficient adsorbents for the toxic materials including heavy metals [166], [167], [168]. Among the various nanomaterials used for toxic metal sorption, magnetite has a special relevance due the ease of solid-liquid separation, in contrast to other non-magnetic nanomaterials [169], [170].

Fe_3O_4 nanoparticles have received attention due to a combination of properties, such as super paramagnetism and low toxicity [171], [172]. There are reports available for the sorption of uranium on magnetite [173], [174]. However, the aggregation of bare Fe_3O_4 nanoparticles in aqueous medium prepared by coprecipitation is a major limitation [175]. In order to overcome the above drawbacks, the surface of the magnetite nano particle is coated with various organic and inorganic functional molecules. These coating molecules not only stabilize nanoparticles but also provide terminal functional groups that can be utilized for the sorption of metal ions.

Recently organosilane, carboxylate and phosphonate graffted on MNPs have been demonstrated to be superior anchoring groups, while not affecting the properties of the

MNP deleteriously. Reports are available for the strong interaction between magnetite nanoparticle and phosphate moity via the formation of P–O–Fe bond and most the interesting moiety seems to be triphosphate [176].Though sodium tripolyphosphate (STPP) is widely used in food and drug industry[177] but it is less common as an adsorbent for the extraction of actinides except uranium.

The outstanding metal complexing behavior of the phosphate group has prompted an investigation into the effectiveness of polyphosphate grafted Fe_3O_4 nanomaterial as a sorbent for radionuclides. This thesis will describe the results from the sorption experiments for Am(III) and Eu(III) from acidic nuclear waste solution using the synthesized polyphosphate grafted Fe_3O_4 nanomaterial and the various parameters that influence the mechanism of sorption.

4.2 Synthesis of Polyphosphate Functionalized Fe_3O_4

The preparation of Polyphosphate grafted Fe_3O_4 nanomagnets (PPNMs) was performed in a basic medium. Fe^{2+} and Fe^{3+}salts were dissolved in oxygen-free water at ratio of 1: 2.8. The temperature of the reaction medium was maintained at 70^{o}C in N_2 atmosphere under constant stirring for half an hour. About 30 ml of (25%) NH_4OH was then added to the reaction solution and kept for another 30 min under the same reaction condition. 10ml of 0.2 g/ml aqueous solution of sodium tripolyphosphate was added to the above reaction mixture, and temperature was slowly raised to 90^{o}C and maintained for 60 min. The black coloured precipitate was thoroughly washed with water, magnetically separated and the product were dried at 60 ^{o}C .

4.3 Characterization

XRD analysis

The single-phase cubic inverse spinel PPNM structure, with lattice constant a = 8.373 Å is evident by the appearance of six characteristic diffraction peaks, (220), (311), (400), (422), (511) and (440) in the XRD pattern as shown in **Fig. 4.1**. The lattice constant value is very close to the reported value for magnetite (a = 8.375 Å). The formation of highly crystalline particles confirmed due the presence of sharp and intense diffraction peaks. From X-ray line broadening, the crystallite size of PPNMs was estimated to be approximately 10 nm.

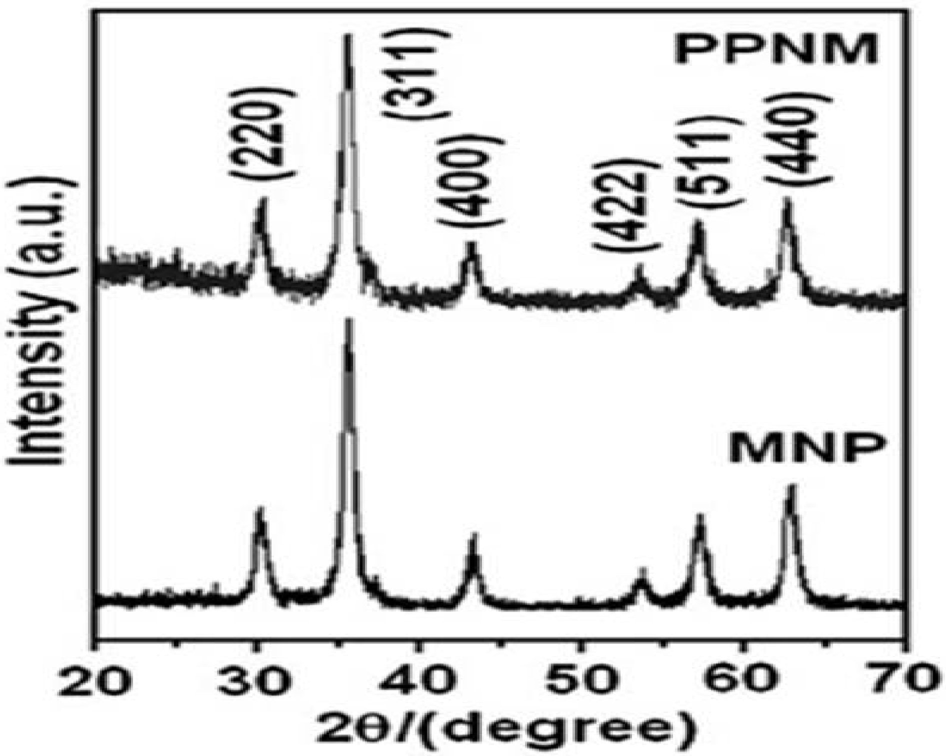

Figure 4.1: X-ray Diffractogram of MNP and PPNM

FTIR spectroscopy

The surface functionalization of Fe_3O_4 nanomaterial by polyphosphate is confirmed by the FTIR spectrum presented in **Fig. 4.2**. From the FTIR spectra of STPP and polyphosphate functionalized Fe_3O_4 show that bands for STPP are well-resolved, while those of the PPNMs are rather broad and less intense.

The characteristic vibrational bands for STPP appear at 1215 cm^{-1} (P=O stretching), 1160 and 1130 cm^{-1} (asymmetric and symmetric stretching vibrations in the PO_2 group), 1078 cm^{-1} (asymmetric and symmetric stretching vibrations in the PO3 group), and 918 and 715 cm^{-1} (asymmetric and symmetric stretching of the P–O–P bridge).Though these bands were absent in the spectrum of bare Fe_3O_4 nano particle whereas they appear in the spectrum of PPNMs with a small shift in the band position in the range of 700–1250 cm^{-1} with bands at 710, 900, 1026, 1087 and 1167 cm^{-1}.This suggest the grafting of sodium tri polyphosphate on the surface of Fe_3O_4 nano particles. Further, the intense peak at around 575 cm^{-1} in the PPNMs can be attributed to the Fe–O stretching vibrational mode of Fe_3O_4.

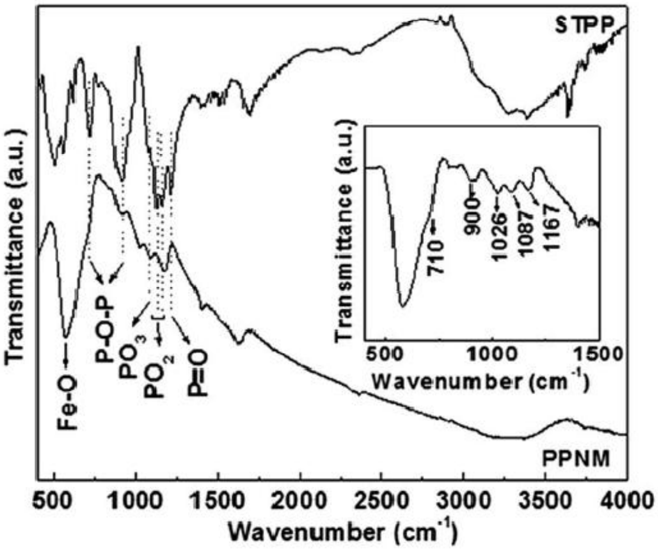

Figure 4.2: FTIR spectrum of STPP and PPNM

DLS measurement

DLS result as shown in **Fig. 4.3**, indicates that the major population of these particles generate an aqueous colloidal dispersion with a mean hydrodynamic diameter in the range of 20 to 100 nm with an average diameter at about 40 nm. The size observed in DLS is bigger due to the presence of hydrated organic moieties and the inherent polydispersity in the distribution [178], [179].

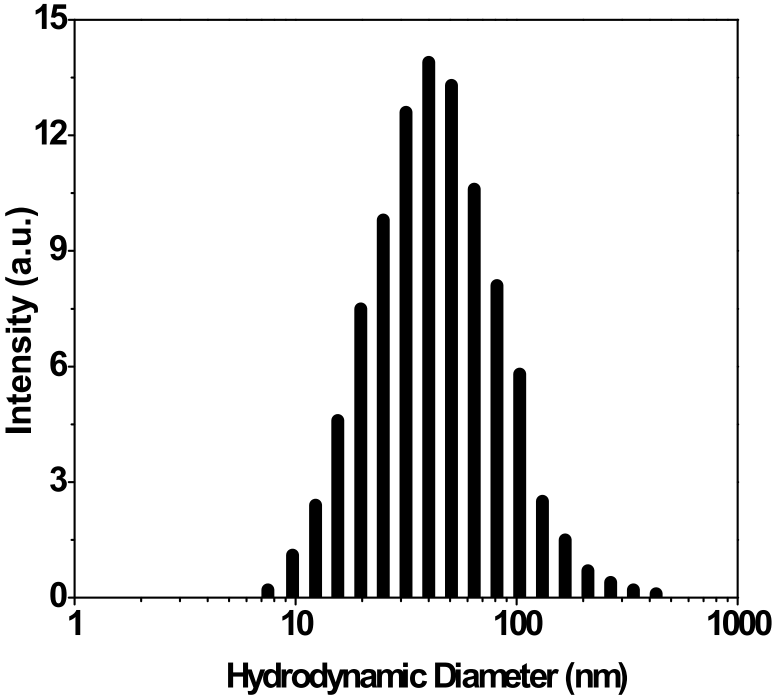

Figure 4.3: DLS curve for PPNM

Zeta potential measurement

The electrostatic charge on the surface of the polyphosphate functionalized Fe_3O_4 is evident from zeta potential measurements. The variations in the zeta potentials of PPNM particles with varying pH values in different concentration of nitrate medium are shown in Table 4.1 and Table 4.2.

Zeta potential values at pH 5with the variation of NO_3^- are also measured. The high negative charge on these particles arises from the functionalization of phosphate groups on MNP. Moreover, the high negative surface charge of PPNMs (at pH > 4) at low NO_3^- concentration make their use as an efficient sorbent material for metal ion.

Table 4.1: pH dependent zeta-potential of PPNMs in difference concentration of perchlorate solution in water (perchlorate concentration was maintained by addition of $NaClO_4$)

pH	Zeta-potential (mV)	
	0.01 M nitrate solution	0.1 M nitrate solution
6	-26.3	-12.9
5	-17.9	-10.0
4	-15.1	-7.0
3	-12.5	-5.4

4.4 Sorption Experiments

Sample preparation and batch extraction

Weighed amount (~100 mg) of polyphosphate functionalized Fe_3O_4 sorbent was added to 10 ml of a solution containing ^{241}Am/ $^{152+154}$Eu activity at a desired pH and fixed ionic strength for 30 min (except for kinetic studies) in a mechanical shaker at a fixed speed at room temperature. After equilibration, the sorbent loaded with Am (III)/Eu (III) were separated from the aqueous solution using a hand held permanent magnet. The concentration of the radionuclides in the supernatant was measured in a scintillation gamma counter. The ionic strength of the solution was maintained using $NaClO_4$ as a background electrolyte due to non-complexing nature of ClO_4^- ion.

Table 4.2: Zeta-potential of aqueous solution of PPNMs in presence NO_3^- ions (NO_3^- ion concentration was maintained by addition of $NaNO_3$)

Concentration of NO_3^- ions	Zeta-potential at pH 5 in presence difference concentration of NO_3^- ions
0.6	-2.9
0.45	-4.2
0.30	-5.9
0.15	-10.3

pH values of the solutions were adjusted using $HClO_4$ or NaOH. Due to close chemical proximity between the trivalent actinides and lanthanides, inactive Eu solution at different concentrations was used in presence of $^{152+154}$Eu tracer activity during isotherm studies. This was carried out to avoid the radiation dose associated with high concentrations of ^{241}Am. All reagents were of AR grade and used without further purification. Doubly distilled water was used throughout the experiment for the preparation of the reagents. All the experiments were carried out in triplicate and the results were found to be within error limit of ± 5%.

Effect of pH on extraction of metal ions

As Am (III) forms different positively charged species at different pH medium with Am^{3+}_{aq} being the major species up to pH 6. From the pH range of 6-8, $AmOH^{2+}$ is formed whereas above pH 8 up to pH 12, the predominant species is $Am(OH)_2^+$ with little contribution from $Am(OH)_{3(aq)}$ above pH 11. Due to the similar chemistry Eu (III) is also understood to form similar positively charged species in the same pH range.

zeta potential value of PPNMs at varying pH showed high negative surface charge beyond pH 4.So with the negative surface charge of the PPNMs and the positively charged species formed by Am (III) and Eu(III), we expected to observe an increasing trend of Am (III)/Eu (III) sorption by PPNMs with increasing pH (pH 1 to 6 studied due to acidic nature of radioactive waste) as shown in **Fig. 4.4**.

There was a gradual increase of extraction with the increase of pH. To understand the nature of extraction, pH dependent sorption experiments were performed at two different ionic strengths (0.1 M and 1.0 M) and it proved that the nature of interaction between Am(III)/Eu(III) and PPNMs are electrostatic in nature.

Increasing ionic strength led to decrease in sorption efficiency for both the radionuclides studied at all the pH values. The reason is also quite understandable, with higher ionic strength of the medium causing greater stabilization of the charged species which creates a barrier in the electrostatic interactions between two charged species resulting in lower sorption efficiency. The sorption study with varying pH for both Am(III)/Eu(III) was carried out in presence of $NaClO_4$ due to its non-complexing nature in order to investigate the sorption mechanism.

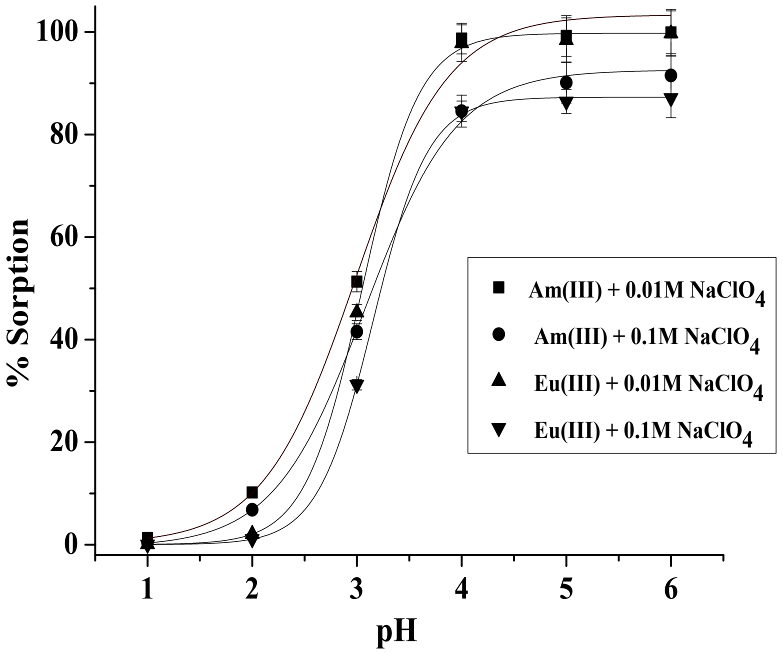

Figure 4.4: Effect of feed pH on the sorption of Am and Eu by PPNM; volume of aqueous solution: 2 mL, weight of the PPNM-20 mg, time of equilibration- 1 h

Optimization of contact time

In order to investigate the kinetics parameters of PPNMs, sorption studies of Am(III)/Eu(III) from pH 6 solution having 0.01M ionic strength were carried out. The plot is shown in **Fig. 4.5,** shows that the sorption of metal ions increase with contact time upto 10 mins and thereafter it becomes almost constant. It is evident that both the radionuclides attain equilibrium in ~ 10 min time signifying fast kinetics of equilibration. To ensure maximum metal ions uptake, contact time for all the batch experiments were fixed at 1 hour.

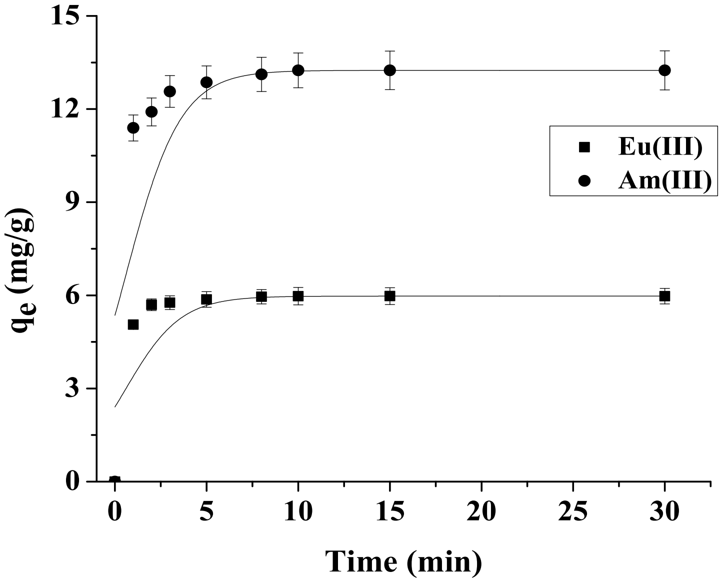

Figure 4.5: Effect of sorption time on the equilibrium sorption capacity of PPNM for Am and Eu, pH of the solution- 6, weight of AA-MWCNT ~ 20 mg, volume of aqueous solution- 2 mL

Sorption kinetics

Different mechanisms of mass transfer of the metal ions from the bulk solution to the external surface of PPNMs controlled the kinetics of the sorption process. Kinetics of the sorption process using PPNMs was studied for ^{241}Am and $^{152+154}$Eu.Most frequently, two different kinetic models: Lagergren's first order model, and Pseudo second order model have been considered for elucidating the sorption mechanism.

i. Lagergren's first order kinetic model:

$$\log(q_e - q) = \log q_e - \frac{k_{ads}\, t}{2.303} \qquad (4.1)$$

where, q (mg.g^{-1}) is the metal ion concentration onthe sorbent at time't', q_e is the metal ion concentration on thes orbent at equilibrium, and k_{ads} (min^{-1}) is the first order rate constant.

ii. Pseudo second order kinetic model

$$\frac{t}{q} = \frac{1}{k_2 \quad q_e^2} + \frac{t}{q_e} \tag{4.2}$$

Where, k_2 ($g.mg^{-1}.min^{-1}$) is the pseudo second order rate constant.

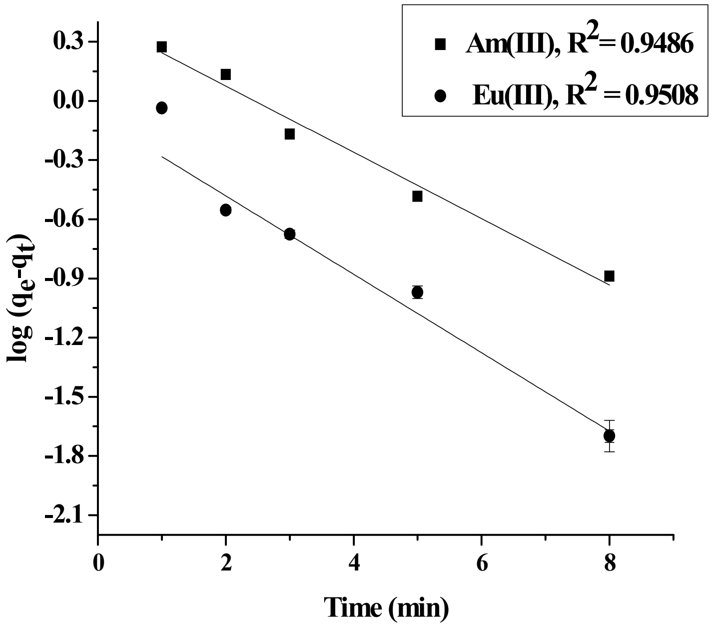

(a)

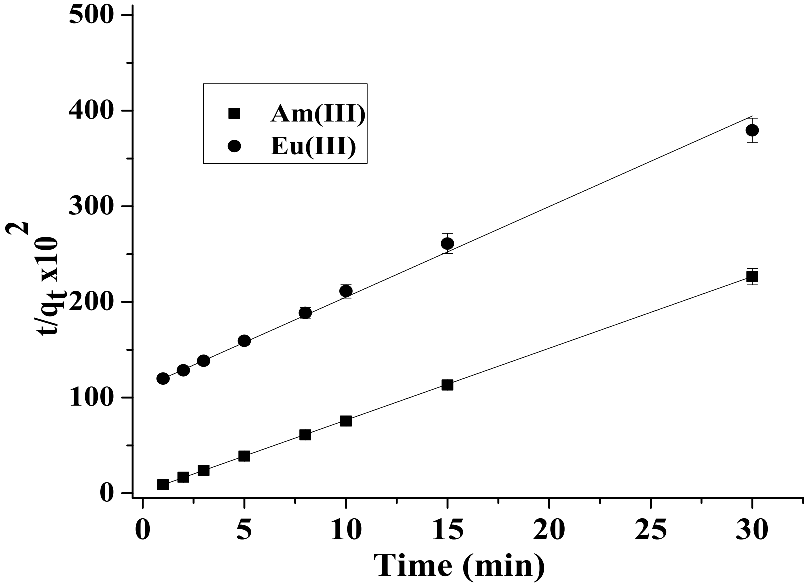

(b)

Figure 4.6: Lagergren's first order kinetic model (a), and Pseudo 2nd order kinetics model (b), for the sorption of Am and Eu, volume of aqueous solution: 2 mL, weight of the PPNM ~20 mg, time of equilibration- 1 h.

4.4.1.1 Pseudo 2nd order kinetics for sorption of Am(III) and Eu(III) by PPNMs

The linear plots for both pseudo 1st order as well as pseudo 2nd order are given in **Fig. 4.6**. Strongest correlation for both the radionuclides were found with the pseudo 2nd order equation (R^2 values - 0.989 and 0.992 for both Eu(III) Am(III) repectively and which signifies that the sorption process was controlled by chemisorption. The R^2 values corresponding to pseudo 1st order equation for Am(III) and Eu(III) were 0.948 and 0.950 respectively. The values of pseudo-second-order rate parameter [k_2,(g.mg^{-1}·min^{-1})] and equilibrium sorption capacity q_e (mg.g^{-1}) can also be found in Table 4.3.

Table 4.3: Parametrs for pseudo second order and pseudo first order kinetics modelling for the extraction of Am(III) and Eu (III) using PPNM

Radionuclides	Pseudo second order kinetics			Pseudo first order kinetics
	q_e (mg/g)	K_2 (g/(mg min)	R^2	R^2
Eu (III)	10.56	0.004	0.989	0.950
Am (III)	13.33	0.008	0.992	0.948

Sorption isotherm

Adsorption isotherm studies are very important to understand the sorption mechanism of an absorbent. Langmuir isotherm assumes homogenous distribution of sorption sites without interaction between sorbed molecules and the sorption is a monolayer. In case of the Freundlich model, diversity of the sorption sites and or diverse nature of the sorbed species, the sites are distributed heterogeneously. We carried out the isotherm studies of Eu(III) from pH 6 solution. Close proximity of the chemistry of the actinides and lanthanides along with high radiation dose associated with higher concentration of Am(III) led us to study Eu(III) for isotherm studies. **Fig. 4.7** shows the isotherm plot of Eu(III) for PPNMs. Initially rapid increase of amount of metal ion sorption was there followed by a plateau at higher concentration of Eu. Maximum sorption capacity of Eu(III) was found to be 10.6 mg.g^{-1} of PPNM.

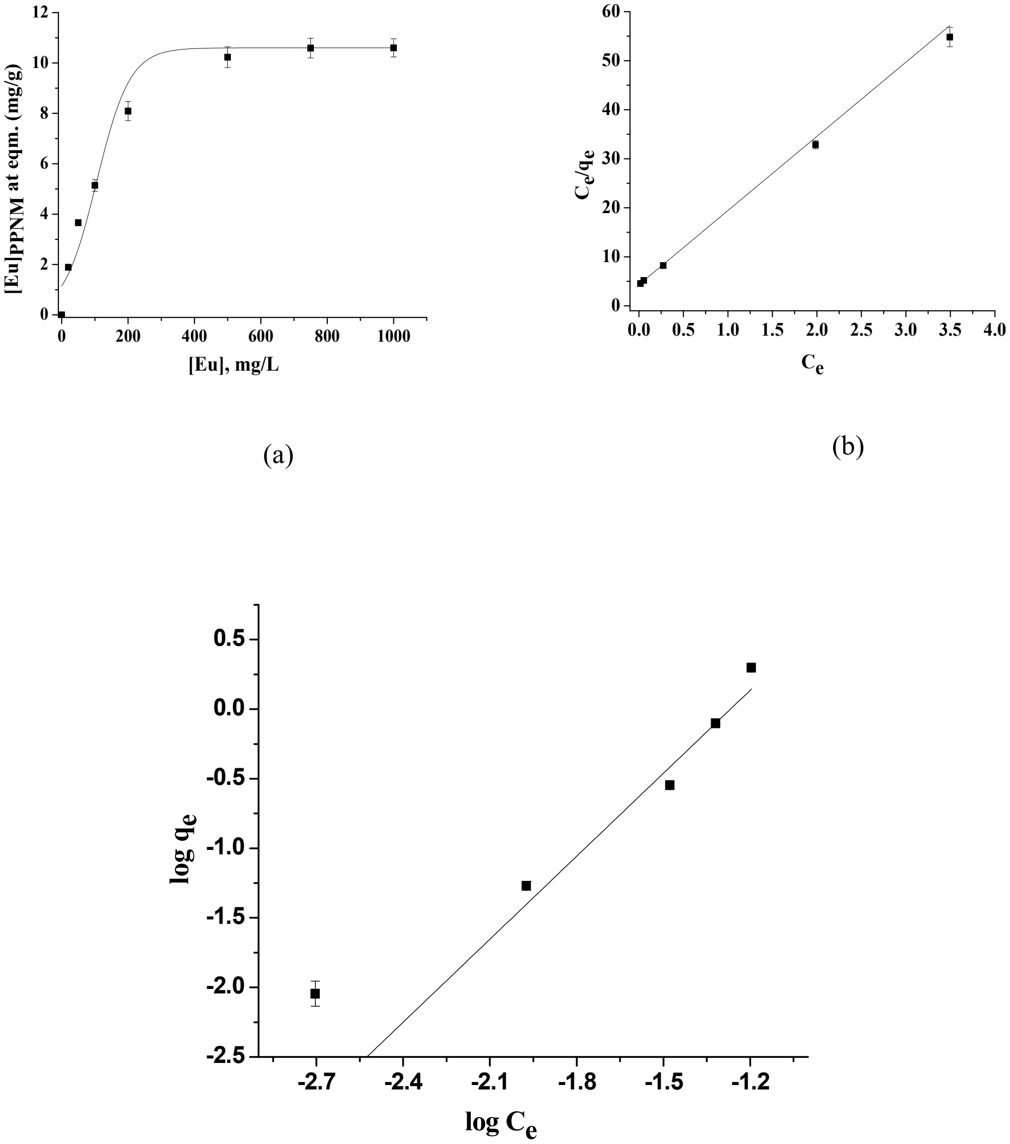

(a)

(b)

(c)

Figure 4.7: Variation in sorption with Eu concentration (a), Langmuir isotherm (b) and Freundlich isotherm (c) for Eu sorption by PPNM

The observed data were further subjected to Langmuir and Freundlich isotherm treatment fitting. Various parameters obtained from different isotherms are given in Table 4.4. Stronger correlation was found with Langmuir isotherm (R^2 = 0.993) compared to Freundlich isotherm (R^2 = 0.946). From the Langmuir plot, maximum sorption capacity of Eu(III) was found to be 10.58 mg/g which is in very close to the maximum sorption capacity determined experimentally. Hence the sorption of Eu(III) and analogously Am(III) in PPNMs takes place by chemical reaction, the sorption is monolayer and is limited by the availability of the complexing sites.

Table 4.4: Different isotherm constant and corosponding R^2 values for the sorption of Eu (III) using PPNM

Isotherm	Values of Parameters obtained				
	q_{max} (mg/g)	k_f ($mmol^{1-n}$ L^n g^{-1})	B (L/mmol)	n^{-1}	R^2
Langmuir	10.58	-	3.51	-	0.993
Freundlich	-	1.84	-	0.673	0.946

Effect of nitrate ion

Radioactive waste solutions comprise a nitric acid medium, and the complexing nature of nitrate ions leads to a reduction in the sorption efficiency. Therefore, it is important to evaluate the effect of nitrate ions on the sorption of Am(III) in two different pH solutions without any ClO_4^- ion but varying concentrations of nitrate ions. The results are shown in **Fig. 4.8**.

At pH 6, it is observed that increasing nitrate concentration up to 0.3M has no effect on the sorption of Am(III) by PPNMs. Further increase of nitrate concentration from 0.3M to 1M led to continuous decrease of Am(III) sorption efficiency of PPNMs. This could be attributed to the competition between the surface negative charges of PPNMs and nitrate ions present in the solution. Hence at pH 6, the larger number of negatively charged functional groups of PPNMs are able to compete better with nitrate ions for the Am(III).

In case of pH 3 solutions, the rate of decrease of % adsorption with increasing nitrate ion concentration was found to be marginal initially. However, it is found to be significant with the increase of nitrate ion concentration in solution. This is mainly because of the presence of lower fraction of de-protonated ligand species at pH 3.

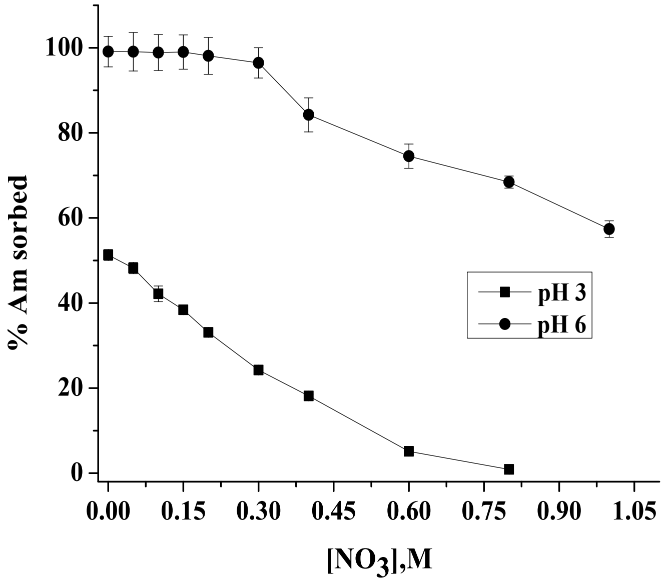

Figure 4.8: Effect of nitrate concentration on the sorption efficiency of Am by PPNM; volume of aqueous solution: 2 mL, weight of the PPNM ~20 mg, time of equilibration- 1 h

Desorption and Reusability

It is imperative to study the reusability of a sorbent for practical applications and desorption study is pre-requisite to study the reusability. The results from the pH dependent sorption of Am(III) and Eu(III) indicate the possibility of desorption by acidic solution. Hence desorption studies were carried out using 0.1M and 0.2M HNO_3 and the results indicated that quantitative desorption of Am(III) is possible in three contacts from the Am(III) loaded PPNMs using both the strippant solutions. With this results from the desorption studies of Am(III) from the PPNMs in the background, reusability study was carried out using Am(III) solution at pH 6. After each sorption cycle, the sorbent was desorbed with 0.2M HNO_3 thrice, washed with de-ionized water and contacted with fresh Am(III) solution at pH 6. The results as indicated in Table 4.5, show that even after 10 successive cycles of sorption and desorption, the PPNMs do not lose its sorption efficiency with > 97% sorption efficiency after 10th cycle. Hence, the sorbent show excellent reusability which is very important for practical applications.

Table 4.5: Reusability study of the PPNMs

No. of Cycle	Sorption (%)
1	98.97
2	98.69
3	98.71
4	98.16
5	98.23
6	98.03
7	97.84
8	97.22
9	97.13
10	97.05

4.5 Summary of the Investigation

The results reported in this chapter are summarized as follows. Co-precipitation of Fe^{2+} and Fe^{3+} ions in alkaline medium followed by surface functionalization using sodium tripolyphosphate resulted in Polyphosphate functionalized Fe_3O_4 nanomagnets (PPNMs). Different characterization techniques (FTIR, XRD, zetapotential, DLS etc.) show the formation of a stable single phase Fe_3O_4 nanostructure with average diameter of 40 nm with a coating of sodium tripolyphosphate on the surface of the Fe_3O_4 nanoparticles. Extraction study shows that the sorption efficiency of PPNMs for both trivalent actinide and lanthanide increases with solution pH, whereas increasing ionic strength of the medium led to a decreasing trend.The kinetics of sorption for both the radionuclides by the PPNMs is found to follow pseudo second order kinetics with equilibrium attained in ~ 5 min. The isotherm study indicates that the adsorption process follws Langmuir model for this material. A maximum sorption capacity of approx.10 mg/g for Eu(III) was demonstrated. The reusability study shows that even after 10 successive cycles of operation the PPNMs maintain their sorption efficiency.

Chapter 5 : Extraction of f-Elements Using Pyridine-2,6-Dicarboxamide and Diglycolamide Functionalized Titania

Chapter 5

Extraction of f- Elements Using Pyridine-2,6-Dicarboxamide and Diglycolamide Functionalized Titania

5.1 Introduction

Surface functionalized TiO_2 (anatase) finds applications in actinide separation.[180] Amide derivatives of carboxylic acid, which are completely incinerable, are also stided for actinides separatio [181], [182], [183], [184], [185] . Further coordination with metal ions will be augmented by ligands with pre-orgaized conformations. In view of the above fact, pyridine-2,6-dicarboxamide (DPA) and diglycolamide (DGA) ligands are functionalized on the surface of titania. Amides and nitrogen-bearing heterocyclic systems, based on DIAMEX and SANEX processes, are highly effective sorbents due to the covalent character being bolstered by soft nitrogen atoms. In this present study, there is a synergy of the properties of both pyridine and amide moieties. Dipicolinic acid is used as a complexing agent for the extraction of actinides having various oxidation states.[186] [187] [188] The aim of present investigation is to functionalize TiO_2 with DPA and DGA functional group, followed by the evaluation of the material for efficient separation of f-block elements. Different parameters were studied to determine the sorption mechanism, kinetics, and maximum sorption capacity of the DPA and DGA functionalized TiO_2.

5.2 Preparation of adsorbents

Pyridine-2,6-dicarboxamide functionalized titania

The Pyridine-2,6-dicarboxamide (DPA) functional group was introduced on the surface of titania (TiO_2) by a three step chemical process.

I) Preparation of 2,6-pyridinedicarboxylic chloride

II) Preparation of Silane-dipicolinamide (Silane-DPA)

III) Surface functionalization of TiO_2 using Silane-DPA

A detailed description of the synthesis steps are reported in Chapter 2. A schematic of the preparation is presented below:

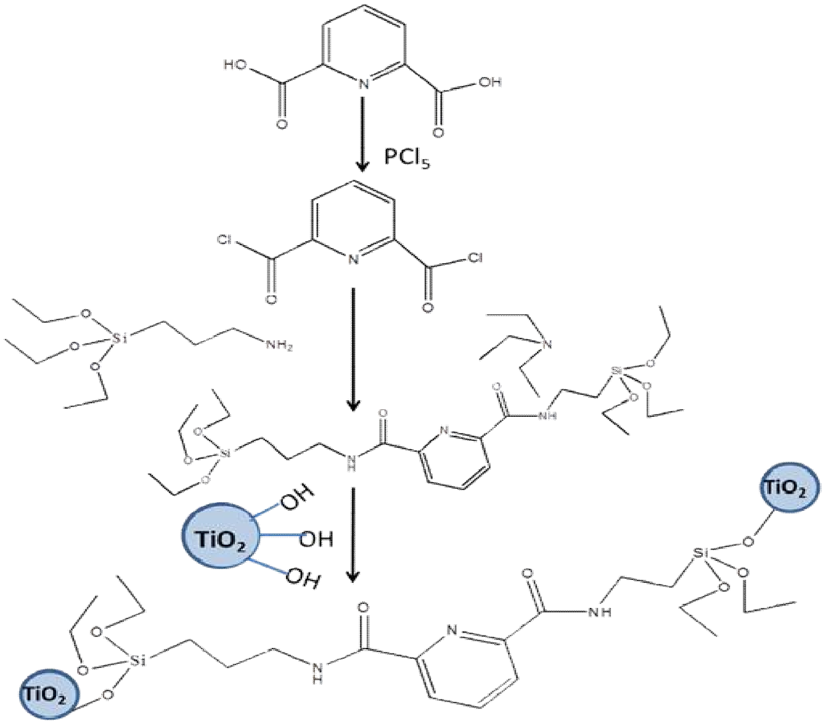

Figure 5.1: The simplified scheme for the synthesis of the DPA functionalized TiO_2

Synthesis of diglycolamic acid functionalized TiO_2

The diglycolamide (DGA) functional group was introduced on the surface of titania (TiO_2) by a two step chemical process.

I) Synthesis of silane – diglycolamic acid (Silane – DGAH)

II) Preparation of DGAH functionalized TiO_2

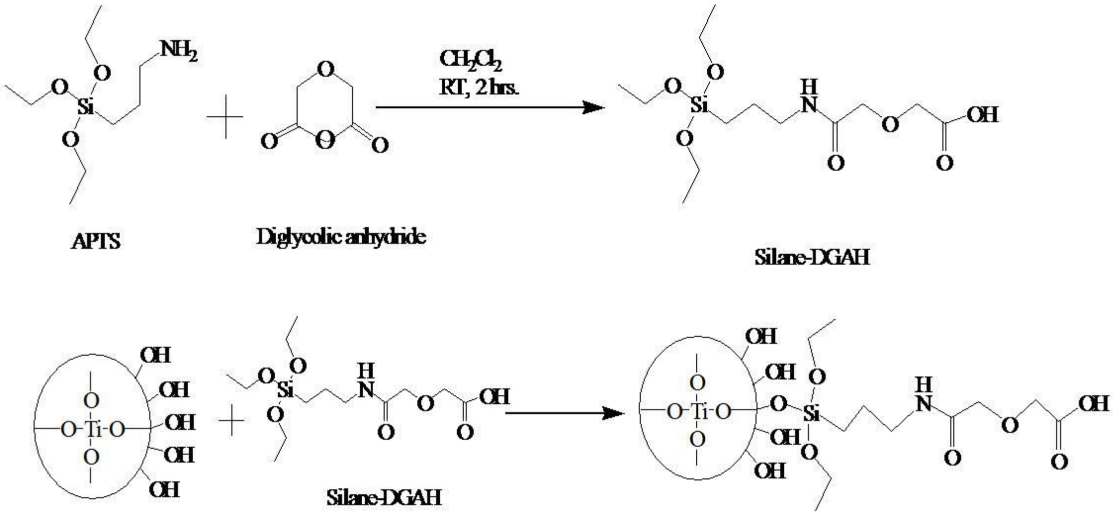

Figure 5.2: The simplified scheme for the synthesis of the DGA functionalized TiO_2

A detailed description of the synthesis steps are reported in Chapter 2. A schematic of the preparation is presented above.

5.3 Characterization

Pyridine-2,6-dicarboxamide functionalized titania

5.3.1.1 FTIR spectroscopy

The surface functionalization on the anatase was investigated by FTIR spectroscopy as shown in **Fig. 5.3(a)**. In FTIR, the oversaturated peaks below 700 cm^{-1} was attributed to Ti-O and Ti-O-Ti bonds, while the peak at 780 cm^{-1} corresponds to Si-O-C bond.[189] The intense peak at 1040 cm^{-1} was attributed to Si-O bond, whereas the shoulder 1102 cm^{-1} and 1194 cm^{-1} correspond to C-N stretching.[190] The peaks at 1434 and 1537 cm^{-1} were assigned due to pyridine moiety, while peak at 1657 cm^{-1} was assigned to amide functionality. Two consecutive peaks at 2845 and 2947 cm^{-1} were assigned to $-CH_2$ groups.[191] A broad peak around 3300 cm^{-1} to 3600 cm^{-1} can be attributed to hydrogen bonded hydroxyl group as well as amine moieties or might be a combination of both the functionalities.

5.3.1.2 EDX spectroscopy

The EDX spectrum of the functionalized material shows the presence of Si, indicating the presence of functionalizing hetero-atoms on the surface as shown in **Fig. 5.3(b)**. Additionally, peaks corresponding to O, C and N were also detected. Testifying to the sorption ability of the functionalized TiO_2, Th was detected in the area map of sorbent exposed to Th containing waste stimulant. This is presented in **Fig. 5.3 (f)**, and uniform distribution of Th was observed.

5.3.1.3 Thermogravimetric analysis

Thermal stability of the functionalized sorbent is shown in **Fig. 5.3 (c)**.The stability with respect to temparature for the sorbent revealed that a moderate weight loss was observed upto 400ºC, while in the temperature range 400-600ºC a drastic weight loss is noticed. TiO_2 is not expected to decompose in this temperature range. Therefore, the entire mass loss can be attributed to the thermal decomposition of the functional groups. There was a total of 4.7 mg weight loss observed for ~ 17.7 mg of TiO_2 sample, which corresponds to 26.5 % functionalization.

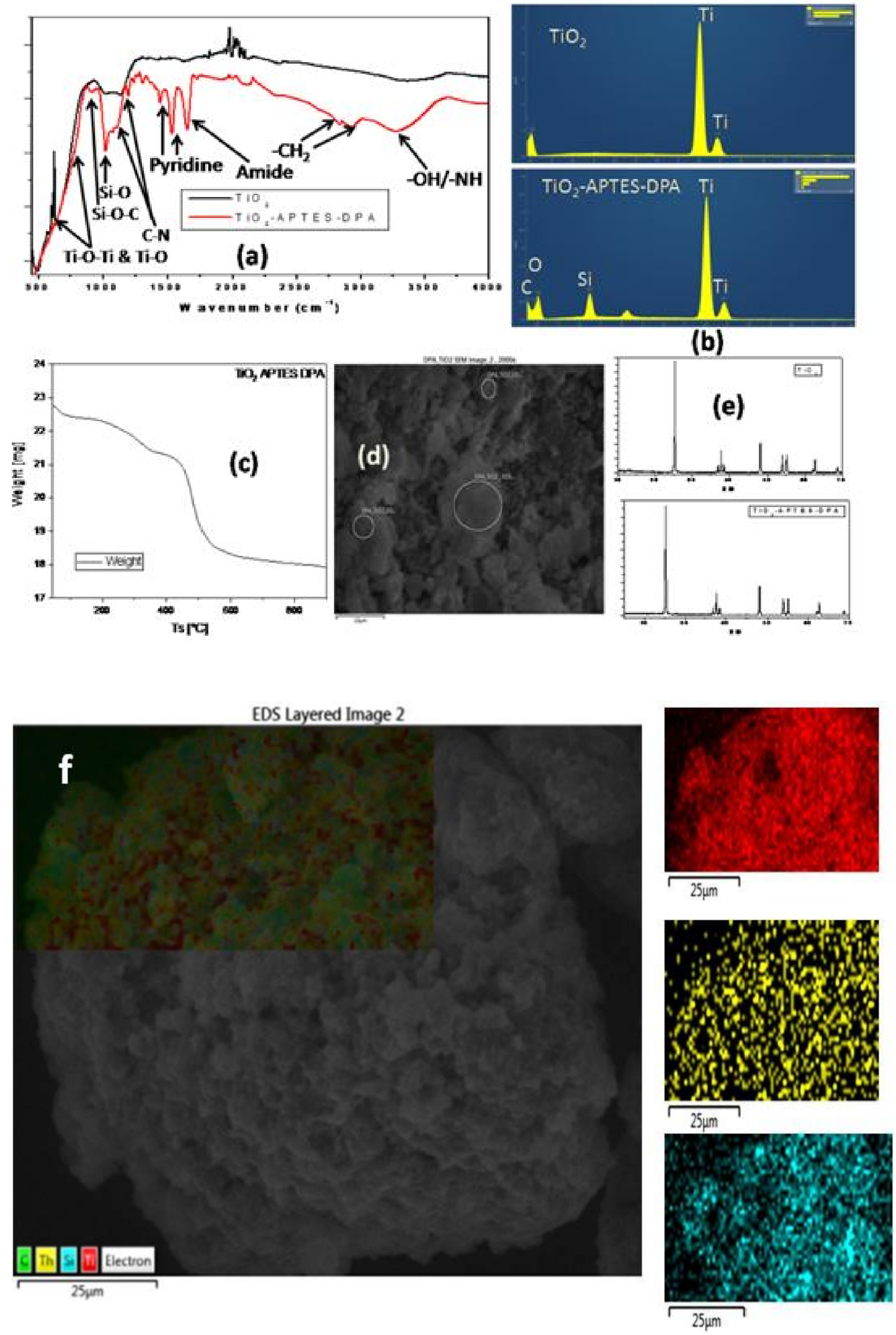

Figure 5.3: (a) FTIR spectra for TiO_2 and DPA-TiO_2; (b) EDX spectra for TiO_2 and DPA-TiO_2; (c) Thermo gravimetric analysis of DPA-TiO_2; (d) SEM image for DPA-TiO_2; (e) XRD pattern for TiO_2 and DPA-TiO_2; (f) EDS layered image showing uptake of Th on the surface of DPA functionalized TiO_2 (Red: Ti; Yellow: Th; Blue: Si)

5.3.1.4 SEM study

SEM image of the sorbent is shown in **Fig. 5.3(d)**. This gives an idea on the surface morphologies. The functionalization also confirm by the surface morphology change from precursor to the product as studied by SEM.

5.3.1.5 XRD study

XRD spectra for TiO_2 and DPA functionalized TiO_2, are shown in **Fig. 5.3 (e)**. The similarity of XRD peak pattern in both TiO_2 and DPA-TiO_2confirmed that there is no modification of anatasecrystal structure during functionalization. The XRD spectra for precursor revealed the presence of anatase phase due to the signature triplet peaks at 2θ: 37°, 38° and 39°. After functionalization with DPA-TiO_2, no change in the characteristic peaks in XRD was observed.

5.3.1.6 XPS study

XPS spectra of DPA functionalized titania and Eu loaded sorbent are shown in Fig 5.4. Ti-$2p_{3/2}$ peak appear at 458.6 eV (**Fig. 5. 4a**) shows the presence of TiO_2. O-1s and C-1s spectra (**Fig. 5.4b, 5.4c**) also indicate the presence of the functional group. The presence of three different types of nitrogen species are confirmed by deconvoluted N-1s peak (**Fig. 5.4e**). Peak at ~135.7 eV appear for Eu-4d peak of pure Eu_2O_3. In the present case, peak at 136.5 eV is observed for Eu-4d peak (**Fig. 5.4f**) of Eu_2O_3. The 0.8 eV shift of Eu-4d peak indicates the adsorption of Eu on the surface of DPA functionalized TiO_2.

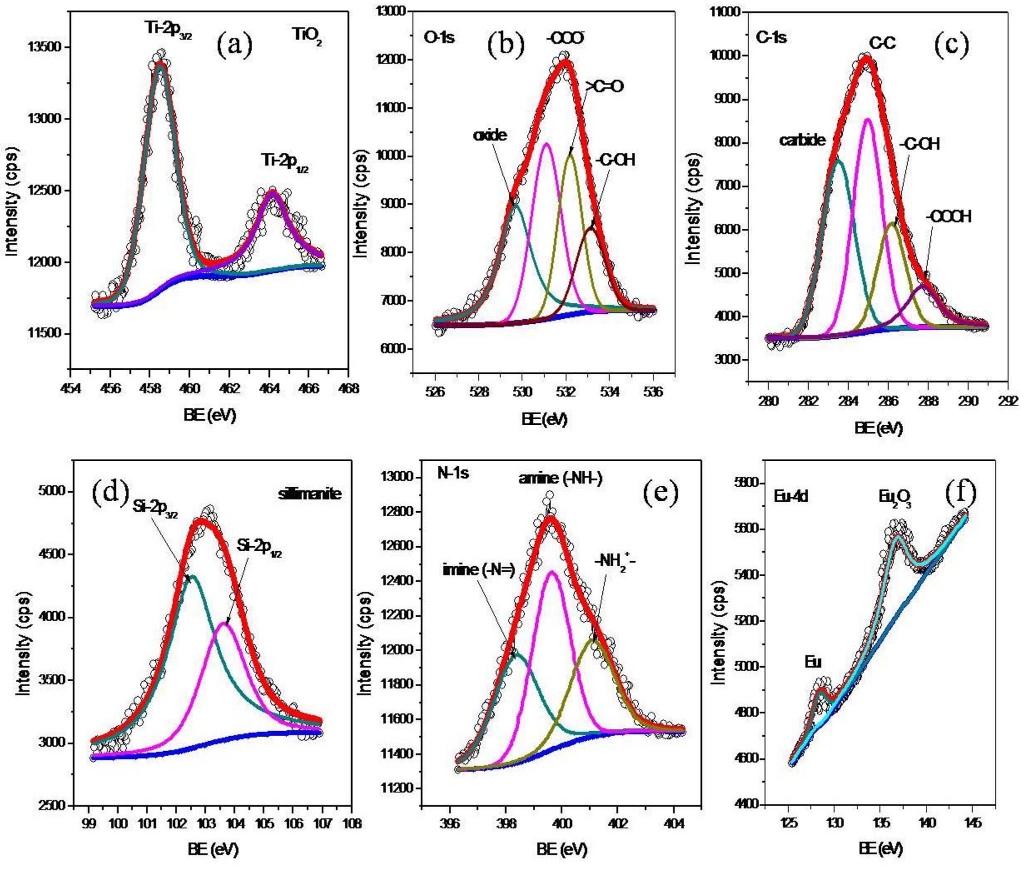

Figure 5.4: Deconvoluted XPS spectra of (a) Ti_{2P} peak; (b)O_{1s} peak; (c) C_{1s} peak; (d) Si_{2p} peak; (e) N_{1s} peak; (f) Eu_{4d} peak for Eu-DPA-TiO_2 complex

5.3.1.7 XANES and EXAFS study

Fig. 5.5 shows the normalised XANES spectrum of standard Eu_2O_3 along with Eu loaded DPA samples at Eu L3 edge. The +3 oxidation state of Eu ions, confirmed by the absorption edge position. The spectral features of Ti K edge XANES spectra are marked as A, B, C, D, E and F. The XANES profile of Ti in DPA- TiO_2 sample is matches with anatase TiO_2. The pre edge feature shows three peaks A, B and C, which originate from the transition of Ti 1s electron to Ti_{3d}/O_{2p} hybridized states. The intensity of A, B and C is maximum for DPA. These peaks intensity depends on the local structural distortion around the Ti atoms. Highly distorted local structure is confirmed by the maximum intensity for

DPA. Quantitative analysis of EXAFS spectra gives the local structure around the absorbing atom. In case of qualitative analysis, the oscillations in the absorption spectra μ(E) has been converted to absorption function χ (E) defined as follows:

$$\chi(E) = \frac{\mu(E)-\mu_0(E)}{\Delta\mu_0\,(E_0)} \qquad (5.1)$$

Where, $E_0$is the energy of absorption edge, $\mu_0(E)$is bare atom background and $\Delta\mu_0\,(E_0)$ is the step in $\mu(E)$ value at the absorption edge. The wave number dependent absorption coefficient χ (K) obtained from the energy dependent absorption coefficient $\chi(E)$ using the relation,

$$K = \sqrt{\frac{4\pi^2 m\,(E-E_0)}{h^2}} \qquad (5.2)$$

where, m is the electron mass. χ (K) is weighted by k^2 to amplify the oscillation at high K and the $\chi(k)k^2$ functions are Fourier transformed in *R* space to generate the χ (R) versus *R* spectra in terms of the real distances from the center of the absorbing atom. The set of EXAFS data analysis programme available within Demeter software package have been used for EXAFS data analysis. This includes background reduction and Fourier transform to derive the χ (R) versus *R* spectra from the absorption spectra (using ATHENA software), generation of the theoretical EXAFS spectra starting from an assumed crystallographic structure and finally fitting of experimental data with the theoretical spectra using ARTEMIS software. The χ (R) versus *R* plots generated using fourier transform of μ (E) versus E spectra following the methodology described above are shown in **Fig 5. 5** at Eu L3 edge and Ti K edge.The Fourier transform spectrum is phase uncorrected spectra, where the coordination peak in fourier transform spectra is appeared at slightly lower inter-atomic distances *(R)* compared to actual bond length. The theoretical scattering paths are generated from the DFT optimizes guess structure. The bond length, coordination number and disorder factor is kept as the variable during the fitting process. The obtained fitting results are tabulated in Table 5. 1. The first peak at 1.9 Å is contribution of two oxygen coordination cells at 2.19 Å and 2.39 Å with approximately two and eight oxygen atoms respectively. The second coordination peak for Eu:DPA-TiO_2 is appeared to be merged in first coordination peak at 2.5 Å. The second and third coordination peaks are fitted using the N and C coordination's at 3.01 Å and 3.88 Å. The Fourier transform spectra of Ti K edge in DPA are similar to anatase TiO_2 (**Fig. 5.6**), which was also observed in XANES spectra discussed above. The anatase TiO_2 structure is used as initial guess structure. The first peak at 1.4 Å is contribution of 6 oxygen atoms and the second and third peak between 2 - 3.5 Å is contribution of Ti-Ti coordination shells. Since the DPA sample had higher distortion, its pre edge peak was higher.

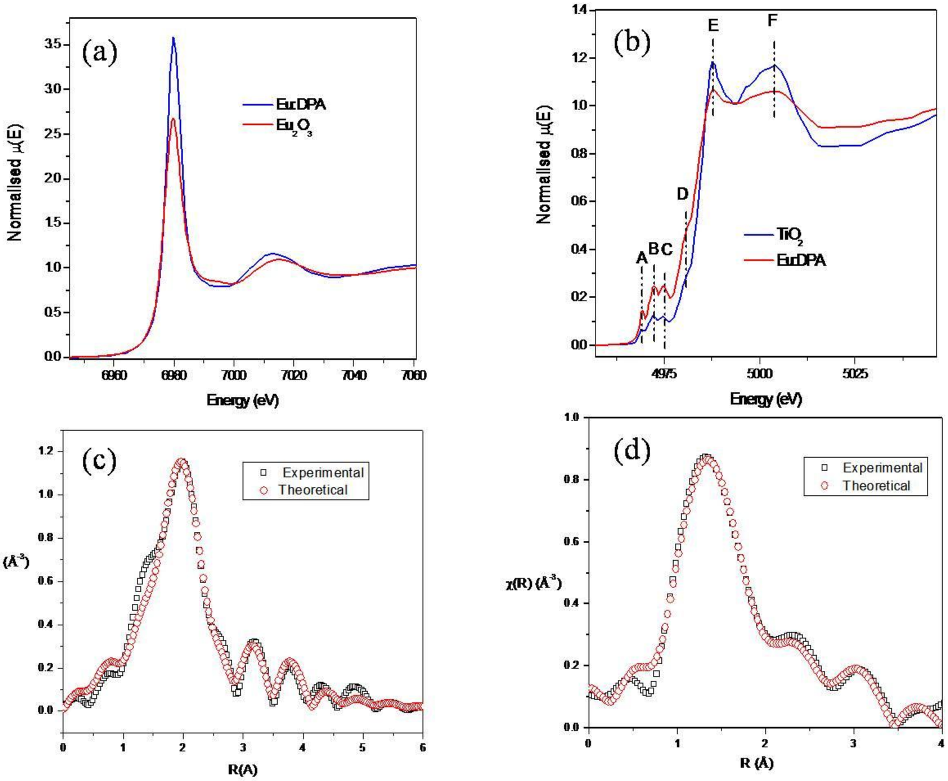

Figure 5.5 : (a) Normalised XANES spectra at Eu L3-edge for Eu-DPA-TiO_2 complex vis-a-vis Eu_2O_3; (b) Ti K-edge for Eu-DPA-TiO_2 complex vis-a-vis Eu_2O_3; (c) Fourier transformed EXAFS spectra at Eu L3-edge for Eu-DPA-TiO_2 complex (The experimental spectra are represented by scatter points and theoretical fit is represented by solid line); (d) Fourier transformed EXAFS spectra at Ti K-edge of Eu-DPA-TiO_2 complex (The experimental spectra are represented by scatter points and theoretical fit is represented by solid line)

Table 5.1: Bond length, coordination number and disorder factor obtain by EXAFS fitting at Ti K-edge and Eu L3 edge.

Ti K edge			Eu L3 edge		
Path	Parameters	Eu:DPA	Path	Parameters	Eu:DPA
Ti-O	R (Å)	1.88±0.02	Eu-O	R (Å)	2.19±0.01
	N	4.03±0.24		N	2.26±0.27
	σ^2	0.0036±0.0010		σ^2	0.0015±0.0010
Ti-Ti	R (Å)	2.83±0.03	Eu-O	R (Å)	2.39±0.02
	N	3.16±0.24		N	7.91±0.98
	σ^2	0.0014±0.0011		σ^2	0.0048±0.0017
Ti-Ti	R (Å)	3.58±0.03	Eu-N	R (Å)	3.01±0.04
	N	1.05±0.12		N	4.52±0.56
	σ^2	0.0014±0.0011		σ^2	0.0072±0.0013

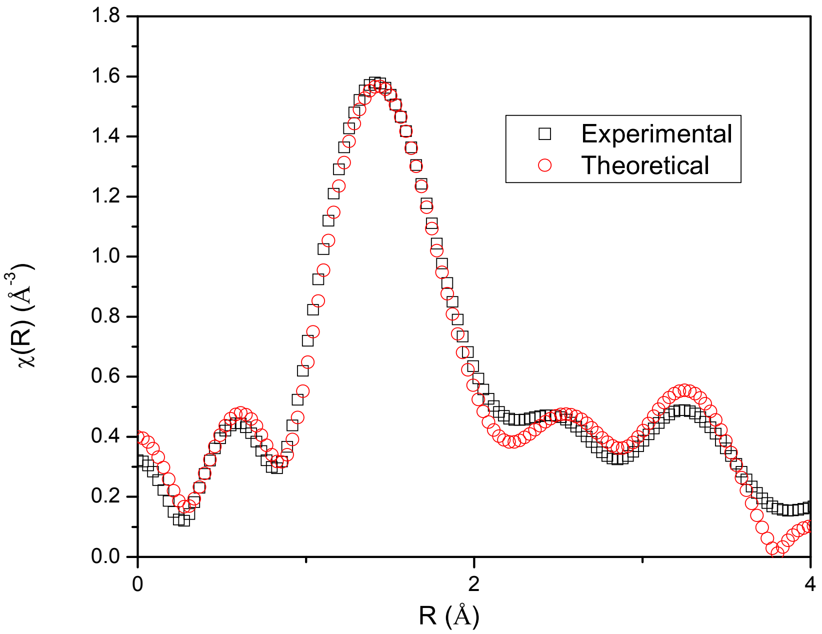

Figure 5.6: Fourier transformed EXAFS spectra at Ti K-edge of Anatase TiO_2

5.4 Sorption Studies

The extraction efficiency for Am^{3+}, Eu^{3+}, $UO_2{}^{2+}$ and Th^{4+} from various acidic aqueous feed were evaluated. 2 mL aqueous phase containing tracer of metal ion having acidity ranging from 0.01 M - 6 M HNO_3 was allowed to equilibrate for 2 h with 20 mg of sorbent material. It was then centrifuged for 2 min with 180 rpm to separate both the phases completely. Then suitable aliquots from aqueous phase were collected and used for estimation of the metal ions. ^{241}Am and $^{152/154}Eu$ isotopes were used for the experiment. 60 keV gamma of Am and 121 keV gamma of Eu has been chosen for their estimation by NaI (Tl) well type gamma counter. Sorption experiments were carried out for the elements separately. To limit the counting statistics as well as dead time of the detector, aliqouts were taken such a way that the counts were in the range of 10000-50000, as the partition coefficient for the metal ion can be expressed by following equation.

$$K_d = \frac{(c_0 - c_e)}{c_e}\frac{v}{w} \qquad (5.3)$$

where, c_0 and c_e are the concentration of metal ion before and after sorption repectively. v and w are represent the volume of aqueous phase and the weight of the sorbent, respectively.

Americium and Europium extraction by DPA functionalized TiO_2

5.4.1.1 Effect of Acidity

The extraction efficiency of Am^{3+} and Eu^{3+} were evaluated as a function of aqueous feed acidity in terms of K_d values (**Fig. 5.7)**. The K_d values for Eu^{3+} were found to exceed that of Am^{3+}. This can be attributed to the fact that lanthanides are harder acid compared to actinides based on Pearson hard-soft acid-base concept. The 5f orbitals of actinides are much more defused compared to the 4f orbitals of lanthanides. The ligating sites for the sorbent are basically from the carbonyl group of DPA and nitrogen atom of the pyridine ring, i.e. oxygen based hard base. Therefore, the ligating site would have preferential complexation ability for the lanthanides compared to the actinides. The K_d values were found to decrease with increase in feed acidity. A drastic reduction in K_d values were observed beyond 4 M HNO_3. At higher feed acidity there is a large availability of H^+ ion. These H^+ ions compete with the trivalent metal ions reflected in the lower K_d values. Amide moieties of the sorbent and the pyridine N atom are the coordinating sites for the metal ion. The sorption of the metal ion can be presented by the following equations.

$$R_2CONH + Eu^{3+}/Am^{3+} \overset{K_d}{\rightarrow} (R_2CONH)_nEu^{3+}/Am^{3+} \quad (5.4)$$

$$R_2CONH + H^+ \overset{K_H}{\rightarrow} (R_2CONH)_nH^+ \qquad (5.5)$$

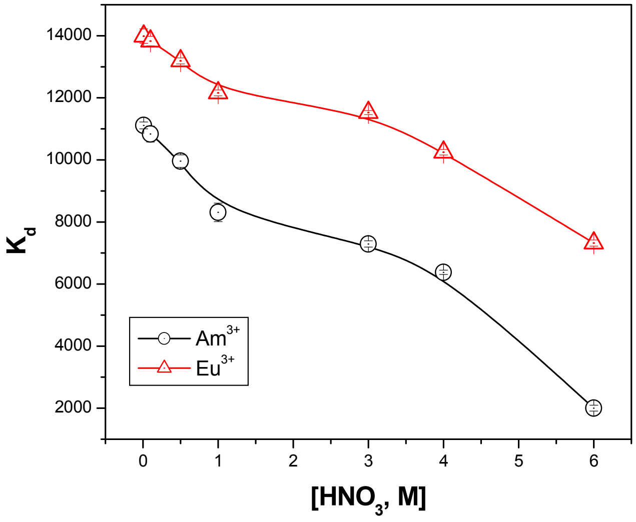

Figure 5.7: Effect of feed acidity on the sorption of Am^{3+} and Eu^{3+} by DPA-TiO$_2$; volume of aqueous solution: 2 mL, weight of the DPA-TiO$_2$-20 mg, time of equilibration- 2 h

5.4.1.2 Sorption kinetics

The sorption kinetics lends insights into the sorption phenomena. The following equation shows the fractional achievement of equilibrium (F).

$$F = \frac{c_t}{c_{t,e}} \qquad (5.6)$$

where, c_t and c_{te} are the concentration of metal ion in aqueous phase at time t and at equilibrium. The F value was found to decrease with increase in the time of equilibration. Eu^{3+} was found to reach equilibrium more drastically compared to Am^{3+} as seen from **Fig. 5. 8**. Based on the previous approach, different kinetics models were exploited using their linear equation. The model which yields regression coefficients closer to unity is likely to be the operative model. The following models were analyzed

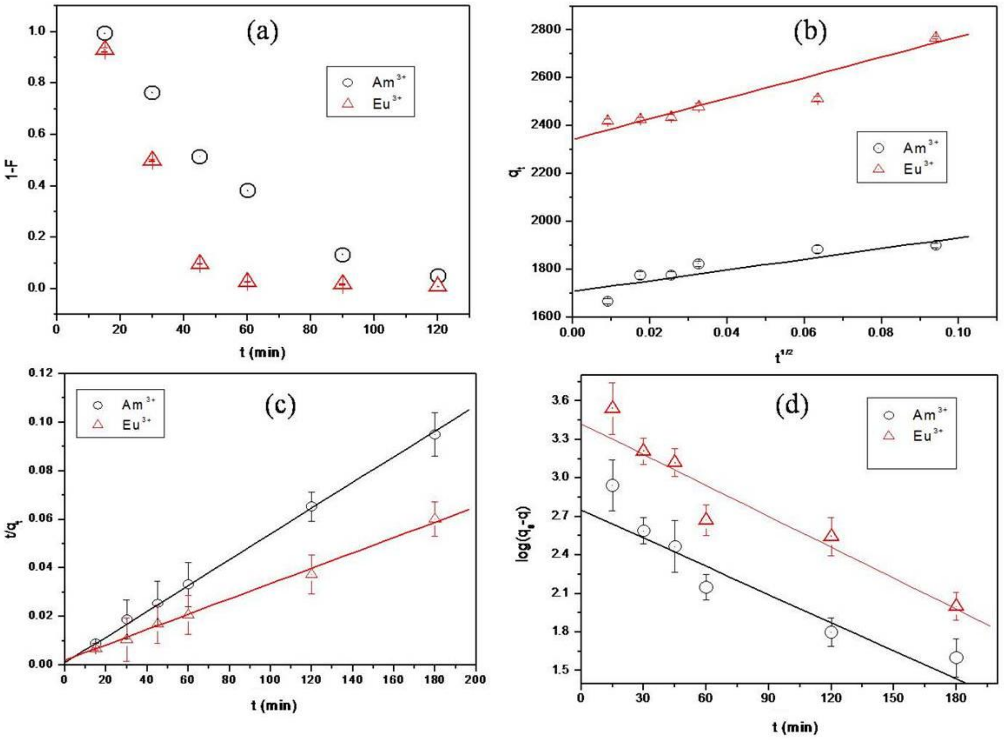

Figure 5.8: Analysis of sorption kinetics model for Am^{3+} and Eu^{3+} (a) The fraction of completion of sorption process by time; (b) Intra particle diffusion model; (c) Pseudo 2nd order kinetics model; (d) Lagergren first order reaction kinetics model. volume of aqueous solution: 2 mL, weight of the DPA-TiO_2 ~20 mg, time of equilibration- 2 h

Lagergren $first$ order: $lo\,g(q_e - q) = logq_e - \frac{k_L t}{2.303}$ (5.7)

Intra particle diffusion: $q = k_I\sqrt{t} + C$ (5.8)

Pseudo 2nd order: $\frac{t}{q} = \frac{1}{k_2 q_e^2} + \frac{t}{q_e}$ (5.9)

where, q_e and q are the metal ion adsorbed at equilibirum and at time t. k's are the rate constant correspond to the model. **Fig. 5.8** shows the analysis of the kinetics models for the sorption, whereas Table 5.2 is summarizing the analytical results. Based on the regression coefficient values, the sorption is predominantly proceeding via pseudo 2nd order kinetics.

The rate constants for Eu^{3+} and Am^{3+} were found to be 8.6 x $10^{-4}$and 6.1 x 10^{-4} mg/g/min, respectively.

Table 5.2: Analytical results for sorption kinetics using different models

Metal ion	Lagergren first order kinetics			Intra particle diffusion			Pseudo 2^{nd} order kinetics		
	q_e	k_{ads}	R^2	k_p mg g^{-1} min^{-1}	C	R^2	q_e mg g^{-1}	k_2 mg $g^{-1}min^{-1}$	R^2
Am	15	0.03	0.904	31	19	0.955	71	6.1E-04	0.999
Eu	19	0.04	0.935	39	31	0. 943	97	8.6E-04	0.999

5.4.1.3 Adsorption isotherm

The sorption data was fitted for the Langmuir isotherm, Dubinin-Radushkevich isotherm, Freundlich isotherm and Tempkin isotherm. **Fig. 5.9** shows the analysis of different isotherm models for the present system, while Table 5.3 summarizes the results. Regression analysis shows the adsorption mechanism to be predominantly of the Langmuir type. This analysis also revealed that the theoretical capacity of the sorbent for Am^{3+} and Eu^{3+} is 67 mg/g and 93 mg/g, respectively. This is due to the higher sorption energy for Eu^{3+} (16.8 kJ/mol) compared to Am^{3+} (11.3 kJ/mol) as obtained from D-R isotherm analysis. The sorption energy values also indicate the sorption as chemisorption indicating the chemical interaction between the f block elements and the carboxylic acid groups from the sorbent. The 'n' values evaluated from Freundlich isotherm indicate simple rather than cooperative sorption.

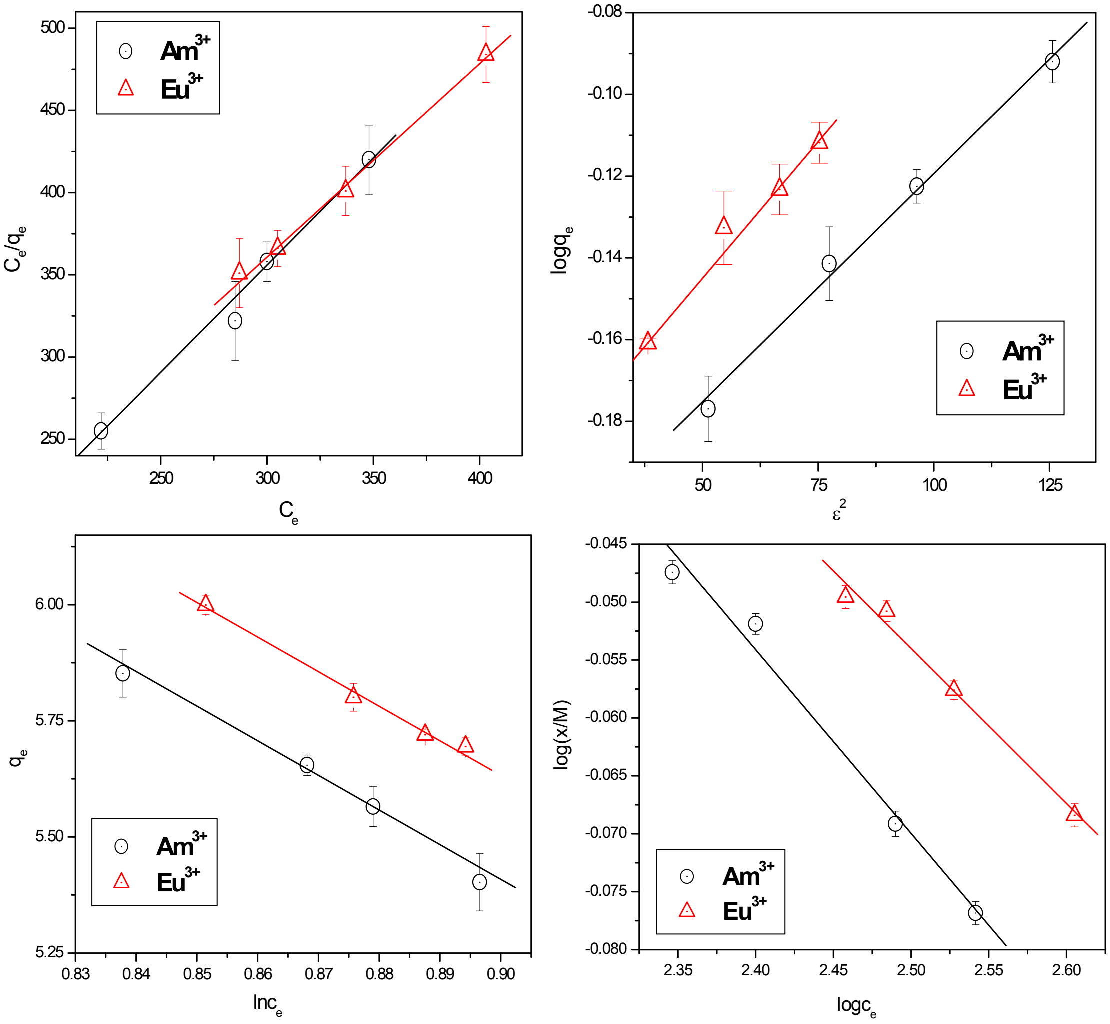

Figure 5.9: Different isotherm model for understanding the sorption of Am^{3+} and Eu^{3+}(a) Variation of C_e/q_e with C_e for Langmuir isotherm; (b) Variation of $\log q_e$ with ε^2 for D.R. isotherm; (c) Variation of q_e with $\ln C_e$ for Tempkin isotherm; (d) Variation of $\log q_e$ with $\log C_e$ for Fruendlich isotherm

Table 5.3: Analytical results obtained by using Langmuir, D-R, Freundlich and Tempkin isotherm

Metal ion	Langmuir			Dubinin-Radushkevich			Freundlich			Tempkin		
	q_e (mg/g)	b (l/mol)	R^2	x_m (mg/g)	E (kJ/mol)	R^2	K_f (mg/g)	n	R^2	A_T (L/mg)	b	R^2
Am	67	0.03	0.999	71	11.3	0.987	66	11	0.968	15	37	0.955
Eu	93	0.04	0.999	89	16.8	0.992	98	10	0.966	13	39	0.932

Uranium and Thorium extraction by DPA functionalized TiO_2

5.4.1.4 Effect of Acidity

The efficiency of extraction for UO_2^{2+} and Th^{4+} were measured as a function of feed acidity in terms of K_d values (**Fig. 5.10)**. The distribution coefficient values for Th^{4+} were found to exceed that of UO_2^{2+}. This result can be explained as the fact that the higher effective charge of Thorium compared to Uranium leds to more electrostatic interaction with the DPA ligand. The ligating sites for the sorbent are basically from the carbonyl group of DPA and nitrogen atom of the pyridine ring. The K_d values were found to increasee with decrease in feed acidity. There were a drastic reduction in K_d values beyond 1 M HNO_3. This can be explained as higher feed acidity there is a large availability of proton these proton compete with the trivalent metal ions resulting in the lower K_d values for metal ions.

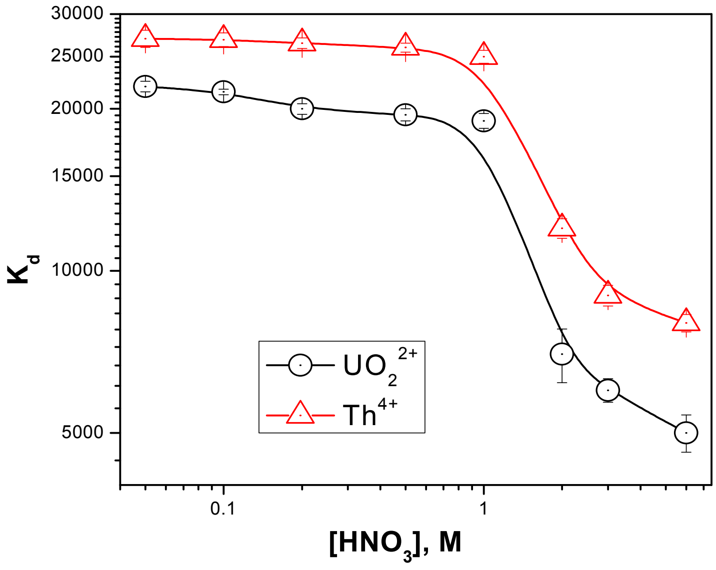

Figure 5.10: Effect of feed acidity on the sorption of UO_2^{2+} and Th^{4+} by DPA-TiO_2; volume of aqueous solution: 2 mL, weight of the DPA-TiO_2-20 mg, time of equilibration- 2 h

5.4.1.5 Optimization of contact time

In order to optimize the required time for equilibration, experiments were conducted for Uranium and Thorium uptake at 0.5 M acidity using sorbent dose of 10 mg mL^{-1} **Fig. 5.11** shows that the sorption of both the metal ions increase with contact time upto 60 mins and thereafter it becomes almost constant. To ensure maximum uranium uptake, contact time for all the batch experiments were fixed at 2 hour. The fractional achievement of equilibrium (F) was expressed as follows

$$F = \frac{c_t}{c_{t,e}} \qquad (5.10)$$

where, c_t and c_{te} are the concentration of metal ion in aqueous phase at time t and at equilibrium. The F value was found to decrease with increase in the time of equilibration.

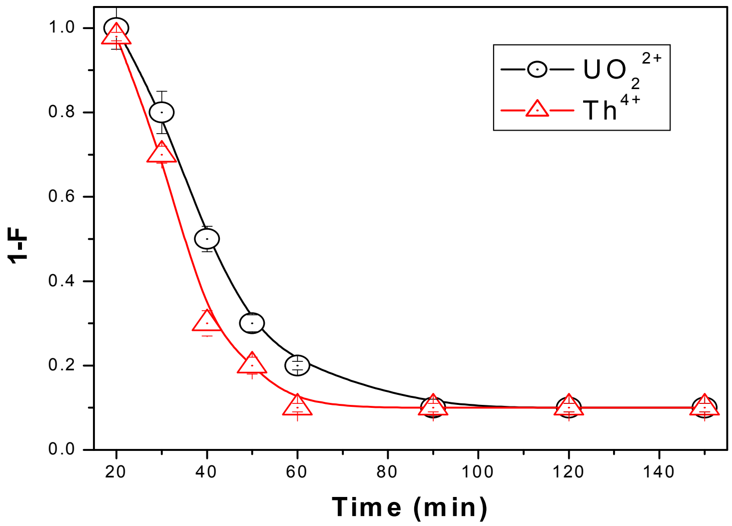

Figure 5.11: Analysis of sorption time on the equilibrium sorption capacity of DPA-TiO_2 for UO_2^{2+} and Th^{4+}, feed solution acidity 0.5 M, weight of DPA- TiO_2 ~ 20 mg, volume of aqueous solution- 2 mL

5.4.1.6 Sorption kinetics

Kinetics of the sorption process using DPA functionalized TiO_2 were studied for U and Th. Most frequently, three different kinetic models: Lagergren's first order model, Pseudo second order model and Intra particle diffusion model have been considered for elucidating the sorption mechanism. **Fig. 5.12** shows the analysis of the kinetics models for the sorption, whereas Table 5.4 is summarizing the analytical results. Based on the regression coefficient values, the sorption is predominantly proceeding via pseudo 2nd order kinetics. The rate constants for UO_2^{2+} and Th^{4+} were found to be 5.9 x $10^{-4}$and 8.2 x 10^{-4}mg/g/min, respectively.

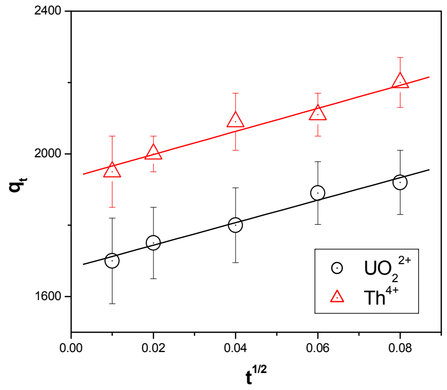

(a)

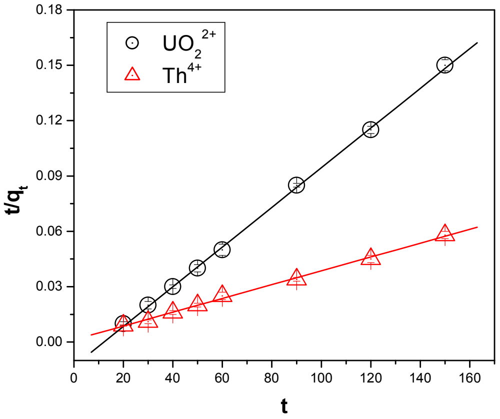

(b)

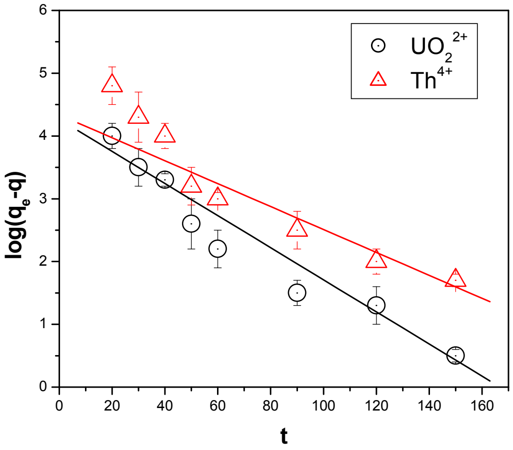

(c)

Figure 5.12: Analysis of sorption kinetics model for UO_2^{2+} and Th^{4+}, (a) analysis of intra particle diffusion model (b); analysis of Pseudo 2nd order kinetics model; (c) analysis of Lagergren first order reaction kinetics model. volume of aqueous solution: 2 mL, weight of the DPA-TiO_2 ~20 mg, time of equilibration- 2 h

Table 5.4: Analytical results for sorption kinetics using different models

Metal ion	Lagergren first order kinetics			Intra particle diffusion			Pseudo 2^{nd} order kinetics		
	q_e mg g^{-1}	k_{ads}	R^2	k_p mg g^{-1} min^{-1}	C	R^2	q_e mg g^{-1}	k_2 mg g^{-1} min^{-1}	R^2
U	21	0.05	0.817	42	22	0.949	91	5.9E-04	0.997
Th	24	0.06	0.866	47	27	0. 958	97	8.2E-04	0.995

5.4.1.7 Sorption isotherm

The Uranium and Thorium sorption on DPA-TiO_2 are plotted and fitted in both the Freundlich, Langmuir , D-R isotherm and Temkin adsorption isotherms models. **Fig. 5.13** shows the analysis of different isotherm models for the present system, while Table 5.5 summarizes the results. The regression analysis clearly indicates the predominance of Langmuir isotherm due to the closeness of R^2 values to the unity. This analysis also revealed that the theoretical capacity of the sorbent for UO_2^{2+} and Th^{4+} is 111 mg/g and 125 mg/g, respectively. The sorption energy values indicate the sorption as chemisorption process. The 'n' values evaluated from Freundlich isotherm indicate simple rather than cooperative sorption..

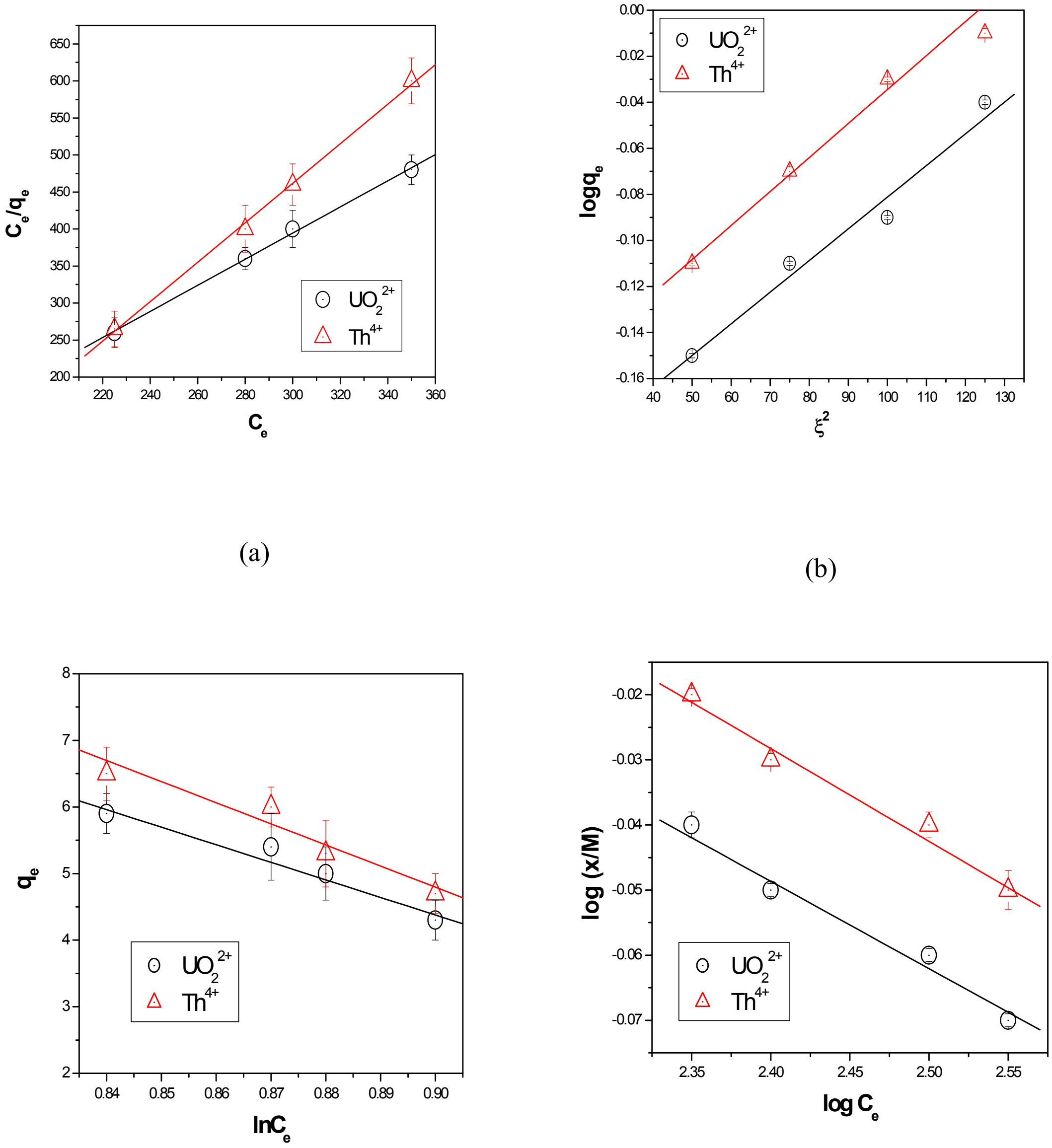

(a)

(b)

(c)

(d)

Figure 5.13: Different isotherm model for understanding the sorption ofUO_2^{2+} and Th $^{4+}$ (a) Variation of C_e/q_e with C_e for Langmuir isotherm; (b) Variation of $\log q_e$ with ε^2 for D.R. isotherm; (c) Variation of q_e with $\ln C_e$ for Tempkin isotherm; (d) Variation of $\log q_e$ with $\log C_e$ for Fruendlich isotherm

Table 5.5**:** Analytical results obtained by using Langmuir, D-R, Freundlich and Tempkin isotherm

Metal ion	Langmuir			Dubinin-Radushkevich			Freundlich			Tempkin		
	q_e (mg/g)	b (l/mol)	R^2	x_m (mg/g)	E (kJ/mol)	R^2	K_f (mg/g)	n	R^2	A_T (L/mg)	b	R^2
U	111	0.07	0.997	107	17.9	0.937	101	8	0.957	19	41	0.971
Th	125	0.09	0.996	131	22.7	0.942	128	15	0.962	23	45	0.969

Americium and Europium extraction by DGA functionalized TiO_2

5.4.1.8 Effect of pH

The sorption of Am(III) and Eu(III) metal ions by DGA functionalized TiO_2 is strongly dependent on the pH of the aqueous feed solution. The variation in the distribution coefficient of Am(III) and Eu(III) as a function of nitric acid concentration is shown in **Fig. 5.14**. It is observed that the distribution coefficient of both Eu(III) and Am(III) decreases with increase in the concentration of nitric acid. This is mainly due to the formation of different species by Am(III) at different pH medium includes $Am^{3+}aq$ (major species up to pH 6), $Am(OH)^{2+}$ (mostly formed from pH 6–8) , $Am(OH)_2^+$ (predominant species above pH 8 up to pH 12), with little contribution from $Am(OH)_3(aq)$ above pH 11. So with the increase of pH of the feed solution the negative surface charge of functionalized TiO_2 leads to increase in sorption efficiency of Am(III), present as positively charged species.

Because of the nearly similar chemical behaviour of Eu^{3+} it can be considered as a homolog of trivalent actinides, which results in very similar physical and chemical properties. $^{152+154}$Eu is an important fission product in nuclear waste and is a threat to the environment. At pH < 5, Eu exists in an aqueous medium as Eu^{3+} , $Eu(OH)^{2+}$ (mostly formed from pH 6–8), $Eu(OH)_2^+$(predominant species above pH 8 up to pH 12) , $Eu(OH)_3$ above pH11. Hence the trend of Eu(III) sorption with increasing pH was identical with that of Am(III).

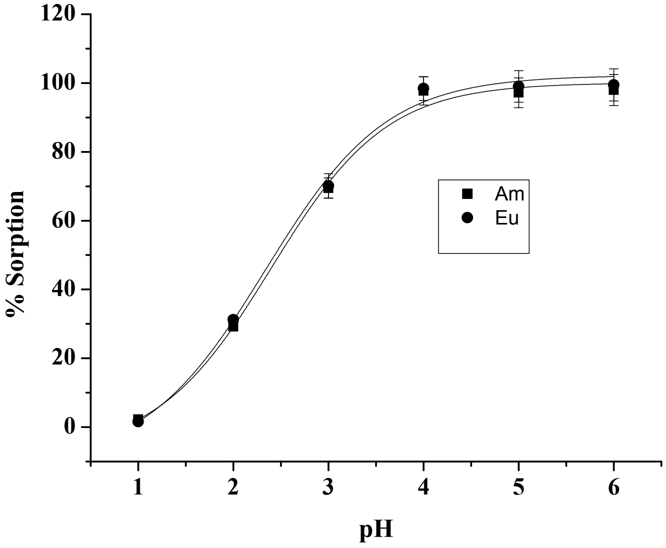

Figure 5.14: Effect of feed pH on the sorption of Am^{3+} and Eu^{3+} by DGA-TiO_2; volume of aqueous solution: 2 mL, weight of the DGA-TiO_2-20 mg, time of equilibration- 1h

5.4.1.9 Sorption kinetics

Kinetics of the sorption process using DGA functionalized TiO_2 was studied for both ^{241}Am, $^{152+154}$Eu. For both the radionuclides, rapid sorption is observed in the initial stages of equilibration followed by the establishment of equilibrium occurring within 30 min and hence in further experiments the contact time was kept for 1 h to achieve complete equilibrium. Generally, it is described that at the initial stages there are vacant surface sites available for sorption hence the sorption increases quickly. However, at the later stages the remaining vacant surface sites are difficult to occupy due to the repulsion from the sorbate molecules. Attempts were made to model the kinetic data with two different models i.e. Lagergren's first order model, and Pseudo second order model for both ^{241}Am and $^{152+154}$Eu and the result are shown in Table 5.6. The corresponding linear regression coefficient (R^2) values for the linear curves of log (q_e–q) vs. t and t/$q_t$vs. t for both the metal ions showed that that sorption process follows the pseudo 2nd order kinetics model.

Table 5.6 : Analytical results for sorption kinetics using different models

Radionuclides	Pseudo second order kinetics			Pseudo first order kinetics
	q_e (mg/g)	K_2 (g/(mg min)	R^2	R^2
Eu (III)	33.56	0.007	0.991	0.942
Am (III)	30.33	0.004	0.987	0.954

5.4.1.10 Sorption Isotherm

Isotherm studies were carried out for DGA functionalized TiO_2 using Eu at pH 5 shown in (**Fig. 5.15**). Initially, the amount of metal sorption increased quickly with increasing metal concentration in the solution and then plateaus. The experimental data were plotted using two most commonly used isotherms, i.e. Langmuir and Freundlich isothermmodel are given in Table 5.7. The linear plots for Langmuir and Freundlich isotherms shows that Langmuir isotherm model fits the experimental data better than the Freundlich model. Maximum sorption capacities of DGA functionalized TiO_2 for Eu(III) was observed to be 34.2 mg/g. Thus the sorption of Eu(III) on the DGA functionalized

TiO_2 limited by the availability of the ligand complexing sites due to saturation effect according to Langmuir model and it is also proved that there is no multilayer sorption of Eu(III).

Table 5.7 :Different isotherm constants and corresponding R^2 values for the sorption of Eu(III) by DGA-TiO_2

Radionuclide	Langmuir isotherm			Freundlich isotherm		
	q max (mg g-1)	B ($Lmmol^{-1}$)	R^2	k_f ($mmol^{1-n}L^n$ g^{-1})	n	R^2
Eu(III)	34.2	2.86	0.993	-1.13	4.8	0.957

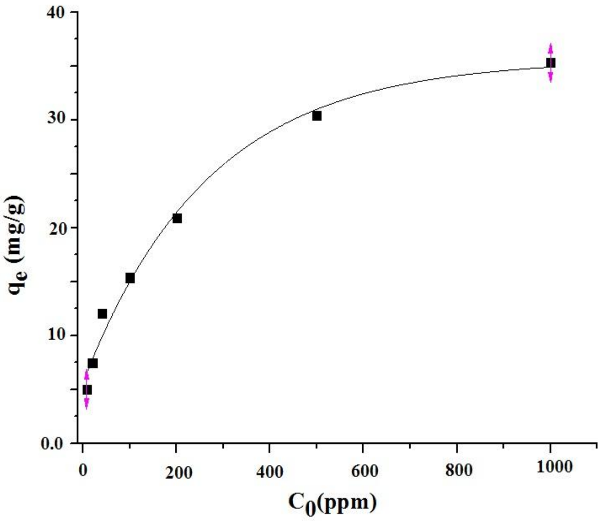

Figure 5.15: Effect of initial concentration of Eu (III) for sorption by DGA – TiO_2

5.4.1.11 Desorption and Reusability

Am(III) and Eu(III) was desorbed from loaded DGA functionalized TiO_2 using different desorbing agents such as 1 M HNO_3solution, 0.1 M oxalic acid solution and 0.05 M DTPA in 0.1 M HNO_3 shown in Table 5.8. It was observed that quantitative desorption of the radionuclides is possible in two contacts. There were no change in the sorption efficiency for the radionuclides by the functionalized TiO_2 for successive five cycles of operation

Table 5.8: Percentage desorption of Am (III) from DGA-TiO_2

Desorbing Agent	**Desorption (%)**
1 M HNO_3	96.8
0.05 M DTPA in 0.1 M HNO_3	99.2
0.1 M Oxalic Acid	95.3

5.5 Radiolytic Stability of the Sorbent

Processing actinides results in high radiolytic exposure to the sorbent and the energy deposited into the sorbent by radiations can lead to bond breakage and a reduction in efficiency. The ideal sorbent should show high stability in presence of drastic radiological as well as chemical environments. In view of these, the sorbent was exposed to various gamma dose and with the irradiated functionalized sorbent, the K_d values were measured. There was a decreasing trend in distribution coefficient values with irradiation dose. However, the radiation effects were not so much drastic and hence, the sorbent is concluded to have significant radiolytic stability. **Fig. 5.16** depicts the K_d values for UO_2^{2+}, Th^{4+}, Am^{3+} and Eu^{3+} using sorbent irradiated with different gamma dose.

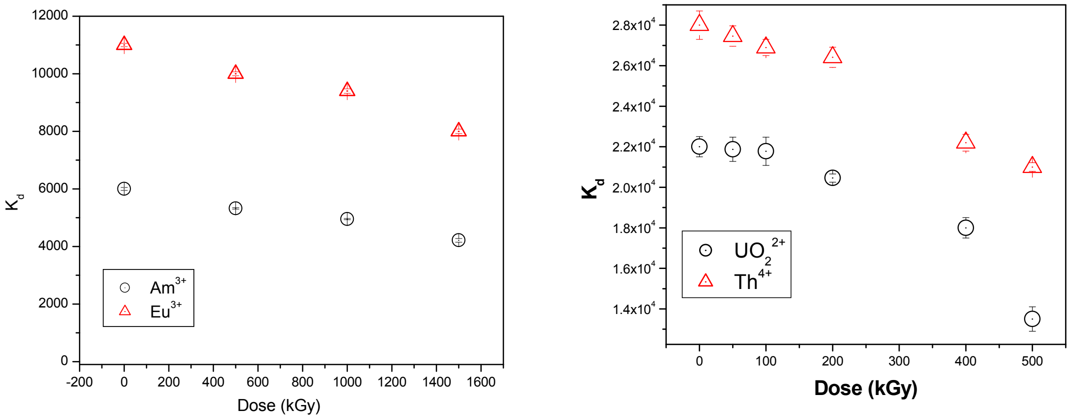

Figure 5.16: Radiolytic stability of the sorbent

5.6 *Summary of the Investigation*

Based on the study reported in this chapter following conclusion have been summarized. Dipicolinic acid functionalized TiO_2 through an amino ethoxysilane bridge was synthesized, characterized and evaluated for extraction of f – elements. DPA functionalized anatase efficiently sorp actinides and $Eu^{3+}$from aqueous acidic medium through chemical interaction.The ligating sites from DPA moieties being a hard base showed preferential complexation with trivalent lanthanide (Eu) compared to trivalent actinide (Am) and tetra valent actinide (Th) over hexa valent actinide (U). The Langmuir isotherm and pseudo 2nd order kinetics models were found to be predominately operative. The maximum sorption capacity for Am (III) and Eu(III) were found to be 67 mg g^{-1} and 93 mg g^{-1}, where as for U(VI) and Th (IV) it 111 mg g^{-1} and 125 mg g^{-1} respectively. The complexation of $Eu^{3+}$with this DPA functionalized TiO_2sorbent was experimentally investigated using EXAFS, XANES and XPS. The Gibbs free energy of complexation measured by DFT study validate the experimental observation.

Diglycolamide (DGA) was functionalized on the surface of titania by two step chemical reaction. The synthesized material used for the extraction of Am(III) and Eu(III) from nuclear waste solution. The sorption of Am(III) and Eu(III) metal ions by DGA functionalized TiO_2 is dependent on the pH of the aqueous feed solution. The kinetics of sorption for both the radionuclides by the DGA –TiO_2 is found to follow pseudo second order kinetics with equilibrium attained in ~ 30 min. The maximum sorption capacity for Eu(III) was found to be approx. 34 mg g^{-1} . The DFT calculated solvent phase free energy of adsorption for Am^{3+} ion was lower than Eu^{3+} ion as observed in the experiments (Details of DFT calculation is discussed in Chapter 6). The material shows good recylalable property.

Chapter 6: Studies of Metal Ligand Complexation Using Density Functional Theory

Chapter 6

Studies of Metal Ligand Complexation Using Density Functional Theory

The successful development of novel materials, fuels, and processes can be achieved with a strong fundamental understanding of the underlying physics and chemistry of materials. In order to identify a new ligand or alter existing ones, understanding the nature of ion-ligand interactions along with the structural parameters, binding energies, and solvent effect would be of immense utility. In this context, computational chemistry provides useful insights at the molecular level and is viewed as a complementary technique to experiment; while also guiding experiments in certain cases.

A variety of computational methods have been discussed in the literature ranging from semi-empirical to ab-initio. Each method has advantages and limitations in terms of cost, time, accuracy and usefulness for a particular application. For initial screening of the molecular system of interest, semi-empirical methods can be handy. Although the Hartree-Fock (HF) method is considered to be the cheapest among ab initio methods, its inability to capture the electron correlation limits its applicability. The Moller-Plesset (MP_n) and Couple-Cluster-Singlet-Double (CCSD) methods are reasonably accurate but rather expensive as only small molecular system can be tackled. Density functional theory (DFT) is the most popular electronic structure calculation method for large molecular system with affordable accuracy. Further, one can select the density functional from a wide variety of DFT functional for a specific interest of application. The accuracy of any computational methods also depends on the size and type of the selected basis set. The size and type of the basis set can be considered as per the desired molecular properties to be determined. Choice always involves a balance between accuracy and computational cost. Therefore there is an inevitable tradeoff between the functional and size of the basis set depending on the molecular size and chemical properties.

Further, for heavy elements, the scalar relativistic effective core potentials (ECP) are used to take care of relativistic effect. Furthermore, the majority of the quantum electronic structure calculations are performed in the gas phase. Since, most of the chemical process happens to occur in solution phase, it is imperative to include the solute-solvent interactions in quantum electronic structure calculations. The solute-solvent interactions can be incorporated either explicitly or implicitly.

In the explicit scheme, huge number of solvent molecules are placed surrounding solute molecules which requires electronic relaxation as well as geometry relaxation of the complete solute-solvent system. This explicit solvation approach is rather time consuming and thus impractical. In implicit model, the solvent is replaced with continuum which simulates the electro static conduction of the solvent. Among many, conductor like screening model (COSMO) is the most popular which uses scaled-conductor approximation to derive the polarization charges of the continuum, caused by the polarity of the solute. Knowing the electric charge on the molecule, the charge q* on the surface segments can be calculated.

In the present thesis, density functional theory (DFT) based methods using the localized basis sets are adopted for all the calculations. We have used several exchange-correlation energy functionals, such as generalized gradient approximation (GGA), Hybrid and meta-hybrid functional. The individual computational methods used will be discussed in the respective chapters under the subsection computational details. The theoretical basis for all the methods used throughout the thesis is outlined here.

6.1 Schrodinger Wave equation

The well-known time-independent Schrodinger equation of a system of N nuclei with N electrons can be expressed as

$$H\Psi(x_1,x_2,\ldots,x_N; R_1,\ldots,R_{Nn}) = E\ \Psi(x_1,x_2,\ldots,x_N; R_1,\ldots,R_{Nn}) \tag{6.1}$$

Where $x_1,x_2,\ldots,x_N$ correspond to the spin and cartesian coordinates and $R_1,\ldots,R_{Nn}$ represent the nuclear coordinates of the Nn nuclei. The Hamiltonian operator is written as,

$$H = -\frac{\hbar^2}{2m_e}\sum_{\mu=1}^{N_e}\nabla_\mu^2 - \frac{\hbar^2}{2}\sum_{k=1}^{N_n}\frac{\nabla_k^2}{m_k} - \sum_{\mu=1}^{N_e}\sum_{k=1}^{N_n}\frac{Z_k e^2}{4\pi\varepsilon_0 |\vec{r}_\mu - \vec{R}_k|} + \sum_{\mu=1}^{N_e}\sum_{\nu>\mu}^{N_e}\frac{e^2}{4\pi\varepsilon_0 |\vec{r}_\mu - \vec{r}_\nu|} + \sum_{j=1}^{N_n}\sum_{k>j}^{N_n}\frac{Z_k Z_j e^2}{4\pi\varepsilon_0 |\vec{R}_j - \vec{R}_k|} \tag{6.2}$$

In principle, the time-independent Schrodinger equation can be applied to any system of interest and can be solved exactly. However, this is limited in real world problems by computation cost, driven by a large number of variables for larger systems. Hence, certain approximations are imposed to make many body problems more tractable.

6.2 Born-Oppenheimer Approximation

The large difference in mass and velocity between electrons and a heavy nuclei is exploited for one such approximations, where the exact wave function Ψ(r,R) can be approximated as a product of an electron and a nuclear part. This splitting of the wave function into nuclear and electronic components is popularly known as the Born-Oppenheimer approximation.

$$\Psi_{tot}(x,R) = \Psi_{elec}(x,R)\ X\ \Psi_{nuc}(R) \tag{6.3}$$

Because of the large difference in their masses, the electrons can be approximated as if they are moving in the field of fixed nuclei. The electronic Hamiltonian for fixed nuclear coordinates can be expressed as:

$$H = -\frac{\hbar^2}{2m_e}\sum_{\mu=1}^{N_e}\nabla_\mu^2 - \sum_{\mu=1}^{N_e}\sum_{k=1}^{N_n}\frac{Z_k e^2}{4\pi\varepsilon_0 |\vec{r}_\mu - \vec{R}_k|} + \sum_{\mu=1}^{N_e}\sum_{\nu>\mu}^{N_e}\frac{e^2}{4\pi\varepsilon_0 |\vec{r}_\mu - \vec{r}_\nu|} \qquad (6.4)$$

This indicates that the electronic wave function depends only on the electronic coordinates and does not explicitly depend on nuclear coordinates. In turn, the electronic Schrödinger equation can then solved be as

$$H\,\Psi_{elec} = E_{elec}\Psi_{elec} \qquad (6.5)$$

However, it should be kept in mind that the electronic energy E_{elec} represents only one component of the total energy of the electronic system, which is given by sum of electronic energy, nuclear repulsion energy and the nuclear kinetic energy.

$$E_{tot} = E_{elec} + E_{nuc} \qquad (6.6)$$

6.3 Variational Principle

Once the wave function is constructed, all the quantum observable properties of the system can be determined by calculating the expectation values of the corresponding operators. However, in practice, the electronic Schrödinger equation cannot be solved exactly for the many-electron atomic and molecular systems of practical importance. The approximated solution of Schrodinger equation can be obtained by employing the variational principle to estimate the energy of the ground state eigenfunction ψ_0. According to the variational principle, the expectation value (E) of the Hamiltonian operator using any trial wave function (t_{trial}) is always greater than or equal to the true ground state energy (E_0). The trial function depends on some variational parameters.

where, $E = \frac{\langle \psi_{trail} | H | \psi_{trail} \rangle}{\langle \psi_{trail} | \psi_{trail} \rangle}$ (6.7)

6.4 The Hartree-Fock Method

Solving the Schrodinger equation for an N electrons system is a computationally challenging task because of the electron-electron repulsion terms. Hartree developed the so called self-consistent field (SCF) procedure which was further improved by incorporating the electron exchange by Fock and Slater. The Hartree or the Hartree-Fock method introduces one-electron orbitals in terms of which the wave function is expressed as a simple product or a determinant respectively.

$$\Psi_{HF} = \frac{1}{\sqrt{N!}} \begin{vmatrix} \chi_1(x_1) & \chi_2(x_1) & . & . & \chi_N(x_1) \\ \chi_1(x_2) & . & . & . & \chi_N(x_2) \\ . & . & . & . & . \\ . & . & . & . & . \\ \chi_1(x_N) & . & . & . & \chi_N(x_N) \end{vmatrix} \tag{6.8}$$

The Variational Principle allows an approximate solution to the Schrodinger equation: $E = <\Psi|H|\Psi> \geq E_0$. Hartree-Fock wavefunction then substituted into the expectation value generates

$$E_{HF} = <\Psi_{HF} |H| \Psi_{HF}> \tag{6.9}$$

$$= \sum_{\mu=1}^{N} < \chi_\mu | h_\mu | \chi_\mu > + \frac{1}{2} \sum_{\mu=1}^{N} \sum_{\nu=1}^{N} [< \chi_\mu \chi_\nu | \frac{1}{r_{12}} | \chi_\mu \chi_\nu > - < \chi_\mu \chi_\nu | \frac{1}{r_{12}} | \chi_\nu \chi_\mu >] + Vnn \tag{6.10}$$

Where, the $h_\mu = -\frac{1}{2}\nabla_\mu^2 - \sum_{k=1}^{N_n} \frac{Z_k}{r_{\mu k}}$ is a one electron operator. The double integrals are the Coulomb and Exchange integrals, respectively. Anti-symmetry requirement makes the Exchange integral appear. The variational principle yields the integro-differential equation that the spin-orbitals must satisfy:

$$\{h_\mu + V_{HF}(x_\mu)\}\chi_\mu = \varepsilon_\mu \chi_\mu \tag{6.11}$$

$$V_{HF}(x_\mu) = \sum_{\nu=1}^{N}[J_\nu(x_\mu) - K_\nu(x_\mu)] \tag{6.12}$$

$$J_\nu(x_1) = \int |\chi_\nu(x_2)|^2 \frac{dx_2}{r_{12}} \tag{6.13}$$

$$K_\nu(x_1)\chi_\mu(x_1) = [\int \chi_\nu(x_2)^* \chi_\mu(x_2)\frac{dx_2}{r_{12}}]\chi_\nu(x_1) \tag{6.14}$$

The effective Hartree-Fock potential V_{HF} is an operator containing both a Coulomb (J) and a non-local Exchange operator (K). This is then added over all electrons. In reality, HF spin-orbitals are expanded in a basis set and the Variational problem simplifies into finding the optimum values of the expansion coefficients. The resulting practical equations are the Roothaan-Hartree-Fock equations.

The Hartree-Fock method satisfies the exchange requirements perfectly, but accounts poorly for electron correlation effects. The HF energy is always greater than the true ground state non-relativistic energy and the difference between the two is the correlation energy. To obtain chemical accuracy, post-Hartree-Fock methods must such as Moller-Plesset perturbation theory, Configuration Interaction, or Coupled Cluster methods are often used.

6.5 Density Functional Theory

The main idea of DFT is to replace the much complicated N-electron wave function and the associated Schrodinger equation with the simple electron density ρ (r). The Thomas-Fermi model is a quantum statistical model which assumes that the electrons are uniformly distributed over the six-dimensional phase space.

Thomas and Fermi (1927) computed the kinetic energy, and Dirac (1930) computed the Exchange correlation energy and the overall energy formula in terms of electron density as follows:

$$E_{TF}[\rho] = C_F \int \rho^{5/3}(\vec{r})d\vec{r} - Z\int \frac{\rho(\vec{r})}{r}d\vec{r} + \frac{1}{2}\iint \frac{\rho(\vec{r}_1)\rho(\vec{r}_2)}{r_{12}}d\vec{r}_1 d\vec{r}_2 + C_X \int \rho^{4/3}(\vec{r})d\vec{r} \qquad (6.15)$$

A large number of modifications have been proposed to improve the Thomas-Fermi model. However, none of them could predict the bonding in molecules. Further, the accuracy in atomic systems is very poor and thus the methods are of not much practical importance. An important breakthrough in density based theory came after the work of Hohenberg and Kohn (H-K) in 1964.

The electron density, for any molecular system, is a function of only three spatial coordinates. The first H-K theorem states that the ground state energy of an N-electron system in an external potential v(r) is a unique functional of its ground state electron density ρ(r) .

$$\rho(\mathbf{r}_1) = N \int |\Psi(\vec{x}_1, \vec{x}_2, .., \vec{x}_N; \vec{R}_1, .., \vec{R}_{Nn})|^2 \, d\sigma_1 d\vec{x}_2 .. d\vec{x}_N \qquad (6.16)$$

The integral of the density over all space equals N. The total energy can be written as

$$E[\rho] = T[\rho] + V_{ee}[\rho] + \int \rho(\vec{r})V(\vec{r})d\vec{r} \qquad (6.17)$$

In 1965, Kohn and Sham invented an indirect way of calculating the kinetic energy functional thereby making the DFT method an efficient tool for carrying out rigorous calculations. The reference system of fictitious non-interacting particles has a rigorous solution in terms of single electron wave functions, or molecular orbitals. These are called the Kohn-Sham orbitals. Thus, we can express the kinetic energy exactly for the reference system as the sum of the expectation value of the Laplacian for each "electron".

$$T_S[\rho_S] = -\frac{1}{2}\sum_{j=1}^{N} < \chi_j \,|\nabla_j^2|\, \chi_j > \qquad (6.18)$$

Provided that the density of the real system,ρ = ρ_S = $\sum_{j=1}^{N}\sum_{\sigma} \,|\chi_j(\vec{r},\sigma)|^2$. Then, the energy functional is written as:

$$E[\rho] = T_S[\rho] + J[\rho] + V_{nn}[\rho] + Exc[\rho] \qquad (6.19)$$

Where all the unknown pieces are collected into the Exchange Correlation energy,

$$Exc[\rho] = T[\rho] - T_S[\rho] + E_{ee}[\rho] - J[\rho]. \qquad (6.20)$$

The main challenge in implementing DFT is to find a good approximation to the exchange-correlation energy functional Exc[ρ]. There are various approximations to calculate Exc[ρ], such as Local Density Approximation (LDA), Local Spin density Approximation (LSDA), Generalized Gradient Approximation (GGA) and many other hybrid functionals.

This approach can be used to elucidate the type of complexation with applications for actinide extraction, which is the utility of DFT in this thesis. Actinide Partitioning', considered a vital step in the proposed HLLW management. It requires the selective sequestration of minor actinides from a mixture of of fission and activation products. Several methods of separation such as TRUEX, TRPO,DIDPA, DIAMEX have been developed for this purpose.Recently, a new class of extractant, namely, diglycolamide has been developed which shows many advantages over other extractants due to the ease of synthesis, milder stripping condition and complete incinerability.

Among variousdiglycolamide, N, N, N′, N′-tetraoctyldiglycolamide (TODGA) and N, N, N′, N′-tetra-2-ethylhexyl diglycolamide (T2EHDGA) have been extensively studied for the removal of actinides and lanthanides from nuclear waste. There are many experimental studies available for the complexation and extraction of actinides with diglycolamide extractant [51, 127, 192,193] but theoretical studies [194,195] are rather limited, which can elucidate the type of complexation of actinides in different oxidation state through molecular level understanding and hence can assist in choosing the efficient extractants for actinides separation. In view of the potential application of diglycolamide based ligands for the radioactive waste managment and their intriguing complexation behaviour, in this chapter we have undertaken an extensive and systematic study of the complexation reaction of DGA with the *f*- elements by investigating the structure, bonding, energetic and thermodynamical parameters using the DFT calculations.

6.6 Computational Protocols

In order to keep the computational system tractable and economical, tetramethyldiglycolamide (TMDGA) has been used instead of tetraoctyl derivative. TMDGA was chosen as a model compound for TODGA since the thermodynamic selectivity for f elements does not change with increasing alkyl chain length. The consideration of shorter alkyl chain molecule instead of longer alkyl chain molecule is quite common in computational chemistry [196].The structure of TMDGA and its complexes with f elements were optimized using generalized gradient approximated BP86 functional with split valence plus polarization (SVP) basis set (which is equivalent to 6-31G* basis set) as implemented in the TURBOMOLE package [197] i.e. C (7s4p1d) / [3s2p1d], N (7s4p1d) / [3s2p1d], O (7s4p1d)/[3s2p1d] ,H (4s)/[2s], U (14s13p10d8f1g)/[10s9p5d4f1g], Pu (14s13p10d8f1g)/[10s9p5d4f1g].

In the case of La^{3+}, Eu^{3+}, Lu^{3+}, UO_2^{2+}, Pu^{4+}, Am^{3+} and Cm^{3+}, an effective core potential was used, where 46 electrons for La and 28 electrons for Eu and Lu are kept in the core respectively, whereas the number of core electron was 60 for the actinides. The BP86 functional is faster and more accurate for predicting the geometry and vibrational frequencies [198], but the accuracy of the energetics compared to the hybrid functional is poor due to non-consideration of non-local HF part in the exchange functional. Therefore, the total energies were calculated with the B3LYP functional[199] employing triple zeta valence plus double polarization (TZVPP) basis set[200] using equilibrated structures obtained at the BP86/SVP level of theory. The hybrid B3LYP (Becke's three-parameter nonlocal hybrid exchange correlation functional, Becke-Lee-Yang-Parr) functional was found to be superior in the prediction of the energetic due to inclusion of the non-local HF contribution in the exchange functional. The aqueous and organic solvent effects in the energetics were incorporated using the COSMO approach [201]. The optimization of the complexes with Pu^{4+} was performed using quintet spin states. The default COSMO radii were used for all the elements except La^{3+}, Eu^{3+}, Lu^{3+} Pu^{4+}, Am^{3+} and Cm^{3+} for which the values of COSMO radii used were 2.03, 1.90, 1.79, 2.0, 1.99 and 1.95 Å respectively.. The dielectric constant, ε of water and dodecane was taken as 80 and 1.8. The gas phase optimized geometries were used for the single point energy calculation in COSMO phase. The computation of solvation energy for metal ions in water is performed using explicit monomer water solvation model. The free TMDGA and their complexes with metal ions were optimized without imposing any symmetry restriction.

Quantum electronic structure calculation has an extra-ordinary potential for calculating global and local indices that describe the inherent reactivity of chemical species quantitatively and is thus very useful to describe the host -guest type interaction. Chemical systems are generally characterized by its electronic chemical potential, μ and absolute hardness, η and are defined as [202]

$$-\mu = (I+A)/2 = \chi\eta = (I-A)/2 \qquad (6.21)$$

where I is the ionization potential and A is the electron affinity. Here, χ is called the absolute electronegativity. According to Koopmans' theorem [203], I and A can be obtained as

$$I = -E_{HOMO} \qquad A = -E_{LUMO} \quad (6.22)$$

If donor acceptor system is brought together, electrons will flow from that of lower χ to that of higher χ, until the chemical potentials become equal. The amount of charge transfer, ΔN can be calculated by applying the following formula [204]

$$\Delta N = (\chi M - \chi L) / \{2(\eta M + \eta L)\}. \qquad (6.23)$$

Here, M stands for metal ion, which acts as Lewis acid i.e. acceptor and L stands for ligand i.e. TMDGA, which acts as Lewis base i.e. donor.

6.7 Structure and Structural Parameters

The acceptance of computational methods is prerequisite for modeling any chemical system which can be tested by comparing the calculated structural parameters of the chemical species of interest with the experimental data wherever is obtainable.

Structure of UO_2^{2+} and Pu^{4+} ions in aqueous and nitric acid solution

The calculated structural parameters and existing experimental results are presented in Table.6.1 We have considered the penta-hydrated UO_2^{2+} and nona-hydrated Pu^{4+} ion to model the aqueous phase calculation. The existence of penta-hydrated UO_2^{2+} and nona-hydrated Pu^{4+} ion was earlier established from the EXAFS study[205] [206].The optimized structures of various aqueous and nitrate species of UO_2^{2+} and Pu^{4+} ions are displayed in **Fig. 6.1.** In **Fig. 6.1 (a),** the UO_2^{2+} ion was found to be coordinated with five water molecules in an almost planar fashion. The U-O (O of H_2O) and U-O_{ax} bond length was found to be in close agreement with the reported experimental results. The optimized structure of nonahydrated Pu^{4+} ion was shown in **Fig. 6.1 (b)**, where the centrally located

Pu^{4+} ion was found to be in distorted tricapped trigonal prismatic shape. The average Pu-O distance was found to be very close to the distance predicted by EXAFS study.The decahydrated structure of Pu^{4+}ion has been optimized (**Fig. 6.1(c)**) to study its stability from the calculated value of free energy of the reaction. The Pu-O bond distance was found to be elongated slightly compared to $Pu^{4+}(H_2O)_9$ to accommodate one more water molecules in the first solvation shell of $Pu^{4+}(H_2O)_{10}$. The optimized structures of $UO_2(NO_3)_2$ and $Pu(NO_3)_4$are displayed in **Fig. 6.1(d and e)** and that of $UO_2(NO_3)_2(H_2O)_2$ in **Fig. 6.1(f)**. In $UO_2(NO_3)_2(H_2O)_2$, the U-O (O of H_2O), U-O (O of NO_3) and U-O_{ax}bond length was found to be in close agreement with the reported experimental results [207] [208] (Table 6.1).We have optimized the structure of $Pu(NO_3)_4(H_2O)_3$which is displayed in **Fig. 6.1(g)**. In case of $Pu(NO_3)_4(H_2O)_3$, the Pu-O (O of H_2O) and Pu-O (O of NO_3) bond distances were found to be in close agreement with the reported experimental result [209].

Table 6.1: Calculated structural parameters of hydrated and nitrate salt of Pu^{4+} and UO_2^{2+} ion at BP/SVP level of theory.

Chemical species	M-O_H			M-O_{ax}			M-O_N		
	cal	exp	Δ	cal	exp	Δ	cal	exp	Δ
$UO_2^{2+}(H_2O)_5$	2.46	2.41	0.05	1.76	1.76	0.0			
$UO_2(NO_3)_2$				1.77			2.39		
$UO_2(NO_3)_2(H_2O)_2$	2.54	2.40	0.14	1.78	1.76	0.02	2.46	2.53	0.06
$Pu^{4+}(H_2O)_9$	2.45	2.39	0.06						
$Pu^{4+}(H_2O)_{10}$	2.48								

$Pu(NO_3)_4$							2.36		
$Pu(NO_3)_4(H_2O)_3$	2.53	2.38	0.15				2.45	2.49	0.04

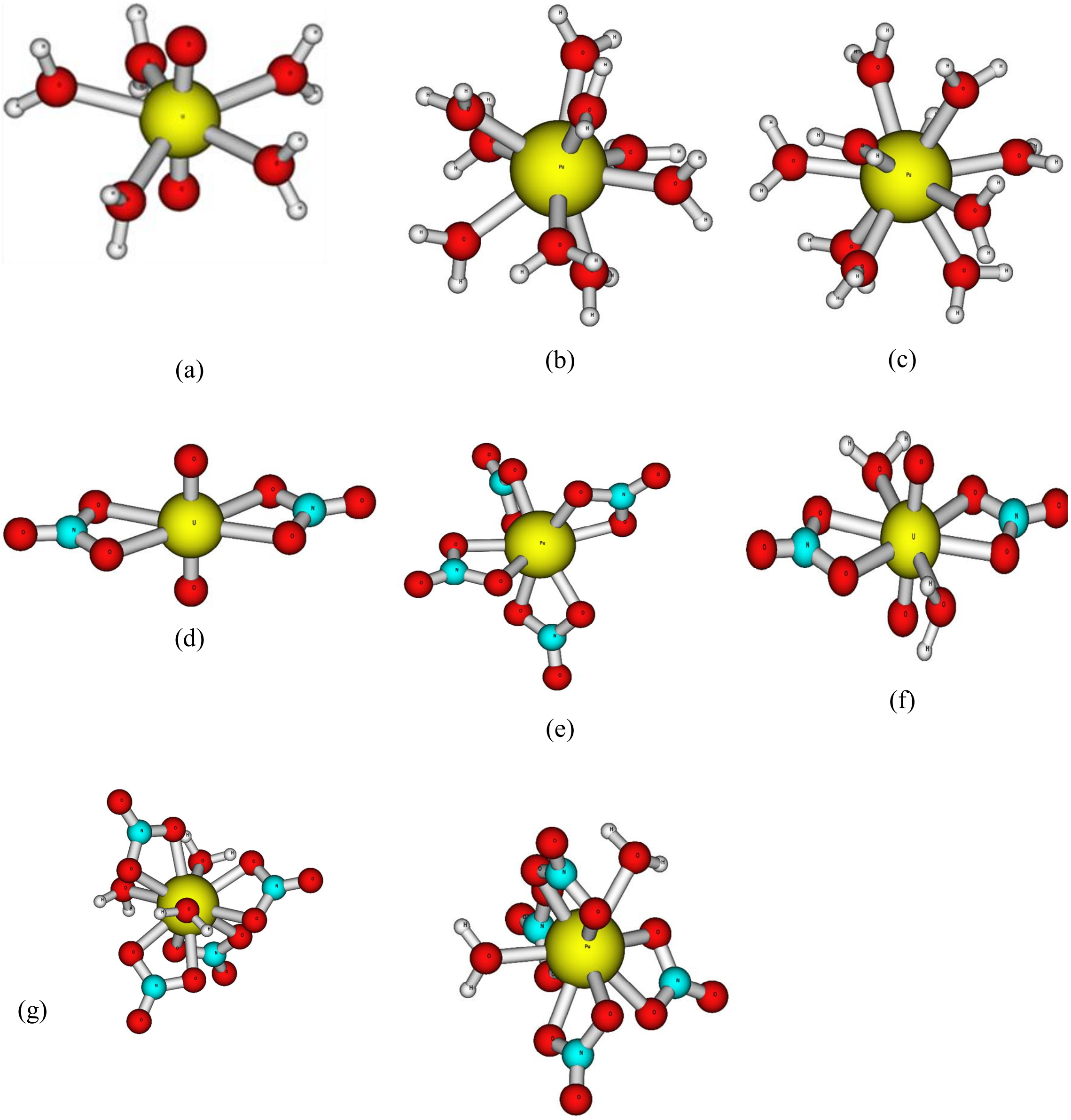
(a) (b) (c)

(d) (e) (f)

(g) (h)

Figure 6.1: Optimized structures of hydrated and nitrate salt of UO_2^{2+} and Pu^{4+} at BP/SVP level of theory (a) UO_2^{2+}-$(H_2O)_5$ (b) Pu^{4+}-$(H_2O)_9$ (c) Pu^{4+}-$(H_2O)_{10}$ (d) $UO_2(NO_3)_2$ (e) $Pu(NO_3)_4$ (f) $UO_2(NO_3)_2(H_2O)_2$ (g) $Pu(NO_3)_4(H_2O)_3$and (h) $Pu(NO_3)_4(H_2O)_2$

We have also optimized the deca coordinated Pu$(NO_3)_4(H_2O)_2$ and is presented in (**Fig. 6.1(h)**). The Pu-O (O of H_2O) and Pu-O (O of NO_3) bond distances were found to be in close agreement with the reported theoretical result as well as with that of a deca-coordinated hydrated Pu$(NO_3)_4(H_2O)_3$species (Table 6.1).

The calculated structural parameters using present computational methods are in close agreement with the reported experimental results

Structure of ligand and its complexes with UO_2^{2+} and Pu^{4+} ions

6.7.1.1 Metal ion-ligand complexes of ratio 1:1 and 1:2

The optimized structures of complexes of UO_2^{2+} and Pu^{4+} ions with TMDGA in 1:1and 1:2 stoichiometry are displayed in **Fig. 6.2** and **Fig. 6.3** respectively. The calculated structural parameters are listed in Table 6.2. In the complexes of metal ions with TMDGA, the C=O bond distance was found to be lengthened compared to free TMDGA. The metal ions were found to be coordinated via three O donor atoms of TMDGA. In 1:2 stoichiometry, two TMDGA units are coordinated to the UO_2^{2+} ion from the opposite direction in identical fashion almost in the same plane, whereas in case of Pu^{4+} ion two TMDGA units are coordinated in perpendicular fashion to each other.. The U-O bond distance (1.752Å) of uncomplexed$UO_2^{2+}$was slightly lengthened (1.765Å) due to complexation with TMDGA. The M-O (amide O) bond distance for $UO_2^{2+}$was found to be longer (2.249Å) than for Pu^{4+} ion (2.185Å) indicating stronger interaction for Pu^{4+} ion. The M-O (amide O) bond distance was found to be shorter than the M-O

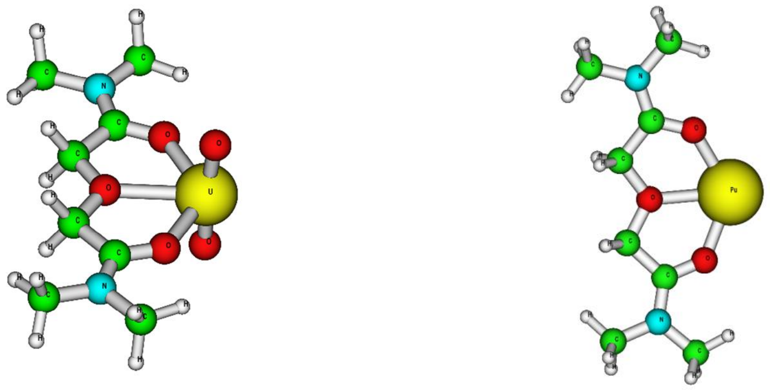

Figure 6.2: Optimized structures of complexes of $UO_2^{2+}$and Pu^{4+} ions with TMDGA in the absence of nitrate ion (1:1) at BP/SVP level of theory.

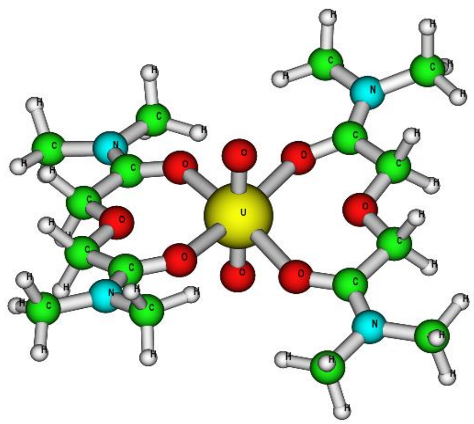

Figure 6.3: Optimized structures of complexes of UO_2^{2+} ion with TMDGA in the absence of nitrate ion (1:2) at BP/SVP level of theory.

(ethereal O) bond distance (2.519Å for UO_2^{2+} and 2.43Å for Pu^{4+} ion) and plays the dominant role in the coordinated interaction. The strong coordinating ability of amide O donor over ethereal O donor of TMDGA is further confirmed from the large red shifting (342cm^{-1}) in the amide C=O stretching frequency compared to the red shift (163cm^{-1}) in the ethereal O frequency after complexation with the metal ions.

Table 6.2: Calculated structural parameters (in Å) of $UO_2(TMDGA)_2$ and $Pu(TMDGA)_3$ at BP/SVP level of theory.

Species	Stoichiometry (M:L)	M-O(amide O)	C=O	M-O (ethereal O)
UO_2^{2+}-TMDGA	1:1	2.249	1.284	2.519
Pu^{4+}-TMDGA	1:1	2.185	1.29	2.43
$UO_2^{2+}(TMDGA)_2$	1:2	2.424	1.260	2.765
Pu^{4+} $(TMDGA)_2$	1:2	2.21	1.30	2.455
Pu^{4+} $(TMDGA)_3$	1:3	2.341	1.279	2.569

6.7.1.2 Metal ion-ligand complexes of ratio 1:3

The optimized structure of complex of Pu^{4+} ion with three TMDGA units is displayed in **Fig.6.4** and the structural parameters are listed in Table 6.2. Three TMDGA units are coordinated to the Pu^{4+} ion in a distorted tricapped trigonal prismatic fashion.The optimized structure of complexes of UO_2^{2+} ion with two TMDGA and Pu^{4+} ion with three TMDGA in presence of nitrate are displayed in **Fig. 6.5**. The calculated structural parameters are listed in Table 6.3. In case of $UO_2(NO_3)_2(TMDGA)_2$ complex, the central UO_2^{2+} ion was found to be coordinated to two TMDGA ligands and two nitrate ions in mono-dentate mode leading to distorted octahedral coordination sphere. In case of $Pu(NO_3)_4(TMDGA)_3$ complex, the central Pu^{4+} ion was found to be coordinated to three TMDGA ligands in nona-coordinated mode in the first sphere of coordination and four nitrate ions reside in the second sphere of coordination leading to charge neutralized species which is then extracted into the organic phase.

The coordination structure is described as twisted tricapped trigonal prismatic, in which the three C–O–C either O atoms occupy the capping position and the two trigonal faces are formed by the C=O atom groups. The M-O (amide O) bond distance for $UO_2^{2+}$was found to be (2.542Å) in qualitative agreement with the experimental results of 2.421Å. Similarly, the M-O (amide O) bond distance for Pu^{4+} ion (2.381Å) was found to be in qualitative agreement with the X-ray results of 2.299Å. Further, the M-O (ethereal O) for UO_2^{2+} was found to be 3.06Å which is little bit off from the experimental results of 2.614Å. For, Pu^{4+} ion, M-O (ethereal O) was found to be 2.561Å in close agreement with the experimental results of 2.470Å. It is interesting to note that the M-O (amide O) bond distance in both $Pu(NO_3)_4(TMDGA)_3$ (2.38Å) and $UO_2(NO_3)_2(TMDGA)_2$ complex (2.54Å) were found to be lengthier due to the presence of nitrate ion compared to the absence of nitrate ion (2.424Å and 2.341Å for UO_2^{2+} and Pu^{4+} respectively) as the nitrate ion reduces the effective positive charge on the metal ion thus causing the ion-dipole electrostatic interaction weaker. Further, M-O (O of NO_3) bond distance in $UO_2(NO_3)_2(TMDGA)_2$complex (2.36-2.46Å) was found to smaller than that of M-O (amide O) bond distance (2.524Å).The calculated structural parameters using present computational methods are in close agreement with the reported experimental results and thus authenticate the acceptance of the present computational methodology.

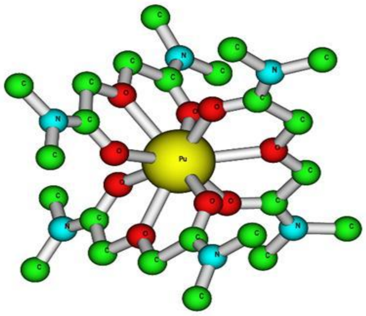

Figure 6.4: Optimized complexes of Pu^{4+} with TMDGA in the absence of nitrate ion (1:3) at BP/SVP level of theory (H atoms are excluded for better view).

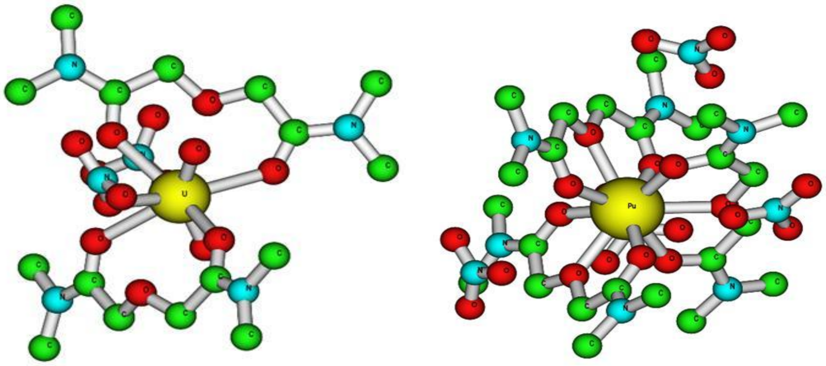

Figure 6.5: Optimized complexes of UO_2^{2+} and Pu^{4+} with TMDGA with nitrate at BP/SVP level of theory (H atoms are excluded for better view).

Table 6.3: Calculated structural parameters of $UO_2(NO_3)_2(TMDGA)_2$ and $Pu(NO_3)_4(TMDGA)_3$ at BP/SVP level of theory.

Complex	M-O(-C=O)			C=O	M-O (NO_3)	M-O (ethereal O)			U-O_{ax}	
	cal	exp	Δ			cal	exp	Δ	cal	exp
$UO_2(NO_3)_2(TMDGA)_2$	2.54	2.42	0.12	1.24	2.41	3.06	2.61	0.44	1.80	1.75
$Pu(NO_3)_4(TMDGA)_3$	2.38	2.29	0.08	1.26		2.56	2.47	0.09		

6.7.2.3 *Structural parameters of trivalent f elements with TMDGA*

The metal : ligand ratio of 1 : 3 hydrated metal ion-nitrate complexes optimized structures of La^{3+}, Eu^{3+}, Lu^{3+}, Am^{3+} and Cm^{3+} ions are displayed in **Fig. 6.6**. Two nitrate ions are found to be coordinated to the metal ion in a bi-dentate mode and one nitrate ion in mono-dentate mode whereas all five water molecules are directly coordinated to the metal ion. The calculated structural parameters are listed in Table 6.4. The M-O (O of NO_3) was found to be shorter than M-O (O of H_2O) bond length for all the metal ions studied here.

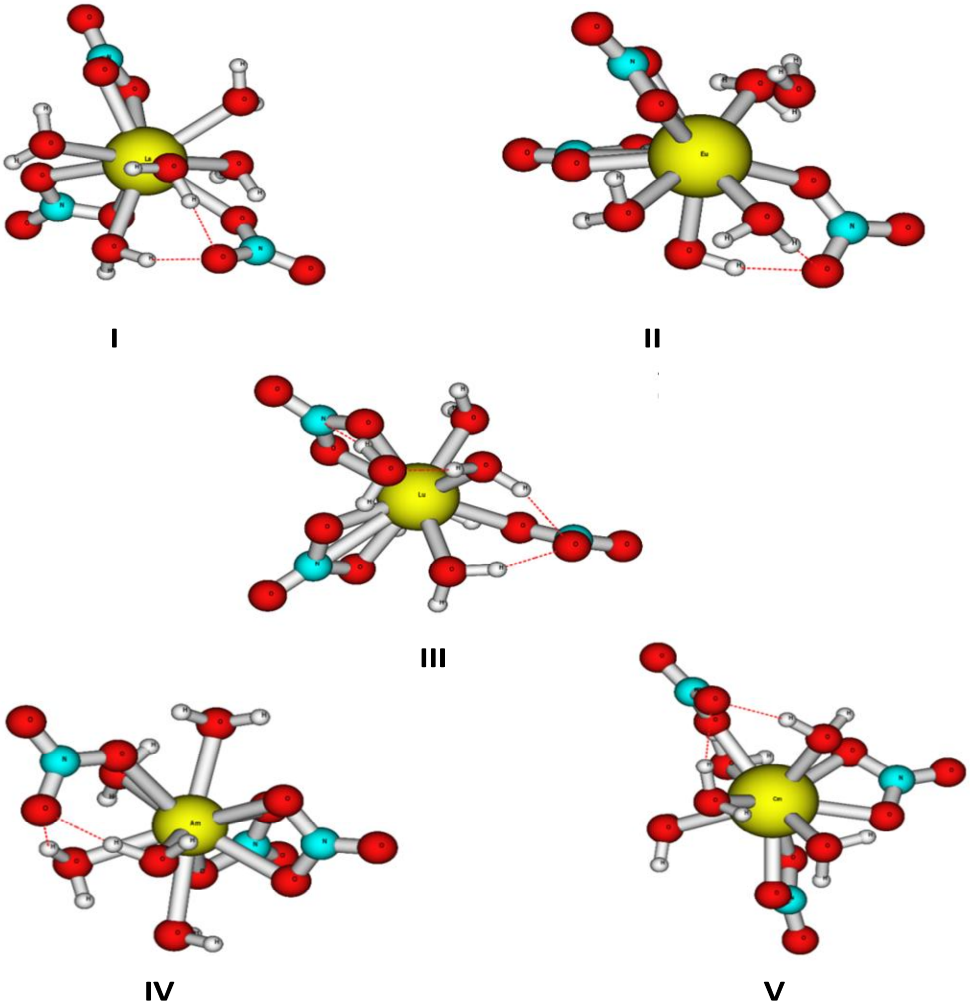

Figure 6.6: Optimized structures of hydrated metal ion complexes with nitrate ion at the BP/SVP level of theory with 5 coordinating water molecules. (I) La^{3+}; (II) Eu^{3+}; (III) Lu^{3+}; (IV) Am^{3+}; (V) Cm^{3+}

Table 6.4: Calculated bond distances (Å)of the M-$(NO_3)_3$ complex at the BP/SVP level of theory

Metals	M-$(NO_3)_3$-$(H_2O)_5$		M-$(NO_3)_3$
	M-O (O of NO_3)	M-O(O of H_2O)	
La	2.58 - 2.62	2.58 - 2.65	2.49 - 2.50
La	(2.62, 2.85, 2.66, 2.88, 2.69, 2.70)	(2.66, 2.58, 2.56, 2.56, 2.52)	
Eu	2.48 - 2.51	2.48 - 2.62	2.38 - 2.40
Lu	2.34- 2.37	2.38 - 2.40	2.24- 2.26
Am	2.49- 2.54	2.52 - 2.63	2.37- 2.39
Cm	2.47-2.50	2.49 - 2.65	2.37 -2.39

Values in the parentheses represent the experimental results.

The calculated structural parameters of metal complex with TMDGA in presence of nitrate are listed in Table 6.5. The nine-fold coordination of the metal ions were found from 3 units of TMDGA (**Fig. 6.7**). The three nitrate anions were residing outside the first coordination sphere for charge nutralization of the metal ion complex to enable it to be transferred in the dodecane phase. In the complexes of metal ions the average M-O (O atom of C=O) bond distance follows the order La^{3+}>Eu^{3+}>Am^{3+}>Cm^{3+}>Lu^{3+}. The M-O (O atom of C=O) bond distance was found to be shorter than the M-O (O atom of ether link) bond distance.

The M-O (O of nitrate) bond distance was found to be shorter than that of M-O (O atom of C=O) and the M-O (O atom of ether link) bond distance due to the 'pulling effect' of the nitrate ion on the central metal ion.

In case of 1:3, metal:ligand complex where the TMDGA ligand was found to be coordinated through three O donor atoms providing nona-coordination to the central metal ions. The calculated structural parameters are given in Table 6.5. The M-O (O atom of C=O) bond distance follow the order La^{3+}> Am^{3+}> Cm^{3+}>Eu^{3+}>Lu^{3+}. Similarly, the C-O (O atom of ether link) bond distances follow the order: La^{3+}> Am^{3+}>Eu^{3+}> Cm^{3+}>Lu^{3+}. The M-O (O atom of ether link) bond distance was found to be higher than the.M-O (O atom of C=O) bond distance The observed almost same M-O bond distance confirms the similar chemical properties of Eu^{3+}, $Am^{3+}$and Cm^{3+} so their individual separation from the nuclear waste is a difficult task and therefore, poses a challenge to the chemist to develop an efficient ligands for their extraction and separation.

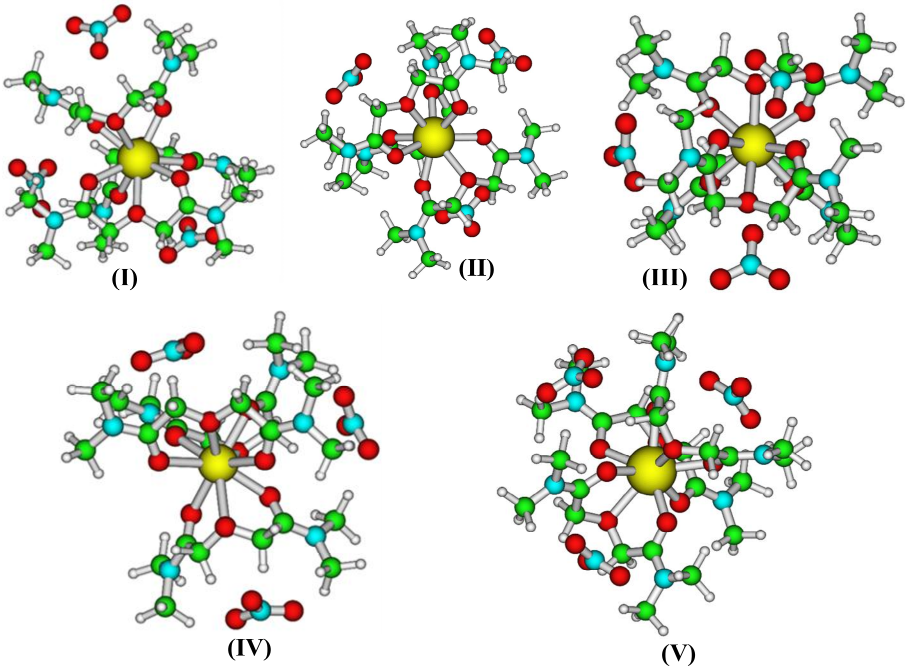

Figure 6.7: Optimized structures of the metal complexes with TMDGA in 1:3 stoichiometric at the BP/SVP level of theory in presence of nitrate anion. (I) La^{3+}; (II) Eu^{3+}; (III) Lu^{3+}; (IV) Am^{3+}; (V) Cm^{3+}.

Table 6.5: Calculated structural parameters (Å) of the 1:3 complexes in presence of nitrate ion.

Metal ion	M-O (O of C=O)	M-O (O of ether)	C=O
La	2.46 - 2.60	2.65 - 2.80	1.24- 1.26
Eu	2.43- 2.56	2.54 - 2.74	1.24- 1.25
Lu	2.24- 2.38	2.40 - 2.58	1.24- 1.25
Am	2.39- 2.52	2.55 - 2.81	1.25-1.26
Cm	2.36 - 2.48	2.52 - 2.70	1.25-1.26

6.8 Binding Energy and Free Energy of Extraction in Gas Phase

Hexa and tetra valent actinides

Preferential selectivity of a particular material ion for a coordinating ligand can be electronic, entropy driven or solvent mediated. Consequently, the gas phase binding energy plays an important role in the initial screening and selectivity of the metal ions. It is calculated using the complexation reaction in gas phase as

$$\Delta E_{gas} = E_{ML_m(NO_3)_{n(gas)}} - (E_{M(gas)} + nE_{NO_3(gas)} + mE_{L(gas)}) \qquad (6.24)$$

Where $E_{ML_m(NO_3)_{n(gas)}}$, $E_{M(gas)}$ and $E_{L(gas)}$, represent the total energy of the metal ion-ligand-nitrate complex, metal ion and the ligand respectively. The calculated values of binding energy are given in Table 6.6. It is seen that the binding energy of Pu^{4+} ion with TMDGA either in presence or absence of

nitrate ion is found to be much higher than that of UO_2^{2+} ion. The value of gas phase binding energy, ΔE for Pu^{4+} ion (-769.96 kcal/mol) was found to be higher than that of UO_2^{2+} ion (-235.17 kcal/mol) by -534.79 kcal/mol for 1:1 stoichiometry and by 700.71kcal/mol for 1:2 stoichiometry. The binding energy for the incoming second TMDGA ligand was found to be smaller than the incoming first ligand for both UO_2^{2+} (102.08 kcal/mol) and Pu^{4+} (267.99 kcal/mol) ion. In order to find out the reason of higher binding energy of Pu^{4+} ion over UO_2^{2+} ion, the natural population analysis (NPA) was performed to compute the charge on the metal ion and the atomic orbital population. The calculated value of residual charge on the metal ions and the atomic orbital population is presented in Table 6.7. From NPA analysis, it is seen that there is small extra orbital contribution to the inner d and f subshells of the metal ion indicating that the interaction of metal ion with TMDGA ligand has some covalent character. The f subshells were found to be more diffused than the d sub shells in absence of nitrate ion. The contribution from g subshells is nearly negligible. The charge transfer was found to be more in Pu^{4+} ion complex than that of UO_2^{2+} ion complex leading to higher binding energy for Pu^{4+} ion than that of UO_2^{2+} ion.The charge transfer was shown to be more in 1:3 stoichiometry than that of 1:1 and 1:2 stoichiometry as more number of donor atoms is involved in the coordination.

Table 6.6: Reaction energetic values (kcal/mole) of complexes of UO_2^{2+} and Pu^{4+} with TMDGA (L) at B3LYP/TZVP level of theory.

Various stoichiometric reaction	ΔE	ΔH	$T\Delta S$	ΔG_{gas}	ΔG_{sol}
UO_2^{2+} + L = UO_2^{2+}-L	-235.17	-235.76	-12.20	-223.55	19.13
UO_2^{2+}-L + L = UO_2^{2+}-$(L)_2$	-102.08	-102.67	-13.50	-89.16	-65.14
UO_2^{2+} +2L = UO_2^{2+}-$(L)_2$	-337.25	-338.43	-25.71	-312.71	-46.00
Pu^{4+} + L = Pu^{4+}-L	-769.96	-770.55	-11.81	-758.74	281.77
Pu^{4+}-L + L = Pu^{4+}-$(L)_2$	-267.99	-268.58	-14.33	-254.25	-176.25
Pu^{4+} + 2L = Pu^{4+}-$(L)_2$	-1037.96	-1039.14	-26.14	-1012.99	105.52

Pu^{4+}-$(L)_2$ + L = Pu^{4+}-$(L)_3$	-133.39	-133.99	-17.21	-116.77	-86.22
Pu^{4+} + 3L = Pu^{4+}-$(L)_3$	-1171.35	-1173.12	-43.36	-1129.76	19.29
UO_2^{2+} +$2NO_3^-$ + 2L = $UO_2(NO_3)_2(L)_2$	-514.00	-516.36	-51.36	-465.00	-27.36
Pu^{4+} +$4NO_3^-$+ 3L = $Pu(NO_3)_4(L)_3$	-1798.98	-1803.11	-91.77	-1711.34	-137.42

Further, in order to understand the nature of interaction, the energy of highest occupied molecular orbital (HOMO) and lowest unoccupied molecular orbital (LUMO) and their energy gap for free metal ion and ligand was evaluated and are displayed in Table 6.8.The $E_{HOMO-LUMO}$ of Pu^{4+} ion (4.96eV) and UO_2^{2+} (5.09eV) ions was found to be rather high indicating hard nature of both Pu^{4+} and UO_2^{2+} ion. But, the calculated value of absolute electronegativity, χ, for Pu^{4+} (43.88eV) ion was found to be much higher than that of UO_2^{2+} (20.91eV) ion suggesting its strong accepting nature over UO_2^{2+} ion. The absolute hardness, η was found to be more or less comparable for both Pu^{4+} (2.48eV) and UO_2^{2+} (2.54eV) ion. The tridentate DGA ligand with hard O donor represents the class of hard base as manifestedin the value of $E_{HOMO-LUMO}$ (6.88eV) and the value of χ (3.15eV) and η (3.44eV).The amount of charge transfer, $\Delta N$was also calculated for the donor acceptor interaction. The higher the value of charge transfer, ΔN, higher is the metal-ligand interaction. In the present case, the value of ΔN was found to be higher with Pu^{4+} (3.43) over UO_2^{2+} (1.48) ion and hence confirms the higher binding energy for Pu^{4+} over UO_2^{2+} ion.

Table 6.7: Calculated charges (a.u) on U and Pu and orbital population using NPA analysis in complexes of UO_2^{2+} and Pu^{4+} with TMDGA at B3LYP/TZVP level of theory.

element	Stoichiometry (M:L)	charge	n (s)	n (p)	n (d)	n (f)	n (g)
U	1:1	2.22	4.08	11.73	11.36	2.58	0.00
Pu	1:1	2.53	4.02	11.97	10.30	5.14	0.00
U	1:2	1.94	4.14	11.76	11.41	2.71	0.00
Pu	1:2	2.32	4.10	11.96	10.83	4.76	0.00
Pu	1:3	1.85	4.17	11.98	10.98	5.00	0.00
U	1:2 (nitrate)	1.65	4.18	11.83	11.45	2.87	0.00
Pu	1:3 (nitrate)	1.87	4.17	11.98	10.92	5.04	0.00

Table 6.8: Calculated various molecular descriptors at B3LYP/TZVP level of theory.

	E_{HUMO}(eV)	E_{LUMO}(eV)	$E_{HUMO-LUMO}$(eV)	χ (eV)	η(eV)	ΔN
UO_2^{2+}	-23.46	-18.36	5.09	20.91	2.54	1.48
Pu^{4+}	-46.36	-41.39	4.96	43.88	2.48	3.43
$UO_2^{2+}(H_2O)_5$	-17.45	-11.88	5.57	14.66	2.78	0.92
$Pu^{4+}(H_2O)_9$	-25.02	-21.61	3.41	23.31	1.71	1.95
TMDGA	-6.59	+0.28	6.88	3.15	3.44	
$UO_2^{2+}(H_2O)_5$	-9.76	-4.38	5.37	7.07	2.68	0.83
$Pu^{4+}(H_2O)_9$	-10.73	-7.32	3.40	9.02	1.70	1.18

The topology of electron density is used in AIM (atom in molecule) theory to describe the bond critical point (BCP) in a molecule [210]. Two most important topological parameters are electron density (ρ) and the Laplacian of electron density ($\nabla^2\rho$) which is calculated here using AIM theory as implemented in GUI version of ADF2012 package. The strength of a chemical bond is reflected in the electron density at BCP (ρ). The larger the value of ρ, the stronger the corresponding chemical bond.

Similarly, the Laplacian at BCP is the measure of covalent bonding ($\nabla^2\rho < 0$) and closed-shell bonding, for example ionic, coordination, hydrogen-bonding or van der Waals interactions ($\nabla^2\rho > 0$). The calculated values of various topological parameters ρ and $\nabla^2\rho$

for $UO_2^{2+}(TMDGA)_2$ and $Pu^{4+}(TMDGA)_3$ at BCP are reported in the Table 6.9 . From the table it is seen that the average value of ρ is positive but was found to be higher in Pu^{4+} ion than UO_2^{2+} ion. Similarly, average value of $\nabla^2\rho$ was found to be positive indicating the closed shell interaction between donor atoms and acceptor metal ions and the value was found to be higher with Pu^{4+} ion compared to UO_2^{2+} ion indicating more ionic character for Pu^{4+} ion than UO_2^{2+} ion. Further, the values of ρ and $\nabla^2\rho$ for ether O atoms interactions with corresponding metal ions were found to be smaller compared to amidic O atoms indicating stronger interaction with amidic O over ethereal O atoms.In presence of nitrate ion, the binding energy was found to be increased significantly compared to the absence of nitrate ion as shown in Table.6.6. The binding energy of UO_2^{2+} was found to be increased by -176.75kcal/mol and for Pu^{4+} ion, the increment was -627.63kcal/mol. The charge transfer was found to be more in Pu^{4+} ion complex than that of UO_2^{2+} ion complex. This is reflected in the interaction energy i.e the interaction energy with nitrate ion is higher than without nitrate ion for both Pu^{4+} and UO_2^{2+} complexes with TMDGA. The substantial charge on the metal atom obtained from natural population analysis (Table 6.7.) indicates the charge-dipole type interaction. The transfer of charge was found to be much higher in the presence of nitrate ion which in turn increases the interaction energy further. The thermodynamic free energy of complexation, ΔG for Pu^{4+} and UO_2^{2+} complexes in gas phase has also been computed and the values are presented in Table 3. It is seen that the change in enthalpy, ΔH of the complexation reaction is negative indicating enthalpy favorable process. The value of ΔH is found to be more negative in the presence of nitrate ion. Further the value of ΔH is found to be higher for Pu^{4+} compared to UO_2^{2+} ion towards TMDGA. The calculated value of entropy change ΔS is also given in the same table. The value of ΔS is found to be negative signifying entropy unfavorable process. It is known that the metal ion ligand complexation from aqueous phase is a collective structure breaking and structure making process. The metal ion complexation is a structure making process, whereas during complexation the hydrated ion is dehydrated leading to release of water molecule, which is a structure breaking process. The former leads to negative entropy contribution whereas later leads to positive entropy contribution. This can be explained as follows. Though, the release of water molecules during dehydration is a structure breaking process, the released water molecules form a stable water cluster through hydrogen bonding, which in turn fails to add positive entropy contribution due to assembling of remaining reactant species. But, point to be noted, that though the entropy is negative, it cannot surpass the high negative enthalpy value leading to negative free energy indicating favorable complexation reaction. The value of free energy change, ΔG is found to be smaller than that of ΔH as TΔS is negative. It is also interesting that the value of TΔS is found to be more negative in the presence of nitrate ion.

Table 6.9: Calculated topological parameters using AIM module of ADF package

Complex	BCP	ρ	$\nabla^2\rho$
$UO_2(TMDGA)_2$	U-O1	0.05990	0.21472
	U-O2	0.06067	0.21763
	U-O3	0.06062	0.21536
	U-O4	0.06079	0.21676
	U-O5 (ether O)	0.02664	0.10916
	U-O6 (ether O)	0.02631	0.10822
$Pu(TMDGA)_3$	Pu-O1	0.07136	0.25944
	Pu-O2	0.07550	0.26311
	Pu-O3	0.07287	0.26766
	Pu-O4	0.07279	0.25131
	Pu-O5	0.07356	0.27152
	Pu-O6	0.07606	0.28302
	Pu-O7 (ether O)	0.03902	0.16317
	Pu-O8 (ether O)	0.03881	0.16643
	Pu-O9 (ether O)	0.04108	0.15629

To study the complexation behaviour of Ln/An ions with TMDGA the step wise binding energy in the gas is determined. The stepwise complexation of diglycolamide ligand with trivalent f – elements M^{3+}(M=La, Eu, Lu, Am and Cm) can be represented by the following reaction,

$$M^{3+} + nL \longleftrightarrow M^{3+}\text{-}L_n \ (n=1\text{-}3) \qquad (6.25)$$

The stepwise complexation is correlates with the stepwise binding energy,

$$\Delta E_n = E_{M^{3+}\text{-}Ln} - (E_{M3+} + nE_L) \qquad (6.26)$$

as shown from **Fig. 6.8** and Table 6.10 the successive addition of ligand, the binding energy was found to increase due to the interaction of the metal ion with the more numbers of O from donor atoms.

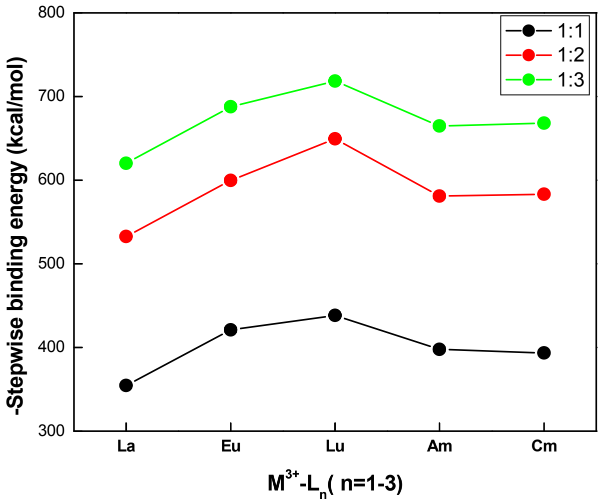

Figure 6.8: Stepwise binding energy in the gas phase of the M^{3+}-$(L)_n$ complexes (n=1-3) at the B3LYP/TZVPP level of theory

Table 6.10: Calculated gas phase binding energy (kcal/mol) of metal ions with TMDGA in different stoichiometric without nitrate anion at B3LYP/TZVPP level of theory.

	1:1			1:2			1:3		
	bare ion	hydrated	cluster	bare ion	Hydrated	cluster	bare ion	hydrated	cluster
La	-354.45	125.20	59.10	-532.55	-52.89	-118.99	-620.31	-140.65	-206.74
Eu	-420.99	116.07	49.97	-599.60	-62.53	-128.63	-687.89	-155.74	-221.84
Lu	-438.42	134.74	68.75	-649.32	-76.15	-142.24	-718.53	-145.36	-211.45
Am	-397.79	120.23	54.13	-580.92	-62.89	-128.99	-664.74	-148.11	-214.21
Cm	-393.38	127.52	61.42	-583.26	-62.35	-128.45	-668.15	-147.41	-213.51

To get more insights in the bonding and interaction of trivalent f – elements with TMDGA, population analysis and topological parameters are evaluated.

To determine the charge on the metal ion and the atomic orbital population, natural population analysis (NPA), for the M^{3+}-$(TMDGA)_3$ complexes (M=La, Eu, Lu, Am and Cm) was performed.The calculated value of NPA charge and atomic orbital population is listed in Table 6.11.

Table 6.11: Atomic charges and orbital populations using natural population analysis on the metal ion for the M^{3+}-$(TMDGA)_3$ complexes at the B3LYP/TZVPP level of theory

M^{3+}	Charge	n (s)	n (p)	n (d)	n (f)	n (g)
La	2.27	2.12	5.98	0.605	0.006	0
Eu	1.94	4.14	11.99	10.83	6.07	0.000
Lu	2.01	4.18	11.99	10.80	13.99	0.000
Am	1.96	4.15	11.98	10.74	6.14	0.001
Cm	2.01	4.16	11.98	10.75	7.08	0.001

The residual charge on Am^{3+}(1.96) ion was found to be higher than Eu^{3+} (1.94) and Cm^{3+}(2.01) indicating the highest interaction energy for Eu^{3+} ion. Further, from the NPA analysis, extra orbital contributions to the inner s, d and f sub shells of the metal ion (Eu, Am and Cm) indicates some covalent character. The *d* sub shells were found to be more diffused than the *s*, and *f* sub shells. The *f* sub shell of Am was found to be more diffused than the others.The highest occupied molecular orbital (HOMO) and lowest unoccupied molecular orbital (LUMO) energy was also calculated for M^{3+}-$(TMDGA)_3$ complexes (M=Eu and Am). The HOMO-LUMO energy gap (E_{H-L}) for the trivalent metal ions (Eu=5.33 eV and Am=3.97 eV) are found to be high indicating strong acceptor (i.e., strong acid) so that it can provide strong electrostatic interaction with a strong donor (O atom) based ligands (i.e., strong base), TMDGA with a high E_{H-L} value of 6.88 eV. The different selectivity of the metal ions towards the ligands is due to different contribution from HOMO-LUMO of the respective metal ion-ligand system. In order to calculate the fractions of electron transferred from the donor TMDGA ligand (L) to the metal ion (M), theoretical values for absolute electronegativity and absolute hardness for Eu and Am metal ions were calculated. The theoretical value of absolute electronegativity of Eu and Am metal ions are 34.52 eV and 30.41 eV and absolute hardness are 2.66 eV and 1.98 eV respectively. This indicates that Am metal ion is soft acid and Eu metal ion is hard acid. As per HSAB principle, hard-hard and soft-soft interaction are preferred among acid-bases interactions. The high energy HOMO and large value of hardness (η=3.44eV) and electronegativity (χ=3.15eV) indicates that TMDGA is a hard base and hence undergoes favorable complexation with the Eu^{3+} ion over Am^{3+} ion. The favorable donor-acceptor interaction is further evaluated by the large value of charge transfer ΔN for the Eu^{3+}-$(TMDGA)_3$ complex (2.56) over the Am^{3+}-$(TMDGA)_3$ complex (2.51) and thus also supports their extraction behaviors.

6.9 Atom in Molecule Topological Parameters

The bond critical point is calculated here using the AIM theory of ADF package at B3LYP/TZ2P level of theory.The calculated values of various topological parameters ρ, $\nabla^2\rho$ and ellipticity (ε) for M^{3+}-$(TMDGA)_3$ complexes (M= Eu and Am) are tabulated in Table 6.12 and BCP are shown in **Fig. 6.9**.The presence of nine BCP from nine O donor atoms to centrally located metal ions. The average value of ρ is positive but small and was found to be higher in case of Am^{3+} ion (0.046) than Eu^{3+} ion (0.041).Similarly, average value of $\nabla^2\rho$ was found to be positive showing the closed shell interaction and the value was found to be little higher with Am^{3+} ion (0.214) compared to Eu^{3+} ion (0.189) indicating more ionic character for Am^{3+} ion complex than Eu^{3+} ion.

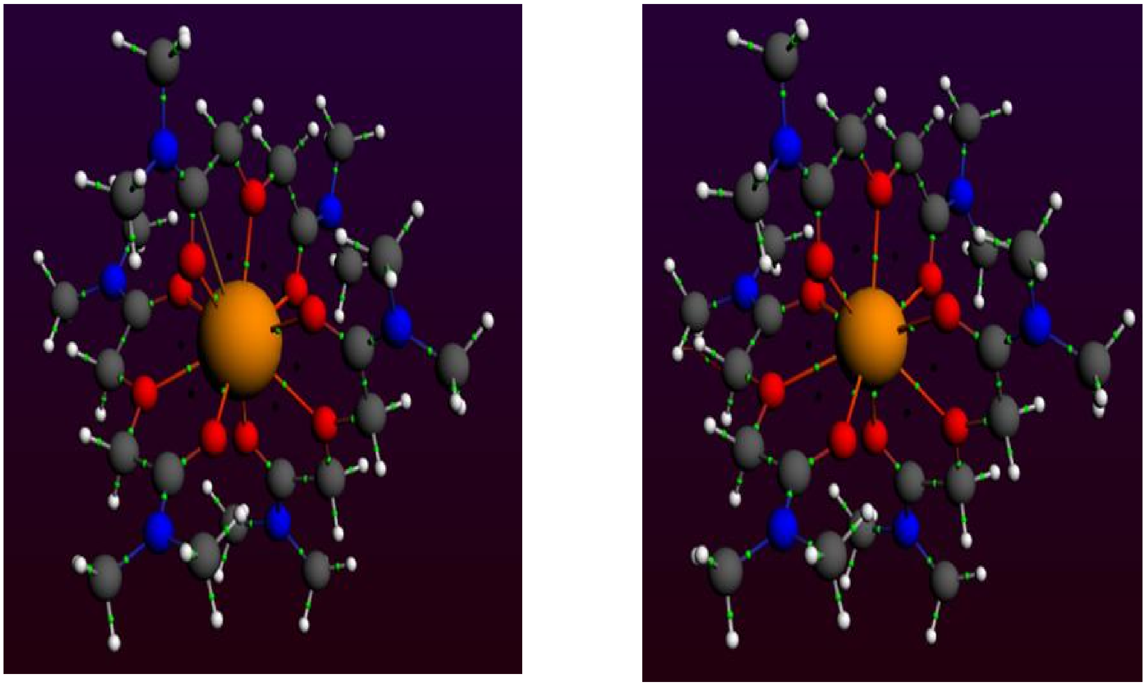

Figure 6.9: Calculated bond critical point from O atoms to the metal ion of the (a) $Eu^{3+}(TMDGA)_3$ and (b) $Am^{3+}(TMDGA)_3$ complexes at B3LYP/TZ2P level of theory.

Table 6.12: Average electron density and Laplacian of electron density and elliptisity for the M^{3+}-$(TMDGA)_3$ and aqua complexes at the B3LYP/TZ2P level of theory using Bader's AIM calculation.

Complex TMDGA	BCP	Avg.ρ	Avg. $\nabla^2\rho$	Avg.ε [$\varepsilon = (\lambda 1/\lambda 2) - 1$]
La	La-O	0.037	0.144	0.016
Eu	Eu-O	0.041	0.189	0.196
Lu	Lu-O	0.045	0.200	0.014
Am	Am-O	0.046	0.214	0.517
Cm	Cm-O	0.046	0.200	0.018

6.10 Free Energy of Extraction

Hexa and tetra valent actinides using thermodynamic cycle in solvent phase

Though the gas phase free energy of complexation was adequate to capture the experimental selectivity of Pu^{4+} ion over UO_2^{2+} ion towards TMDGA, it will be more practical if the calculation is performed in the solution phase. The metal ions are extracted from the aqueous environment, where it remains in a strongly hydrated form. Hence, it is indispensable to compute the solvation energy of the metal ions in aqueous environment for accurate prediction of extraction energy. In order to account for the aqueous solvent effect, we have considered the monomer water model [211]

$$M_{(gas)} + mH_2O_{(aq)} \rightarrow M(H_2O)_{m(aq)} \quad (M/m= UO_2^{2+}/5 \text{ and } Pu^{4+}/9) \qquad (6.27)$$

The nona coordinated hydrated Pu^{4+} and penta coordinated hydrated UO_2^{2+} was used for the geometry optimization and the total energy calculation was done. The gas phase optimized structure was used to calculate the solvation free energy using COSMO solvation model.The computed values of free energy of solvation after standard state entropy corrections for Pu^{4+} and UO_2^{2+} using monomer water solvation model are -1413.86kcal/mol and -365.06 kcal/mol respectively. The free energy of extraction, ΔG_{ext} for Pu^{4+} and UO_2^{2+} with TMDGA from aqueous phase was calculated using Born-Haber thermodynamic cycle (Scheme-1, **Fig. 6.10**). The free energy of solvation of TMDGA and its complexes with Pu^{4+} and UO_2^{2+} without and with nitrate ion in the aqueous phase are calculated and given in Table 6.13 and Table 6.14. The difference in the free energy of solvation of complexes of Pu^{4+} and UO_2^{2+} with TMDGA is found to be higher compared to its corresponding complexes with nitrate.This is due to the nitrate ions screen the charge on the metal ion from the solvent reduces the free energy of solvation value. The free energy values in the solvent phase are found to be smaller than that of in the gas phase. The solvent-metal ion interaction in the solvent phase decreases the interaction of metal ion with ligand thereby decreasing the free energy value. The free energy of extraction, ΔG_{ext} has two contributory components, one is assigned from the gas phase and other one is from the solvent phase.The calculated values of $\Delta\Delta G_{sol}$are presented in Table 6.13 and 6.14. From Table 6.13, it is seen that in the absence of nitrate ion, the value of $\Delta\Delta G_{sol}$supersedes the value of $\Delta G_{gas}$for both UO_2^{2+} and Pu^{4+} ions leading to positive value of ΔG_{ext}in solvent of dielectric constant 2. In presence of nitrate ion, the value of ΔG_{gas}supersedes the positive value of $\Delta\Delta G_{sol}$ for only Pu^{4+} ion leading to negative value of ΔG_{ext} (see Table 6.14) at dielectric constant 2 but remains positive for UO_2^{2+} ion.This clearly demonstrates the role of nitrate ion in the modeling of the complexation reaction. Further, in order to screen whether solvent of higher dielectric constant can be better organic solvent than dodecane or not, the calculation was extended to solvent of higher dielectric constant up to 40. The calculated values of ΔG_{ext} along with other free energy components are presented in Table.6.13 and Table 6.14. From Table 6.13, it is seen that in the absence of nitrate ion, the value of $\Delta\Delta G_{sol}$supersedes the value of $\Delta G_{gas}$for both UO_2^{2+} and Pu^{4+} ions leading to positive value of ΔG_{ext} in solvent of dielectric constant 2 but above 5, the value of ΔG_{ext}becomes negative.Both the solvation energy of the ligand as well as the metal ion-ligand complexes is found to be increased with increasing dielectric constant of the solvent leading to decreased $\Delta\Delta G_{sol}$which in turn increases the free energy of extraction, ΔG_{ext} for both Pu^{4+} and UO_2^{2+} ion with increasing dielectric constant. Whereas, in presence of nitrate ion the value of ΔG_{ext} (Table 6.14) was found to be decreased with increased dielectric constant due to increase value of $\Delta\Delta G_{sol}$ for both Pu^{4+} and UO_2^{2+}.

$$\begin{tikzcd}
M^{3+}{}_{(gp)} \arrow[d, "\Delta G_{sol[M]}"] & +\ 3\ NO_3^-{}_{(gp)} \arrow[d, "\Delta G_{sol[NO3]}"] & +\ 3L_{(gp)} \arrow[d, "\Delta G_{sol[L]}"] \arrow[r, Leftrightarrow, "\Delta G_{gp}"] & ML_3\ (NO_3)_3\ {}_{(gp)} \arrow[d, "\Delta G_{sol[ML3(NO3)3]}"] \\
M^{3+}{}_{(aq)} & +\ 3\ NO_3^-{}_{(aq)} & +\ 3L_{(org)} \arrow[r, Leftrightarrow, "\Delta G_{ext}"] & ML_3\ (NO_3)_3\ {}_{(org)}
\end{tikzcd}$$

Figure 6.10: Explicit solvation approach using monomer water of Scheme-1

The change in Gibbs free energy of extraction, ΔGext can be obtained by the Born-Haber thermodynamic cycle in terms of the free energy change in gas phase, ΔG(gas), and the solvation free energies of the products and reactants, ΔΔG(sol). The overall complexation reaction is characterized by the free energy of extraction,

ΔGext as

$$\Delta G_{ext} = \Delta G_{gas} + \Delta\Delta G_{sol}$$

$$\Delta G_{gas} = G_{MLm(NO3)n_{gas}} - (G_{M_{gas}} + n\, G_{NO3_{gas}} + m\, G_{L_{gas}})$$

$$\Delta\Delta G_{sol} = \Delta G_{MLm(NO3)n_{org}} - (\Delta G_{M_{aq}} + n\, \Delta G_{NO3_{aq}} + m\, \Delta G_{L_{org}})$$

Table 6.13: Calculated values of free energy (kcal/mol) using explicit monomer water model without nitrate ion at B3LYP/TZVP level of theory (Scheme-1 of Fig.6.10).

Di-electric constant (ε)	$\Delta G_{sol\ (L)}$	$\Delta G_{sol\ (MLn)}$		$\Delta\Delta G_{sol}$		ΔG_{ext}	
		UO_2^{2+}	Pu^{4+}	UO_2^{2+}	Pu^{4+}	UO_2^{2+}	Pu^{4+}
2	-7.31	-51.23	-174.19	328.63	1261.60	15.92	131.84
5	-14.85	-93.76	-317.67	301.18	1140.76	-11.52	10.99
10	-18.37	-110.83	-374.90	291.16	1094.09	-21.55	-35.67
15	-19.71	-116.92	-395.26	287.75	1077.74	-24.95	-52.01
20	-20.42	-120.04	-405.70	286.04	1069.43	-26.67	-60.33
25	-20.85	-121.94	-412.05	285.00	1064.38	-27.70	-65.38
30	-21.15	-123.22	-416.31	284.32	1061.01	-28.38	-68.75

35	-21.37	-124.14	-419.38	283.83	1058.58	-28.88	-71.18
40	-21.53	-124.83	-421.69	283.46	1056.75	-29.25	-73.00

Table 6.14: Calculated values of free energy (kcal/mol) using explicit monomer water model with nitrate ion at B3LYP/TZVP level of theory (Scheme-1, Fig.6.10).

Di-electric constant (ε)	$\Delta G_{sol\ (L)}$	$\Delta G_{sol\ (MLn)}$		$\Delta\Delta G_{sol}$		ΔG_{ext}	
		UO_2^{2+}	Pu^{4+}	UO_2^{2+}	Pu^{4+}	UO_2^{2+}	Pu^{4+}
2	-7.31	-16.40	-21.54	465.52	1618.38	0.50	-92.97
5	-14.85	-32.06	-42.21	464.98	1620.33	-0.03	-91.02
10	-18.37	-38.93	-51.20	465.12	1621.91	0.10	-89.44
15	-19.71	-41.48	-54.47	465.24	1622.65	0.22	-88.70
20	-20.42	-42.82	-56.18	465.32	1623.07	0.30	-88.28
25	-20.85	-43.64	-57.23	465.37	1623.32	0.35	-88.03

30	-21.15	-44.19	-57.93	465.42	1623.51	0.40	-87.84
35	-21.37	-44.59	-58.38	465.44	1623.70	0.42	-87.65
40	-21.53	-44.89	-58.82	465.46	1623.75	0.44	-87.60

This explicit solvation scheme is based on the solvation model of Dolg et al [212]. The metal and nitrate ions were considered to be isolated hydrated species. It is interesting to study when the metal and nitrate ions remain as an ion pair in highly acidic aqueous solution (>3N HNO_3).

$$\begin{tikzcd}
M(NO_3)_{3\,(gp)} \arrow[d, "\Delta G_{sol[M(NO3)3]}"] & + & 3L_{(gp)} \arrow[r, phantom, "\overset{\Delta G_{gp}}{\Longleftrightarrow}"] \arrow[d, "\Delta G_{sol[L]}"] & ML_3\,(NO_3)_{3\,(gp)} \arrow[d, "\Delta G_{sol[ML3(NO3)3]}"] \\
M(NO_3)_{3\,(aq)} & + & 3L_{(org)} \arrow[r, phantom, "\overset{\Delta G_{ext}}{\Longleftrightarrow}"] & ML_3\,(NO_3)_{3\,(org)}
\end{tikzcd}$$

Figure 6.11: Explicit solvation approach using monomer water of Scheme-2

This solvation approach is based on the explicit solvation model using monomer water. The gas phase metal nitrate with first solvation sphere water molecules (assuming 2/3 water units) was solvated as

$M(NO_3)_{m\,(gas)} + nH_2O_{(aq)} \rightarrow M(NO_3)_m(H_2O)_{n(aq)}$ m/n=2, 2 for UO_2^{2+} and 3/4 for Pu^{4+} (6.28)

The computed value of free energy of extraction, ΔG_{ext}, for the transfer of metal ions from aqueous to dodecane phase using hydrated metal nitrate according to Scheme-2,(**Fig. 6.11)** is listed in Table 6.15. The calculated value of ΔG_{gp} as well as $\Delta\Delta G_{sol}$ was found to be positive which makes free energy, ΔG_{ext} positive suggesting that the extraction is unfavourable. Hence, the extraction of hydrated metal nitrate using explicit monomer water solvation model is not workable due to positive free energy of extraction.

The free energy of extraction using thermodynamic cycle as per scheme-1 (Table 6.14) is found to be negative for Pu^{4+} ion (-92.97kcal/mol) whereas it is small positive for UO_2^{2+} ion (0.50kcal/mol). This preferential extraction of Pu^{4+} ion over UO_2^{2+} ion was observed in the solvent extraction experiment. This free energy based prediction is the major finding of the work.

Table 6.15: Calculated value of thermodynamic parameters (kcal/mol) for the extraction of different hydrated nitrate of UO_2^{2+} and Pu^{4+}ions with TMDGA using B3LYP/TZVP level of calculation at 298.15K (Scheme-2; monomer water model).

M^{n+}	Δ G(gp)	ΔGsol M(NO3)n	ΔG sol (L)	ΔGsolMLn(NO3)m	ΔG ext	ΔΔG sol
$UO_2(NO_3)_2(H_2O)_2$	20.29	-29.88	-7.31	-16.40	55.72	35.42
$Pu(NO_3)_4(H_2O)_3$	9.24	-16.86	-7.31	-21.54	25.61	16.36
$Pu(NO_3)_4(H_2O)_2$	9.24	-16.86	-7.31	-21.54	26.51	17.26

The free energy of extraction, ΔG_{ext}, data from aqueous to *n*-dodecane organic phase with TMDGA ligand for 1:3 stoichiometric complexation reactions are based on the following reaction.

$$M^{3+}_{(aq)} + 3\ TODGA_{(org)} + 3\ NO_3^-{}_{(aq)} \leftrightarrow M(NO_3)_3\cdot 3TODGA_{(org)} \quad (6.29)$$

Scheme-1 indicates that solvation energy of metal ion is important in the process. Hence, the solvation of metal ion has been considered using two different solvation approaches: explicit monomer water and cluster water solvation model. The details are presented below.

Explicit solvation approach using monomer water of Scheme-1. The metal ion with 9 water units in first solvation shell was solvated in COSMO phase as

$$M^{+}_{(gas)} + 9H_2O_{(aq)} \rightarrow M^{+}(H_2O)_{9(aq)} \qquad (6.30)$$

The computed value of free energy of extraction, ΔG_{ext}, for the transfer of metal ions from aqueous to dodecane phase using explicit solvation of only bare metal ion based on Scheme-1 is given in Table 6.16. The computed value of ΔG_{ext} was found to be negative indicating that TMDGA ligands are able to extract the metal ions from aqueous phase to the dodecane phase. The free energy of extraction was found to be highest for Eu^{3+} ion and lowest for La^{3+} ion and in between the value of Lu^{3+}, Am^{3+} and Cm^{3+}. The calculated preferential selectivity order as follows $Eu^{3+}>Lu^{3+}>Am^{3+}>Cm^{3+}>La^{3+}$.

$$\begin{tikzcd}
M^{3+}{}_{(gp)} \arrow[d, "\Delta G_{sol[M]}"] & +\ 3\ NO_3^-{}_{(gp)} \arrow[d, "\Delta G_{sol[NO3]}"] & +\ 3L_{(gp)} \arrow[d, "\Delta G_{sol[L]}"] \arrow[r, Leftrightarrow, "\Delta G_{gp}"] & ML_3\ (NO_3)_{3\ (gp)} \arrow[d, "\Delta G_{sol[ML3(NO3)3]}"] \\
M^{3+}{}_{(aq)} & +\ 3\ NO_3^-{}_{(aq)} & +\ 3L_{(org)} \arrow[r, Leftrightarrow, "\Delta G_{ext}"] & ML_3\ (NO_3)_{3\ (org)}
\end{tikzcd}$$

Figure 6.12: Scheme 1, Thermodynamic cycle for the extraction of metal ion where the metal ion and nitrate ion are considered to be as separate solvated species

Though the calculated solution phase selectivity order does not exactly match the experimental trend but the gas phase calculated value nicely follows the experimental trend. From the values it is observed that the selectivity predicted using gas phase free energy becomes changed after inclusion of $\Delta\Delta G_{sol}$ arising due to solvent effect. Also, the value has been reduced drastically due to dielectric screening of the solvent. So solvent plays a important role in the thermodynamic selectivity.

Table 6.16: Calculated values of the thermodynamic parameters (kcal/mol) for the extraction of Ln-An in presence of nitrate anion with TMDGA at the B3LYP/TZVPP level of calculation (T=298.15K; Scheme-1)

M^{3+}	$\Delta G_{(gp)}$	$\Delta G_{sol(M)}$	$\Delta G_{sol(NO3)}$	$\Delta G_{sol(ML3(NO3)3}$	ΔG_{ext}	$\Delta\Delta G_{sol}$
La	-901.99	-711.37	-54.23	-14.77	-22.25	879.74
Eu	-975.20	-775.55	-	-15.62	-32.12	943.08
Lu	-1011.09	-813.34	-	-16.05	-30.64	980.44
Am	-947.43	-755.00		-16.43	-25.71	921.72
Cm	-948.51	-756.81	-	-15.78	-24.33	924.18

Water cluster solvation approach of Scheme-1. In this scheme, the cluster solvation approach of Goddard et al was used where within a cluster of water molecules, the metal ion is submerged as:

$$M^{+}_{(gas)} + (H_2O)_{9(aq)} \rightarrow M^{+}(H_2O)_{9(aq)} \qquad (6.31)$$

Here, the cluster of water consisting of 9 water units was used for the optimization of the structures followed by the evaluation of total energy. The default COSMO radii of atoms were considered for the solvation effect calculation. The computed value of free energy of extraction, ΔG_{ext}, for the transfer of metal ions from aqueous to dodecane phase using explicit solvation of bare metal ion according to Scheme-1 is listed in Table 6.17.

The computed value of ΔG_{ext} was found to be positive and hence indicating that the extraction of metal ions using cluster solvation model is not workable.In Scheme-1, the metal ion was considered to be as isolated hydrated species.In the presence of nitrate ions, the hydrated metal ions prefer to coordinate with the nitrate ions. The free energy of extraction was then further computed using thermodynamic cycle of Scheme-2, **Fig. 6.13**. The solvation of metal nitrate has been considered using two different solvation approaches: mainly, explicit monomer and cluster water solvation model as follows.

Table 6.17 : Calculated value of the thermodynamic parameters (kcal/mol) for the extraction of hydrated Ln-An in presence of nitrate anion with TMDGA at the B3LYP/TZVPP level of calculation (T=298.15K; Scheme-1)

M^{3+}	$\Delta G_{(gp)}$	$\Delta G_{sol(M)}$	$\Delta G_{solM(NO3)3}$	$\Delta G_{sol(ML3(NO3)3}$	ΔG_{ext}	$\Delta\Delta G_{sol}$
La	-901.99	-754.01	-54.23	-14.77	20.38	922.38
Eu	-975.20	-818.19	-	-15.62	10.51	983.90
Lu	-1011.09	-855.98	-	-16.05	11.99	1023.08
Am	-947.43	-797.64	-	-16.43	16.92	964.36
Cm	-948.51	-799.45	-	-15.78	18.31	966.82

Explicit solvation approach using monomer water of Scheme-2.

This solvation scheme is based on the explicit salvation of metal nitrate using monomer water.The calculated free energy of extraction, ΔG_{ext}, values for the transfer of metal ions from aqueous to dodecane phase according to Scheme-2 is listed in Table 6.18.

$$\begin{tikzcd}
M(NO_3)_{3\,(gp)} \arrow[d, "\Delta G_{sol[M(NO3)3]}"] & + & 3L_{(gp)} \arrow[d, "\Delta G_{sol[L]}"] \arrow[r, Leftrightarrow, "\Delta G_{gp}"] & ML_3\,(NO_3)_{3\,(gp)} \arrow[d, "\Delta G_{sol[ML3(NO3)3]}"] \\
M(NO_3)_{3\,(aq)} & + & 3L_{(org)} \arrow[r, Leftrightarrow, "\Delta G_{ext}"] & ML_3\,(NO_3)_{3\,(org)}
\end{tikzcd}$$

Figure 6.13: Scheme 2, Thermodynamic cycle for the extraction of metal ion where the metal ion is considered to be as hydrated nitrate form

The calculated ΔG_{gp} is found to be negative only for La^{3+} ion. The contribution of high positive value of $\Delta\Delta G_{sol}$ makes the overall extraction free energy, ΔG_{ext} positive suggesting unfavourable extraction process. Hence, the extraction of hydrated metal nitrate using explicit monomer water solvation model is not workable due to positive free energy of extraction.

Water cluster solvation approach of Scheme-2.

Here, the cluster of water molecules was considered for solvation of the metal nitrate.The calculated value of free energy of extraction for the transfer of metal ions from aqueous to organic phased using Scheme-2 is listed in Table 6.19. The calculated value of ΔG_{ext} was found to be positive and more positive compared to monomer water model suggesting that the extraction of metal ions using this solvation model is thermodynamically unfavourable. Though Scheme-1 model was exergonic it fails to captures the correct trend of Ln/An extraction with TODGA.

Table 6.18 : Calculated value of thermodynamic parameters (kcal/mol) for the extraction of different nitrate of Ln-An with TMDGA using B3LYP/TZVPP level of calculation at 298.15K (Scheme-2; monomer water model

M^{3+}	$\Delta G_{(gp)}$	$\Delta G_{sol(M)}$	$\Delta G_{solM(NO3)3}$	$\Delta G_{sol(ML3(NO3)3}$	ΔG_{ext}	$\Delta\Delta G_{sol}$
La	-7.30	-24.82	-6.81	-14.77	23.19	30.49
Eu	1.97	-10.26	-	-15.62	16.64	14.66
Lu	0.76	-10.07	-	-16.05	15.66	14.90
Am	2.50	-11.06	-	-16.43	17.59	15.08
Cm	1.44	-10.81	-	-15.78	16.93	15.48

Table 6.19 : Calculated value of thermodynamic parameters (kcal/mol) for the extraction of metal nitrate of Ln-An with TMDGA using B3LYP/TZVPP level of calculation at 298.15K (Scheme-2; cluster water model).

M^{3+}	$\Delta G_{(gp)}$	$\Delta G_{solM(NO3)3}$	$\Delta G_{sol(ML3(NO3)3}$	ΔG_{ext}	$\Delta\Delta G_{sol}$
La	-7.30	-47.60	-14.77	33.92	45.98
Eu	1.97	-33.04	-15.62	38.10	39.42
Lu	0.76	-32.85	-16.05	29.70	38.44
Am	2.50	-33.85	-16.43	32.68	40.38
Cm	1.44	-33.59	-15.78	29.68	39.72

This is due to non-consideration of dispersion correction. Therefore, dispersion correction was performed using the Grimme's DFT-D3 [213] methodology. The calculated results using DFT-D3 for the monomer and cluster water model are presented in Table 6.20 and Table 6.21 respectively.From the Table 6.20, it is seen that the calculated value of metal ion solvation energy was found to be increased after dispersion correction. The gas phase metal-nitrate-ligand complexation free energy was found to be increased substantially. After dispersion correction, the free energy of extraction for the metal ions was seen to follow the order: Lu>Eu>La, which was also observed in the solvent extraction experiments. The cluster model (Table 6.21) also predicts the same trend as observed in the experiments. Both the monomer and cluster water model correctly predicts the experimental trend for Lanthanides.

Table 6.20 : Calculated values of the thermodynamic parameters (kcal/mol) for the extraction of different hydrated Ln-An in presence of nitrate anion with TMDGA at B3LYP-D3/TZVPP level of calculation (T=298.15K; Scheme-1, monomer water).

M^{3+}	$\Delta G_{(gp)}$	$\Delta G_{sol(M)}$	$\Delta G_{solM(NO3)3}$	$\Delta G_{sol(ML3(NO3)3}$	ΔG_{ext}	$\Delta\Delta G_{sol}$
La	-955.13	-770.26	-54.23	-14.77	-16.52	938.61
Eu	-1028.57	-842.49	-	-15.66	-18.60	1009.96
Lu	-1068.91	-877.56	-	-16.04	-24.26	1044.64

Table 6.21: Calculated values of the thermodynamic parameters (kcal/mol) for the extraction of different hydrated Ln-An in presence of nitrate anion with TMDGA at the B3LYP-D3/TZVPP level of calculation (T= 298.15K; Scheme-1, cluster water).

M^{3+}	$\Delta G_{(gp)}$	$\Delta G_{sol(M)}$	$\Delta G_{sol(ML3(NO3)3}$	ΔG_{ext}	$\Delta\Delta G_{sol}$
La	-955.13	-755.24	-14.77	-31.54	923.59
Eu	-1028.57	-827.47	-15.66	-33.62	994.94
Lu	-1068.91	-862.54	-16.04	-39.28	1029.62

The present DFT based study demonstrates the structure, bonding, energetic and thermodynamic parameters of lanthanides and actinides metal ion with diglycolamide in gas phase and solvent phase.The presence of nitrate ion and water molecules are found to be indispensable in order to model the extraction of lanthanides and actinides ion from the aqueous phase to the dodecane organic solvent phase using COSMO solvation approach. The computed value of ΔG_{ext} using thermodynamic cycle was found to be exergonic indicating that TMDGA ligands are able to extract the metal ions from aqueous phase to the dodecane phase.Bonding analyses were performed to study the ionic and covalent nature of interaction of metal ions with TMDGA ligand.In the present case lower analogue of TODGA (TMDGA) has been used to simulate the experimental selectivity to keep the computation tractable. The results from the present study helps in the understanding of Ln/An complexation with amide based ligand and hence in the improved design of ligands for actinides and lanthanides from nuclear waste solution.

6.11 DFT Study for the Complexation of Actinides with Amido Amine Functionalized MWCNT

Computational methodology

All-electron Kohn–Sham DFT calculations were performed by using quantum chemical program Turbomole. The optimized structureand total energy of AA-SWNT and its complexes with uranyl and americium in presence of nitrate anions were computed using generalized gradient approximated hybrid B3LYP density functional employing SVP basis set i.e. O (7s4p1d)/[3s2p1d], C(7s4p1d)/[3s2p1d], H(4s1p)/[2s1p], and N(7s4p1d)/[3s2p1d], U(14s13p10d8f1g)/[10s9p5d4f1g],and Am(14s13p10d8f1g)/[10s9p5d4f1g]. Further, single point energy of all the optimized structures were computed using hybrid B3LYP functional employing TZVP basis set i.e O (11s6p2d1f)/[5s3p2d1f], C(11s6p2d1f)/ [5s3p2d1f], H(5s2p1d)/[3s2p1d], N(11s6p1d) / [5s3p1d], Am(14s13p10d8f1g)/[10s9p5d4f1g], and U(14s13p10d8f1g)/[10s9p5d4f1g]. B3LYP is a hybrid functional contains Becke's 3 paramater exchange correlation functional which uses 3 parameters to mix in the exact Hartree-Fock exchange correlation and Lee, Yang and Parr correlation functional that recovers dynamic electron correlation. COSMO is a continuum solvation model which considers the polarization charges on the medium caused by the polarity of the solute molecule inside a molecular cavity surrounded by solvent dielectric continuum from a scaled-conductor approximation. Aqueous phase calculation are more accurate in COSMO because water with infinite permittivity ($\varepsilon \approx 80$) behaves like an ideal conductor. All structures are visualized with MOLDEN.

DFT calculations

1:1 complex between the actinide ion (UO_2^{2+} and Am^{3+}) and AA-MWCNT in presence of nitrate ions are considered following the complexation reaction mentioned in

Equation 6.32. The optimized structures of the AA-MWCNT are shown in **Fig. 6.14(a).** The amidoamine unit attached with a carbon atom at the open edge of the CNT is projected outward. The optimized complex structures of the UO_2^{2+} and $Am^{3+}$with AA-MWCNT in presence of NO_3^- ions are shown in **Fig. 6.14(b)** and **Fig. 6.14(c)**, respectively. Only NO_3^- ions are considered in the first coordination shell of the actinide ions owing to the stronger coordination ability of NO_3^- than H_2O molecules. The carbonyl oxygen of amide part and the nitrogen of the amine part of the amidoamine unit in AA-MWCNT are coordinated with the metal ion. As shown in the **Fig. 6.14(b)**, for uranium complex, two NO_3^-coordinate to the central uranium ion in bidentate mode, amidoamine unit of CNT coordinates in bidentate mode, give rise to 8-coordinated complex including the two coordination from two oxo groups. For, Am complex, bidentate coordination from three $NO_3^-$and same for the amidoamine also result in 8-coordination environment. The bond distances between the metal coordination center and the donor atom (O and N) for the optimized structures are summarized in Table 6.22. For both of the complexes, smaller M-O(C=O) bond length than that of M-O(NO_3) indicates that amide carbonyl has stronger coordination ability than the nitrates. Again, for both of the complexes, Smaller metal to carbonyl oxygen distance than that of metal to nitrogen suggests that carbonyl oxygen have stronger coordination ability than the amine nitrogen. The M-O(C=O) bond length is smaller (2.378 Å) for the U complex compared to the Am complex (2.399 Å). This indicates that AA-MWCNT has stronger complexation ability for U compared to Am. The coordination nature of amide carbonyl oxygen and amine nitrogen can also be seen from the elongation of C=O (1.267 or 1.260 Å from 1.230 Å) and C-N (1.468 and 1.475 Å from 1.454 Å) bonds after complexation which is the result of coordination with the metal ions by the donor sites.

$$M^{n+} + n\,NO^{3-} + \text{AA-MWCNT} \longrightarrow M(NO_3)_n\,\text{AA-MWCNT} \quad (6.32)$$

The binding energy and free energy change of the complexation reaction (equation 6.32) for UO_2^{2+} and $Am^{3+}$are shown in Table 6.23. The ΔG values for the two actinide ions are very negative both in gas and aqueous phase, indicating favorable nature of the adsorption of these radionuclides on the AA-MWCNT as depicted by our experiments. It can also be seen from the table that ΔE or ΔG values are reduce significantly from gas phase to solution phase, suggesting that the solvation/hydration of the metal ions plays a crucial role in the complexation process. The role of solvation of metal ions can clearly be understood from the table that the gas phase ΔE_{gas}or $\Delta G_{gas}$is higher for Am^{3+} compared to UO_2^{2+}, whereas, the solution phase ΔE_{aq} or ΔG_{aq} is higher for UO_2^{2+} (-168.317 kcal mol^{-1} or -105.359 kcal mol^{-1}) compared to Am^{3+} (-107.964 kcal mol^{-1} or -56.657 kcal mol^{-1}) which is good agreement with our experimental adsorption studies that AA-MWCNT have higher capacity for UO_2^{2+}(20.66 mg g^{-1}) than Am^{3+}(6.10 mg g^{-1}).

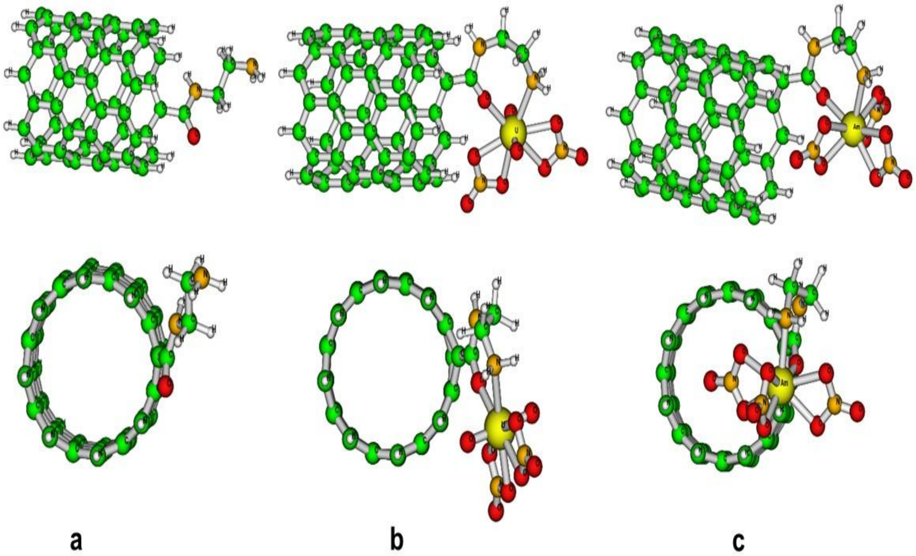

Figure 6.14: Geometric optimized molecular structures of the (a) AA- MWCNT, (b) $UO_2(NO_3)_2$ AA-MWCNT complex, and (c) $Am(NO_3)_3$AA-MWCNT complex at B3LYP/SVP level of theory.

Table 6.22: Calculated M-O and M-N distances in Å for the AA-MWCNT and its complexes with UO_2^{2+} and Am^{3+} in presence of nitrate ions

Bonds	Molecular System		
	$UO_2(NO_3)_2$AA-MWCNT	$Am(NO_3)_3$AA-MWCNT	AA-MWCNT
M-O(C=O)	2.378	2.399	
M-N(NH_2)	2.689	2.615	
M-O(NO_3)*	2.503	2.474	
C=O(Amide)	1.267	1.260	1.230
C-N(Amine)	1.468	1.475	1.454

*Averages of all the M-O distances between M and NO_3^-.

Table 6.23: .Calculated binding energy (ΔE) and Gibbs free energy change(ΔG)in kcal mol^{-1} of complexation reactions in gas and aqueous phase between the metal ions and AA-MWCNT in presence of nitrate ions.

Complexation of	ΔE_{gas}	ΔG_{gas}	ΔE_{aq}	ΔG_{aq}
UO_2^{2+}	-591.627	-528.663	-168.317	-105.359
Am^{3+}	-1041.645	-990.338	-107.964	-56.657

6.12 DFT Study for the Complexation of Actinides and Lanthanides with DPA Functionalized TiO_2

Computational methodology

Structures of free Dipicolinic acid (DPA) functionalized on a (101) TiO_2 surface [214] and its complexes with lanthanide and actinide ions in presence of nitrate ion have been optimized using Becke-Lee-Young-Parr (B3LYP) density functional employing split-valence plus polarization (SVP) basis set as implemented in the TURBOMOLE suite of program .

Optimization of the structure was carried out keeping the structure of TiO_2 fixed. The scalar relativistic effective core potentials (ECP) were used for Eu^{3+} ion where 28 electrons and for $Th^{4+}$and UO_2^{2+} ions where 60 electrons were kept in the core. The septate spin state was used during the computation of structure and energy. Optimization was performed without any symmetry restrictions. B3LYP functional was used to compute the free energy at 298.15K. The solvent phase was accounted for using popular conductor like screening model (COSMO). The dielectric constant of water was taken to be 80. The model complexation reaction was used as follows

$$[M(H_2O)_9]^{3+}_{(aq)} + 3NO_3^-{}_{(aq)} + L_{(aq)} \longrightarrow M(NO_3)_3\text{-}L_{(aq)} + 9H_2O \quad (M=Eu/Am) \quad (6.33)$$

Structural parameters

The minimum energy structures of free TiO_2-DPA molecule are displayed in **Fig. 6.15**, whereas complex of Eu^{3+} and Am^{3+} ions towards TiO_2-DPA in presence of nitrate are displayed in **Figs. 6.16** and **Fig. 6.17** respectively. From the optimized structure, the Ti-O (O of APTES) distance was found to be 2.028Å, whereas Si-O (O from TiO_2) distance was of 1.693Å. The calculated structural parameters for complex of lanthanide and actinide ions towards TiO_2-DPA are presented in Table 6.24. The metal oxygen bond distance with amidic O was found to be shorter than that of ethereal O atom indicates that the amidic O will leads to stronger interaction compared to ethereal O atom. Point to be noted, metal oxygen bond distance with nitrate O was found to be shorter than that of both amidic O and ethereal O atoms for moth the ions.

Thermodynamical free energy of complexation

The free energy of complexation for both lanthanide and actinide ions with TiO_2-DPA in the gas phase and solution phase is presented in Table 6.25. The explicit hydration of trivalent both metal ions with 9 water molecules in the first solvation shell was considered for evaluating the complexation free energy as it was found to reproduce the experimental solvation energy quite accurately. But for thorium and uranium they are ten and nine respectively.The entropy of complexation was found to be positive and high. The well known COSMO solvation approach was used to simulate the solvent phase as it was able to predict the solvent phase properties quite accurately. The aqueous phase was modeled using dielectric constant of 80. The calculated solution phase free energy of adsorption is given in Table 6.25. TiO_2-DPA molecule was found to be selective for Eu^{3+} ion over Am^{3+} and Th^{4+} ion over UO_2^{2+} in both the gas and solution phases.

Bonding analysis

In order to get an insight into the nature of bonding in the complexes of metal ions with TiO_2-DPA, The method of natural population analysis (NPA) was utilized study the charge on the metal ions and atomic orbital population in the complexes.

The calculated values are presented in Table 6.26. The large positive charge on the metal ions indicates the ion-dipole type of interaction. From NPA, it is revealed that there is small extra orbital contribution to the inner s, and f sub shells and significant contribution in the d sub shells of the metal ion indicating that the interaction of metal ion with ligand has some covalent character. The s and f sub shells are less diffused than the d subshell.

Table 6.24: Calculated structural parameters (in Å) of metal ions with TiO_2-APTES-DPA in presence of nitrate ion.

System	M-$O_{C=O}$ (Å)	M-$O_{ethereal}$ (Å)	M-O_{NO3} (Å)
$Eu(NO_3)_3$-L	2.51- 2.72	2.65	2.41- 2.46
$Am(NO_3)_3$-L	2.57- 2.75	2.67	2.44 – 2.50
$Th(NO_3)_4$-L	2.55- 2.62	2.77	2.44 - 2.64
$UO_2(NO_3)_2$-L	2.64 -2.76	2.91	2.44 – 2.50

Table 6.25: Calculated value of Gibbs free energy (kcal/mol) in the gas and aqueous phase

Equilibrium reaction	Free energy of adsorption (kcal/mol)	
	Gas phase	Aqueous phase
$[Eu(H_2O)_9]^{3+}{}_{(aq)} + 3NO_3^-{}_{(aq)} + L_{(aq)} \rightarrow Eu(NO_3)_3\text{-}L_{(aq)} + 9H_2O$	-617.6	-135.1
$[Am(H_2O)_9]^{3+}{}_{(aq)} + 3NO_3^-{}_{(aq)} + L_{(aq)} \rightarrow Am(NO_3)_3\text{-}L_{(aq)} + 9H_2O$	-612.7	-129.9
$[Th(H_2O)_{10}]^{4+}{}_{(aq)} + 4NO_3^-{}_{(aq)} + L_{(aq)} \rightarrow Th(NO_3)_4\text{-}L_{(aq)} + 10H_2O$	-915.2	-114.1
$[UO_2(H_2O)_5]^{2+}{}_{(aq)} + 2NO_3^-{}_{(aq)} + L_{(aq)} \rightarrow UO_2(NO_3)_2\text{-}L_{(aq)} + 5H_2O$	-343.7	-80.41

Table 6.26: Calculated charge and orbital population using NBO analysis gas phase at the B3LYP/TZVP level of theory.

System	charge	s	p	d	f
$Eu(NO_3)_3$-L	1.77	4.17	11.99	10.90	6.14
$Am(NO_3)_3$-L	1.83	4.19	11.99	10.78	6.19
$Th(NO_3)_4$-L	1.72	4.21	11.99	11.13	0.93
$UO_2(NO_3)_2$-L	1.81	4.17	11.76	11.49	2.73

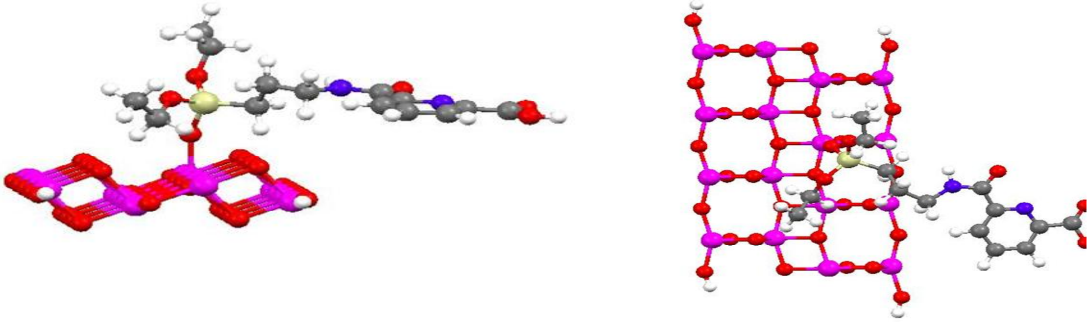

Figure 6.15: Optimized structures of TiO_2-APTES-DPA molecule

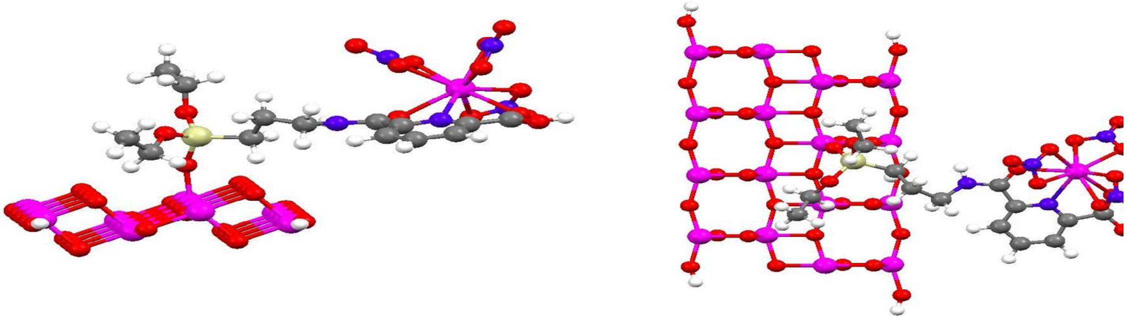

Figure 6.16: Optimized structure of TiO_2-APTES-DPA-$Eu(NO_3)_3$

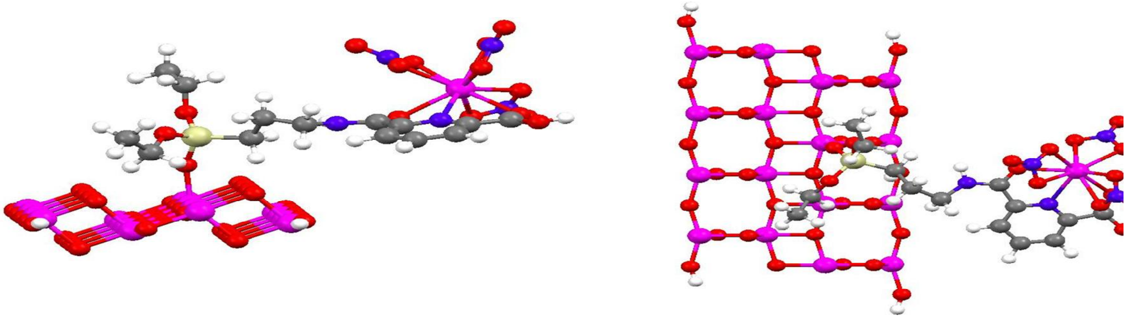

Figure 6.17: Optimized structure of TiO_2-APTES-DPA-$Am(NO_3)_3$

6.13 DFT Study for the Complexation of Trivalent Actinide and Lanthanide with DGA Functionalized TiO_2

Computational methodology

Structures of free DGA functionalized on a (101) TiO_2 surface and its complexation with Eu^{3+} and Am^{3+} ions along with nitrate ion have been optimized.Structural optimization and thermodynamical parameters were calculated using B3LYP density functional employing SVP basis set. During optimization the anatase structure was kept fixed. The septate spin state was used during the computation of structure and energy. Optimization was performed without any symmetry restrictions. The free energy was computed at 298.15K using B3LYP functional. The hybrid B3LYP functional was used in predicting the thermodynamic properties of actinides. The solvent phase was accounted for using popular conductor like screening model (COSMO). The model complexation reaction was used as follows

$$[M(H_2O)_9[^{3+}{}_{(aq)} + 3NO_3^-{}_{(aq)} + L_{(aq)} \longrightarrow M(NO_3)_3\text{-}L_{(aq)} \quad +9H_2O \quad (M=Eu/Am) \qquad (6.34)$$

Since, there is very small effect on the solvation energy between the gas phase and solvent phase geometry , the aqueous solvent effect was integrated by performing single point energy calculation using the optimized geometry obtained from B3LYP level of theory employing COSMO solvation model.

Structural parameters

The minimum energy structures of free DGA functionalized TiO_2 molecule are displayed in **Fig. 6.18(a)**, whereas complex of Eu^{3+} and Am^{3+} ions towards DGA-TiO_2 in presence of nitrate are displayed in **Fig. 6.18(b)** and **Fig. 6.18(c)** respectively. From the optimized structure, the Ti-O (O of APTES) distance was found to be 2.03 Å, whereas Si-O (O from

TiO_2) distance was of 1.70Å. The calculated structural parameters for complex of Eu^{3+} and Am^{3+} ions towards DGA-TiO_2 are presented in Table. 6.27. The metal oxygen bond distance with amidic O was found to be shorter than that of ethereal O atom indicates that the amidic O will leads to stronger interaction compared to ethereal O atom. Point to be noted, metal oxygen bond distance with nitrate O was found to be shorter than that of both amidic O and ethereal O atoms for moth the ions.

Thermodynamical free energy of complexation

The Gibbs free energy of adsorption for both Eu^{3+} and Am^{3+} ions with DGA- TiO_2 in the gas phase and solution phase is presented in Table 6.28. The explicit hydration of both metal ions with 9 water molecules in the first solvation shell was considered for evaluating the complexation free energy. The entropy of complexation was found to be positive and quite high. The well known COSMO solvation approach was used to simulate the solvent phase as it was able to predict the solvent phase properties quite accurately. The aqueous phase was modeled using dielectric constant of 80. DGA- TiO_2 molecule was found to be selective for Eu^{3+} ion over Am^{3+} ion in both the gas and solution phases.

Conclusion

The DFT calculated solvent phase free energy of adsorption for Eu^{3+} ion was found to be higher than Am^{3+} ion as observed in the experiments. Different bonding analysis indicates the electrostatic and small covalent nature of interactions between the metal ions and the DGA-TiO_2 molecule.

Table 6.27: Calculated structural parameters (in Å) of complexes of Eu^{3+} and Am^{3+} ion with DGA-TiO_2 in presence of nitrate ion.

System	M-$O_{C=O}$ (Å)	M-$O_{ethereal}$ (Å)	M-O_{NO3}(Å)
$Eu(NO_3)_3$-L	2.46, 2.59	2.65	2.41- 2.46
$Am(NO_3)_3$-L	2.52, 2.62	2.66	2.44 – 2.49

Table 6.28: Calculated value of Gibbs free energy (kcal/mol) in the gas and aqueous phase

Equilibrium reaction	Free energy of adsorption (kcal/mol)	
	Gas phase	Aqueous phase
$[Eu(H_2O)_9]^{3+}_{(aq)} + 3NO_3^-{}_{(aq)} + L_{(aq)} \longrightarrow Eu(NO_3)_3\text{-}L_{(aq)} + 9H_2O$	-536.7	-55.47
$[Am(H_2O)_9]^{3+}_{(aq)} + 3NO_3^-{}_{(aq)} + L_{(aq)} \longrightarrow Am(NO_3)_3\text{-}L_{(aq)} + 9H_2O$	-529.3	-51.55

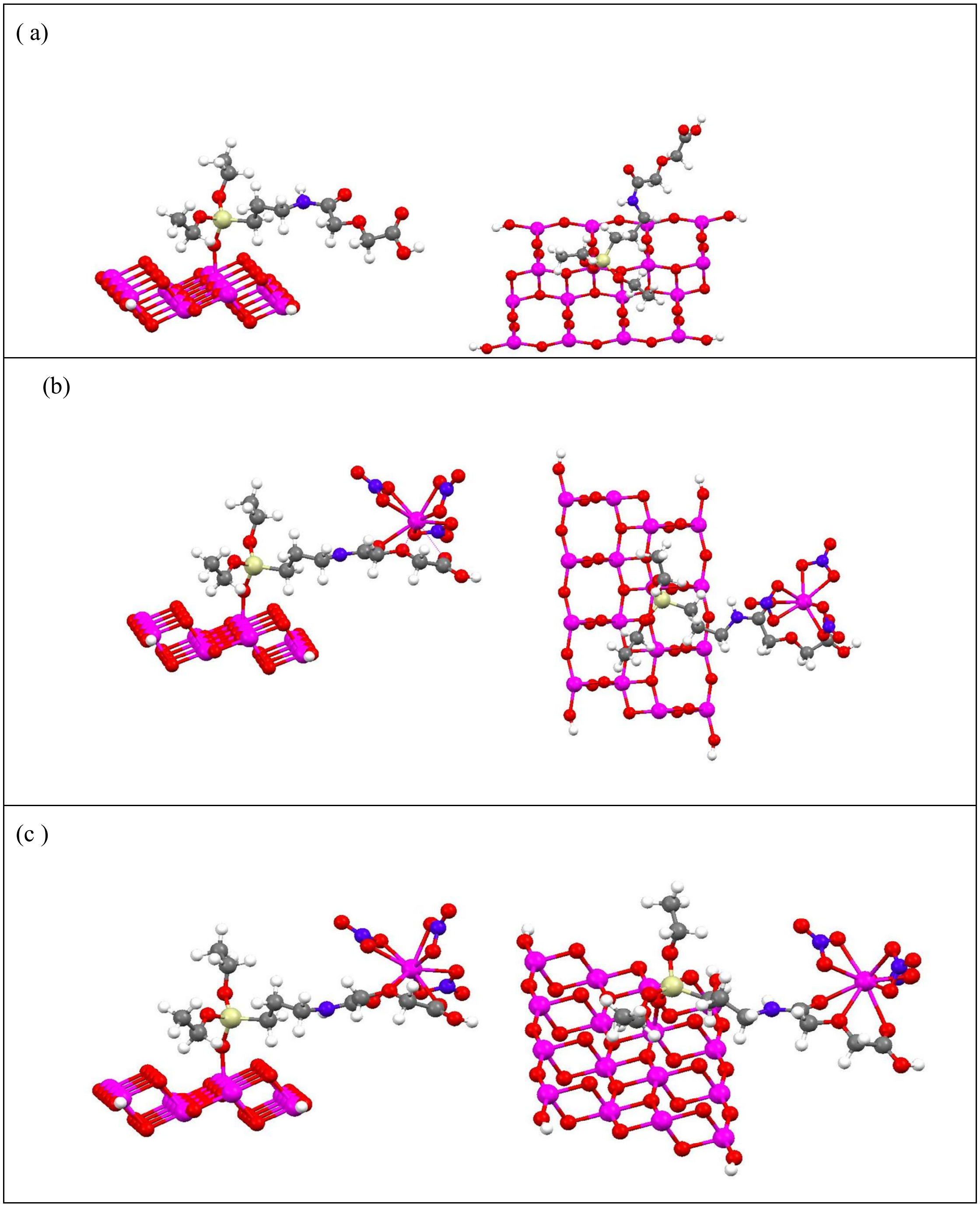

Figure 6.18: Optimized structures of (a)TiO_2-APTES-DGA molecule (b) TiO_2-APTES-DGA-$Eu(NO_3)_3$ (c) TiO_2-APTES-DGA-$Am(NO_3)_3$

6.14 Summary of the Investigation

The results reported in this chapter are summarized as follows. Structure, bonding, energetic parameter and thermodynamic parameters of UO_2^{2+} and Pu^{4+} ion with TMDGA ligand in the gas and solvent phase are reported using density functional theory. The calculated structure obtained at BP86/SVP level of optimization was found to be in close agreement with the experimentally reported structural data. The free energy of extraction, ΔGext, of UO_2^{2+} and Pu^{4+} ions from aqueous phase to the dodecane solvent phase was computed using the Born-Haber thermodynamic cycle in conjunction with COSMO (conductor like screening model) solvation approach. The results using the concept of hydrated metal nitrate fail to capture the experimental selectivity trend, whereas our present results based on thermodynamic cycle using separate hydrated metal ion and nitrate species capture the experimental selectivity.

In case of extraction of trivalent actinides and lanthanides using DGA based ligand the calculated value of ΔGext was found to be exergonic indicating that TMDGA ligands are able to extract the metal ions from the aqueous phase to the dodecane phase. The calculated preferential selectivity follows the order $Eu^{3+} > Lu^{3+} > Am^{3+} > Cm^{3+} > La^{3+}$, whereas the distribution ratio in the solvent extraction experiments follows the trend $Lu^{3+} > Eu^{3+} > Cm^{3+} > Am^{3+} > La^{3+}$. Though the calculated selectivity order in the solution phase does not exactly match the experimental trend the gas phase calculated value follows the experimental trend nicely. Dispersion corrected (DFT-D3), free energy of extraction for the lanthanide ions follow the order: Lu > Eu> La, validate the result of solvent extraction experiments. The present results successfully capture the experimental selectivity order taking into account the complete molecular stoichiometry, anions and experimentally used organic solvents. In the present case, a lower analogue of TODGA (TMDGA) has been used to simulate the experimental selectivity to keep the computation tractable.

References

---

[1] www.iaea.org Nuclear Technology Review, September 2018.

[2]IAEA Nuclear Technology Review **2009**, IAEA, Vienna, 3.

[3]World Nuclear Association, Nuclear power in India,http://www.worldnuclear.org/info/inf53.htm

[4] Seaborg, G.T. *Nucleonics*, **1949**, *5*, 16.

[5] Seaborg, G.T.; Katz, J. J. *The Actinide elements*, Ed I, McGraw – Hill book company, Inc. **1954**, 733

[6] Kim J.I. *Nucl. Eng. Technol.* **2006***, 38(6)*, 459.

[7] Arnikar, H. J. *Essentials of Nuclear Chemistry*, Wiley Eastern Limited, New Delhi, 2nd edn., 1988

[8]PhD thesis of Raut, D. R. Mumbai University **2011**.

[9] Bajaj, S. S.; Gore, A. R. *Nucl. Eng. Des.* **2006**, *236*, 701.

[10] Semenov, B. A.; Oi, N. *Nuclear Fuel Cycles- Adjusting to new realities*, IAEA Bulletin, Vienna, Austria, 1993.

[11] Anderson, H. H.; Asprey, L. B. *Solvent extraction process for plutonium*, US patent No. 2924506, **1947**.

[12] Irish, E.R. *Description of PUREX plant process*, U. S. Tech. Rep., HW-60116,**1959.**

[13] Schulz, W.; Navratil, J. D.; Talbot, A. E. *Science and technology of tributyl phosphate*, CRC Press, Florida, **1984.**

---

[14] McKay, H.A.C.; Miles, J.H.; Swanson, J.L. *Applications of Tributyl Phosphate inNuclear Fuel Reprocessing, In —Science and Technology of Tributyl Phosphate*, CRC Press Inc., Boca Raton, Florida, **1990**, *3*, 55.

[15] Holder, J.V. *Radiochim. Acta*. **1978**, *25*, 171.

[16] *Classification of Radioactive Waste*, IAEA Safety Standards No GSG-1, IAEA,Vienna, Austria, 2009.

[17] Banerjee, D.; Rao, M. A.; Samanta, S. K. *DAE. BRNS Symposium on Emerging Trends in Separation Science and Technology, (SESTEC),* **2006***,* 264.

[18] Kumar, A.; Varshney, L.; Bhalerao, P.;Kaushik C. P.; Raj, K. *DAE. BRNS Symposium on Emerging Trends in Separation Science and Technology, (SESTEC),***2008***,* 179.

[19] Choppin, G. R.; Ridberg, R. J.; Lilljenzin, J. O. *Rdiochemistry and Nuclear Chemistry* 2nd edition, Oxford, Butterworth Communication.

[20] Composition of HLW calculated, Achutan, P. V. (private communication)

[21] McCombie, C. *Phys. Today*. **1997**, *50*, 56.

[22] Alexander, W. R.; McKinley, L. E. *Deep geological disposal of radioactive waste*, 2007, Elsevier, Amsterdam, The Netherlands.

[23] Kaushik, C.P.; Mishra, R.K.,;Sengupta, P.; Kumar, A.; Das, D.; Kale, G.B.; Raj, K. (2006), *J. Nucl. Mater.* **2006***,358*, 129.

[24] Fukasawa, T.; Inagaki, Y.; Arima, T.; Sato, S. *Procedia Chemistry*, **2016**, *21*, 365-370.

[25] Ansari, S.; Pathak, P. N.; Mohapatra, P. K.; Manchanda, V. K. *Separation and Purification Reviews.***2011**,*40(1),* 43-76.

---

[26] Horwitz, E. P.; Kalina, D. G.; Vandrift, G.F.; Schulz, W.W. *Solv. Extr. Ion Exch.*, **1985**,*3*, 75.

[27] Schultz, W.W.; Horwitz , E.P. *Sep. Sci. Technol.* **1988**, *23*, 1191.

[28] Chitnis, R.R.; Wattal, P. K.; Ramanujam, A.; Dhami, P.S.; Goparkrishnan, V.; Bauri, A.K.; Banergy, A. *J. Radioanal. Nucl. Chem*, **1999**, *240*, 721.

[29] Zhu, Y.; Jio, R.; Wang, S.; Fan, S.; Leu, B.; Zheng, H.; Zhou, S.; Chen, S. *ISEC-1983*, Denver, Colorado, USA.

[30] Zhu,Y.; Jiao, R. *Nucl. Technol.* **1994**,*108*, 361.

[31] Jiao, R.; Wang, S.; Fan, S.; Liu, B.; Zhu, Y. *J. Nucl. Radiochem.* **1985**, *7*, 65.

[32] Morita, Y.; Kubota, M. *J. Nucl. Sci. Technol*,**1987**, *24*, 227.

[33] Morita, Y.; Yamaguchi, I.; Kondo,Y.; Shirahashi, K.; Yamagishi, I.; Fujirawa, T.; Kubota, M. IAEA-TECDOC-783, IAEA ,Vienna ,**1995** , 93.

[34] Cuillerdier, C.; Musikas, C.; Hoel, P.; Nigond, L.; Vitart, X. *Sep. Sci. Technol.* **1991**, *26*, 1229.

[35] Cuillerdier, C.; Musikas, C.; Nigond, L. *Sep. Sci. Technol.* **1993**, *28*, 155.

[36] Nigond, L.; Musikas, C.; Cuillerdier, C. *Solv. Extr. Ion Exch.* **1994**, *12,* 261.

[37] Nigond, L.; Musikas, C.; Cuillerdier, C. *Solv. Extr. Ion Exch.* **1994**, *12*, 297.

[38] Mahajan, G. R.; Prabhu, D. R.; Manchanda, V. K.; Badheka, L. P. *Waste Management.* **1998**, *18*, 125.

[39] Kumbhare, L. B.; Prabhu, D. R.; Mahajan, G. R.; Sriram ,S.; Manchanda, V. K. *Nucl. Technol.* **2002**, *139*, 253.

---

[40] Purroy, D.S.; Baron, P.; Christiansen, B.; Glatz, J. P.; Madic, C.; Malmbeck, R.; Modolo, G. *Sep. Purif. Technol*. **2005**, *45*, 157.

[41] Spjuth, L.; Liljenzin, J. O.; Hudson, M. J.; Drew, M.G.B.; Iveson, B.P.; Madic, C. *Solv. Extr. Ion Exch*. **2000**, *18*, 1.

[42] Stephan, H.; Gloe, K.; Bager, J.; Muhl, P. *Solv. Extr. Ion Exch*. **1991**, *9*, 435.

[43] Stephan, H.; Gloe, K.; Bager, J.; Muhl, P. *Solv. Extr. Ion Exch*. **1991**, *9*, 459.

[44] Sasaki, Y.; Choppin, G. R. *Anal. Sci*. **1996**, *12*, 225.

[45] Sasaki, Y.; Choppin, G.R. *J. Radioanal. Nucl. Chem*. **1997**, *207*, 383.

[46] Sasaki, Y.; Adachi, T.; Choppin, G. R. *J. Alloy comp*. **1998**, *271-273*, 799.

[47] Sasaki, Y.; Choppin, G.R. *Radiochim. Acta*. **1998**, *80*, 85.

[48] Sasaki, Y.; Choppin, G. R. *J. Radioanal. Nucl. Chem*. **2000**, *246*, 267.

[49] Narita, H.; Yaita, T.; Tamura, K.; Tachimori, S. *Radiochim. Acta*, **1998**, *81*, 223.

[50] Narita, H.; Yaita, T.; Tachimori, S. *Solvent Extraction for the 21st Century, Proceedings of ISEC'99*, Barcelona, Spain, July, 1999; Society of Chemical Industry: London, 2001, *1*, 693.

[51] Sasaki, Y.; Sugo, Y.; Suzuki, S.; Tachimori, S. *Solv. Extr. Ion Exch*. **2001**, *19*, 91.

[52] Diamond, R. M.; Street, K.; Seaborg, G. T. *J. Am. Chem. Soc.* **1954**, *76*, 1461.

[53] Baybarz, R. D.; Weaver, B. S.; Kinser, H. B. *Nucl. Sci. Engg.* **1963**, *17*, 457

[54] Weaver, B.; Kappelmann, F. A. *J. Inorg. Nucl. Chem.*, **1968,** *30*, 263

[55] Hudson, M. J.; Hagström, I.; Spjuth, L.; Enarsson, Å.; Liljenzin, J. O.; Skålberg,M.; Iveson, P. B.; Madic, C.; Cordier, P.Y.; Hill, C.; Francois, N. *Solv. Extr.Ion. Exch.*, **1999,** *178*, 221.

---

[56] Cordier, P.Y.; Hill, C.; Baron, P.; Madic, C.; Hudson, M. J.; Liljenzin, J. O. *J.Alloys Compds*. **1998,** *738*, 271.

[57] Kolarik, Z.; Müllich, U.; Gassner, F. *Solv. Extr. Ion. Exch.* **1999**, *17*, 23.

[58] Kolarik, Z.; Müllich, U.; Gassner, F. *Solv. Extr. Ion. Exch.* **1999**, *17*,1155.

[59] Geist, A.; Hill, C.; Modolo, G.; Foreman, M. R.; Weigl, M.; Gompper, K.; Hudson, M. J.; Madic, C. *Solv. Extr. Ion Exch.* **2006,** *24*, 463.

[60] Modolo, G.; Odoj, R. *Solv. Extr. Ion Exch*., **1999,** *17(1)*,33.

[61] Modolo, G.; Odoj, R.; Baron, P. *Proc. Global 99 (International Conference onFuture Nuclear Systems)*, Jackson Hole, Wyoming, USA, August 29-September3, **1999**

[62] Madic, C.; Hudson, M. J.; Liljenzin, J. O.; Glatz, J. P.; Nannicini, R.; Facchini, A.; Kolarik, Z.; Odoj, R. EUR 19149, European Commission, Luxembourg , **2000.**

[63] Zhu, Y.; Chen, J.; Jiao, R. *Solv. Extr. Ion Exch*. **1996,** *14*, 61.

[64] Ahrland, S.; Liljenzin, J.O.; Rydberg, J.*Solution Chemistry*, In ‛Comprehensive Inorganic Chemistry’, Pergamon Press, Oxford, **1973**, *5*, 465.

[65] Liu, G.; Beitz, J. V. *The chemistry of the actinide and transactinide elements*, volume 3, chapter 18, edited by Morss, L. R.; Edelstein, N. K.; Fuger, J. Springer, **2006**.

[66] Huheey, J. E., Keiter, E.A., Keiter, R.L., Medhi, O.K. *Some Descriptive Chemistry of the Metals in Inorganic Chemistry Principles of Structure and Reactivity*, Dorling Kindersley,2006, 369

[67] Choppin, G. R.; Jensen, M.P. *The chemistry of the actinide and transactinide elements, volume* 4, chapter 23, edited by Morss, L.R.; Edelstein, N. K.; Fuger, J. Springer 2006.

---

[68] Ahrland, S.; Liljenzin, J.O.; Rydberg, J. Solution chemistry, in *Comprehensive Inorganic Chemistry*, *J.C. Bailar Jr., H.J. Emeleus, R. Nyhlom and A.F.T. Dickenson(Eds.)*, Pergamon Press, Oxford, **1973**, 465.

[69] Spitsyn, V.I.; Gelman, A.D.; Krot, N.N.; Mefodiyeva, M.P.; Zacharova, F.A.; Komokov, Y.A.; Shilov, V.P.; Smirnovam, I.V. *J. Inorg. Nucl. Chem*. **1969**, *31*, 2733.

[70] Choppin, G.R.; Allard, B. *Handbook on the physics and chemistry of the Actinides (Eds.) A.J. Freeman and C. Keller*, Elsevier Science Publ,**1985**, 407.

[71] Cotton, F. A.; Wilkinson, G. *Advanced Inorganic Chemistry*, 5th ed.; Wiley: NewYork, 1988, 980-993

[72] Hay, P. J.; Martin, R. L.; Schreckenbach, G. *J. Phys. Chem. A* **2001**, *104*, 6259.

[73] Fischer, R.; Werner, G. D.; Lehmann, T.; Hoffmann, G.; Weigel, F. *J. Less-Common Met.* **1981**, *80*, 121.

[74] Hollemann, A. F.; Wiberg, N. *Lehrbuch der Anorganischen Chemie*, 101. Auflage; de Gruyter, Berlin, **1995**, 1793-1821.

[75] PhD thesis of Schlosser, F., Technische Universität München , 2006.

[76] Wick, O.J. "*Plutonium Hand Book: A Guide to the Technology*", Gordon and Breach, New York, **1967**, *1*, 438.

[77] Rainey, R.H. USAEC Report CF-59-12-95,1959.

[78] Cleveland, J. M. "*The chemistry of plutonium*", Gordon and Breach, New York, **1970**, 84.

[79] Choppin, G. R.; Rao, L. F. Radiochim. Acta.**1984**, *37*, 143.

[80] Pearson, R.G. *J. Am. Chem. Soc*. **1963**, *85*, 3533.

---

[81] Martell, A.E.; Smith, R.M.; Motekaitis, R.J.; *Critically selected stabilityconstants of metal complexes database version 5.0.* NIST standard reference data, Gaithersburg, MD 1998.

[82] Shannon, R.D. Acta Crystallogr. **1976**, *32A*, 751.

[83] Jensen, M. P.; Beitz, J. V.; Rogers, R. D.; Nash, K. L. J. Alloys Compnd. **2000**, *303/304*, 137.

[84] Eigen, M.; Wilkins, R.G. Adv. Chem. Ser. **1965**, *49* , 55.

[85] Marcus, Y.; Kertes, A. S. *Ion exchange and solvent extraction of metal complex.*1969

[86] Fendler, H. J. *J. Membr. Sci.* **1987**, *30*, 323.

[87] Larivière, D.; Cumming, T. A.; Kiser,S.; Li, C.; Cornett, R. J. J. Anal. At. Spectrom. **2008**, *23*, 352–360.

[88] Tranter, T. J. *Solid-phase extraction technology for actinide and lanthanide separations in nuclear fuel reprocessing*., 2011

[89] Florek, J.; Giret, S.; Juère, E.; Larivière ,D.; Kleitz, F. Dalton Trans. **2016**, *45*, 14832.

[90] Handley, H.W.; Jones, P.; Ebdon, L.; Barnett, N.W. 'Research and development topics in analytical chemistry', *Analytical Proceedings*,**1991**, *28*, 37.

[91] Sudderth, R.B., Kordosky, G.A. 'Some practical considerations in the evaluation and selection of solvent extraction reagents', *Chemical Reagents in the Mineral Processing Industry*. Eds Malhotra, D. and Riggs, W.F., S.M.E., Littleton Colorado,1986, 181–196.

[92] Eschrich, H., Ochsenfeld, W. *Sep. Sci. Technol*, **1980**,*15(4*), 697–732.

---

[93] Lumetta, G.J.; Wester, D.W.; Morrey, J.R.; Wagner, M.J. (1993), *Solv. Extr. Ion Exch.* **1993**, *11(4),*663–682.

[94] Barney, G.S., Cowan, R.G. *Separation of Actinide Ions from Radioactive Waste Solutions Using Extraction Chromatography*, WHC-SA-1520-FP, Westinghouse Hanford Company, Richland, Washington, 1992.

[95] Hoshi, H.; Wei, Y.; Kumagai, M.; Asakura, T.; Morita, Y. *J. of Alloys and Compounds*, **2004**, *374*, 451–453.

[96] Modolo, G.; Asp, H.; Schreinemachers, C.; Vijgen, H. *Radiochim. Acta*. **2007**, *95*, 391–397

[97] Zhang, A.; Kuraoka, E.; Hoshi, H.; Kumagai, M. *J. Chromatogr. A*, **2004**, *1061*, 175–182.

[98] Wei, Y.; Zhang, A.; Kumagai, M.; Watanabe, M.; Hayashi, N. *J. Nucl. Sci. Technol.* **2004**, *41*, 315–322.

[99] Zhang, A., Wei, Y., Kumagai, M., Koma, Y. (2005) *J. Alloys Compd.* **2005**,*390*, 275–281.

[100] Zhang, A.; Hu, Q.; Wang, W.; Kuraoka, E. *Ind. Eng. Chem. Res.* **2008***,* *47*, 6158–6165.

[101] Wei, Y.; Hoshi, H.; Humagai, M.; Asakura, T.; Morita, Y. *J. Alloys Compd.***2004***, 374*, 447–450.

[102] Wei, Y.; Kumagai, M.; Takashima, Y. *Nucl. Technol.* **2000**, *132*, 413–423.

[103] Hoshi, H.; Wei, Y.; Kumagai, M.; Asakura, T.; Morita, Y. *J. Alloys Compd.* **2006**, *408–412*, 1274–1277.

---

[104] Mimura, H.; Hoshi, H.; Akiba, K.; Onodera, Y. *J. Radioanal. Nucl.* 2001, 247(2), 375–379.

[105] Sengupta, A.; Gupta, N. K. *J. Environ. Chem. Eng.* **2017***, 5 ,* 5100.

[106] Trewyn, B. Heterogeneous catalysis for today’s challenges: synthesis, characterization and applications, Royal Society of Chemistry Publishing, Cambridge, 2015.

[107] Auerbach , S. M.; Carrado, K. A.; Dutta, P. K. *Handbook of zeolite science and technology*, Marcel Dekker, New York, 2003.

[108] Valdés, M. G.; Pérez-Cordoves, A. I.; Díaz-García, M. E., Trends. Anal. Chem. **2006**, *25*, 24–30.

[109] Baile, E.; Fernández, L.; Vidal, A. Canals,P. *Zeolites and zeolite-based materials in extraction and microextraction techniques*; Analyst, **2019**, *144*, 366

[110] Uddin, F. *Metall.Mater.Trans. A*. **2008**, *39(12)*, 2804-2814.

[111] Prabhu, P.*;* Prabhu, *B. A Review on Removal of Heavy Metal Ions from Waste Water using Natural/ Modified Bentonite* ; MATEC Web of Conferences **2018**,*144*, 202.

[112] Sadegh, H.; Ghoshekandi, R.S.; Masjedi, A.; Mahmoodi, Z.; Kazemi, M. *Int. J. Nano Dimens.***2016***, 7*,109–120

[113] Fu, F.; Wang, Q. *J. Environ. Manage.* **2011**, *92*, 407.

[114] Rao, G.P.; Lu, C.; Su, F. *Sep. Purif. Technol.* **2007**, *58*, 224.

[115] Kumar, R.; Khan, M. A.; Haq, N. *Crit. Rev. Environ. Sci. Technol.* **2014**, *44* ,1000.

[116] Salam, M.A. *Int. J. Environ. Sci.Technol.* **2013***, 10* , 677.

[117] Farghali , A. A.; Tawab, H. A. A.; Moaty, S. A. A.; Khaled, R. *J. Nanostruct. Chem.* **2017**, *7*, 101.

[118] Chen, C. L.; Li, X. L.; Wang, X. K. *Radiochim. Acta.* **2007**, *95*, 261.

[119] Ma, F.; Qu, R.; Sun, C.; Wang, C.; Ji, C.; Zhang, Y.; Yin, P. *J. Hazard. Mater.* **2009**, *172*, 792.

[120] Guibal, E. *Sep. Purif. Technol.* **2004**, *38*, 43.

[121] Hsien, T.Y.; Rorrer, G. *Ind. Eng. Chem. Res.* **1997**, *36* , 3631.

[122] Atia, A. A. *Hydrometallurgy*, **2005**, *80*, 13.

[123]Griffith, C. S.; De Los Reyes, M.; Scales, N.; Hanna, J. V.; Luca, V. *ACS Appl. Mater. Interfaces.* **2010**, *2*, 3436.

[124] Donald, I. W.; Metcalfe, B. L.; Taylor, R. N. *J. Mater. Sci.* 1997, 32, 5851.

[125] Carolan, J. V. *J. Hazard. Mater.* **2016***, 318*, 266.

[126]PhD thesis of Shusterman, J. A. University of California, Berkeley, 2015.

[127] Ansari, S. J.; Pathak, P.N.; Mohapatra, P. K.;. Manchanda, V. K. *Chem. Rew.* **2012**, *112*, 1751.

[128] Hudson, M. J.; Harwood , L. M.; Laventine, D. M.; Lewis, F. W. *Inorg. Chem*. **2013**, *52*, 3414.

[129] Benedict, M.; Pigford, T. H.; Levi, H. W. *Nuclear Chemical Engineering*, Mc.Graw Hill Book Company, US, 2nd edn. **1981**, 172.

[130] Srinivasan, N.; Nadkarni, M. N.; Balasubramanian, G.R.; Chitnis ,R.T.; Siddiqui, H.R. *BARC Report, Report-643*, Bhabha Atomic Research Centre, Mumbai, India, 1972.

---

[131] Rattan, S. S.; Reddy, A.V.R.; Mallapurkar, V.S.; Singh, R. J.; Prakash, S. *J. Radioanal. Nucl. Chem*. **1981**, *67*, 85.

[132] Mohapatra, P.K., Ph.D. Thesis, University of Bombay,1993.

[133] G.F. Knoll, *J. Radioanal. Nucl. Chem*. **2000**, *243* ,125.

[134] Sood, D.D.; Reddy, A.V.R.; Ramamoorthy, N. "*Fundamentals of Radiochemistry*", 2nd ed., IANCAS publication, BARC, Mumbai,2004.

[135] Cahn, R.W.; Haasen, P.; Kramer, E.J.; Material Science and Engineering: Characterisation of Materials, VCH Publisher Inc., New York, 1991

[136]Zhou, W.; Wang, Z. L.; Scanning microscopy for nanotechnology: Techniques and applications, Springer science and business media, New York, 2006.

[137]Dabrowski, A. *Adv.Colloid Interface Sci.* 2001, *93*, 135.

[138] McKay, G.; Porter, J. F. *Process Safety and Environmental Protection*, **1997**,*75*, 171.

[139] Das, D.; Das, N.; Mathew, L. *J. Hazard. Mater.* **2010**, *184*, 765.

[140] Allen, S. J.; Gan, Q.; Matthews ,R.; Johnson, P. A. *Bioresour. Technol.***2003, *88***, 143.

[141] Sheha, R. R.; Metwally, E. *J. Hazard. Mater.* **2007**, *143*, 354.

[142] Ho, Y. S. *Scientometrics*. **2004**, *59*, 171.

[143] Rudzinski, W.; Plazinski, W. *Langmuir*. **2008**, *24*, 5393.

[144] Rudzinski, W.; Plazinski, W. *J. Phys. Chem. C*. **2007**, *111*,15100.

[145] Allen, S. J.; Gan, Q.; Matthews, R.; Johnson, P. A. *J. Colloid Interface Sci.* **2005**, *286*, 101.

---

[146] Febrianto, J.; Kosasih, A. N.; Sunarso, J.; Ju, Y. H.; Indraswati, N.; Ismadji, S.*J.Hazard.Mater.* **2009**, *162*, 616.

[147]McKay, G.; Ho, Y. S.; Ng, J. C. Y. *Sep.Purif. Methods.* **1999**, *28*, 87.

[148] Plazinski, W.; Rudzinski,W.; Plazinska, A. *Adv.Colloid Interface Sci.* **2009**, *152*, 2.

[149] Ho, Y. S. *Water Research*, **2006**, ***40***, 119.

[150]Rudzinski,W.; Plazinski,W. *J. Phys. Chem. B.* **2006**, *110*,16514.

[151] Ho, Y. S.; McKay, G., *Adsorp. Sci.Technol.* **1998**, *16*, 243.

[152] Ho, Y. S.; McKay, G. *Water Research*, **2000**, *34*, 735.

[153] Sen Gupta, S.; Bhattacharyya, K. G. *Adv.Colloid Interface Sci*. **2011**, *162*, 39.

[154] A. K. Singh Deb et. al., *J. Hazard. Mater.* **2018**, 345, 63–75.

[155] Ma, F.; Qu, R.; Sun, C.; Wang, C.; Ji, C.; Zhang, Y.; Yin, P. *J. Hazard. Mater.* 2009, 172 ,792.

[156] Fasfous, I. I.; Dawoud, J.N. *Appl. Surf. Sci*. **2012**, *259*, 433.

[157]Song, M.; Wang, Q.; Meng, Y. *J. Radioanal. Nucl. Chem.* 2012, 293, 899.

[158] Chen, J.H.; Lu, D.Q.; Chen, B.; OuYang, P. K., *J. Radioanal. Nucl. Chem*. **2013**, *295*, 2233.

[159] Zong, P.; Gou, J. *J. of Mol. Liq*. **2014**, *195*, 92.

[160] Ho, Y. S. *J. Hazard Mater*.2006, 136, 681.

[161] Guillaumont, R.; Mompen, F.J.; Fanghanel, T.; Fuger, J.; Grenthe, I.; Neck,V.; Palmer, D.A.; Rand, N. L. Chemical thermodynamics. vol. 5, Elsevier Science Publication, 2003.

---

[162] Atwood, D. A.; Radionuclides in the environment, in: Wang, X.; Li, J. (Eds.), Chapter: Europium, John Wiley & Sons, 2013.

[163] Singha Deb, A. K., Pahan, S., Dasgupta, K., Panja, S., Debnath, A. K., Dhami, P. S., Ali, S. K., Kaushik, C. P., Yadav, J. S.: *J. Hazard. Mater*. **2018**, *345*, 63 .

[164] Yan,W.; Lien, H.L.; Koel, B. E.; Zhang, W. X. *Environ Sci: Processes Impacts.***2013***, 15*, 63.

[165] Zhang, L.; Fang, M. *Nano Today*. **2010***, 5***,** 128.

[166] Qu, X.; Alvarez Pedro, J. J.; Li, Q. *Water Res* **2013***, 47*, 3931.

[167] PhD Thesis of Englates, K. E. submitted to University of Texas at USA, 2011.

[168] Hua, M.; Zhang, S.; Pan, B.; Zhang. W.; Zhang, Q. *J Hazard Mater.* **2012***, 211/ 212*, 317.

[169] Xu, P.; Zeng, G. M.; Lian Huang, D. L.; Feng, C. L.; Hu, S.; Zhao, M. H.; Lai, C.; Wei, Z.; Huang, C.; Xie, G. X.; Liu, Z. F. *Sci Total Environ.* **2012***, 424*, 1.

[170] Singh, S.; Barick, K. C.; Bahadur, D. *J Hazard Mater.* **2011***, 192,*1539.

[171] Katsoyiannis, I. A.; Althoff, H. W.; Bartel, H.; Jekel, M. *Water Res.* **2006***, 40,* 3646.

[172] Duffó, G. S.; Farina, S. B.; Schulz, F. M. *J. Nucl. Mater.* **2013** *, 438*, 116.

[173] Scott, T. B.; Allen, G. C.; Heard, P. J.; Randell, M. G. *Geochim. Cosmochim. Acta.* **2005***,69*, 5639.

[174] Missana ,T.; Maffiotte ,C.; García-Gutiérrez, M. *J. Colloid Interface Sci.* **2003***, 261*, 154.

[175] Boyer, C.; Whittaker, M. R.; Bulmus, V.; Liu, J.; Davis, T. P. *NPG Asia Mater*. **2010**, *2*, 23.

---

[176] Sahoo, H.; Pizem, T.; Fried, D.; Golodnitsky, L.; Burstein,C.; Sukenik N.; Markovich, G.Langmuir, **2001**, *17*, 7907.

[177] Palmeira-de-Oliveira, R.; Palmeira-de-Oliveira, A.; Gaspar,C.; Silvestre,S.; Martinez-de-Oliveira, J.; Amaral,M. H.; Breitenfeld, L.*Int. J. Pharm.***2011**, *421*, 130.

[178] Wan, J.; Cai ,W.; Meng, X.; Liu, E. *Chem. Commun.*2007, 5004.

[179]. Wong, J. E.; Gaharwar, A. K.; Muller-Schulte, D.; Bahadur D. ; Richtering, W.*J. Nanosci. Nanotechnol.***2008**, *8*, 4033.

[180] Patel, P.R.C. *Desalin. Water Treat.* **2014**, *52*, 481. ; Jolliffe, A.; Hanley, T. L.; *Chem. Commun.* **2015**, 51 , 11433.

[181] Suzuki, H.; Sasaki, Y.; Sugo, Y.; Apichaibukol, A.; Kimura, T. *Radiochim. Acta*. **2004**, *92*, 463.

[182] Tian, G.; Zhang, P.; Wang, J.; Rao, L. *Solv. Extr. Ion Exch.* **2005**, *23*, 631.

[183] Babain, V. A.; Alyapyshev, M. Yu.; Kiseleva, R. N. *Radiochim. Acta.* **2007**, *95*, 217.

[184] Lapka, J. L.; Paulenova, A.; Alyapyshev, M. Yu.; Babain, V. A.; Herbst, R. S.; Law, J. D. *Radiochim. Acta.* **2009**, *97*, 291.

[185] Ansari, S. A.; Pathak, P. N.; Husain, M.; Prasad, A. K.; Parmar, V. S.; Manchanda, V. K. *Radiochim. Acta.* **2006**, *94*, 307.

[186] Romanovskiy, V. N.; Babain, V. A.; Alyapyshev, M. Yu.; Smirnov,I. V.; Herbst, R. S.; Law, J. D.; Todd, T. A. *Sep. Sci. Technol.* **2006**, *41*, 2111.

[187] Alyapyshev, M. Yu.; Babain, V. A.; Smirnov, I. V. *Radiochem.* (Radiokhim. Engl. Ed.) **2004**, *46*, 270.

---

[188] Alyapyshev, M. Yu.; Babain, V. A.; Smirnov, I. V.; Shadrin, A. Yu. *Czech. J. Phys.* **2006**, *56*, 469.

[189] Saravanan, P.; Jayamoorthy, K.; Kumar, S. A. *J. Sci.Adv.Matr. Dev.* **2016**, *1*, 367.

[190] Aneja, K. S.; Bohm, S.; Khanna, A. S.; Bohm, H.L. M. , *Nanoscale*, **2015**, *00*, 1.

[191] Hong, G.W.; Ramesh, S.; Kim, J.H., Lee, H.S. *J. Nanosci. Nanotechnol.* **2015**, *15*, 8048.

[192] Zhu, Z. X.; Sasaki, Y.; Suzuki, H.; Suzuki, S.; Kimura, T. *Ana. Chim. Acta*. **2004**, *527*,163.

[193] Modolo, G.; Asp, H.; Schreinemachers, C.; Vijgen, V. Solv. Ext. Ion. Exch. 2007, 25, 703.

[194] Gong, Y.; Hu, H. S.; Rao, L.; Li, J.; Gibson, J. K. *J. Phys.Chem.A.* **2013***, 117*, 10544.

[195] Gong, Y.; Hu, H.; Tian, G.; Rao, L.; Li, J.; Gibson, J.K. *Angew. Chem.* **2013**, *52*, 6885.

[196] Hirata, M.; Guilbaud, P.; Doblera, M.; Tachimori, S. *Phys. Chem. Chem. Phys.* **2003**, *5*, 691.

[197] Turbomole V6.3 (2009) A development of University of Karlsruhe and Forschungszentrum Karlsruhe GmbH (1989-2007) TURBOMOLE GmbH, since (2007).

[198] Neese, F. *Coord. Chem. Rev.* **2009**, *253*, 526.

[199] Becke, A. D. *J. Chem.Phys.* **1993**, *98*, 5648.

[200] Weigend, F.; Ahlrichs, R. *Phys. Chem. Chem. Phys.* **2005**, *7,* 3297.

[201] Klamt, A. *J. Phys. Chem.* **1995**, *99*, 2224.

[202] Pearson, R. G. *Inorg. Chem.* **1988**, *27*, 734.

[203] Parr, R.G.; Yang, W. *Density functional theory of atom and molecules*, Oxford University Press, 1989, New York.

---

[204] Parr, R.G.; Pearson, R.G. *J. Am. Chem. Soc*. 1983, 105, 7512.

[205] Semon,L.; Boehme, C.; Billard, I.; Hennig, C.; Lutzenkirchen, K.; Reich, T.; Rossberg, A.; Rossini, I.; Wipff, G. *Chem. Phys. Chem.* **2001***, 2,* 591.

[206] Conradson, S. D.; Clark, D. L.; Neu, M. P.; Runde, W.H.; Tait, C.D. *Characterizing the plutonium aquo ions by XAFS spectroscopy*. Los Alamos Sci. **2000,** *26*, 418.

[207] Barnes, C. E.; Shin, Y.; Saengkerdsub, S.; Dai, S. *Inorg. Chem.* **2000***, 39 ,*862.

[208] Taylor, J. C.; Mueller, M. H. *ActaCryst. 1965,* 19, 536.

[209] Allen, P. G.; Veirs, D. K.; Conradson, S. D.; Smith, C. A.; Marsh, S. F. *Inorg. Chem.* **1996***, 35 ,* 2841.

[210] Matta, C. F.; Boyd, R. J. *An introduction to the Quantum Theory of Atoms in Molecules*, Matta, C. F.; Boyd, R. J., 2007 WILEY-VCH Verlag GmbH & Co. KGaA, Weinheim; Page 1-34.

[211] Bryantsev, V. S.; Diallo, M. S.; Goddard, W. A. *J. Phys. Chem. B*. 2008, 112, 9709.

[212] Ciupka, J.; Cao-Dolg, X.; Wiebke, J.; Dolg, M. *Phys. Chem. Chem. Phys*. **2010**, *12*, 13215.

[213] Bryantsev, V.S.; Diallo, M.S.; Goddard, W.A. *J. Phys. Chem. B*. **2008**, *112*, 9709.

[214] Meroni, D.; Presti, L. L.; Liberto, G. D.; Ceotto, M.; Acres,R. G.; Prince, K. C.; Bellani, R.; Soliveri, G.; Ardizzone, S. *J. Phys. Chem. C* **2017***, 121*, 430.

Thesis Highlight

Title of thesis: Preparation and Characterization of Ligand Functionalized Solid Support for the Selective Extraction of f- Elements
Name of the Student: Sumit Pahan
Name of the CI/OCC: Bhabha Atomic Research Centre **Enrolment No.: CHEM01201504001**
Discipline: Chemical Sciences **Sub-Area of Discipline:** Nuclear Waste management
Date of viva voce: 18/04/2021

High level liquid waste generated from reprocessing of spent nuclear fuel contains bulk of fission products along with minor actinides. Efforts has been made in recent past in India for separation of actinides in pure form which can be further used for societal benefits. During the present thesis work, functionalized solid phase sorbents were synthesized for the selective and efficient recovery of f- elements from nuclear waste solution. Some important radionuclides (Uranium, Americium and Europium) have been modeled for this dissertation study. The key highlights of the thesis work are as follows:

synthesis of five different solid phase sorbents (Amidoamine functionalized carbon nanotube, Poly amidoamine functionalized chitosan, Dipicolinamide functionalized titania, Diglycolamide functionalized titania and Poly phosphate functionalized magnetite) were carried out and characterized using XPS, Raman, FTIR, XRD, EDEX etc. All these synthesized materials were evaluated for the extraction of f-elements from nuclear waste. The effect of pH, equilibration time, ionic strength and other ions during extraction and their ability to use in multiple cycle of operation has been investigated. The radiolytic stability of the materials also appraised for their use in nuclear waste management. Based on isotherm sorption data it was concluded that the sorption follows chemisorption mechanism.

Elaborated study for the mechanism of complexation between the modelled metal ion and the synthesized sorbent using Density functional Theory (DFT) were also performed.

The main outcome of the work is that all the functionalized sorbents selectively extract f- elements at lower pH condition.

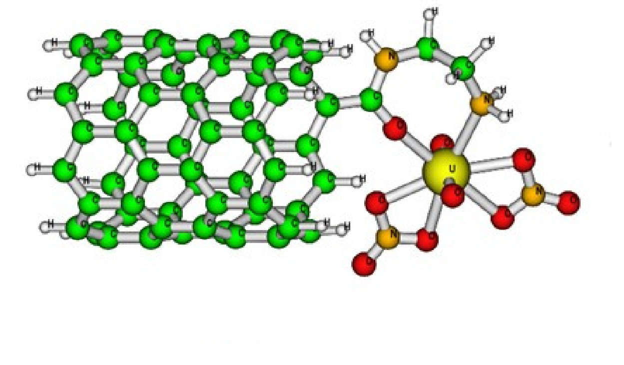

Figure 1. ***Molecular structures of the Uranium complex with amidoamine functionalized MWCNT***

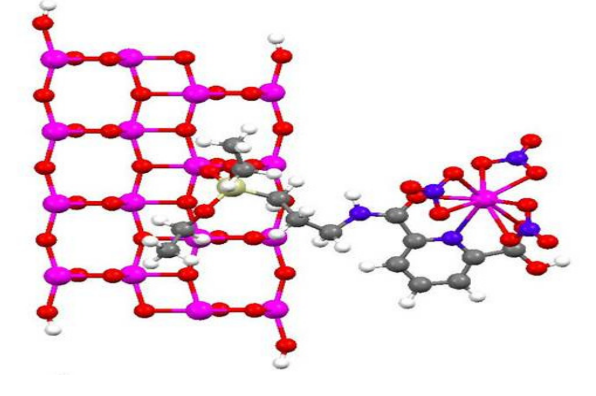

Figure 2. ***Molecular structures of the Americium complex with dipicolinamide functionalized titania***